PNNL-13782 Rev. 1

Pacific Northwest
National Laboratory
Operated by Battelle for the
U.S. Department of Energy

Analysis of Induced Gas Releases During Retrieval of Hanford Double-Shell Tank Waste

BE Wells
JM Cuta
SA Hartley
LA Mahoney
PA Meyer
CW Stewart

September 2002

Prepared for the U.S. Department of Energy
under Contract DE-AC06-76RL01830

DISCLAIMER

PACIFIC NORTHWEST NATIONAL LABORATORY
operated by
BATTELLE
for the
UNITED STATES DEPARTMENT OF ENERGY
under Contract DE-AC06-76RL01830

Printed in the United States of America
Available to DOE and DOE contractors from the
Office of Scientific and Technical Information,
P.O. Box 62, Oak Ridge, TN 37831-0062;
ph: (865) 576-8401
fax: (865) 576-5728
email: reports@adonis.osti.gov
Available to the public from the National Technical Information Service,
U.S. Department of Commerce, 5285 Port Royal Rd., Springfield, VA 22161
ph: (800) 553-6847
fax: (703) 605-6900
email: orders@ntis.fedworld.gov
online ordering: http://www.ntis.gov/ordering.htm

(8/00)

PNNL-13782 Rev. 1

Analysis of Induced Gas Releases During Retrieval of Hanford Double-Shell Tank Waste

BE Wells
JM Cuta
SA Hartley
LA Mahoney
PA Meyer
CW Stewart

September 2002

Prepared for
the U.S. Department of Energy
under contract DE-AC06-76RL01830

Pacific Northwest National Laboratory
Richland, WA 99352

Abstract

Radioactive waste is scheduled to be retrieved from Hanford double-shell tanks AN-103, AN-104, AN-105 and AW-101 and transferred to the vitrification plant beginning in about 2009. Retrieval may involve decanting the supernatant liquid and/or mixing the waste with jet pumps. In these four tanks, which contain relatively large volumes of retained gas, both operations are expected to induce buoyant displacement gas releases that can potentially raise the tank headspace hydrogen concentration to a level very near the lower flammability limit. This report describes the theory and detailed physical models for both the supernatant decant and jet mixing processes and presents the results from applying the models to these operations in the four tanks. The technical bases for input parameter distributions are elucidated.

Executive Summary

Retrieval of Hanford radioactive tank waste from four double-shell tanks (DSTs), AN-103, AN-104, AN-105, and AW-101, to the vitrification plant is planned for 2009 to 2019. Retrieval will involve decanting the supernatant liquid and/or mixing the waste with two large jet mixer pumps. All four tanks retain sufficient gas to reach or exceed the lower flammability limit (LFL) if a large fraction of the retained gas volume were released suddenly. They also exhibit spontaneous buoyant displacement gas release events (BDGREs).

Given this relatively large volume of retained gas and a history of relatively large spontaneous gas releases, retrieval operations need to be planned carefully to ensure they can be performed safely. The large mixer pumps planned to be installed to aid retrieval can quickly mobilize most of the waste in the tank. Upon pump startup, they could release a large fraction of a tank's stored gas in a short time. Decanting the supernatant liquid can be expected to induce a series of BDGREs by reducing the hydrostatic pressure and causing the stored gas to expand.

Detailed models of the gas release behavior during both supernatant decant and initial mixer pump operation have been developed that include the dominant phenomena and important mechanisms that can potentially exacerbate gas releases. This report describes the development of the models, the selection of inputs, and the results of simulations of supernatant decant and initial waste mixing in the four tanks.

Gas Releases Induced by Supernatant Decanting

Supernatant liquid is to be decanted by a transfer pump installed just above the top of the sediment layer. As the liquid is removed, the hydrostatic pressure on the gas retained in the sediment layer decreases, causing the trapped gas bubbles to expand, which increases the gas volume fraction. Portions or "gobs" of the sediment with a sufficiently high initial gas volume fraction will become buoyant and undergo BDGREs. Once buoyant, gobs induced to rise by the decant are assumed to behave like those participating in spontaneous gas releases.

The initial gob size and gas fraction distributions are determined by tank historical behavior and measured data, as is the gas release rate when a BDGRE occurs during decant. Sediment suspended during prior BDGREs increases the density of the liquid, which increases the buoyancy of the gobs relative to the liquid and hence further promotes BDGREs.

As the supernatant depth decreases the tank headspace increases, so the same gas release volume will produce a progressively lower hydrogen concentration. At some point, the depth will decrease to a level where there is insufficient potential energy to yield the waste, and gas releases will effectively cease. Thus, the highest hydrogen concentrations resulting from induced BDGREs tend to occur early in the process.

A Monte Carlo simulation approach was used in the modeling. A large number of model runs were performed with different sets of input to correctly portray the combined uncertainty of the input parameters in the results. The input sets for each run were selected from probability

distributions for each parameter such that the entire uncertainty range was covered. Probability distributions representing the results were then derived from the set of outputs from all the runs. The results were most sensitive to the liquid and sediment densities, which determine the gas volume fraction at neutral buoyancy and the gas fraction and size of the initial BDGRE.

The base case simulation comparing the gas release behavior of the four tanks used a decant rate of 200 gpm. Three additional cases were studied: a 30-gpm decant rate, a control strategy to pause the decant when the hydrogen concentration exceeded the action level of 6,250 ppm and then restart at 500 ppm, and a second control strategy to backfill with water at the same rate as the decant to limit the decrease in hydrostatic pressure.

The results of the simulations in AN-105 are summarized as follows:

- The peak hydrogen concentration at the 95% confidence level remained at or below 8,300 ppm in all cases (ranging from a maximum of 8,300 ppm in the base case to 7,600 ppm for the water backfill control strategy).
- The median value of the fraction of retained gas in the sediment layer released during decant was only 0.09, and 0.22 or less at the 95% confidence level.
- Reducing the decant rate to 30 gpm had essentially no effect on the peak hydrogen concentration or any other output parameter except to increase the total decant time in proportion to the lower rate.
- The stop-start control strategy had a minimal effect on the peak hydrogen concentration but extended the time for decant by about a factor of 3.
- Backfilling the tank with water did not significantly change the hydrogen concentration at the 95% confidence level but prevented BDGREs in over 76% of the cases.

The simulations for Tanks AN-103, AN-104, and AW-101 exhibited induced BDGRE behavior similar to that of AN-105. The peak hydrogen concentration distribution for AN-104 was similar to AN-105 because its slightly larger retained gas volume was balanced by a correspondingly larger headspace. Because of its much lower retained gas volume, the peak hydrogen concentrations in AW-101 remained well below the action level of 6,250 ppm for all cases. Because AN-103 contains more than twice the retained gas volume of AN-105 and the initial gas volume fraction is more likely to be closer to neutral buoyancy, its peak hydrogen concentration at the 95% confidence level was much larger, 21,100 ppm, exceeding 50% of the LFL (approximately 20,000 ppm).

Though these predictions indicate that AN-103 has a greater potential hazard than the other tanks, the results are much more uncertain. There have been too few spontaneous BDGREs in this tank from which to derive statistically valid input distributions. It may be that decant-induced gas releases in this tank will follow its historical trend in a series of small releases that do not challenge flammability. However, the high uncertainty should engender a corresponding level of caution in planning its retrieval.

Gas Releases Induced by Initial Mixer Pump Operation

Mixing induced by submerged jets is capable of mobilizing sediment by creating hydrodynamic shear and pressure forces that exceed the strength of the material. This disruption of sediment causes the release of retained gas bubbles that eventually enter the tank headspace. Thus, gas release is expected from the region of waste actually disrupted. A powerful mixer pump may potentially affect a large waste volume at a relatively high rate, which by design suspends a large fraction of the mobilized solids in the liquid layer. As described above, this increases the density of the supernatant, reducing the neutral buoyancy gas fraction and potentially inducing BDGREs in gobs that were not buoyant when mixing began.

The model developed to simulate this process treats gas releases from both the direct disturbance of the mixer pump and the subsequent induced BDGREs. It consists of two independent parts: the first estimates the volume of waste actually mobilized by a mixer pump of known characteristics running at a given speed and duration; the second determines the headspace hydrogen concentration resulting from a specified schedule of pump runs, each of which mobilizes a given volume of waste. The first model is built on turbulent free jet theory, and the second is a direct adaptation of the detailed supernatant decant model described above, with relatively minor modifications.

The mixing model assumes that the flow from the pump nozzles behaves as a turbulent jet impinging on and slowly penetrating a wall of weak solid material. The net hydraulic power of the jet delivered to the waste at the penetration zone is set equal to the power required to yield the solid matrix. Jet theory applied to this energy balance shows that the maximum volume of waste disturbed is proportional to the quantity $(u_0 d_0)^3$, where u_0 and d_0 are the initial jet velocity and nozzle diameter, respectively, while the time required to achieve this disturbance is proportional to $u_0 d_0$. The model was used to extrapolate gas release data from initial mixing tests in SY-101 to degassing AN-105 with much larger mixer pumps. The results indicate that a 26-minute mixer pump run at 1200 rpm (maximum speed) would theoretically mobilize 5% of the sediment volume in AN-105. A 76-minute run at the same speed mobilizes about 20% of the sediment.

The gas release model results for AN-105 indicate that 5% of the sediment can be mobilized per pump run on a schedule of one run per day and the headspace maintained well below the LFL. The median of the peak hydrogen concentration for this schedule is 7,500 ppm with 18,100 ppm at the 95% confidence level. Raising the disturbance to 20% of the sediment layer per run per day exceeds 50% of the LFL with 28,400 ppm of hydrogen at the 95% confidence level.

AN-104, with a larger headspace than AN-105, has a 95% confidence level at 18,500 ppm for runs disturbing 20% of the sediment layer every 24 hours. The low gas volume of AW-101 allowed for runs disturbing 20% of the sediment layer on a schedule of three times per day. The median peak hydrogen concentration is 6,900 ppm, and the 95% confidence level is 8,800 ppm. The large headspace of AN-103 is overwhelmed by the high gas content, with pump runs disturbing only 5% of the sediment layer every 24 hours, producing a median peak hydrogen concentration of 15,300 ppm and a 95% confidence level of 26,000 ppm.

Contents

Figures

Tables

1.0 Introduction

This report describes an investigation performed by Pacific Northwest National Laboratory (PNNL) for CH2MHILL Hanford Group, Inc. (CHG) on potential flammable gas releases from proposed retrieval operations in four double-shell tanks (DSTs). The tanks are AN-103, AN-104, AN-105, and AW-101.[(a)] The operations, which involve removing or decanting the supernatant liquid or mixing the waste with two jet mixer pumps, or both, are planned for waste feed delivery to the vitrification plant in 2009–2019. Such operations are challenging in these tanks because each of them has exhibited spontaneous buoyant displacement gas release events (BDGREs) that have ranged from less than 1 to more than 30 standard cubic meters of gas (30–1,200 scf) containing 30 to 60% hydrogen. Only twice have these releases raised the headspace hydrogen concentration to more than 25% of the lower flammability limit (LFL) in AN-105 during the six to seven years that headspace hydrogen concentration has been monitored.[(b)] However, all four tanks retain enough gas to reach or exceed the LFL if a large enough fraction of the retained gas volume were released suddenly (Hedengren et al. 2000).

Given this relatively large volume of retained gas, retrieval operations could potentially create a hazardous gas release. The large mixer pumps that are planned to be installed have the capability of mobilizing most of the waste in the tank. Upon pump startup, they could release a large fraction of a tank's stored gas in a short time. Decanting the supernatant liquid can trigger a series of BDGREs by reducing the hydrostatic pressure and causing the stored gas to expand. Both operations therefore need to be planned carefully to ensure they can be performed safely.

This report presents the results of a detailed model of the gas release behavior during both supernatant decant and initial mixer pump operation that puts the potential for induced gas releases in perspective. Section 2 describes the search for mechanisms that could exacerbate gas release during decant or mixing; Section 3 analyzes gas releases during decant, including the mathematical model, parameter definitions, and analysis results. Section 4 analyzes gas releases during initial mixer pump operation, and Section 5 presents the conclusions and recommendations from the study. Section 6 lists the cited references. Appendixes are provided with detailed tank waste configuration, waste properties, and an analysis of observed gas release behavior. Appendix E is a CD containing the input data sets, models, and outputs of the Monte Carlo simulations and Excel spreadsheets with analyses of historic gas releases.

The rest of Section 1 provides important contextual information upon which the main body of the report is built. Section 1.1 contains background information on flammable gas release behavior, Section 1.2 summarizes the current understanding of the effects of supernatant decanting and some earlier calculation results, and Section 1.3 describes initial mixer pump operation in SY-101 and an earlier degassing plan developed for AN-105.

(a) In this report the prefix 241- has been left off the tank identifiers.

(b) The peak headspace hydrogen concentration in AN-105 was 1.45% on 5/30/96, 1.75% on 8/21/96, and 0.689% on 4/5/97. One-fourth of the LFL in AN-105 is 0.98% hydrogen; the administrative action level for monitoring is 0.625% hydrogen. The LFL for hydrogen is approximately 4.00% (40,000 ppm).

1.1 Background

There are 149 single-shell tanks (SSTs) with capacities from 50 to 1,000 kgal. These tanks were built in the 1940s, 1950s, and early 1960s. In the 1970s and 1980s, 28 DSTs of 1,200 kgal capacity were constructed. Because of concerns about potential and actual leaks, the SSTs were removed from active use in 1980, and much of their liquid waste has been transferred to DSTs. To conserve tank space, the liquid in the DSTs was typically concentrated by evaporation, which in some tanks formed relatively deep layers of sediment as sodium salts precipitated from the cooling liquid.

All Hanford radioactive wastes generate flammable gases by radiolysis of water, decomposition of organic compounds, and corrosion of the steel tank walls. The main fuel components of the waste gas mixture are hydrogen and, at much lower concentrations, ammonia. The gas also contains nitrous oxide (an oxidizer at temperatures above 1,000K), nitrogen (inert component), and very small amounts of methane and other hydrocarbons. The gas mixture can be ignited if its concentration exceeds the LFL. Hydrogen, with an LFL of 4 vol% in air, typically dominates the flammability of the waste gas (Mahoney et al. 2000). Accounting for the effects of the other fuel gases reduces the LFL slightly to 3.7–3.9 vol%.

Flammable gas generation by itself is not a hazard if the gas is released continuously as fast as it is generated. The rate of gas generation is much slower than the headspace ventilation rate, and the mixing is rapid. The highest gas generation rates are less than 100 scf (2.83 m^3) per day, while the nominal DST ventilation rate is 100 scf (2.83 m^3) per minute. Consequently, the background concentration of flammable gas in the headspace of each of the DSTs has remained far below the LFL.

In some DST wastes, specifically those with deeper layers of supernatant and sediment, the generated gas can accumulate in the sediment until a relatively large volume is released rapidly into the tank headspace. This is a BDGRE. Such sudden releases potentially could cause the concentration of the flammable gas mixture in the headspace to reach the LFL, potentially leading to deflagration if an ignition source were present while the tank headspace remained flammable. If the energy of the deflagration were sufficiently high, the tank could be damaged and radioactive waste released.

The four tanks covered in this report, AN-103, AN-104, AN-105 and AW-101, as well as SY-103, all exhibit BDGREs, though none have made the tank headspace flammable since gas monitoring equipment was installed in 1994–95. A detailed analysis of recorded gas releases of these tanks is given in Section 2.3, and measurements of the waste temperature, level, and GRE history are provided in Appendix A. Tank SY-101 had the largest BDGREs, three of which caused the headspace to exceed the LFL, before mixer pump operation halted them in 1993. The intense study of the behavior of this tank led to a general understanding of BDGREs and how to quantify and predict them to some degree.

The data and observations pertaining to BDGREs indicate that the sediment layer consists of a collection of about 10 to 15 regions, or “gobs,” in different stages of gas retention (Meyer et al. 1997; Meyer and Stewart 2001). A BDGRE occurs when one or more of these gobs of sediment

layer accumulates enough gas to become buoyant with respect to the liquid above it. The buoyant gob rises, and the gas it contains expands as the hydrostatic pressure decreases. The expanding gas bubbles yield the surrounding waste and escape into the headspace as the gob disintegrates at the waste surface. The onset of buoyancy and the subsequent gas release are summarized here and treated in more detail in Section 3.

For the gob to initiate a BDGRE, it must be slightly more than buoyant to overcome the restraining force of the sediment strength. That is, the gas fraction of the gob (α_{gob}) must exceed the critical gas fraction (α_C) defined by (Meyer et al. 1997)

$$\alpha_C = \alpha_{NB} + \frac{\beta\tau_y}{\rho_S g h_S} \tag{1.1}$$

where τ_y is the yield stress in shear, ρ_S is the bulk degassed sediment density, g is the acceleration of gravity, and h_S is the sediment depth. The coefficient, β, is the ratio of the yield stress in tension to the yield stress in pure shear. The stress at yielding may be given by $\beta\tau_y$, where $1 \le \beta \le \sqrt{3}$. In this study, $\beta = 1$ is used because this provides good correlation between the measured and calculated gas fractions in select DSTs (Meyer et al. 1997). The neutral buoyancy void fraction, α_{NB}, is defined in terms of the densities of the liquid and sediment as

$$\alpha_{NB} = 1 - \frac{\rho_L}{\rho_S} \tag{1.2}$$

where ρ_L is the supernatant liquid density. Eq. (1.2) shows that increasing the liquid density lowers the buoyancy point.

The volume of gas released in a BDGRE is determined from the specific gob geometry and void fraction. The in situ volume of gas in a right circular cylindrical gob is given by

$$V_{gas} = h_S \frac{\pi}{4} D_{gob}^2 \alpha_{gob} \tag{1.3}$$

where D_{gob} is the gob diameter and α_{gob} is its gas volume fraction. At the moment the gob breaks free and begins to rise to the surface, $\alpha_{gob} = \alpha_C$. After the gob has risen to the surface, the volume of gas that is released to the tank headspace is given by

$$V_{rel} = \frac{P_S}{P_A} f_{rel} V_{gas} \tag{1.4}$$

where f_{rel} is the fraction of gas released from a gob assuming return to neutral buoyancy at the surface. The average pressure of the gas in the sediment layer, P_S, is given by

$$P_S = P_A + \rho_L g \left(h_C + h_L + \frac{h_S}{2} \right) \tag{1.5}$$

where P_A is the atmospheric pressure, h_C is the crust layer thickness, and h_L is the supernatant depth. The release fraction, f_{rel}, is given by

$$f_{rel} = 1 - \frac{\alpha_{NB}(1-\alpha_C)}{\alpha_C(1-\alpha_{NB})}\frac{P_A}{P_S} \tag{1.6}$$

After the gob has released the portion of its gas defined by Eq. (1.6) and compresses as it falls back to the sediment layer, its gas volume fraction will be reduced to

$$\alpha_{gob} = \left[\frac{P_S}{P_A}\frac{(1-\alpha_{NB})}{\alpha_{NB}} + 1\right]^{-1} \tag{1.7}$$

While a buoyant displacement can occur when the gas volume fraction in the sediment reaches the critical value, gas release will be minimal unless the buoyant potential energy exceeds the energy required to yield the displaced material. A large fraction of the buoyant energy is dissipated in other processes, so the required buoyant energy is much greater than that which would just yield the waste. Stewart et al. (1996a) developed an energy model to account for this. The ratio between the buoyant energy, E_b, and the energy required to yield the gas-bearing gob participating in the buoyant displacement, E_y, is termed the "energy ratio" and may be expressed as

$$\frac{E_b}{E_y} = \frac{\alpha_C \rho_L g h}{(1-\alpha_C)\varepsilon_y \tau_y}\left[\left(1+\frac{1}{\gamma}\right)\ln(1+\gamma) - k\right] \tag{1.8}$$

where h is the distance from the center of the participating gob to the top of the liquid layer, and ε_y is strain at failure, taken to be unity. The parameters γ and k are

$$\gamma = \frac{\rho_L g h}{P_A} \tag{1.9}$$

$$k = \frac{\alpha_{NB}(1-\alpha_C)}{\alpha_C(1-\alpha_{NB})} \tag{1.10}$$

Based on experimental observations and tank behavior, gas can be released when the energy ratio exceeds 3, and significant releases (approximating the release fraction defined by Eq. 1.6) can occur above energy ratios of 5.[(a)]

Because AN-103, AN-104, AN-105, and AW-101 exhibit spontaneous BDGREs at a nearly random frequency, it is impossible to compute a "window" for intrusive activities during which

(a) A more precise definition of rise distance (h) that accounts for the actual buoyancy of the gob at the surface is developed in Section 3. The energy ratio thresholds for gas release with this definition are adjusted accordingly.

no gas releases will happen. Releases of as much as 10 to 20 cubic meters of gas can be expected and should be planned for during any operation in these tanks. At the same time, the global waste disturbances resulting from supernatant decanting and initial mixing can induce additional BDGREs. Section 1.2 describes how this occurs during supernatant decant.

1.2 Supernatant Decanting

The supernatant is planned to be decanted by a transfer pump installed just above the top of the sediment layer. As the liquid is removed at constant rate, the hydrostatic pressure on the gas in the sediment layer decreases and causes it to expand increasing the gas volume fraction. This is the mechanism that triggers gas release during decant. Gobs with a sufficient initial gas volume fraction will become buoyant and undergo BDGREs.

Once buoyant, rising gobs are assumed to behave like those participating in spontaneous gas releases. The initial gob size and gas fraction distributions are determined by tank historical behavior and measured data, as is the actual gas release behavior when a BDGRE occurs during decant. However, as the supernatant depth decreases the tank headspace increases, so the same gas release will produce a progressively lower hydrogen concentration. At some point, the supernatant depth will be insufficient to provide the energy required to yield the waste, as defined by Eq. (1.8), and gas releases will effectively cease. Thus the highest hydrogen concentrations resulting from induced BDGREs can be expected early in the process.

The possibility of these potential BDGREs to occur and to reach the LFL was investigated for Tank AN-105 in 1999.[(a)] This analysis assumed an initial gob size distribution dictated by the sizes of circles, representing individual gobs, that can be fit inside a larger circle representing the tank. The distribution was chosen such that the mean gob diameter was consistent with the mean historic gas release volumes (from Meyer et al. 1997). Initial gas volume fractions equally spaced from neutral buoyancy (Eq. 1.1) down to the minimum value (approximately as given by Eq. 1.7) were assigned to each gob. The largest gob was conservatively assigned the largest gas fraction. This resulted in the modeled tank having about twice the retained gas volume as actually measured. The decant rate was set at 100 gpm.

Figure 1.1 shows the predicted headspace hydrogen concentration over the entire decant process. Because of the linear distribution of gas fraction over the gobs, the induced BDGREs are evenly spaced. Despite the conservative gas volume, the peak headspace hydrogen concentration was well below the LFL, though it exceeded the action level of 6,250 ppm (CHG 2000) during the first two BDGREs. The peak hydrogen concentration for the largest induced release was roughly equivalent to the largest historical GRE, where the hydrogen concentration reached 17,000 ppm. Only five of the ten gobs contained enough gas initially to become buoyant during the decant. These results are consistent with those of the much more complete and detailed analysis presented in Section 3.

(a) PNNL letter report TWS99.44 Rev. 1, August 1999. *Potential for Inducing Gas Releases in Double-Shell Tanks During Retrieval*, by CW Stewart, PA Meyer, and BE Wells.

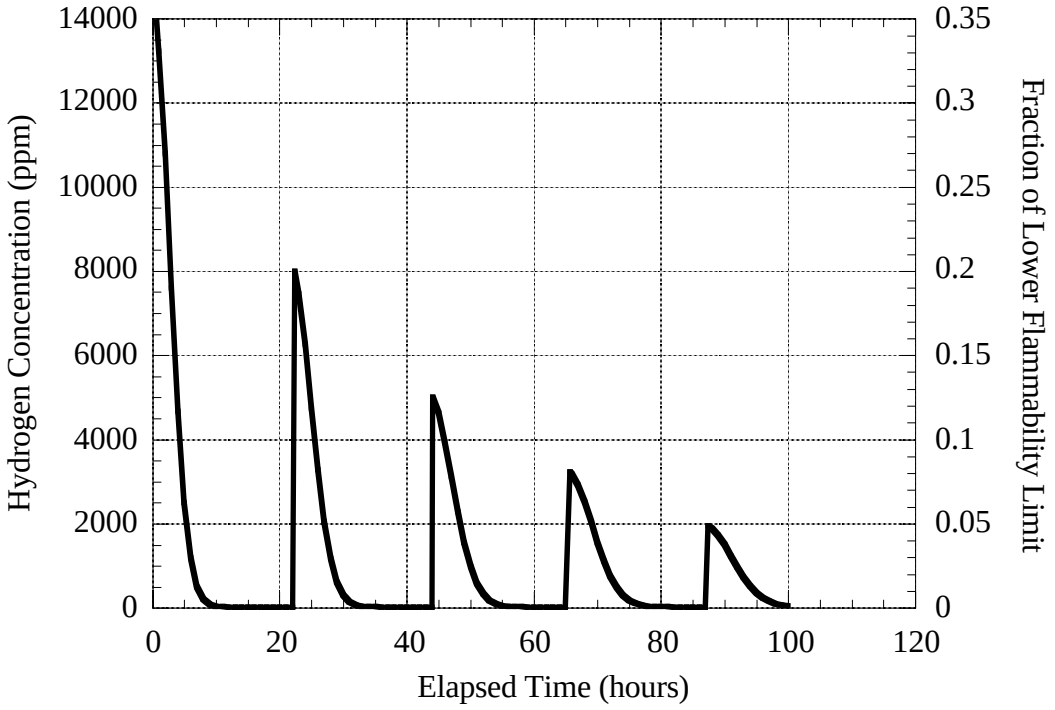

Figure 1.1. Predicted Headspace Hydrogen Concentration in Tank AN-105 During Supernatant Decant from Previous Analysis[(a)]

1.3 Mixer Pump Degassing

Mixer pump operation in SY-101 provided insight into gas releases induced by jet mixing (Allemann et al. 1994; Brewster et al. 1995). The pump was installed on July 3, 1993, just over a week after a 6,000-scf (170 m^3) spontaneous BDGRE. Initial pump operations (Phase A) were extremely gentle because of concerns that pump operation might trigger a major GRE. This initial, low-speed testing did very little to disturb the waste or release gas, but it did show that 5-minute pump runs called "bumps" were required to prevent nozzle plugging. Bumps continued about every other day up to the start of high-speed testing on October 21, 1993. One significant induced BDGRE and two much smaller releases were observed during this period, indicating that some regions of the tank were probably nearly buoyant.

High-speed mixer pump testing (Phase B) began on October 21, 1993 and continued until December 17, 1993. Testing consisted of a series of pump runs aimed at undisturbed waste and lasting from 20 to 30 minutes at up to almost full speed (920 rpm). Figure 1.2 shows the daily peak hydrogen concentrations and the waste surface level during Phase B testing (Allemann et al. 1994). A large volume of gas was released during the first few weeks.

(a) PNNL letter report TWS99.44 Rev. 1, August 1999. *Potential for Inducing Gas Releases in Double-Shell Tanks During Retrieval*, by CW Stewart, PA Meyer, and BE Wells.

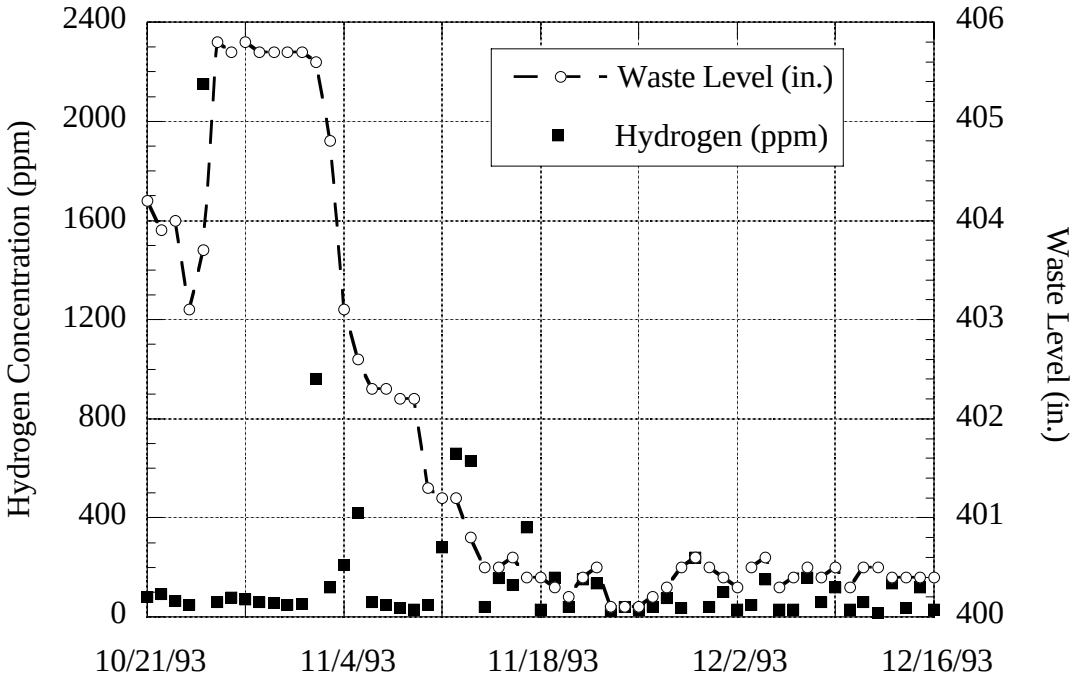

Figure 1.2. Hydrogen Concentration and Waste Level During SY-101 Phase B Mixing

The sudden level rise and high hydrogen concentration on November 1 is a clear example of an induced BDGRE, although the gas release was delayed several days. Two runs, at 320 and 520 rpm, had been made with the jets turned 30 degrees into undisturbed waste. The event occurred during the third run in the same direction at 920 rpm. A significant gas release accompanied the level rise, and another somewhat smaller one signaled the later level drop. But because the level remained relatively constant for over a week before suddenly dropping again, the waste apparently floated on the surface without releasing its gas during that time. No further episodes of this kind were seen. By early December the jets had mixed most of the gas-bearing sediment layer because gas releases for the remainder of Phase B testing were relatively small.

A degassing strategy using the two mixer pumps proposed for retrieval of AN-105 was developed based on the mitigation of SY-101 during Phase B pump operations (Caley et al. 1998). The mixer pumps proposed for AN-105 are significantly more powerful than the mixer pump in SY-101; at their minimum operating speed of 700 rpm, they approximate the maximum performance of the SY-101 mixer pump at its maximum practical speed of 1000 rpm. The degassing plan for AN-105 accommodated mixer pump differences by operating one pump at a time and limiting the duration. The differences in the two pumps are summarized in Table 1.1.

The maximum cumulative gas release for a single day in SY-101 during the Phase B testing was 14.3 m^3 (well below that required to reach the LFL). This gas release resulted from four 20-minute mixer pump runs at 360, 510, 720, and 920 rpm at a fixed angle. The calculated energy supplied to the waste by the pump during this period was approximately 18.2 kW-hr (Caley et al. 1998). A single mixer pump in AN-105, operated at 700 rpm for 24 minutes, was calculated to

Table 1.1. Design Parameters of the SY-101 and W-211 Mixing Pumps

Parameters	SY-101	AN-105 (W-211 Project)
Power	112 kW (150 hp)	224 kW (300 hp)
Speed	100 to 1,180 rpm	700 to 1,200 rpm
Pumping capacity	0.18 m^3/s (2,800 gpm)	0.69 m^3/s (11,000 gpm)
Inlet nozzle location	6.6 m (260 in.) above tank bottom	17.8 cm (7 in.) above tank bottom
Discharge nozzle location	71 cm (28 in.) above tank bottom	45.7 cm (18 in.) above tank bottom
Discharge nozzle diameter	6.6 cm (2.6 in.)	15.2 cm (6 in.)
Tank position	0.9 m (3 ft) west of tank center	6.1 m (20 ft) north and southeast of tank center (2 pumps total)

supply equivalent energy for a roughly equivalent waste disturbance. It was suggested that during degassing each W-211 mixer pump be run individually at 700 rpm for 24 minutes in varying directions to remove the bulk of the stored gas before being operated simultaneously at full power.

1.4 Improving the Models and Predictions

The work described above was performed in 1998 (Caley et al. 1998) and 1999.[(a)] During this time the most urgent safety issue at Hanford was the waste level growth phenomenon occurring in SY-101. The supernatant decant and mixer pump degassing issues were relegated to low priority. Except for a scoping calculation for supernatant decant in SY-103,[(b)] no further analysis or development was performed.

In February and March of 2001, the Defense Nuclear Facility Safety Board (DNFSB) staff reviewed the earlier decanting model and results and questioned the assumption that induced GREs should be similar to historical spontaneous releases. In response to the DNFSB review, a workshop was held at PNNL in July 2001 to identify plausible mechanisms that could increase BDGREs beyond historical observations. Experts with considerable experience in the Hanford flammable gas issue participated from PNNL, CHG, and other contractors. The team developed a relatively long list of potential mechanisms that might exacerbate induced releases during both supernatant decant and initial mixing.

(a) PNNL letter report TWS99.44 Rev. 1, August 1999. *Potential for Inducing Gas Releases in Double-Shell Tanks During Retrieval*, by CW Stewart, PA Meyer, and BE Wells.
(b) PNNL letter report TWS01.01, September 2000. *A Strategy for Remediation and Return-to-Service for Tank 241-SY-103*, by BE Wells and CW Stewart.

The list of mechanisms was reviewed in detail, and calculations were performed as appropriate to evaluate whether they could have a significant effect. Several important mechanisms were selected for inclusion in improved models for the processes. The results were reviewed by an ad hoc committee of PNNL and CHG staff that included scientists, managers, and nuclear safety and licensing experts. The detailed explanation and disposition of each of the proposed mechanisms is the subject of Section 2.

The assimilation of the model improvements, development of input parameter distributions for the Monte Carlo analysis (itself a significant improvement in modeling strategy), and results of the improved models were reviewed during a series of meetings from August through November 2001. The results of the improved supernatant decant model were presented to the DNFSB on November 19, 2001. The models and results are discussed in Sections 3 and 4.

2.0 Phenomena That Could Amplify Gas Releases

This section describes potential mechanisms that could produce gas releases during supernatant decanting and mixer pump degassing that are larger than those observed historically. The list was developed by a group of experts from PNNL and CHG in a workshop held July 3, 2001. Each of the proposed mechanisms was evaluated for inclusion in the enhanced gas release model described in Section 3. Those included are so indicated in the discussion. Phenomena active during supernatant decanting are evaluated in Section 2.1 and those accompanying initial mixer pump operation in Section 2.2. A reanalysis of the historical gas release data is given in Section 2.3.

2.1 Phenomena Active During Supernatant Decanting

Some phenomena relating to gas release may actually be caused by the decant process and do not occur during spontaneous GREs. These generally involve void growth during depressurization, which is shown to be different from accumulation of internally generated gas. These factors are generally included in the enhanced model for the depressurization process.

Other mechanisms take effect after a gob has become buoyant. Though the process of void growth to buoyancy is much faster during decant than during gas accumulation leading to spontaneous GREs, the actual release process must occur on fundamentally the same length and time scales as historic spontaneous GREs. Thus gob interactions resulting from the release process itself should be similar regardless of the process by which buoyancy is achieved, though there may be differences in degree. These effects, for the most part, are not included specifically in the model but are assumed to be included within the historic GRE data.

Section 2.1.1 describes proposed mechanisms that could make more gobs buoyant at the same time. Section 2.1.2 covers potential changes in the effective material strength. Changes in the shape of the void profile are discussed in Section 2.1.3; the effect of local disturbances during the release of the first gob is treated in Section 2.1.4; and Section 2.1.5 discusses global effects on the release of the first gob. Various other issues are covered in Section 2.1.6.

2.1.1 Mechanisms Making More Gobs Buoyant at the Same Time

Though gas releases from each gob during decant may be indistinguishable from historic releases, the decant process may cause more gobs to release at or near the same time, causing a much larger than historical release. The most important of these mechanisms are the uncertain changes in gob size and void distribution that have occurred in the past few years due to waste cooling, as described in subsection 2.1.1.4.

2.1.1.1 Lateral Void Migration

Lateral movement of retained gas from a high-void gob into surrounding regions during depressurization by an unknown mechanism brings more gobs to near-buoyancy at the same time.

Not included in model. This concept is incorrect. Bubbles can only move down a pressure gradient established by the surrounding fluid. In a hydrostatic pressure field, the force on a bubble is strongly upward, which would prevent significant lateral migration. Even if it could occur, lateral migration would be opposite the proposed mechanism. A locally higher void region would create a lower hydrostatic pressure due to its relative buoyancy. This pressure sink would tend to draw bubbles from lower void surroundings, making the void higher still.

2.1.1.2 Faster Gas Expansion

During decant, the average void in the tank is greater than that during natural growth because all the gas is expanding.

Included in model. While the average void increases as the hydrostatic pressure decreases, the difference in void between gobs increases because the change in void with pressure increases with void. Natural gas generation produces a constant void growth. This means that during decant the gob with the highest void will grow fastest, so the next gob in line will be relatively less buoyant when the first one goes—causing BDGREs to occur at wider intervals. The local void change with pressure is included in the enhanced model (see subsection 2.1.3.3).

2.1.1.3 Bypass of Background Release

Decant bypasses background gas release mechanisms and could make gobs buoyant that would not have been so under natural conditions.

Not included in model. This effect is inconsequential. The gobs affected by this phenomenon would become buoyant toward the end of decanting, when headspace is at a maximum and hydrostatic pressure at a minimum. This effect is not included in the enhanced model.

2.1.1.4 Changes in Observed Gob Size and Void Distribution

Changes in BDGRE behavior in the last few years, with more very small releases, may be changing the distribution of gob sizes and the relative void fraction.

Included in model. This trend increases uncertainty in historic tank behavior. Several tanks have had few or no large, historically typical gas releases in several years. However, the waste levels have stayed constant or decreased, indicating no increase in gas retention. Gob size and gas distribution could be expected to differ from earlier historically inferred parameters, but the direction is not known. A more uniform gob size and void would exacerbate gas releases. This uncertainty is included in the Monte Carlo simulation by wider input distributions on gob size and initial void.

2.1.1.5 Evaporation of Dissolved Gas

Depressurization will cause saturated dissolved gas to come out of solution into existing bubbles. This does not occur during natural void growth and would increase the void at a faster rate than depressurization alone.

Not included in model. This mechanism is inconsequential. Ammonia is the major dissolved gas component with some contribution by nitrous oxide. However, the amount of both of these gases that is dissolved in the liquid is relatively small in the tanks to be decanted. Calculations of bubble expansion during decant based on Henry's law show that the additive effect of dissolved gas is small. This phenomenon is not included in the enhanced model.

2.1.2 Changes in Sediment Strength

The relatively rapid expansion of bubbles and other effects may change the effective yield stress of the sediment. This means that less over-void would be needed to enable a buoyant gob to detach than would be needed during natural void growth. However, none of the proposed mechanisms are significant.

2.1.2.1 Bubble Expansion Decreases Bulk Yield Strength

The solid-liquid matrix surrounding each bubble yields during expansion, reducing the average yield strength. This could reduce the over-void needed to make a buoyant gob break away.

Not included in model. The effect of strength is inconsequential. A lower yield stress lowers the over-void needed for gob detachment, which also reduces the energy of the release. Lower strength makes the length scale smaller, which would tend to make released gobs smaller. However, at the length scale of a gob, the effect of material strength is small and the over-void is minimal. It is also believed that the strength is reduced only in the immediate vicinity of the bubble and does not affect the bulk waste. A local reduction in yield stress would allow individual bubbles to disengage, lowering the gas content of the gob. This effect is not included in the enhanced model.

2.1.2.2 Bypass Slow Relaxation

Faster gas expansion in decant prevents slow "relaxation" of material, which effectively increases the average yield stress.

Not included in model. This effect is inconsequential. Avoiding a postulated relaxation process might increase the bulk yield stress relative to that occurring during natural GREs. This would increase the over-void required to release a gob, increasing the energy of the release and raising the potential for multiple gob releases. However, at the scale of a gob, the effect of material strength is small and the over-void is minimal. This hypothetical effect is not included in the enhanced model.

2.1.2.3 Small Disturbances

Propagation of small vibrations due to transfer pump operation could cause relative particle motion and reduce the bulk waste strength.

Not included in model. Rationale given in subsection 2.1.2.1.

2.1.3 Changes in Void Profile Shape Due to Depressurization

One of the most important results of this study is the conclusion that depressurization is fundamentally different from accumulation of gas generated within the waste. The shape of the void profile is shifted slightly relative to the initial profile. While the shape change is greatest in the latter stages of decant, when headspace is at a maximum and hydrostatic pressure at a minimum, the effect is strong enough to warrant inclusion in the enhanced gas release model.

2.1.3.1 Shape Independent of Gas Generation Rate

The shape of the void profile depends on the linear viscosity profile and Stokes form for bubble velocity and is independent of gas generation rate. Therefore, assuming that gas expansion due to depressurization is equivalent to a rapid gas generation rate, GREs due to depressurization are the same as natural ones.

Not included in model. This hypothesis was later shown to be incorrect. While it is true that the void profile is independent of gas generation rate, it is affected differently by depressurization. Depressurization is not equivalent to a faster gas generation rate (see subsection 2.1.3.3).

2.1.3.2 Faster Time Scale for Depressurization

Bubble/void growth during depressurization is much faster than during natural bubble/void growth by generation and migration. The relative bubble size distribution and gas location can be considered fixed during decant.

Included in model. Difference in time scales is the basis for the enabling assumption of the model. Slow migration sets up initial conditions for a much faster decant process. Time scales are so different that gas generation and migration can be ignored during decant. This is the basic enabling assumption of the decant gas release model.

2.1.3.3 Void Profile Shape Changes During Depressurization

The peak of the void profile shifts upward during depressurization.

Included in model. The effect of pressure on void fraction increases with void and the inverse of the gas pressure according to the following expression:

$$\frac{d\alpha}{dP} = -\frac{\alpha(1-\alpha)}{P} \tag{2.1}$$

Integrating Eq. (2.1) between initial state 0 and final state 1 gives

$$\alpha_1 = \left[\frac{P_1}{P_0}\frac{(1-\alpha_0)}{\alpha_0} + 1\right]^{-1} \tag{2.2}$$

The effect of Eq. (2.2) is to cause the void to increase more rapidly at higher elevations. The change in void compared with the initial profile for a hypothetical decant of 1 to 4 m of supernatant from a tank initially with 5 m of supernatant and 5 m of sediment is shown in Figures 2.1 and 2.2 for parabolic and linear void profiles, respectively. For a parabolic profile,

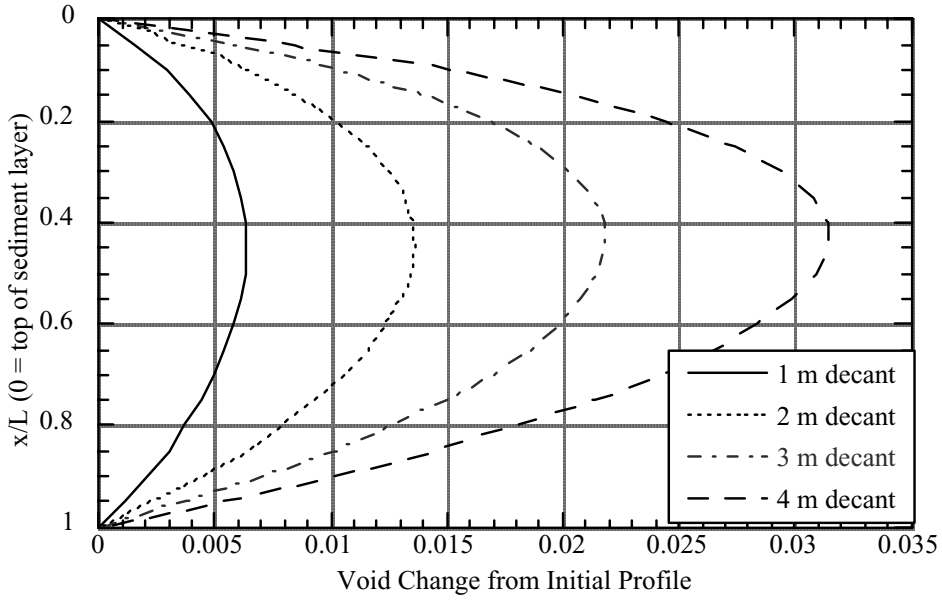

Figure 2.1. Change in a Parabolic Void Profile from Initial Profile During Decant

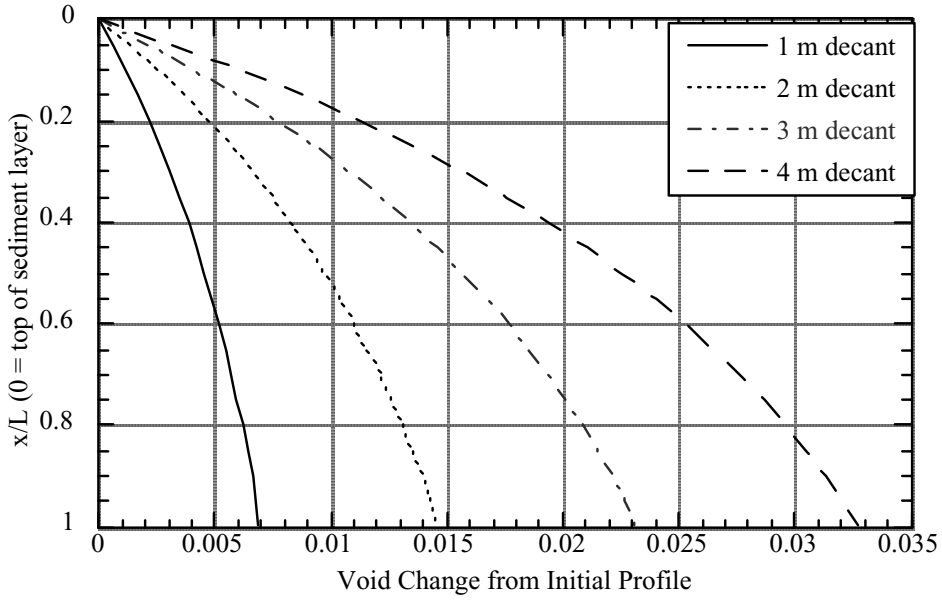

Figure 2.2. Change in a Linear Void Profile from Initial Profile During Decant

void fraction above the peak increases faster, causing the peak to shift upward slightly and reducing the depth of material that becomes buoyant. Also, the average void computed from the void profile increases faster than the effect of the average pressure decrease on the initial average void. For a linear profile the upper portion also grows more rapidly, but the maximum void remains at the bottom. The average of the linear profile lags the effect of pressure on the initial average void, opposite the behavior of the linear profile.

2.1.4 Local Disturbance During Release

The mechanisms in this section all relate to the effects of local disturbances around a releasing gob. The detachment and rise of an over-buoyant gob releases a large amount of potential energy in a few minutes. The fluid motion around a rising gob several meters in diameter can produce large hydrodynamic loads that can move a significant volume of sediment. Also, breaking the forces that were restraining the buoyant gob alters the static force balance of the remaining gobs.

While some of these effects could potentially lead to multiple gob releases or exacerbate single-gob releases, there is no fundamental difference in the dynamics of releases resulting from natural gas accumulation or from depressurization during decant. Therefore, no attempt is made to model any of the specific mechanisms proposed in this section. Their effects are evidenced in observed variation of gas release volume and are included in the gob size and void distributions input to the Monte Carlo simulation.

2.1.4.1 Released Gob Was Restraining an Adjacent Gob

When the buoyant gob releases, part of the restraint on unreleased gobs is removed.

Not included in model: This hypothesis was later shown to be incorrect. Because the primary gob is over-buoyant, it is restrained by adjacent material prior to release. This means that the force it exerts on adjacent gobs is upward, and release of this gob represents a relaxation of the upward force, not removal of a restraining force. The net effect is opposite the proposed mechanism.

2.1.4.2 Stacked Gobs

Release of a part-depth gob causes another gob below it to release.

Not included in model: This hypothesis is implausible. Both gobs would need to be buoyant for both to be released. If both are buoyant, they would act as a single gob. Also, both gobs going buoyant simultaneously would have the same effect as one nominal-sized one.

2.1.4.3 Backflow of Supernatant Removes Overburden

When a gob is released, liquid flows back into the volume it occupied in the sediment. This inflow could sweep overburden off adjacent gobs to make them buoyant.

Not included in model: The upper portion of the sediment is weakest and most subject to disturbance by flow of supernatant. Flow velocities are such that movement of the overburden is minimal. Further, an adjacent gob would need to be nearly buoyant to release. This behavior, if real, is implicitly included in the model through the uncertainty distributions describing historical multiple BDGRE behavior.

2.1.4.4 Overburden Sloughs into the Cavity Left by Rising Gob

Weak material flows to backfill the released gob. This removes overburden to make adjacent gobs buoyant.

Not included in model: Same as subsection 2.1.4.3.

2.1.4.5 Spent Gob Resubmergence

After gas release at the waste surface, it is assumed that a spent gob sinks more or less intact back onto the sediment. When the spent gob contacts the sediment layer, the disturbance could move overburden off another gob so it becomes buoyant.

Not included in model: This hypothesis is implausible. Assuming the spent gob is essentially intact, the outflow of liquid between the falling gob and the sediment would sweep away some of the weak overburden. However, the overburden is immediately replaced by the spent gob, which is probably more negatively buoyant than the overburden it replaces. Also, submergence should be far less energetic than release because the gas content of the falling gob averages less than half of neutral buoyancy.

2.1.4.6 Releasing Gob Lifts Adjacent Sediment

All or part of an adjacent nonbuoyant gob is pulled up, reducing hydrostatic pressure to make it buoyant also.

Not included in model: By definition, a body of sediment that breaks free of the sediment and rises as a single entity is a gob. While a gob must be buoyant on the average, it contains portions that are negatively buoyant and parts that are over-buoyant. The proposed mechanism actually describes the release of a single gob. This behavior is implicitly included in the model through the uncertainty distributions describing historical multiple BDGRE behavior.

2.1.5 Global Disturbance During Release of First Gob

In a global disturbance, release of one gob affects all the remaining waste. This is one area where the decant rate may have an influence, especially for mechanisms involving suspended particles. The effect will be stronger if the period between depressurization-induced GREs is less than the time required for particles to settle out. The most important of these is the reduction of the neutral buoyancy void fraction described in subsection 2.1.5.5. Essentially all of these mechanisms are included in the enhanced decant gas release model.

2.1.5.1 Suspended Solids Increase Hydrostatic Pressure

Suspended solids from prior releases increase the density of the convective layer, which increases the hydrostatic pressure on the nonconvective layer. This pressure increase counteracts some of the expansion from decanting and delays release of subsequent gobs.

Included in model: An increase in hydrostatic pressure compresses stored gas and reduces the void fraction to prevent a gob from becoming buoyant. To illustrate the potential pressure increase, assume an entire gob is suspended in the supernatant and the total volume of supernatant liquid increases by the volume of the gob (i.e., backfills the "hole" left by the suspended gob). Under this scenario, the new density can be calculated by

$$\rho_{CL1} = \frac{H_{CL} A \rho_{CL0} + V_{gob} \rho_{gob}}{H_{CL} A + V_{gob}} \tag{2.3}$$

where H_{CL} is the supernatant depth and A is the tank area. For a large gob, 10 m in diameter and 5 m deep, with a density of 1,600 kg/m^3, suspended in 4 m of supernatant with an initial density of 1,400 kg/m^3, the new density is 1,467 kg/m^3. This raises the pressure beneath 4 m of fluid from 1.568 atm to 1.557 atm, a change of almost 2%, equivalent to 11 cm (7.6 inches and about 21,000 gal) of the original supernatant. Using Eq. (2.2), this pressure change causes a less than 2% reduction in an initial void fraction of 0.10. The effect of solids suspension on the supernatant density and hydrostatic pressure is included in the enhanced model.

2.1.5.2 Gas Release Reduces the Hydrostatic Head

The convective layer depth drops slightly as liquid backfills the "hole" left by the released gas. The corresponding reduced hydrostatic pressure increases the void in remaining gobs.

Included in model: To evaluate this phenomenon, consider the release of all the gas in the large gob described in subsection 2.1.5.1. The 10-m-diameter, 5-m-thick gob contains 39 m^3 of gas in situ, assuming a void fraction of 0.10. Release of this volume would lower the convective layer by 9.5 cm and result in a hydrostatic pressure reduction of only 0.8%, which increases the void fraction by about the same amount. Though insignificant, the effect of gas release on the convective layer volumes and the hydrostatic pressure is included in the enhanced model.

2.1.5.3 Suspension of Solids Increases Supernatant Viscosity

The increased supernatant viscosity could change the size and release characteristics of subsequent gobs.

Not included in model: In classic Rayleigh-Taylor instability, the viscosity difference between layers has a strong influence on the wavelength of the disturbance. In the approximate stability analysis developed to predict the gob diameter (Meyer et al. 1997), the supernatant viscosity was assumed small, and the gob volume was ultimately predicted to be proportional to the sediment yield stress as an approximation of the sediment viscosity. Thus changes in

supernatant viscosity theoretically do not affect the gob size. This is consistent with the assumption that the decant process acts on the gob size and void fraction established by the preceding steady-state period. Supernatant viscosity changes are not explicitly included in the enhanced model, but the distribution of gob sizes generated from the historical BDGREs can be said to implicitly cover the potential effects.

2.1.5.4 Suspension of Solids Reduces Average Overburden

Sediment suspended in the convective layer from prior releases during decant reduces the average overburden on the nonconvective layer, allowing other gobs to release sooner.

Not included in model: This postulation is not correct. Actual, not average, overburden is what determines gob buoyancy. Settling of suspended solids from prior BDGREs would actually add to existing overburden of gobs that have not yet gone. The added overburden would tend to delay their buoyancy slightly. However, this effect is small compared with the effect on neutral buoyancy void fraction discussed in subsection 2.1.5.5. This effect is not included in the enhanced model.

2.1.5.5 Suspension of Solids Reduces the Neutral Buoyancy Void Fraction

Suspension of solids increases the density of the convective layer, which reduces the neutral buoyancy void fraction. Subsequent gobs can therefore be released.

Included in model: Suspended sediment has a strong effect on fluid density. For the example given in subsection 2.1.5.1, an increase in supernatant density from 1,400 to 1,438 kg/m^3 with a sediment density of 1,600 kg/m^3 changes the neutral buoyancy void fraction ($\alpha_{NB} = 1 - \rho_{CL}/\rho_{CL}$) from 0.125 to 0.10, a reduction of 20%. Of course, the entire gob is not suspended but some smaller fraction, possibly 1 to 10%. However, if several gobs are released and a significant fraction of their solids suspended early in decant, the neutral buoyancy void fraction for subsequent gobs would be lowered. There is the potential for all releasable gobs to be released in a rapid sequence. The effect of solids suspension is included in the enhanced model. The fraction of solids suspended is varied in the analysis.

2.1.6 Other Decant Issues

Some of the phenomena in this section did not fit into the categories of prior sections. They include thermal effects and some potential changes in the dynamics of buoyant instability.

2.1.6.1 Slow Thermal Relaxation

The time scale for thermal relaxation is much longer than that of gas expansion. Thus, the temperature profiles of gobs about to be released may be different during decant than during natural growth.

Not included in model: Temperature differences are small. The largest is in AN-104, where the nonconvective layer temperature ranges from 80° to 100°F. Based on observations of

temperature changes in response to natural GREs (Hedengren et al. 2000), release of a gob would expose surrounding unreleased gobs to the lower temperature. Using PV/T = constant, the 20-degree temperature change would reduce the gas volume by 4%. However, the thermal mass of the waste is very high, and this temperature change would require weeks or months to re-equilibrate—much longer than the entire decant process. Lateral temperature nonuniformity effects are not included in the model.

2.1.6.2 Nonequilibrium Thermal Profile

The changing temperatures in resettled gobs could affect release behavior of nearby unreleased gobs.

Not included in model: Same as subsection 2.1.6.1.

2.1.6.3 Atmospheric Pressure Changes

Barometric pressure fluctuations are observed to trigger some GREs that are about ready to release. This effect should approximate the initial stages of decant because the time scales of the pressure change are similar.

Not included in model: This is a potential source of information. The GRE histories of the tanks under consideration can be checked to determine whether GREs that were triggered by a pressure change are different in any significant way from others. However, it is not clear how the results of such a study could be scaled up to the decant process.

2.1.6.4 Decreasing Supernatant Depth

Besides reducing the gob potential energy, lowering the supernatant may change the dynamics of gob release behavior.

Included in model: As the supernatant depth decreases, the hydrostatic pressure on the gas decreases, causing the void in the sediment layer to increase. This is the basic trigger for BDGREs during decant. However, the fraction of the gas that is released also decreases with the hydrostatic pressure by $F = (1-P_0/P_{GAS})$. The release fraction is 50% for P_{GAS} = 2 atm but only 33% for P_{GAS} = 1.5 atm. The potential energy available to cause gas release decreases nonlinearly with supernatant depth such that the later gobs may not release gas at all. These effects were in the original model and are retained in the enhanced model.

2.1.6.5 Dynamics of Buoyant Instability

The natural maximum and minimum unstable gob size may change with depressurization because it is so much more rapid than the natural process.

Not included in model: This hypothesis was later shown to be implausible. The gob size expression developed from an approximate Rayleigh-Taylor stability analysis does not depend on hydrostatic pressure or on the height of the supernatant liquid layer. It does, however, depend

weakly on the neutral buoyancy void fraction, which may decrease after the first GRE (see subsection 2.1.5.5). Therefore, the gob size is expected to be the same for the first event but may change slightly in subsequent releases. The difference is expected to be far less than the uncertainty in the gob size. This is implicitly covered in the analysis, so the potential effect is not included explicitly in the enhanced model.

2.1.6.6 Decant Slowly to Match Natural Time Scale

The lower flow rates (5 to 10 gpm) of current saltwell pumps would perform a decant in months rather than in days. This would more closely approximate the natural time scale.

Investigated: The difference between spontaneous GREs and those induced by decant is more than a matter of time scale alone. It was found that void growth by depressurization of existing gas is fundamentally different from accumulation of gas generated in the waste, though the effect is small for gas fractions of interest. To the extent it accommodates these differences, the enhanced decant gas release model can assess whether much slower decant rates would be advantageous. A sensitivity study showed that the predicted headspace hydrogen concentration is not sensitive to decant rate (Section 3).

2.2 Phenomena Affecting Initial Mixer Pump Operation

Mixing the waste in a tank will release most of the gas stored therein. The desire is to operate the mixer pumps initially so that gas is released in a controlled, predictable manner. Strategies to resolve complications of deploying the mixer pumps may partially degas the tank before the mixer pump is operated. For example, supernatant decant will make it easier to start and run the pump. Specific degassing strategies will need to be modeled when defined. The current modeling effort assumes a degassing scenario similar to SY-101 but using the two W-211 baseline pumps (with bottom inlet) that run in a fixed azimuth one at a time for a relatively short duration. To plan this operation, the ability of these large mixer pumps to mobilize waste needs to be modeled as does the potential for waste mobilization to induce additional gas releases.

Unlike supernatant decanting, where BDGREs are induced by depressurization, the dominant gas release mechanism in mixing is expected to be mobilization of the gas-bearing waste by the jet. The concern is that BDGREs may also be induced that add to the gas released by mixing. Section 2.2.1 addresses direct effects of the jet, while Section 2.2.2 discusses implications of solids suspended by mixing. Section 2.2.3 covers other, nonspecific issues.

2.2.1 Effects of the Jet

The details of mobilizing a sediment bed by a mixer pump jet are not known. However, transient computational fluid dynamics simulations show it to be a complex process of repeated tunneling and collapse that affects a relatively narrow region. This process may induce gas releases or aggravate those already induced by other mechanisms, as discussed in this section.

2.2.1.1 Differences in Mixer Pump Design

The degassing behavior of the baseline W-211 pump with bottom suction may be significantly different than that of the SY-101 pump with high suction.

Not included in model: Bottom suction will tend to produce a neutrally or negatively buoyant jet rather than a buoyant jet as in SY-101. Data show that the buoyancy of the SY-101 jet had a significant effect on the penetration distance. Also, the elevated inlet forces the fluid expelled by the jet to circulate upward, creating a significant lifting force in some situations. Other geometric factors may have as powerful an effect in degassing as the inlet location. However, the only useful data from an actual degassing operation came from SY-101, and there are no data to compare with a similar operation with a bottom-inlet pump. Therefore, while jet buoyancy was considered in developing the model, it was not specifically included in the final form.

2.2.1.2 Mechanical Agitation

If a BDGRE is induced during mixing, the gas release fraction of that gob could be larger due to mechanical agitation if the rising gob is in the area of the jet.

Not included in model: A GRE induced by an increase in the supernatant density due to solids suspension is assumed to release gas until the gob is neutrally buoyant at the surface. This effect is included in the model, but no additional gas release is attributed to fluid agitation. The gob would be rising out of the region of influence of the jet, the region of influence of the jet is relatively small, and the time the rising gob might be exposed to additional turbulence is also small. However, the model includes a reduction in gob volume before it becomes buoyant if it is in the path of the jet.

2.2.1.3 Undermining

The jet penetrates the waste and undermines an area, lifting it up and causing it to become buoyant.

Not included in model*:* Undermining is unlikely. Recent computational simulations show that the jet is more likely to break up the material than to lift it as a coherent body. The bottom inlet of the mixer pump prevents hydraulic lifting, and gobs can be lifted only by dynamic pressure. Also, several factors reduce or prevent significant gas release from a lifted gob: 1) the fraction of gas released in a spontaneous buoyant GRE is less than would be released if the jet disrupted the same volume, 2) some of the gas in a lifted gob would be released in the process of undermining, 3) if a nonbuoyant gob is lifted mechanically so it becomes buoyant at a higher elevation, less energy is released to yield the waste, resulting in a low or negligible gas release. In the limit, a postulated multigob lifting event is similar to supernatant decant. Undermining is not included in the model.

2.2.1.4 Effect of Off-Center Pumps

The two pumps are displaced from the tank center, so one jet will always be impinging on the tank wall (if it runs for a sufficiently long time).

Not included in model: It is unlikely that flow field induced by the jet would erode waste effectively after impingement. However, the model conservatively assumes both jets have an equal effect.

2.2.2 Suspended Solids Effects

As was noted in Section 2.1, suspension of solid particles in the supernatant is a very important factor in inducing BDGREs via decreases in the neutral buoyancy void fraction. This is also a likely occurrence in mixing, as mentioned in subsection 2.2.2.2. Some other effects pertaining to solids are also covered in this section.

2.2.2.1 Increased Supernatant Viscosity

Increases in supernatant viscosity due to solids suspended by mixing and/or gas release may change release behavior.

Not included in model: The effect of higher viscosity would dissipate more energy as the gob rises and thus tends to be moderating rather than exacerbating. Also, gob rise time is short regardless of changes in viscosity.

2.2.2.2 Reduction in Neutral Buoyancy Void Fraction

Mixer pump operation suspends solids, increasing the convective layer density, and reducing the neutral buoyancy void fraction.

Included in model: Solids suspension is a strong effect, as discussed in Section 2.1. The decreased neutral buoyancy void fraction due to solids suspension from both mixing and other induced GREs is included in the model.

2.2.2.3 Dissolution of Solids

Dissolution may occur during mixing if the supernatant is not in equilibrium with the sediment. Dissolution of solids could broaden the region of influence of the jet, release more gas, and increase the density of the supernatant more than suspension alone.

Not included in model: Tanks that have experienced BDGREs, which are of interest in this study, have been stirred periodically by these events over many years so are probably in equilibrium, at least in the major soluble species. No dissolution effects are included in the model.

2.2.3 Other Mixing Issues

This section contains two suggestions that fell outside the preceding categories.

2.2.3.1 Alternative Parameters

The degassing plan should be based on something other than energy input (e.g., effective cleaning radius, momentum).

Not included in model. The degassing plan is not based on parameters such as effective cleaning radius because basic scaling laws demand that the model depend on energy input.

2.2.3.2 Consideration of LANL Safety Analysis

Many exacerbating mechanisms associated with mixing were considered in the Los Alamos National Laboratory Safety Analysis for SY-101 mixing (Sullivan 1995). This document should be reviewed.

Not included in model: The SY-101 LANL Safety Analysis basically ignores detailed mixing and gas release mechanisms, and the major assumption was that mixer pump operation would cause a large GRE. The GRE size was correlated to waste level by extrapolating historic GREs without considering specific mixer pump effects. The document was reviewed and none of the exacerbating mechanisms discussed in the report could be suitably incorporated into the enhanced mixing model.

2.3 Reanalysis of Historical Gas Release Data

To better define the distribution of gob sizes and interaction, a much more detailed analysis was conducted of historic gas releases. This section describes the analysis of GREs in tanks AN-103, AN-104, AN-105, and AW-101 recorded by headspace gas monitoring equipment since 1994–1995 (McCain 2001). While these data have been analyzed before, only recently has it been recognized that many of the events consist of multiple releases occurring relatively close together over a comparatively short time. Headspace hydrogen concentration data for each release event were reviewed to determine whether more than one gob was released. For multigob events, the data were parsed into discrete subevents describing the release of each participating gob. The additional depth of understanding provided by these analyses significantly strengthened the technical basis for the parameter values used for modeling BDGREs during waste retrieval activities.

It was also recognized that the original conservative assumption of instantaneous gas releases (Section 1) was not physically realistic. Using the same rate function used to fit the hydrogen concentration data, gas releases were modeled as functions of time occurring over hours, as observed in the data. This same rate function was used to calculate the rate of suspension of gob material into the supernatant. See the model description in Section 3.1 and the parameter definitions in Section 3.2 for a complete description of these derivations.

The gas release data were parsed into their individual components by applying the exponential gas release model described in Hedengren et al. (2000), which was derived by observing a large number of events. In this model, the hydrogen release rate is assumed to follow the form

$$Q_R = Q_{R0}\left(\frac{t-t_0}{\tau}\right)e^{-\left(\frac{t-t_0}{\tau}\right)} \tag{2.4}$$

where

Q_{R0} = hydrogen release rate constant[(a)]
τ = time to peak release rate
t = current time
t_0 = time at which the release started.

The model uses this release rate in the continuity equation for headspace hydrogen,

$$V_{HS}\frac{dC_H}{dt} = Q_R - Q_{VOUT}C_H \tag{2.5}$$

where

Q_R = model hydrogen release rate (scfm) [from Eq. (2.4)]
Q_{Vout} = headspace ventilation rate (scfm)
V_{HS} = headspace volume (ft^3)
C_H = hydrogen volume fraction in the headspace.

The relationship in Eq. (2.5) is valid as long as $Q_R << Q_V$, which is the case for even the largest GREs. The headspace volume and ventilation rate are assumed constant over the duration of the event. There is also the implicit assumption that the hydrogen gas released in the event very quickly becomes well mixed in the headspace. The hydrogen concentration measurements are therefore assumed to represent the entire headspace. A large body of computational and experimental evidence has shown that this is a reasonable assumption (Huckaby et al. 1997).

The model solves these two equations iteratively, adjusting the parameters Q_{R0} and τ to minimize the cumulative root-mean-square error between the calculated and measured headspace hydrogen concentrations. If the headspace ventilation rate, Q_V, is not known, it must be solved for in the iteration process, subject to the constraint of a reasonable range of possible values and based on physical conditions in the tank and associated ventilation system. When a set of values has been determined that gives an acceptable fit to the hydrogen concentration measurements for the event, total gas release volume due to the GRE can be calculated from the hydrogen release:

$$V_R = \frac{1}{\chi_H}\int_{t_0}^{\infty} Q_R dt = \frac{Q_{R0}\tau}{\chi_H} \tag{2.6}$$

where χ_H is the fraction of hydrogen in the gas retained in the waste.

(a) The peak hydrogen release rate is equal to $Q_{R0}\, e^{-1}$.

For GREs where the measured headspace hydrogen concentration (in ppm) consists of the typical sharp rise followed by an exponential decay, this model does a very good job of characterizing the event. The model fits the changing concentration with time and provides a good estimate of the total hydrogen release volume. Figure 2.3 illustrates this approach for what is clearly a single-release event in AN-104 on October 2, 1995. This event occurred before flow controllers were installed on the tank ventilation system, so the headspace ventilation rate was not known precisely. It was therefore solved for as part of the iterative process of fitting the model to the data. The estimated ventilation rate obtained for this event was 92 scfm, which is a reasonable value for the conditions in the tank at that time.

Since inlet flow controllers were installed in the ventilation systems of the AN farm DSTs in mid-1996, the headspace ventilation rate for AN-103, AN-104, and AN-105 has been maintained at an essentially constant nominal rate, 100 scfm. Figure 2.4 shows a single-release GRE that occurred in AN-105 in 1999. The calculated hydrogen concentration determined with the model is in very good agreement with the measured concentration values. When fitting the model to this event, the headspace ventilation rate was assumed to be constant at the nominal value of 100 scfm, and only the model coefficients Q_{R0} and τ were solved for in the iterative process.

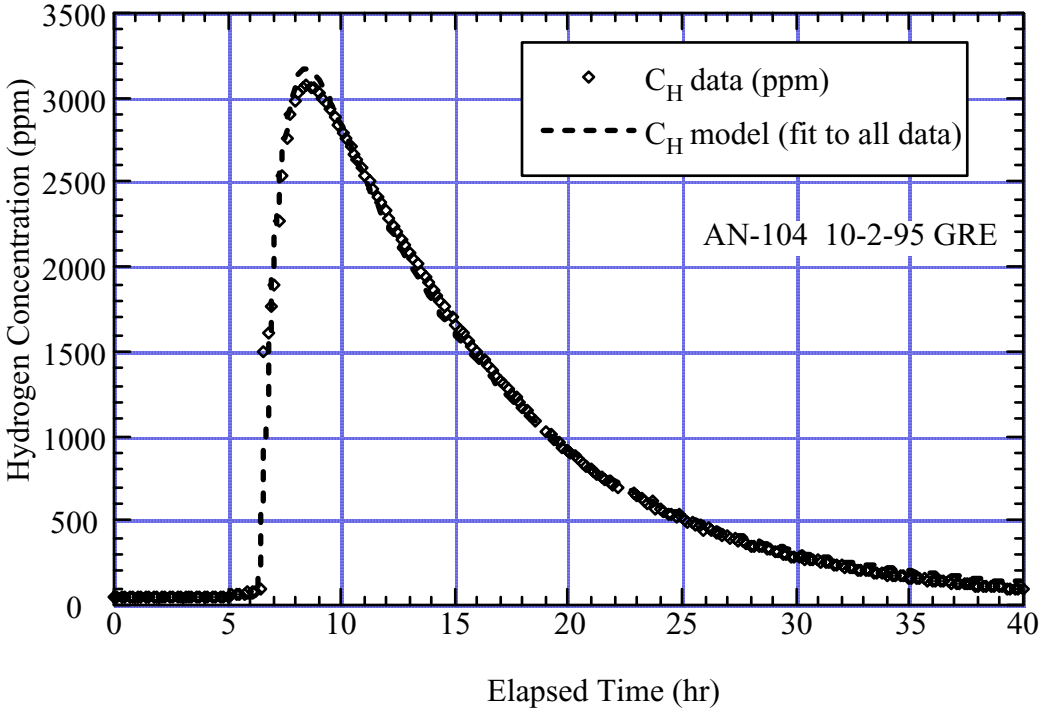

Figure 2.3. GRE in AN-104 on 10/2/95, Comparing Calculated and Measured Headspace Hydrogen Concentrations (ventilation rate unknown; solved for in model application)

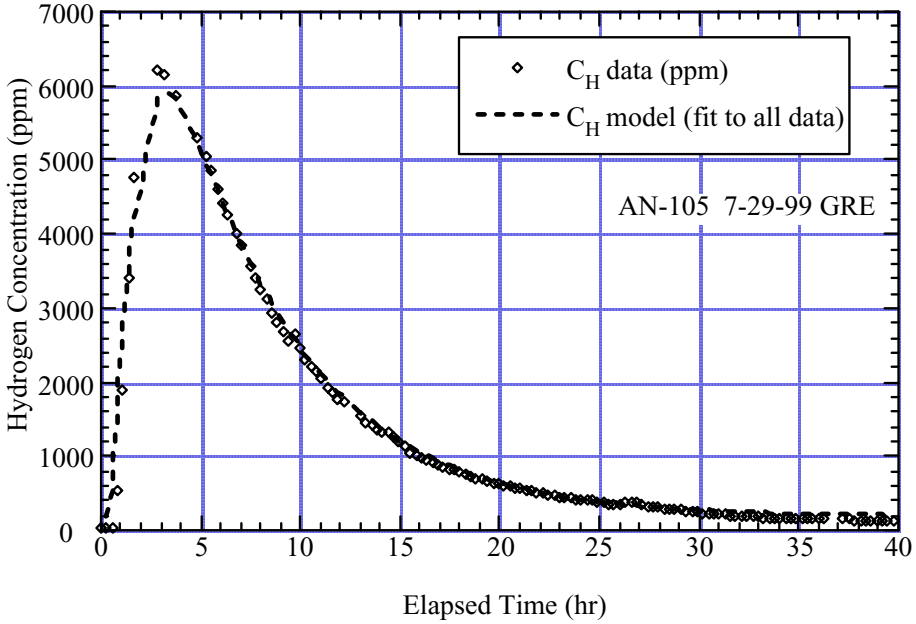

Figure 2.4. GRE in AN-105 on 7/29/99, Comparing Calculated and Measured Headspace Hydrogen Concentrations (ventilation rate known, assumed constant at nominal value of 100 scfm)

Examination of the headspace hydrogen concentration data from tanks AN-103, AN-104, AN-105, and AW-101 shows that GREs in many cases consist of multiple release events. Figure 2.5a shows a number of such releases from two different tanks. The shapes of the hydrogen concentration curves indicate that, in this relatively small sample of multiple-release events, the GREs can consist of two, three, four, or more individual releases. A simple generic model would be unlikely to fit all of these different GREs, even though the underlying events are of the same general character. Further, it is difficult to determine the number of BDGREs in an event until the data are parsed into discrete subevents describing the release of each participating gob.

As an example, if the gas release model is applied to the event in AN-104 on June 2, 2000, treating it as a single release, the “best fit” is that shown by the dashed line in Figure 2.5b. This event consisted of a sharp peak in hydrogen concentration (to 264 ppm), followed by an exponential decay interrupted for a time with a sustained 'hold' at about 200 ppm. Because the ventilation rate is essentially constant and the calculated hydrogen concentration “misses” the time of the peak value and only roughly approximates the shape of the data curve, there is clear evidence that there has been additional gas release since the initial event.

An alternative approach to analysis of such multiple release events has been developed that uses the principle of superposition to parse out the series of gas releases making up the GRE. The model can very accurately represent the peak hydrogen concentration and the exponential decay of the hydrogen concentration as headspace ventilation clears out the released gas and returns to the normal 'background' hydrogen concentration for the tank, and does so very well for those events consisting of a single BDGRE. It is therefore reasonable to suppose that a good

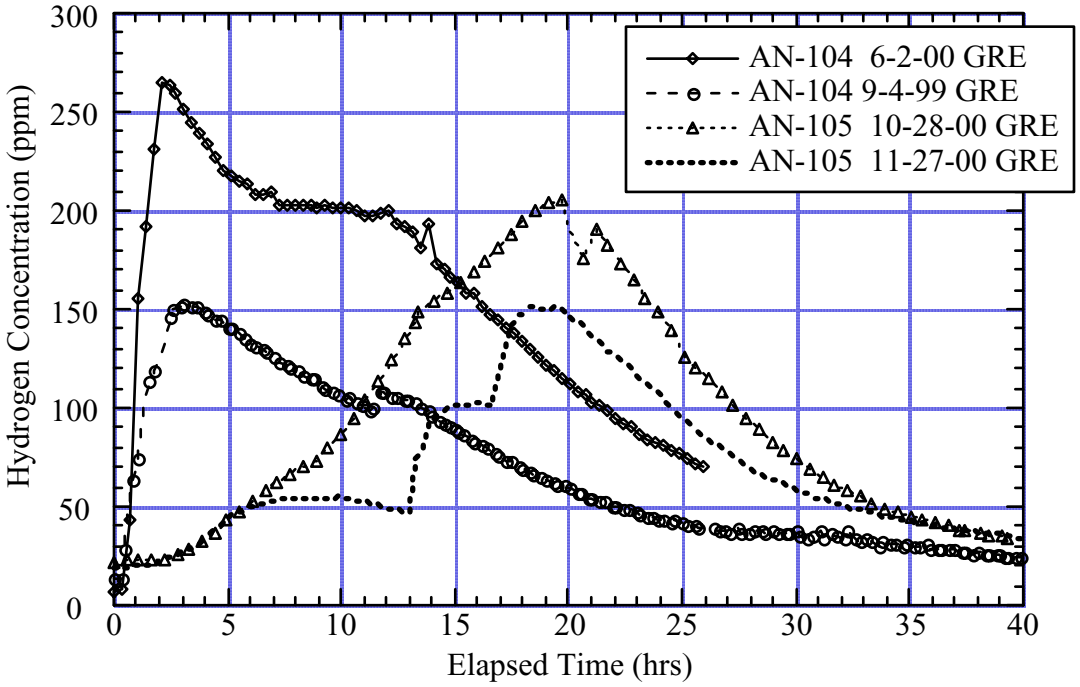

Figure 2.5a. Examples of GREs that Consist of Multiple Releases

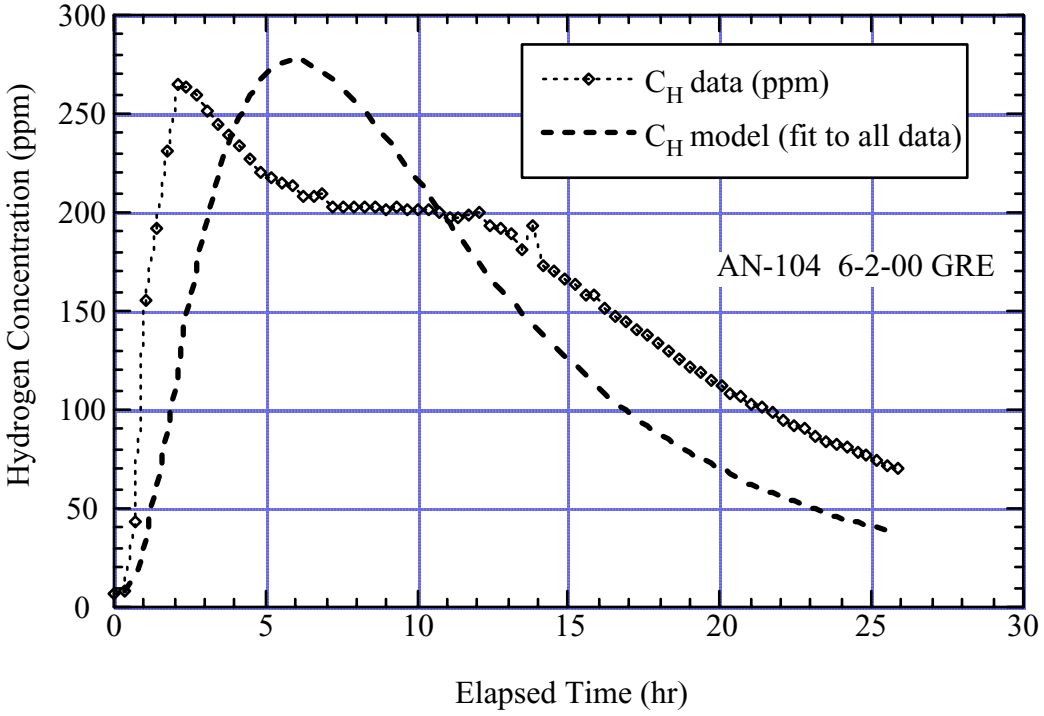

Figure 2.5b. GRE in AN-104 on 6-2-00, Showing Model Fit to All Data Without Differentiation of Separate Releases

estimate of the shape of a subsequent release can be obtained by using the model to estimate the shape of the hydrogen concentration curve for the first release and subtracting that estimated concentration from the measured concentration data. This yields a new curve of hydrogen concentration that is an estimate of the "real" shape of the second release of the event.

Figure 2.6 shows the results obtained with this approach for the multiple-release GRE in AN-104 on June 2, 2000. Instead of fitting the model to the entire data set, the model is initially fit only to the "first peak" of the release, as indicated by the plot of the data during the first five hours of the event. As shown by the short-dashed line in Figure 2.6, the model does an excellent job of fitting this part of the release when constrained to consider only the first five hours of data. Applying the model in this manner yields an estimate of the volume of gas released by the initial release of the event and a predicted concentration history of what was expected to occur had this been the only release during the event.

The curve describing the model prediction for this "first peak" can be used to obtain an estimate of the concentration that would have been obtained in the headspace for the second release, had it occurred on its own. That is, the "real" second peak can be described by this relationship:

$$C_{H\text{'real' 2nd peak}} = C_{H\text{data}} - C_{H\text{ predicted 1st peak}} \tag{2.7}$$

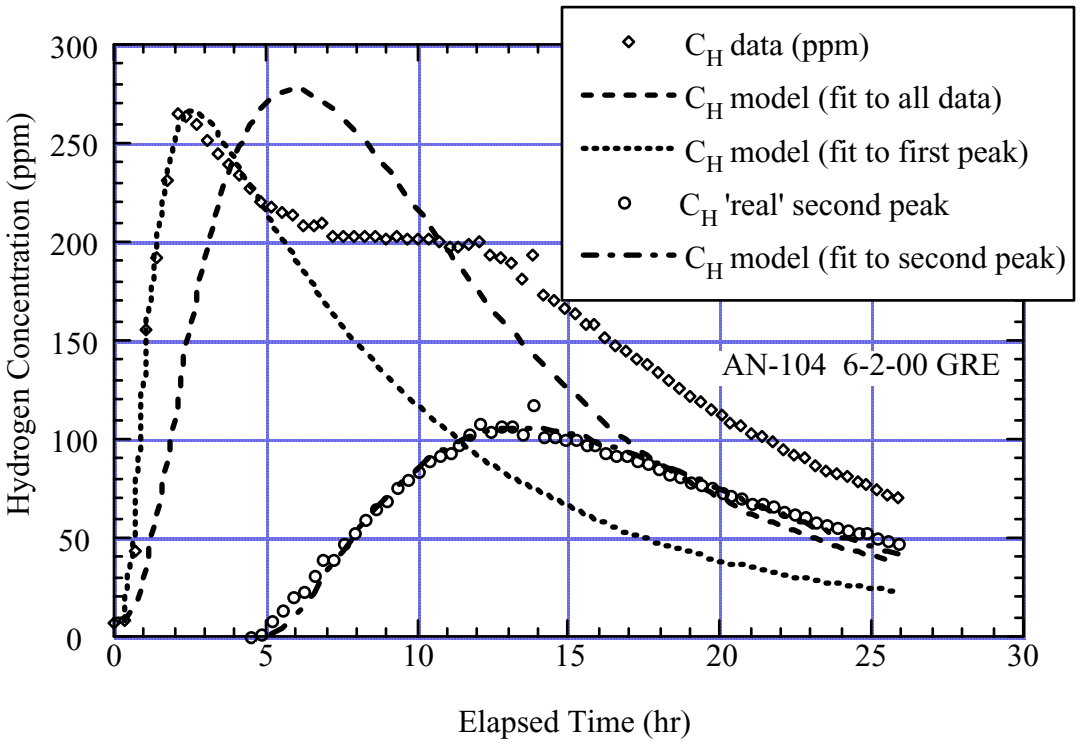

Figure 2.6. GRE in AN-104 on 6-2-00, Parsed into Multiple Releases

The model can be fit to the estimate of the second "real peak" obtained using Eq. (2.7), yielding an estimate of the volume of gas released by the second release of the GRE and a predicted concentration history for the decay of this "second peak" of the event. For the GRE in AN-104 on June 2, 2000, the event appears to parse out into only two separate peaks. However, this process of deconstructing the event as a superposition of releases can be repeated as many times as necessary to uncover all of the significant individual releases in a multiple-release GRE. The total hydrogen gas release for the event is estimated by summing the volumes calculated for the individual events. That is, the total release rate for a multiple-release event can be estimated by summing the contributions of its components via Eq. (2.4) as

$$Q_R = \sum_{i=1}^{N_r} Q_{R0_i} \left(\frac{t - t_{0_i}}{\tau_i} \right) e^{-\left(\frac{t - t_{0_i}}{\tau_i} \right)} \tag{2.8}$$

where N_r is the total number of releases in the GRE. The total release volume is given by the analog to Eq. (2.6) as

$$V_R = \frac{1}{\chi_H} \sum_{i=1}^{N_r} Q_{R0_i} \tau_i \tag{2.9}$$

Table 2.1 summarizes this information for the multiple-release analysis for the event in AN-104 that is illustrated in Figure 2.6.

Table 2.1. Comparing Single- and Multiple-Release Analysis Results for AN-104

Model fit to all data				**Model fit to individual peaks**			
	Peak hydrogen (ppm)		**Total hydrogen release vol (ft^3)**		**Peak hydrogen (ppm)**		**Total hydrogen release vol (ft^3)**
Time of peak	**Data**	**Model**		**Time of peak**	**Data**	**Model**	
6/2/00 8:25	264	277	22	Initial peak: 6/2/00 9:06	266	266	15
				"Real" 2nd peak: 6/2/00 19:48	107	106	11

Treating a GRE as the superposition of a number of individual gas release events makes it possible to apply the gas release model to almost any event, regardless of the shape of the measured concentration history. Figure 2.7 shows additional examples of multiple-release events for GREs with relatively high peak-headspace hydrogen concentrations. None of these appear to consist of a single release, yet all of these are considered BDGREs. If the gas release model is applied by treating each event as a superposition of a number of individual releases, the model estimates the overall gas release behavior quite well. Table 2.2 contains a summary of the total gas release volume for these GREs when analyzed as multiple-release events and compares the results with the values obtained when the model treats the entire event as a single release.

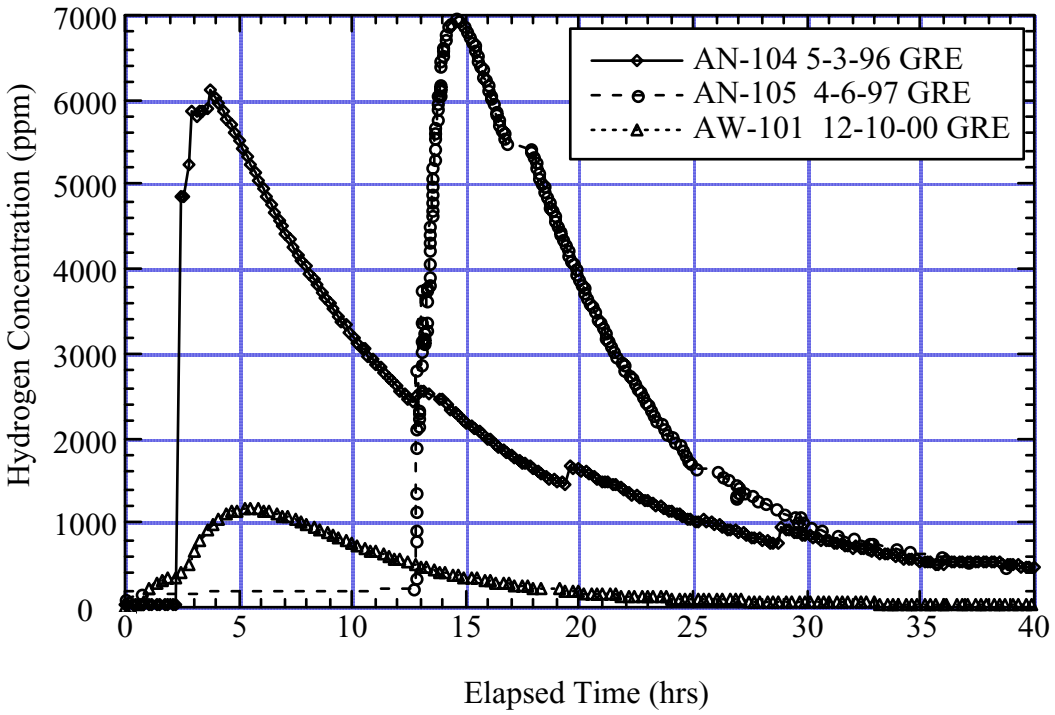

Figure 2.7. Large GREs that Appear to Consist of Multiple Releases

Table 2.2 shows that these two approaches do not produce large differences in the calculated values for total gas release volume obtained for a given event. This is because even in multiple-release events the general shape of a GRE is characterized by a relatively sharp peak in concentration followed by a more or less rapid decay to background concentration levels. For the three relatively large GREs (Figure 2.7), the multiple-release analysis yields total gas release volume about 20–25% higher than the values obtained by treating the event as a single release. The three GREs illustrated in Figure 2.5a, however, are not as "classical" in shape and are generally of much smaller magnitude overall. Rather than consisting of one large release accompanied by three or four lesser releases, these events appear to consist of a series of releases that are very similar in size. It is thus more difficult to obtain a reasonable estimate of the concentration history when treating the event as a single release, and the difference between the results obtained with the two approaches is greater. For these events, the multiple-release approach is clearly preferable. In any event, the model can be expected to give an accurate estimate of the total release volume only when there is sufficient data to properly characterize the overall shape of the GRE, regardless of the number of actual releases it comprises. This analysis assumes that all GREs are governed by essentially the same physical behavior. Therefore, their hydrogen release behavior is similar.

The time-varying release from a single gob event with a set start time (caused by decant or mixing operations, for example) and total release volume can be modeled using the estimated time to the peak release rate. Table 2.3 summarizes the total gas release volume for GREs in AN-103, AN-104, AN-105, and AW-101 since 1995. This table includes all releases in which

Table 2.2. Comparing Single- and Multiple-Release Analysis Results for Different GREs

Model fit to all data				Model fit to individual peaks			
Time of peak	Peak hydrogen (ppm)		Total H_2 rel. vol. (ft^3)	Time of peak	Peak hydrogen (ppm)		Total H_2 rel. vol. (ft^3)
	Data	Model			Data	Model	
AN-104							
5/4/96 1:39	6109	7054	**367**	5/4/96 1:18	6109	6144	329
				5/4/96 7:42	447	461	40
				5/4/96 12:02	378	403	24
				5/4/96 21:02	444	448	42
				5/4/96 5:41	215	223	14
				5/4/96 13:49	172	170	13
							462
9/4/99 12:02	163	163	**11**	9/4/99 12:02	152	153	9
				9/4/99 20:40	32	29	3
				9/4/99 22:13	18	18	1
				9/5/99 19:06	12	10	2
AN-105							**15**
4/6/97 23:46	6980	7467	**347**	4/6/97 23:46	6890	7033	321
				4/7/97 3:02	988	1009	43
				4/7/97 22:14	157	171	20
				4/8/97 12:58	616	644	33
				4/8/97 21:24	188	195	20
							437
10/28/00 6:09	205	167	**20**	10/27/00 21:01	95	76	5
				10/28/00 4:30	142	111	11
				10/28/00 7:08	51	52	4
							19
11/27/00 10:20	151	149	**9**	11/27/00 0:55	55	54	3
				11/27/00 7:50	61	62	3
				11/27/00 12:16	80	78	5
AW-101							**11**
12/10/00 17:22	1162	1118	**90**	12/10/00 14:03	353	352	16
				12/10/00 17:22	965	964	64
				12/10/00 23:28	111	112	10
				12/10/00 11:39	29	31	5
							95

sufficient data were recorded to adequately characterize the overall shape of the release for the event. (This, in general, means that the data were obtained on at least an hourly interval. For some events, data were obtained only on a daily basis, which may be adequate to determine that a release has occurred but not to ensure catching the peak concentration or to characterize the decay curve. These events were omitted from the analysis results shown in Table 2.3.)

Table 2.3. Summary of Gas Release Calculations for GREs in AN-103, AN-104, AN-105, and AW-101

Tank ID	Event ID	Time of Peak	Measured Peak Hydrogen (ppm)	Interpolated Peak Hydrogen (ppm)	Hydrogen Release Volume (ft^3)	Tau	Total Gas Release (m^3)
AN-103	8-22-95 GRE	8/22/95 22:30	1600		92.407	9.406	4.29
AN-103	2-1-99 GRE	1/30/99 13:58	210		13.441	0.538	0.62
AN-103		2/1/99 10:29	560		44.895	4.908	2.08
AN-103	9-4-99 GRE	9/4/99 8:37	1080		71.160	9.488	3.30
AN-103		9/4/99 11:29		192	12.015	4.972	0.56
AN-103		9/5/99 3:16		149	9.677	4.696	0.45
AN-103		9/5/99 18:11		73	4.904	0.526	0.23
AN-103	12-29-99 GRE	12/30/99 3:27	580		33.834	40.374	1.57
AN-103		12/30/99 8:38		105	7.159	21.548	0.33
AN-103	8-6-00 GRE	8/6/00 1:56	200		10.382	11.536	0.48
AN-103		8/6/00 9:32	210		14.664	13.704	0.68
AN-103		8/7/00 0:00	115		9.144	13.506	0.42
AN-103		8/7/00 10:13	150		13.475	85.335	0.63
AN-103		8/8/00 12:38	120		10.778	132.687	0.50
AN-103	10-3-00 GRE	10/3/00 1:54	260		11.640	19.590	0.54
AN-103		10/3/00 21:26		38	3.781	19.587	0.18
AN-103	10-20-00 GRE	10/20/00 17:14	340		24.022	14.130	1.12
AN-103		10/22/00 6:48		189	75.986	1335.856	3.53
AN-104	11-6-94 GRE	11/6/94 17:24	3050		178.640	45.292	11.497
AN-104	2-16-95 GRE	2/16/95 5:08	2089		114.592	30.548	7.375
AN-104	10-2-95 GRE	10/2/95 23:56	3068		182.271	28.728	11.730
AN-104	10-8-95 GRE	10/8/95 11:10	1800		79.993	5.149	5.148
AN-104	5-3-96 GRE	5/4/96 1:39	6109		329.000	14.000	21.173
AN-104		5/4/96 7:42		461	39.600	120.000	2.549
AN-104		5/4/96 12:02		403	24.000	30.000	1.545
AN-104		5/4/96 21:02		448	42.000	150.000	2.703
AN-104		5/5/96 5:41		223	14.400	45.000	0.927
AN-104		5/5/96 13:49		170	13.287	92.395	0.855
AN-104	5-1-97 GRE	5/2/97 7:23	2250		75.259	12.000	4.843
AN-104		5/2/97 7:23		800	42.732	11.006	2.750
AN-104		5/2/97 10:49		40	1.940	1.481	0.125
AN-104	12-2-98 GRE	12/2/98 2:04	550		27.709	22.282	1.783
AN-104		12/2/98 4:08		33	1.769	3.014	0.114

Table 2.3. Summary of Gas Release Calculations for GREs in AN-103, AN-104, AN-105, and AW-101

Tank ID	Event ID	Time of Peak	Measured Peak Hydrogen (ppm)	Interpolated Peak Hydrogen (ppm)	Hydrogen Release Volume (ft^3)	Tau	Total Gas Release (m^3)
AN-104	7-2-99 GRE	7/2/99 20:39	241		13.474	27.499	0.867
AN-104		7/3/99 10:28		106	13.704	355.930	0.882
AN-104	8-1-99 GRE	8/1/99 6:57	181		10.165	35.053	0.654
AN-104		8/1/99 19:53		60	5.899	259.293	0.380
AN-104		8/1/99 20:56		6	0.349	18.181	0.022
AN-104	9-4-99 GRE	9/4/99 12:02	152		8.800	40.000	0.566
AN-104		9/4/99 20:40		29	2.958	179.262	0.190
AN-104		9/4/99 22:13		18	1.025	25.000	0.066
AN-104		9/5/99 19:06		10	1.918	566.901	0.123
AN-104	5-3-00 GRE	5/3/00 15:43	96		5.535	36.257	0.356
AN-104		5/3/00 20:33		206	10.153	13.462	0.653
AN-104		5/4/00 4:40		100	9.598	158.194	0.618
AN-104		5/4/00 15:22		14	0.765	12.862	0.049
AN-104	6-2-00 GRE	6/2/00 9:06	266		15.443	30.013	0.994
AN-104		6/2/00 19:48		106	11.067	192.759	0.712
AN-105	5-30-96 GRE	5/30/96 21:51	14500		540.000	9.000	25.917
AN-105		5/31/96 6:12		7194	603.812	238.556	28.980
AN-105	4-6-97 GRE	4/6/97 23:46	6980		321.399	22.095	15.425
AN-105		4/7/97 3:02		1009	43.205	14.166	2.074
AN-105		4/7/97 22:14		171	19.498	278.872	0.936
AN-105		4/8/97 12:58		644	32.669	16.754	1.568
AN-105		4/8/97 21:24		195	19.570	221.584	0.939
AN-105	9-26-97 GRE	9/26/97 7:09	770		33.233	33.681	1.595
AN-105		9/26/97 18:50		237	9.800	129.789	0.470
AN-105	9-2-98 GRE	9/1/98 19:21	2230		113.665	32.841	5.455
AN-105		9/2/98 4:40		229	4.306	47.754	0.207
AN-105		9/2/98 23:26		206	16.939	339.235	0.813
AN-105	3-7-99 GRE	3/7/99 19:31	760		29.646	61.487	1.423
AN-105		3/8/99 5:18		122	6.665	113.582	0.320
AN-105	7-29-99 GRE	7/28/99 20:44	6208		310.005	46.394	14.879
AN-105	8-2-99 GRE[a]	8/2/99 13:43	3839		203.771	21.528	9.780
AN-105	8-2-99 GRE	8/2/99 13:43	3840		173.702	18.401	8.337
AN-105		8/2/99 18:58		348	22.114	61.580	1.061

Table 2.3. Summary of Gas Release Calculations for GREs in AN-103, AN-104, AN-105, and AW-101

Tank ID	Event ID	Time of Peak	Measured Peak Hydrogen (ppm)	Interpolated Peak Hydrogen (ppm)	Hydrogen Release Volume (ft^3)	Tau	Total Gas Release (m^3)
AN-105		8/3/99 2:10		102	5.507	45.888	0.264
AN-105		8/3/99 8:24		28	1.987	104.677	0.095
AN-105		8/3/99 21:58		42	4.519	246.967	0.217
AN-105	10-27-99 GRE	10/27/99 23:06	180		14.245	185.000	0.684
AN-105		10/28/99 4:05		15	0.580	55.757	0.028
AN-105		10/28/99 5:12		23	0.819	34.158	0.039
AN-105		10/29/99 0:02		21	1.047	83.036	0.050
AN-105	12-31-99 GRE	1/1/00 9:58	186		14.217	170.383	0.682
AN-105	7-21-00 GRE	7/21/00 22:39	146		11.218	273.484	0.538
AN-105	10-28-00 GRE	10/27/00 21:01		76	5.005	182.371	0.240
AN-105		10/28/00 4:30		111	10.815	210.000	0.519
AN-105		10/28/00 7:08		52	3.636	103.872	0.174
AN-105	11-27-00 GRE	11/27/00 0:55	55		3.060	180.000	0.147
AN-105		11/27/00 7:50		62	3.300	44.000	0.158
AN-105		11/27/00 12:16		78	4.875	75.000	0.234
AN-105	12-14-00 GRE	12/14/00 19:47	164		9.016	78.530	0.433
AN-105		12/15/00 2:01		25	1.677	89.006	0.080
AN-105		12/15/00 12:49		9	0.538	89.006	0.026
AN-105	2-23-01 GRE	2/23/01 18:23	82		4.816	189.985	0.231
AN-105	3-21-01 GRE	3/20/01 23:49	337		15.791	43.981	0.758
AN-105		3/21/01 7:51		760	43.657	72.096	2.095
AN-105		3/21/01 16:09		172	6.780	38.778	0.325
AN-105		3/21/01 21:58		165	5.934	37.647	0.285
AN-105		3/22/01 14:10	589		33.735	89.087	1.619
AN-105		3/23/01 7:12		96	3.829	153.781	0.184
AN-105		3/24/01 19:45	166		8.976	144.034	0.431
AW-101	10-3-94 GRE	10/3/94 2:00	5500		262.043	141.158	23.188
AW-101	10-5-94 GRE	10/5/94 11:00	6200		211.260	75.247	18.694
AW-101	11-29-94 GE	11/28/94 16:00	4900		236.716	191.089	20.947
AW-101	2-23-95 GRE	2/23/95 10:37	4600		193.841	42.046	17.153
AW-101	5-8-95 GRE	5/8/95 18:00	1800		166.214	438.529	14.708
AW-101	9-17-95 GRE	9/17/95 0:00	1930		88.618	343.684	7.842
AW-101	9-23-95 GRE	9/23/95 8:00	1460		45.752	51.504	4.049

Table 2.3. Summary of Gas Release Calculations for GREs in AN-103, AN-104, AN-105, and AW-101

Tank ID	Event ID	Time of Peak	Measured Peak Hydrogen (ppm)	Interpolated Peak Hydrogen (ppm)	Hydrogen Release Volume (ft^3)	Tau	Total Gas Release (m^3)
AW-101	9-24-95 GRE	9/25/95 0:00	4660		223.040	131.954	19.737
AW-101	10-16-95 GRE	10/16/95 11:00	1750		77.292	146.388	6.840
AW-101	12-29-95 GRE	12/29/95 17:30	6000		251.794	66.905	22.281
AW-101	5-14-96 GRE	5/14/96 17:56	1383		164.934	256.634	14.595
AW-101	10-30-00 GRE	10/30/00 19:08	259		23.489	179.997	2.079
AW-101	1-16-00 GRE	1/14/00 14:23		82	7.779	457.604	0.688
AW-101		1/16/00 9:59		10	0.536	34.725	0.047
AW-101		1/16/00 11:06	205	88	17.109	476.253	1.514
AW-101		1/16/00 14:25		64	56.385	2569.740	4.990
AW-101		1/19/00 21:03		9	2.065	590.000	0.183
AW-101		1/19/00 21:37		27	30.125	3292.183	2.666
AW-101		1/20/00 2:19		11	0.672	48.000	0.059
AW-101	4-22-00 GRE	4/22/00 4:35		2022	122.550	57.000	10.844
AW-101		4/22/00 6:15		270	13.000	20.000	1.150
AW-101		4/22/00 8:53		366	17.600	20.000	1.557
AW-101		4/22/00 12:45		169	11.815	80.156	1.046
AW-101	9-17-00 GRE	9/17/00 12:08	228		30.123	436.038	2.666
AW-101	9-19-00 GRE	9/19/00 12:35	212		13.540	165.861	1.198
AW-101	9-22-00 GRE	9/22/00 3:27	356		33.411	103.439	2.957
AW-101		9/22/00 13:58		283	13.085	9.669	1.158
AW-101		9/22/00 17:51		403	18.200	14.000	1.611
AW-101		9/23/00 1:44		108	11.100	185.000	0.982
AW-101		9/23/00 17:06		32	4.352	297.412	0.385
AW-101	11-19-00 GRE	11/19/00 10:32	567		43.965	123.000	3.890
AW-101		11/19/00 20:47		54	6.729	256.070	0.595
AW-101	12-10-00 GRE	12/10/00 14:03	353		16.287	21.348	1.441
AW-101		12/10/00 17:22		964	63.914	70.000	5.656
AW-101		12/10/00 23:28		112	10.150	145.000	0.898
AW-101		12/11/00 11:39		31	4.648	333.651	0.411
(a) GRE in AN-105 on 8-2-99, treated as a single release.							

3.0 Analysis of Gas Releases Induced by Supernatant Decant

Transfer, or decant, of supernatant liquid has been proposed as a method for retrieval of radioactive waste to the vitrification plant. The supernatant decant process is expected to induce BDGREs by reducing the hydrostatic pressure on the gas stored in the sediment layer. A detailed model has been developed that simulates this process. The model is described in Section 3.1, and the parameters used in the model are defined in Section 3.2. Analysis results for Tank AN-105 are presented in Section 3.3, and those for AN-103, AN-104, and AW-101 in Section 3.4. The overall conclusions from the decant analysis are given in Section 3.5.

3.1 Mathematical Model

The data and observations pertaining to BDGREs indicate that the sediment layer in those tanks experiencing BDGREs consists of 10 to 15 discrete regions, or "gobs," in different stages of gas retention (Meyer et al. 1997; Meyer and Stewart 2001). In-tank video during large gas releases in SY-101 clearly shows a series of local upwellings from different areas of the tank. Waste temperature profiles before and after GREs observed in other DSTs show the effects of very few of them, indicating localized events. Additionally, based on actual gas release volumes, sediment layer depth, and gas volumes required for buoyancy, only a portion of the sediment layer participates in individual GREs. Finally, this gob concept describes the observed GRE period in relation to the gas generation rate for the BDGRE tanks.

The model simulates the behavior of a number of gobs of gas-bearing sediment during the decant process. It is therefore intended for analyzing tanks that currently exhibit BDGREs. To reiterate, a BDGRE occurs when a portion or gob of the sediment layer accumulates sufficient gas to become buoyant with respect to the overlying liquid. The gob then breaks free of the surrounding sediment and rises to the waste surface, where it releases a portion of its gas into the tank headspace. The gob is assumed to sink back to the sediment layer after releasing enough gas to become negatively buoyant.

This behavior is assumed to occur similarly during decant. The decreasing supernatant depth during decant reduces hydrostatic pressure on the gas stored in the sediment and causes it to expand, increasing the gas volume fraction. The initial conditions are determined by tank historical behavior and measured data, as is the actual gas release behavior when a BDGRE occurs during decant. However, gas expansion and approach to buoyancy during decant are not equivalent to accelerated "natural" gas generation and are not modeled as such. Details of the model are presented in this section.

3.1.1 Depressurization Model

As discussed, the sediment layer consists of a number of regions or gobs in varying stages of gas retention. Gas release is induced from a gob during decant by the decreasing supernatant depth. This reduces hydrostatic pressure on the gas stored in the sediment layer (or individual gobs) and causes it to expand, increasing the gas volume fraction. The assumed waste geometry

is illustrated in Figure 3.1. The pressure of the gas during the decanting process at a given depth within the sediment layer is given by

$$P_{Si}(\eta) = P_A + \rho_{L\,i-1} g\left(h_C + h_{L\,i} + \eta h_S\right) \tag{3.1}$$

where the subscript i denotes the time step, ρ_L is the liquid density, P_A is the atmospheric pressure, and g is the acceleration due to gravity. The thicknesses of the crust, supernatant, and sediment layers are denoted by h_C, h_L, and h_S, respectively. The nondimensional depth η is defined as the depth in the sediment layer, z, divided by the sediment layer thickness, h_S. The initial liquid depth is computed from

$$h_L = h_T - h_C - h_S \tag{3.2}$$

where h_T is the total waste depth. During a decanting process, the supernatant liquid depth is determined by

$$h_{Li} = h_{Li-1} - h_R - h_{GASi-1} \tag{3.3}$$

where h_R is the depth of liquid removed by the decant during a time step (depends on the decant rate), and h_{GAS} is the height associated with the in situ volume of gas released at the previous time step defined by

$$h_{GASi-1} = \frac{P_A}{P_{Si-1}} \frac{Q_{GASi-1}\Delta t}{A_T} \tag{3.4}$$

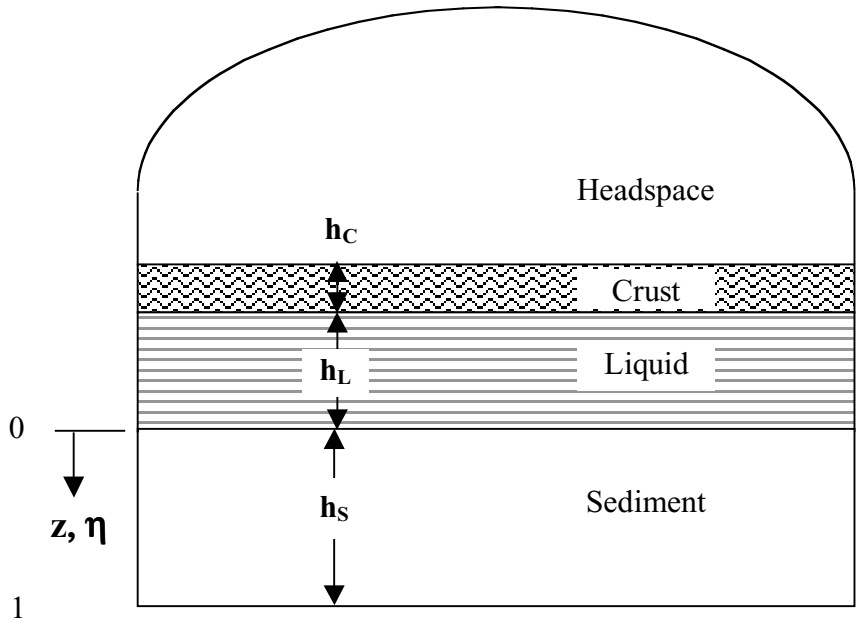

Figure 3.1. Waste Geometry Schematic

In Eq. (3.4), Q_{GASi-1} is the total gas release rate (at headspace pressure) during the previous time step, Δt is the time step, and A_T is the tank cross-sectional area. This term accounts for the "replacement" of gas released from the sediment layer by supernatant liquid. In addition to the reduction of the supernatant liquid thickness, the average pressure of the gas is also altered by any change in the liquid density due to suspension of released gob material, as is discussed below.

The gas volume fraction, or void fraction, in a gob is defined as

$$\alpha = \frac{V_G}{V_G + V_{NG}} \tag{3.5}$$

where V_G is the gas volume and V_{NG} is the nongas volume of solids and interstitial liquid. The effect of the pressure change on the gas volume fraction in the gob(s) can be determined from the ideal gas law to be

$$\frac{d\alpha}{dP_S} = -\frac{\alpha(1-\alpha)}{P_S} \tag{3.6}$$

Measured gas fraction profiles appear to approximate either a linear or parabolic vertical profile over the depth of the sediment layer. Both profiles may be present in a given tank (Hedengren et al. 2000). We postulate that these profiles develop in the following manner. Gas generation and retention in an initially gasless sediment layer will develop a parabolic vertical gas fraction profile (Meyer and Stewart 2001). When a gob with a parabolic profile goes buoyant, only the portion that is buoyant participates. This leaves a portion of the gob on the tank bottom with whatever gas it has already accumulated. As degassed material refills above this portion and the gob accumulates gas for its next cycle, there is initially more gas on the bottom, and the gob assumes a linear profile. When this gob reaches buoyancy, all of it participates in a BDGRE. A parabolic gas fraction profile will then re-develop, and so on. Allowing for a vertical distribution of gas fraction in a gob, the following expression for the gas fraction can be determined by integrating Eq. (3.6) from the initial conditions (denoted by the subscript 0) to time i:

$$\alpha_i(\eta) = \left[\frac{P_i(\eta)}{P_0(\eta)} \left(\frac{1-\alpha_0(\eta)}{\alpha_0(\eta)} \right) + 1 \right]^{-1} \tag{3.7}$$

The change of the average gas fraction in a gob during a decant process can therefore be determined from

$$\alpha_{Ai,n} = \frac{1}{\eta_2 - \eta_1} \int_{\eta_1}^{\eta_2} \alpha_{i,n}(\eta) d\eta \tag{3.8}$$

where the subscript n denotes the particular gob. The limits, η_1 and η_2, are dependent on the vertical gas fraction profile in the gob. The cumulative effect of gas generation on the retained gas volume over the several days required for decant is negligible and is ignored.

The gas fraction profile $\alpha_0(\eta)$ in Eq. (3.7) is defined by either

$$\alpha_0(\eta) = 2\alpha_{A0,n}\eta \tag{3.9}$$

for a linear profile gob or

$$\alpha_0(\eta) = \frac{16}{3}\alpha_{A0,n}\eta(1-\eta) \tag{3.10}$$

for a parabolic gas fraction profile, where $\alpha_{A0,n}$ is the average initial gas fraction in the gob. These profiles are depicted in Figure 3.2.

The average gas fraction growth during a decant is determined by substituting Eq. (3.9) and (3.10) into Eq. (3.8). The limits of the definite integral are dependent on the vertical gas fraction profile. For a gob to become buoyant, its average gas fraction must be the neutral buoyant gas fraction defined by

$$\alpha_{NBi} = 1 - \frac{\rho_{Li-1}}{\rho_S} \tag{3.11}$$

where ρ_S is the sediment or gob degassed density. For a linear gas fraction profile gob the limits are the top and bottom of the sediment layer, so η_1 (recalling that η is the depth into the sediment layer divided by the sediment layer thickness) is zero, and η_2 is equal to unity.

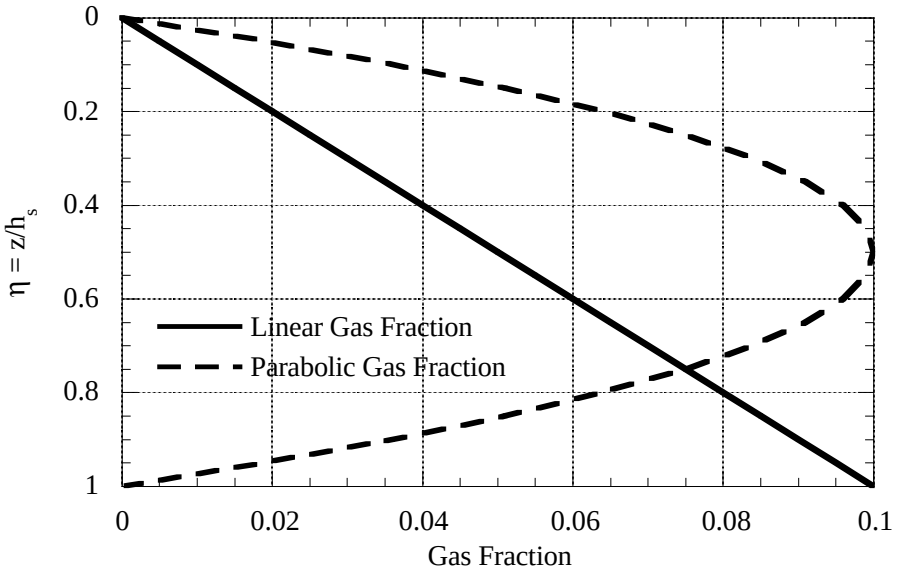

Figure 3.2. Linear and Parabolic Gas Fraction Profiles

For a gob with a parabolic gas fraction profile Eq. (3.10) to become buoyant, its average gas fraction necessarily must also be the neutral buoyant gas fraction. However, the low gas fraction at the bottom of a parabolic profile gob will reach this condition only after the higher gas fraction regions above have already exceeded neutral buoyancy. This is obviously nonphysical. It is clear, therefore, that not all of the gob will reach buoyancy at the same time. The depth in the sediment layer at which that point and the material above it reach buoyancy is the depth at which both the gas fraction at that point and the average gas fraction from the top of the sediment layer down to that point are both equal to the neutral buoyant gas fraction. We define that point as the critical depth into the sediment layer, η_C, or

$$\alpha_A(\eta_C) = \frac{\frac{16}{3}\alpha_{A0,n}}{\eta_C}\int_0^{\eta_C}\eta(1-\eta)d\eta = \frac{16}{3}\alpha_{A0,n}\eta_C\left(\frac{1}{2}-\frac{\eta_C}{3}\right) = \alpha_{NB} \tag{3.12}$$

At height η_C, the gas fraction must also be equal to neutral buoyancy, $\alpha(\eta_C) = \alpha_{NB}$, so

$$\frac{16}{3}\alpha_{A0,n}\eta_C\left(\frac{1}{2}-\frac{\eta_C}{3}\right) = \frac{16}{3}\alpha_{A0,n}\eta_C(1-\eta_C) \tag{3.13}$$

Solving Eq. (3.13) for the critical depth η_C yields 0.75. The limits of integration on Eq. (3.8) for a parabolic profile gob are then $\eta_1 = 0$ and $\eta_2 = 0.75$. This implies that the average gas fraction of interest in regard to buoyant conditions during a decant in a parabolic gob is that at $\eta = 0.75$, or 3/4 of h_S.

3.1.2 Buoyancy Threshold and Gas Release/Material Suspension Models

Gobs with a sufficient initial retained gas volume will become buoyant due to the decant and undergo BDGREs. The gas fraction required for release is slightly greater than for neutral buoyancy to account for the restraining effect of the surrounding nonbuoyant sediment and is defined as the critical gas fraction (Meyer et al. 1997) or

$$\alpha_{Ci} = \alpha_{NBi} + \frac{\beta\tau_y}{\rho_S g h_S} \tag{3.14}$$

where β is ratio of the yield stress in tension to the yield stress in pure shear. The stress at yielding may be given by $\beta\tau_y$, where $1 \le \beta \le \sqrt{3}$. $\beta = 1$ is used in this study. Therefore, when $\alpha_{Ai,n} \ge \alpha_{Ci}$, the gob rises to the waste surface and may release a portion of its gas.

While a BD can occur when the gas volume fraction in a gob reaches the critical value, gas release will be minimal unless the buoyant potential energy exceeds the energy required to yield the displaced material. In addition, a large fraction of the buoyant energy is dissipated in other processes, so the required buoyant energy is greater than that which would just yield the waste. The energy model (Stewart et al. 1996a) introduced in Section 1 is used to account for these phenomena. In the decant model, the "energy model" is the ratio between the buoyant energy,

E_b, and the energy required to yield the gas-bearing gob participating in the buoyant displacement, E_y, given by

$$\frac{E_b}{E_y} = \frac{\alpha_{Ai,n}\rho_{Li-1}gh_i}{(1-\alpha_{Ai,n})\varepsilon_y\tau_y}\left[\left(1+\frac{1}{\gamma}\right)\ln(1+\gamma)-k\right] \tag{3.15}$$

where ε_y is the strain at failure, which is taken to be unity. The distance (h) through which the participating gob can rise and release potential energy is computed based on the actual buoyancy of the gob at the surface and is defined by

$$h_i = h_{Li} + h_S\left\{\frac{1}{2}+\frac{1}{2}\left[P_{Si}\alpha_{Ai,n}+(1-\alpha_{Ai,n})\right]^{\frac{1}{3}} - \frac{\rho_S}{\rho_L}(1-\alpha_{Ai,n})\left[P_{Si}\alpha_{Ai,n}+(1-\alpha_{Ai,n})\right]^{-\frac{2}{3}}\right\} \tag{3.16}$$

The derivation of Eq. (3.16) is provided in Appendix B. The parameters γ and k are determined from

$$\gamma = \frac{\rho_{Li-1}gh_i}{P_A} \tag{3.17}$$

and

$$k = \frac{\alpha_{NB}(1-\alpha_{Ai})}{\alpha_{Ai}(1-\alpha_{NB})} \tag{3.18}$$

Criteria for determining the potential for gas release from a buoyant gob with the energy model (h is given in Eq. 3.16) have been developed by applying the energy model to the results of a set of scaled experiments and to Hanford DSTs that have historically exhibited BDGRE behavior. The input parameters of six DSTs and their energy ratios are summarized in Table 3.1. It is important to note that these inputs are median values and, as well characterized as these DSTs are, uncertainties in their waste properties can produce uncertainties in the model results.

AW-101 has the highest energy ratio and SY-103 the smallest. Because all of the tanks under consideration exhibit periodic BDGREs, the tank results imply that an energy ratio greater than 7.0 indicates that there is sufficient energy in a buoyant displacement to release a large fraction of its gas.

The results of scaled buoyant displacement experiments (Stewart et al. 1996a) were also evaluated. These experiments used a bentonite clay simulant with gas produced in situ by the decomposition of hydrogen peroxide. The model inputs and results are shown in Table 3.2. In the first test case a displacement occurred, but minimal gas was released because the individual gobs did not break apart and release their gas while rising to the surface. An energy ratio of 4.1 was determined for this case.

Table 3.1. Select Hanford DST Waste Properties and Energy Ratio Results (Hedengren et al. 2000; Moore et al. 2000; TWINS database)

Property/Tank	**AN-103**	**AN-104**	**AN-105**	**AW-101**	**SY-101[(a)]**	**SY-103**
Density (kg/m^3)						
Supernatant Layer	1450	1440	1430	1430	1490	1470
Sediment Layer	1737	1579	1572	1553	1700	1600
Layer Thickness (m)						
Waste Level	8.84	9.72	10.41	10.40	10.54	6.91
Crust Layer	0.89	0.41	0.45	0.80	1.00	0.58
Supernatant Layer	4.17	5.26	5.46	6.74	3.70	3.08
Sediment Layer	3.78	4.05	4.50	2.86	5.84	3.25
Sediment Layer Rheology						
Yield Stress (Pa)	160	125	135	150	116	150
Energy Ratio						
E_b/E_y	24	21	21	25	21	7
(a) SY-101 data represent pre-mixer pump conditions (pre 1993).						

Table 3.2. Scaled Buoyant Displacement Experiments Material Properties and Energy Ratio Results

Property/Case	**1**	**2**	**3**	**4**
Density (kg/m^3)				
Supernatant Layer	1000	1000	1000	1000
Sediment Layer	1087	1087	1070	1070
Layer Thickness (m)				
Supernatant Layer	0.105	0.012	0.101	0.011
Sediment Layer	0.047	0.045	0.048	0.048
Sediment Layer Rheology				
Yield Stress (Pa)	67	67	14	14
Gas Release Behavior				
Energetic	Yes	No	Yes	No
Gas Release	Minimal	No	Yes	No
Energy Ratio				
E_b/E_y	4.1	0.7	7.9	2.3

The conditions of the second case are the same as those of the first, but the depth of the liquid layer is reduced. For this case, no active displacement or gas release was observed. The model predicts an energy ratio of 0.7. In the third and fourth cases, a weaker simulant was used. In Case 3, with a predicted energy ratio of 7.9, both an energetic displacement and a gas release were observed. In the final case the liquid layer was reduced, and again no active displacement was observed. A small amount of gas was released, but the mechanism appeared to be percolation rather than buoyant displacement. The energy ratio for this case is 2.3.

The energy ratio for SY-103 is lower than the energy ratio of Case 3. Case 3, however, compared well visually with the large, very energetic buoyant displacements videotaped in SY-101 and is therefore considered to represent a more severe event.

While these observations and the scaled experiment results are not enough to quantify the relation between gas release and energy ratio precisely, they are consistent with these criteria: no disruptive buoyant displacement is predicted for $E_b/E_y<1$, BDs with limited gas release might occur for $E_b/E_y\geq4$, and major gas releases can be expected if $E_b/E_y\geq7$. For the decant analysis, gobs that become buoyant with an energy ratio less than 4.0 are assumed not to release gas.

The total gas release volumes from those gobs that have enough energy to release their gas are determined from the gob's conditions and the condition of the supernatant layer at the time the gob becomes buoyant. The volume of gas in a gob that has risen to the waste surface can be determined from

$$V_{gasAi,n} = \frac{P_{Si}}{P_A} V_{gobn} \alpha_{Ai,n} \tag{3.19}$$

where V_{gob} is the bulk gob volume. In this analysis, the gobs are assumed to be right-circular cylinders with depths equal to the thickness of the sediment layer. All of the sediment volume is assumed to be composed of these gobs. Although this shape is a construct to allow for computational convenience, it is acceptable given that the exact shape of the gobs is unknown. Note that the previously discussed vertical gas fraction profiles in the sediment layer dictate the depth of a gob that will participate in a BDGRE. Further, the pertinent quantity is the gas volume contained in and released from a gob, which is dependent on total gob volume, not gob shape. The gob volume of a buoyant gob may therefore be expressed as

$$V_{gobn} = \frac{\pi}{4} D_n h_{Gn} \tag{3.20}$$

where D_n is the gob diameter and h_{Gn} is the gob height (h_S for linear gas fraction profile and 3/4 h_S for a parabolic gas fraction profile). The total volume of gas released from the gob is given by

$$V_{rel\,n} = V_{gasAi,n} f_{reli} \tag{3.21}$$

Assuming that gas is released at the waste surface until neutral buoyant conditions, the fraction of the gas released, or f_{rel}, is given by

$$f_{reli} = 1 - \frac{\alpha_{NBi}\left(1-\alpha_{Ai}\right)}{\alpha_{Ai}\left(1-\alpha_{NBi}\right)} \frac{P_A}{P_{Si}} \tag{3.22}$$

Combining Eq. (3.21) and (3.22) yields

$$V_{reln} = V_{gobn}\left[\left(\frac{P_{Si}}{P_A} + \frac{\alpha_{NBi}}{\left(1-\alpha_{NBi}\right)}\right)\alpha_{Ai,n} - \frac{\alpha_{NBi}}{\left(1-\alpha_{NBi}\right)}\right] \tag{3.23}$$

When a BDGRE occurs, gas is assumed to be released from the gob at the same time-varying rate as it is during spontaneous BDGREs. The average gas release rate at time i from an individual gob can be computed from the release rate model presented in Hedengren et al. (2000):

$$Q_{Rn} = Q_{R0,n}\left(\frac{t-t_{0,n}}{\tau_n}\right)e^{-\frac{t-t_{0,n}}{\tau_n}} \tag{3.24}$$

where Q_{R0n} is the peak gas release rate (V_{reln}/τ) for gob n, $t_{0,n}$ is the gas release start time, and τ_n is the time to the peak release rate (particular to each gob, see Section 3.2). Because the release rate changes much more rapidly than the headspace hydrogen concentration, it is helpful to integrate Eq. (3.24) to get the average release rate over a time step so the correct release volume will be used even with relatively large time steps. The average gas release rate, $Q_{Ai,n}$, is expressed as

$$Q_{Ai,n} = \frac{Q_{R0,n}}{\Delta t}\int_{t_i}^{t_{i+1}}\left(\frac{t-t_{0,n}}{\tau_n}\right)e^{-\frac{t-t_{0,n}}{\tau_n}}\,dt \tag{3.25}$$

Carrying out the integration gives

$$Q_{Ai,n} = \frac{V_{reln}}{\Delta t}\left[\left(\frac{t_i-t_{0,n}}{\tau_n}+1\right)e^{\frac{t_{0,n}-t_i}{\tau_n}} - \left(\frac{t_{i+1}-t_{0,n}}{\tau_n}+1\right)e^{\frac{t_{0,n}-t_{i+1}}{\tau_n}}\right] \tag{3.26}$$

The total gas release rate at time i during the decant (Q_{GAS} in Eq. 3.4) is simply the sum of $Q_{Ai,n}$ over all gobs, from which the concentration of hydrogen in the headspace can be computed (see Section 3.1.3).

The gas release process is assumed to result from a fraction of the gob volume disintegrating or breaking up to allow bubbles to escape. A fraction of the portion of the gob that disintegrates in this process is assumed to remain suspended and become mixed in the supernatant and not resettle with the rest of the spent gob. The fractional rate of mixing is assumed to be the same as the fractional gas release rate. The volume of gob material released into the supernatant is therefore given by setting the peak gas release rate in Eq. (3.24) to $1/\tau$ (from $Q_{R0}\tau = 1.0$; i.e., maximum release of solids at the maximum gas release rate). Carrying out the integration and multiplying by the nongaseous volume of the gob gives

$$V_{gobRi,n} = V_{NGn}f_{rel0n}\left[\left(\frac{t_i-t_{0,n}}{\tau_n}+1\right)e^{\frac{t_{0,n}-t_i}{\tau_n}} - \left(\frac{t_{i+1}-t_{0,n}}{\tau_n}+1\right)e^{\frac{t_{0,n}-t_{i+1}}{\tau_n}}\right] \tag{3.27}$$

where f_{rel0n} is the fraction of the gas released at the start time of the gas release, and V_{NGn} is the nongaseous volume of the gob given by

$$V_{NGn} = V_{gobn}\left(1-\alpha_{Ai,n}\right) \tag{3.28}$$

with the gas fraction at the time of release. The volume of gob material suspended in the supernatant is given by

$$V_{gobSi} = \sum_{n=1}^{gob\_count} V_{gobRi,n} F \tag{3.29}$$

where F, the fraction of this released material that remains suspended in the supernatant, is determined from historical release data, as discussed in Section 3.2. The gob count, or the number of gobs in the tank, is also addressed in Section 3.2.

Material thus mixing in the supernatant is assumed to remain there for the duration of the simulation. Suspension of the heavier solid particles increases the supernatant density and reduces the neutral buoyancy gas fraction for the gobs that have not previously become buoyant. This may make additional gobs buoyant immediately and allow subsequent gobs to become buoyant earlier than they would without mixing. The dominant effect is to allow multiple BDGREs to be triggered by preceding events. This phenomenon is postulated to cause the multiple release behavior observed in the tanks, as discussed in Section 2.

The liquid density (ρ_L) at time i accounts for the suspension of gob material and is given by

$$\rho_{Li} = \frac{\left(h_{Li}A_T + \sum_{t=1}^{i-1} V_{gobSt}\right)\rho_{Li-1} + V_{gobSi}\cdot\rho_S}{h_{Li}A_T + \sum_{t=1}^{i-1} V_{gobSt} + V_{gobSi}} \tag{3.30}$$

3.1.3 Headspace Hydrogen Concentration Model

The headspace hydrogen concentration is computed from $Q_{GASi}\Delta t$ and the background gas generation of the remaining waste (supernatant and sediment). Consider a tank containing variable volumes of waste and headspace with inflows and outflows as indicated in Figure 3.3. The ventilation inflow, Q_{VIN}, and outflow, Q_{VOUT}, carry air into and the headspace atmosphere out of the tank headspace volume, V_{HS}, respectively. During decant, liquid is removed from the convective layer at the rate Q_{LOUT}. Gas is released from the waste to the headspace at the volumetric rate $Q_{GAS.}$ The headspace atmosphere and the liquid/gas/solid mixture in the waste volume are both assumed to be incompressible for the headspace hydrogen concentration analysis. Q_{LOUT} and Q_{VOUT} are defined as positive for outflow, Q_{VIN} as positive for inflow, and Q_{GAS} as positive for flow from the waste into the headspace.

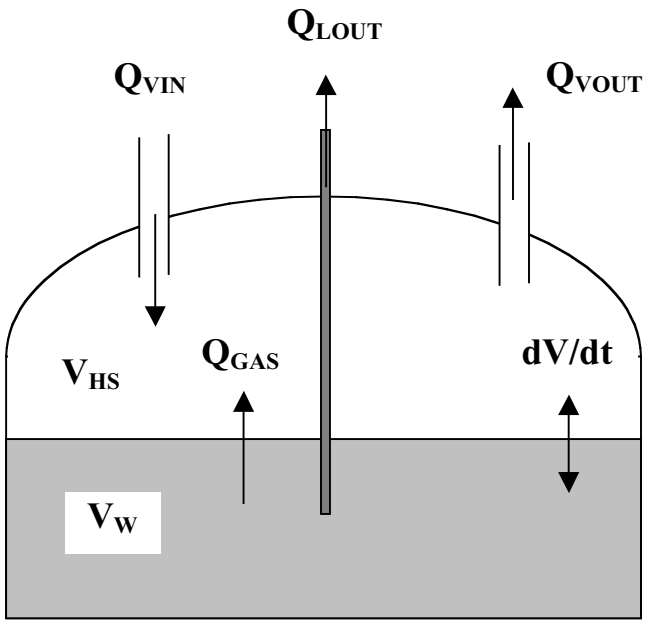

Figure 3.3. Schematic of Tank Flow Paths

Let the volume of the tank be fixed, but allow the headspace volume and waste volume to vary. The incompressible fluid assumption requires that

$$\frac{dV_{HS}}{dt} = -\frac{dV_W}{dt} \tag{3.31}$$

The headspace volume during the decant is computed from

$$V_{HSi} = V_T - (h_C + h_{Li} + h_S)A_T \tag{3.32}$$

where V_T is the tank volume. Continuity on the headspace volume can be expressed as

$$\frac{dV_{HS}}{dt} = Q_{VIN} - Q_{VOUT} + Q_{GAS} \tag{3.33}$$

assuming the released gas leaves the waste at the pressure that retained it, P_{GAS}, and expands isothermally to the headspace pressure, P_{HS}. Also assuming that the effect of retained gas expansion in the waste due to decrease in hydrostatic pressure is minimal, continuity on the waste volume is written as

$$\frac{dV_W}{dt} = -Q_{LOUT} - \frac{P_{HS}}{P_{GAS}}Q_{GAS} \tag{3.34}$$

Substituting Eq. (3.33) and (3.34) into Eq. (3.31) provides an expression for the ventilation outflow, Q_{OUT}, as a function of the other known inflows and outflows:

$$Q_{VOUT} = Q_{VIN} + Q_{GAS}\left(1 - \frac{P_{HS}}{P_{GAS}}\right) - Q_{LOUT} \tag{3.35}$$

The continuity equation for hydrogen in the headspace, assuming that the hydrogen concentration remains small, can be written as

$$\frac{d}{dt}\left(C_H V_{HS}\right) = Q_{GAS}\chi_H - Q_{VOUT}C_H \tag{3.36}$$

where C_H is the headspace hydrogen concentration (vol%) and χ_H is the volume fraction of hydrogen in the waste gas. Expanding the derivative and substituting Eq. (3.34) and (3.35) via Eq. (3.31) yields

$$\frac{dC_H}{dt} = \frac{1}{V_{HS}}\left(Q_{GAS}\chi_H + \left(Q_{VIN} - Q_{GAS}\right)C_H\right) \tag{3.37}$$

An implicit finite difference analog to Eq. (3.37) for time step Δt is

$$\frac{C_{Hi} - C_{Hi-1}}{\Delta t} = \frac{Q_{GASi} \cdot \chi_H - C_{Hi}(Q_{VIN} + Q_{GASi})}{V_{HSi}} \tag{3.38}$$

Solving Eq. (3.38) for C_{Hi} gives

$$C_{Hi} = \frac{C_{Hi-1} + \frac{Q_{GASi} \cdot \chi_H}{V_{HSi}}\Delta t}{1 + \frac{\left(Q_{VIN} + Q_{GASi}\right)}{V_{HSi}}\Delta t} \tag{3.39}$$

3.1.4 Variations of Decant Model

As well as decanting the tank, the effects of two postulated decant control strategies were investigated with the model. These control strategies included a stop-start control strategy and a water backfill.

Tank farm operations (CHG 2000) requires that operations be halted if the gas monitoring instruments measure a hydrogen concentration exceeding a level of 6,250 ppm in the headspace. This control was set to prevent the concentration from reaching the LFL on the assumption that the operation was causing the gas release. Operations can theoretically resume when the hydrogen concentration drops back below 6,250 ppm. However, a lower restart threshold is typically used. The SY-101 mixer pump Safety Assessment (Sullivan 1995) specified a 500-ppm hydrogen concentration for restart. The only change in the model for the stop-start control

strategy is to set the decant rate to zero when the hydrogen concentration rises above 6,250 ppm and restart the decant after the hydrogen concentration falls below 500 ppm.

Because decant-induced BDGREs result from decreasing hydrostatic pressure, it was believed that maintaining pressure by backfilling with water might prevent or reduce the frequency of BDGREs. However, because water is much less dense than the concentrated supernatant, the hydrostatic pressure cannot be maintained and some potential for induced BDGREs remains. A negative side effect of the backfill is that the tank headspace does not increase (except minimally due to gas release) as supernatant is removed. Only minor changes in the model were required for the water backfill control strategy tests. Water was added back to the tank at the same rate as the supernatant was removed, so the waste level changed only with gas release.

$$h_{Wi} = \sum_{t=1}^{i} h_{Rt} \tag{3.40}$$

The pressure of the gas during the decanting process at a given depth in a gob (Eq. (3.1) is then given by

$$P_{Si}(\eta) = P_A + \rho_{L\,i-1} g\left(h_C + h_{L\,i} + \eta h_S\right) + \rho_W g h_{Wi} \tag{3.41}$$

where ρ_w is the water density. The headspace volume (Eq. (3.32) is calculated by

$$V_{HSi} = V_T - (h_C + h_{Li} + h_S + h_{Wi}) A_T \tag{3.42}$$

3.2 Parameter Definitions and Constraints

Most of the model parameters define the initial physical conditions in the waste that can be obtained from directly measuring the waste layers. With few exceptions, all of these parameters have been established with reasonable accuracy and uncertainty for the tanks under evaluation. Parameters that describe the configuration of gas stored in the sediment are much more uncertain. The initial gas retention conditions must be defined by the number of gobs with each gob defined by its size, gas volume fraction, and vertical gas fraction profiles.

The behavior of the waste during decant is described by the rates of the various processes involved. Many of these parameters may be even more uncertain and difficult to define because the models in which they are used are also more inferred from indirect evidence than described from first principles. These parameters include coefficients for the gas release rates function, solids suspension fraction, and the potential energy threshold.

Each of these parameters, even those measured directly, has some uncertainty that can be described by a probability distribution. The bases for the parameter values for the four tanks under evaluation (AN-103, AN-104, AN-105, and AW-101) are presented in the following sections.

For those parameters requiring extensive analysis, AN-105 is presented in detail as the representative tank. It had the largest historic BDGREs next to SY-101, it is one of the first low-activity waste tanks scheduled for retrieval, and it is representative of the other BDGRE tanks in terms of physical and chemical composition. Model parameters for each of the tanks evaluated were developed in a similar fashion, and anomalies from this pattern are noted in each section.

3.2.1 Overall Tank and Waste Configuration and Properties

The tank and waste configuration properties include those parameters that are direct measurements or design specifications, as indicated in Table 3.3. Distributions for the measured parameters are summarized in Table 3.4. The maximum and minimum values are those to which the distributions are truncated. Complete probability distributions for each of the parameters for all tanks evaluated are given in Appendix C.

Table 3.3. Tank and Waste Configuration Parameters

Parameter	Symbol	Source	Reference
Tank Volume	V_T	Design specification	
Tank Area	A_T	Design specification	
Vent Rate	Q_{VIN}	Operational measurement	
Total Waste Thickness	h_T	Enraf buoyancy gauge	Hedengren et al. (2000), Moore et al. (2000), TWINS[(a)]
Crust Thickness	h_C	Temperature profiles	Hedengren et al. (2000), Moore et al. (2000)
Sediment Thickness	h_S	Various measurements	Hedengren et al. (2000), Moore et al. (2000)
Supernatant Liquid Density	ρ_L	Ball rheometer, core samples	Hedengren et al. (2000), Moore et al. (2000) TWINS[(a)]
Sediment Density	ρ_S	Core samples	TWINS,[(a)] Hedengren et al. (2000), Moore et al. (2000)
Hydrogen Concentration in gas stored in Sediment Layer	χ_H	Retained gas sampler (RGS) measurement	Mahoney et al. (1999)
Hydrogen Generation Rate	H_{2G}	Empirical model	Hu (2000)
Initial Gas Volume in Sediment Layer	V_{G0}	Void fraction instrument (VFI) and RGS measurements	Hedengren et al. (2000)
Sediment Yield Stress	τ_y	Ball rheometer	Hedengren et al. (2000)
(a) TWINS: Tank Waste Information System database.			

Table 3.4. Tank and Waste Configuration Parameters: Values and Distributions

Parameter, Distribution (units)		**AN-105**	**AN-104**	**AN-103**	**AW-101**
V_T (m^3)	Point Value	5337.4	5337.4	5337.4	5337.4
A_T (m^2)	Point Value	410.4	410.4	410.4	410.4
Q_{VIN} (cfm)	Point Value	100	100	100	125
h_T normal (m)	Median	10.41	9.72	8.84	10.4
	Maximum	10.51	9.82	8.94	10.5
	Minimum	10.31	9.62	8.74	10.3
	3σ	0.10	0.10	0.10	0.10
h_C uniform (m)	Median	0.45	0.41	0.89	0.80
	Maximum	0.65	0.55	1.21	1.20
	Minimum	0.25	0.27	0.57	0.40
h_S normal (m)	Median	4.50	4.05	3.78	2.86
	Maximum	5.34	4.85	3.92	3.46
	Minimum	3.66	3.25	3.64	2.26
	2σ	0.84	0.80	0.14	0.60
ρ_L normal (kg/m^3)	Median	1430	1440	1450	1430
	Maximum	1520	1548	1544	1516
	Minimum	1340	1332	1356	1344
	2σ	90	108	94	86
ρ_S normal (kg/m^3)	Median	1572	1579	1737	1553
	Maximum	1652	1679	1957	1633
	Minimum	1492	1479	1517	1473
	2σ	80	100	220	80
χ_H normal	Median	0.59	0.45	0.61	0.32
	Maximum	0.644	0.519	0.687	0.352
	Minimum	0.536	0.381	0.533	0.288
	3σ	0.054	0.069	0.077	0.032
H_{2G} (ft^3/day)	Point Value	3.32	4.97	4.26	4.80
V_{G0} (m^3)	Maximum	100	99	183	51
	Minimum	60	64	157	39
τ_y uniform (Pa)	Maximum	250	250	250	250
	Minimum	50	50	50	50

3.2.2 Gob Size and Number

As discussed, the preponderance of evidence requires the sediment layer to be considered as a collection of semi-independently evolving gobs of varying sizes with different degrees of gas retention and relative buoyancy (Meyer et al. 1997; Meyer and Stewart 2001). The volume of gas released from a gob is determined by the size of the gob, the gas volume within the gob, and the fraction of gas that is released during a BDGRE. Inversely, therefore, the size of a gob may be determined from the volume of gas released during a BDGRE.

The hydrogen concentration in a tank's headspace can be used to quantify gas release behavior during BDGREs (Hedengren et al. 2000). Gas release volumes have been determined from historical BDGREs as presented in Section 2.3. From Eq. (3.24), the release volume for a gob can be expressed as

$$V_{re\,ln} = \frac{Q_{R0}\tau_n}{\chi_H} \tag{3.43}$$

The gob volume can then be estimated by combining Eq. (3.20) and (3.21) to yield

$$V_{gobn} = \frac{V_{re\,ln}}{P_S \alpha_{NB} f_{rel}} \tag{3.44}$$

Recall that the analysis of the BDGREs for this study departed from previous analyses (Hedengren et al. 2000, for example) in that the possibility of multiple BDGREs was allowed for in events that were previously thought to be single BDGREs. The identification of multiple BDGRE phenomena is discussed in detail in Section 2.3.

Combining Eq. (3.20) and (3.44) yields the following expression for the gob diameter based on the gas release volume:

$$D_n = \sqrt{\frac{4}{\pi}\frac{V_{re\,ln}}{P_S \alpha_{NB} f_{rel} h_S}} \tag{3.45}$$

The gob diameters determined for AN-105 (including single and multiple release events) in this manner are shown in Figure 3.4.

It appears that BDGRE gob volumes have been decreasing in AN-105 over the period shown. Similar trends are seen in the other tanks. A gob diameter distribution taken directly from this data would have the highest probability at smaller (~1 m diameter) gob sizes. However, a Rayleigh-Taylor stability analysis conducted by Meyer et al. (1997) indicates that gobs with aspect ratios near unity are the least stable. Given our assumption that a gob is represented by a right-circular cylinder with a depth approximately equal to the sediment thickness (supported by the gas fraction profiles), the gob diameters would probably be closer to the sediment thickness and therefore larger (4.5 m diameter). Further, the gobs must be relatively large given the gas

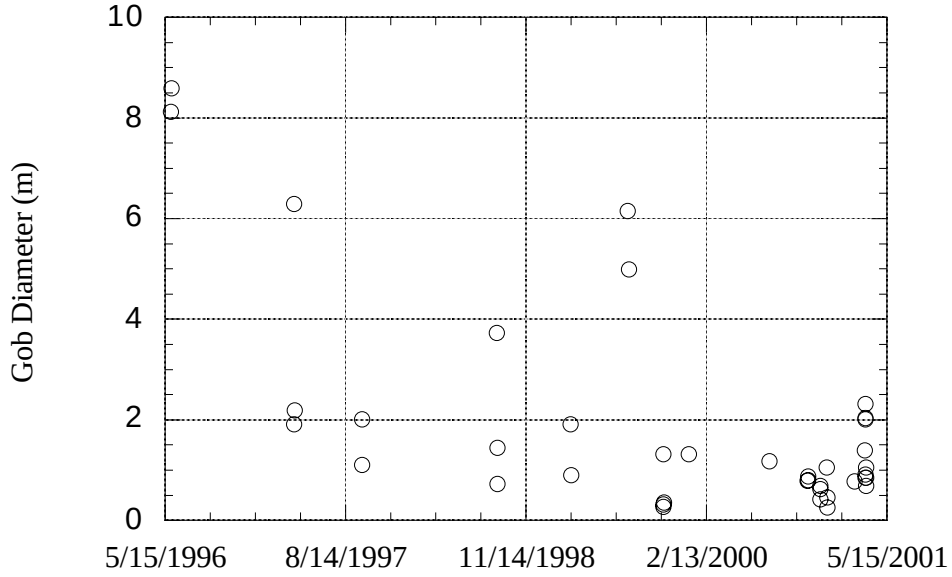

Figure 3.4. Tank AN-105 BDGRE Gob Diameters

generation rate and event frequency and size. This may be seen by considering that about 520 1-m-diameter gobs could be present in a tank. The frequency of events seen in the tanks (Hedengren et al. 2000) clearly does not support this distribution. Finally, it has been determined that it is also more conservative to consider larger gobs.

Thus a gob diameter distribution was chosen that would allow for both small and large gobs but has the most probable gob diameter as the sediment layer depth to approximately the largest historical value. The probability decreases at either end of the distribution as dictated by the tank size, indicating a maximum diameter of 22 m and a minimum of 0. The diameter values were truncated to 11 m (tank radius) and 1 m. The detailed diameter distributions for each tank are presented in Appendix C. The single peak in AN-103 is achieved because the sediment depth and largest historical gob sizes are equivalent.

Based on combinations of the gas release history, gas generation rates, sediment layer volume, and gob volume (Meyer et al. 1997), approximately 10 to 15 gobs are estimated to exist in a tank. The actual number of gobs (gob count) in the tank is determined by the limit of the tank area, or

$$\sum_{n=1}^{gob\_count} \frac{\pi}{4} D_n^2 = A_T \tag{3.46}$$

with D_n randomly selected from its distribution until all of the tank area is occupied. Because the assumed shape is an approximation and the geometric location of an individual gob is irrelevant in this analysis, the non-physical complete occupation of the circular tank area by circular gobs is

ignored. When the remaining tank area is less than that that determined by the minimum gob diameter, the final gob diameter is set by

$$D_n = \sqrt{\frac{4}{\pi} A_T - \sum_{n=1}^{gob\_count-1} D_n^2} \tag{3.47}$$

3.2.3 Gob Gas Fraction and Gas Fraction Profile

The total gas volume in the sediment layer must be inferred from local gas fraction measurements. The initial average gas fraction in a gob is necessarily less than the neutral buoyant gas fraction and is assumed to be greater than approximately 1/4 of this value. This minimum can be computed by the release fraction of gas from a gob and the in situ hydrostatic pressure in the sediment layer. For our purposes, given that low gas-fraction gobs will not be affected by a decant, a fixed minimum of approximately 1/4 of a minimum neutral buoyant gas fraction (dictated by the layer densities in Table 3.4 and Eq. 3.11) is used for the particular tank. The average gas fraction of an individual gob is then randomly selected from the ranges presented in Table 3.5.

Table 3.5. Gas Fraction Ranges

Gas Fraction	AN-105	AN-104	AN-103	AW-101
Minimum	0.02	0.02	0.04	0.02
Maximum	α_{NB}	α_{NB}	α_{NB}	α_{NB}

The distribution shape of the initial average gas fraction is dictated by the initial gas volume in the sediment layer. The assignation of gas fraction to the gob volumes is made by

$$\sum_{n=1}^{gob\_count} \alpha_{A0,n} \lambda \frac{\pi}{4} D_n^2 h_S = V_{G\,0} \tag{3.48}$$

where α_{A0n} is the initial average gas fraction in the gob and λ is a factor that accounts for the vertical gas fraction profile in a gob (see below). A set of gas fractions that satisfy Eq. (3.48) is assigned to a set of gob diameters that meet the constraint of Eq. (3.46).

To have a gas volume from the gob configuration that matched the total gas volume in the sediment layer (Table 3.4), trapezoidal distributions for the gas fractions were used. Higher probabilities were assigned to the minimum gas fractions for each tank (compared with the probability of α_{NB}) except AN-103, where a much higher probability of α_{NB} had to be assigned. This apparent deviation of AN-103 from the gas retention characteristics in the other tanks is supported by the lack of BDGREs in AN-103, the small size of those that do occur, and the slow level growth in the tank (Hedengren et al. 2000).

The rate of buoyancy and the volume of the gob that becomes buoyant are affected by the vertical gas fraction profile in a gob (see Section 3.1.1). This profile also affects the computation

of the total gas volume in the tank (Eq. 3.48). Recall that the average gas fraction of interest in regard to buoyant conditions during a decant in a parabolic gas fraction profile gob is that at 3/4 h_S. The average gas fraction for a parabolic profile gob selected from the distribution range is therefore taken to be this average value, which is higher than the average gas fraction over the entire depth of the gob (see Figure 3.2). The relationship between the average gas fraction from the top to 3/4 of the way down into the gob to that over the entire gob can be computed by

$$\alpha_{A0,n}(\text{entire\_gob}) = \frac{16}{3}\alpha_{A0,n}\int_0^1 \eta(1-\eta)d\eta = 0.889\alpha_{A0,n} \tag{3.49}$$

A binary distribution of either linear or parabolic gas fraction profile is used (Hedengren et al. 2000). For those gobs that have a parabolic profile, λ in Eq. (3.48) is set to 0.889, and for linear profile gobs, 1.0.

An interesting effect of the inferred gas volume is that it reduces the possible range of the initial gas fraction in the gobs for each of the tanks, thereby reducing the variability of the liquid and sediment densities (see Eq. 3.11). This effect is reflected in the parameter distributions presented in Appendix C.

3.2.4 Gas and Solid Release Rate

Gas is released from the gob at the same time-varying rate as it is during spontaneous BDGREs (see Section 3.1.2). The headspace hydrogen concentration recorded during spontaneous BDGREs in each of the tanks under evaluation has been modeled by Eq. (3.24) and (3.37) in Section 2.4. This analysis has provided the time to the peak release rate (τ_n) required in Eq. (3.26) and (3.27), and the results for AN-105 are shown in Figure 3.5. No trend significant

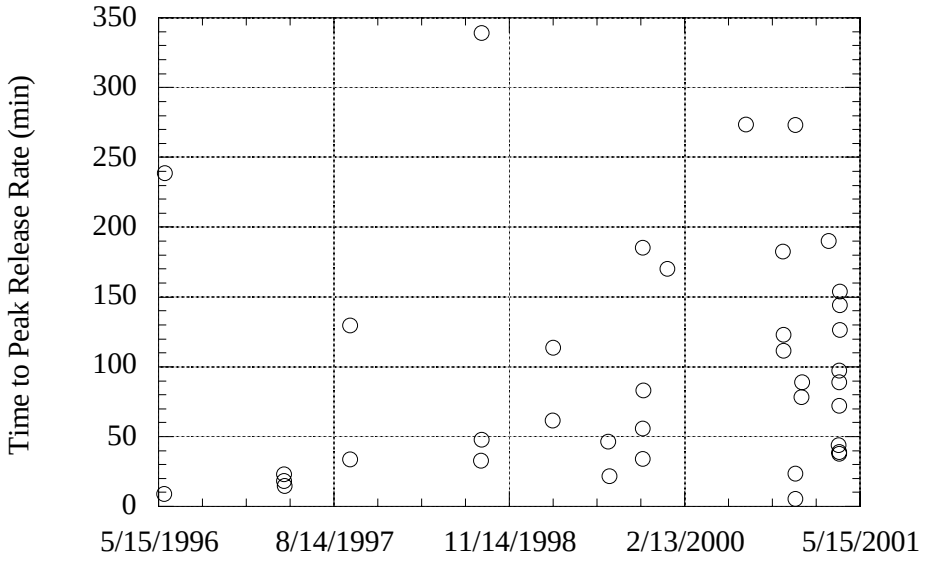

Figure 3.5. Tank AN-105 Time to Peak Release Rates for Spontaneous BDGREs

to this analysis is observable over the time period (approximately six years), and no correlation is observable between τ and the release volume from given events. It is apparent that, even neglecting the uncertainty of the analysis, no definitive τ value is identifiable. Similar results were observed in the other tanks. As a result, the τ value for a gob in a given tank was assigned from a distribution created from that tank's historical release results, as shown in Appendix C.

As discussed, a fraction of the portion of the gob that disintegrates in the gas release process is assumed to remain suspended and become mixed in the supernatant and to not resettle with the rest of the spent gob. The fraction of this released material that remains suspended in the supernatant, F in Eq. (3.29), is determined from the historical headspace hydrogen concentration data.

Numerous historical (spontaneous) BDGRE events have multiple-gob participation (Section 2.3). We have assumed that this multiple gob phenomenon is directly and solely influenced by the suspension of the released material. Therefore, to quantify F, the multiple gob behavior has been described by specific parameters:

- The number of gobs participating in a GRE.
- The fraction of the gas released. This parameter is computed by dividing the total gas release volume of a single or multiple GRE by the total amount of gas stored in the sediment layer.
- The fraction of the tank area participating in BDGREs. This parameter is computed by dividing the total gob area of a single or multiple GRE by the total tank area. The participating gob area is determined directly from the gas release volumes, as discussed in Section 3.2.2.
- The time between gobs.

The results of the spontaneous BDGREs are compared with results generated from a modified decant model. To account for the variability of the input conditions, approximately 400 different sets of inputs were created from the input parameter distributions discussed above. For each input case, a supernatant decant was conducted until a BDGRE was triggered; at that point the decant was stopped. Care was taken in the selection of the input cases to ensure that the initial BDGRE was triggered during the early stages of the decant operation so that the effects of the decant were minimized (reduced supernatant liquid volume, reduced hydrostatic pressure, increased headspace, etc.) to replicate the tank conditions during a spontaneous BDGRE. For each input case, eight values of F were used, ranging from the physically imposed limits of 0 to 1 in a geometric progression and resulting in approximately 3,200 simulations. Comparing the spontaneous BDGRE results to the model BDGRE results indicated applicable values for F.

Spontaneous BDGREs for each tank were selected from those in Table 2.4. Individual events with a total gas release volume greater than 1 m^3 were included in the evaluation. This imposed release volume limit follows from our selection of potential gob diameters discussed in Section 3.2.2. The parameter values determined from the spontaneous events are given in Table 3.6, and model parameter results as functions of F are presented in Figures 3.6 through 3.9.

Table 3.6. Spontaneous BDGRE Behavior Parameters

Parameter		AN-105	AN-104	AN-103	AW-101
Number of Gobs	Maximum	3	3	2	4
	Average	1.4	1.4	1.3	2
	Minimum	1	1	1	1
Fraction of Gas Released	Maximum	0.322	0.111	0.014	0.144
	Average	0.073	0.039	0.008	0.091
	Minimum	0.008	0.004	0.005	0.020
Fraction of Tank Area Participating	Maximum	0.267	0.148	0.023	0.114
	Average	0.061	0.052	0.015	0.072
	Minimum	0.007	0.006	0.008	0.016
Time Between Gobs (hrs)	Maximum	31.9	8.3	37.6	7.9
	Average	14.7	3.9	37.6	3.7
	Minimum	3.3	0.5	37.6	1.7

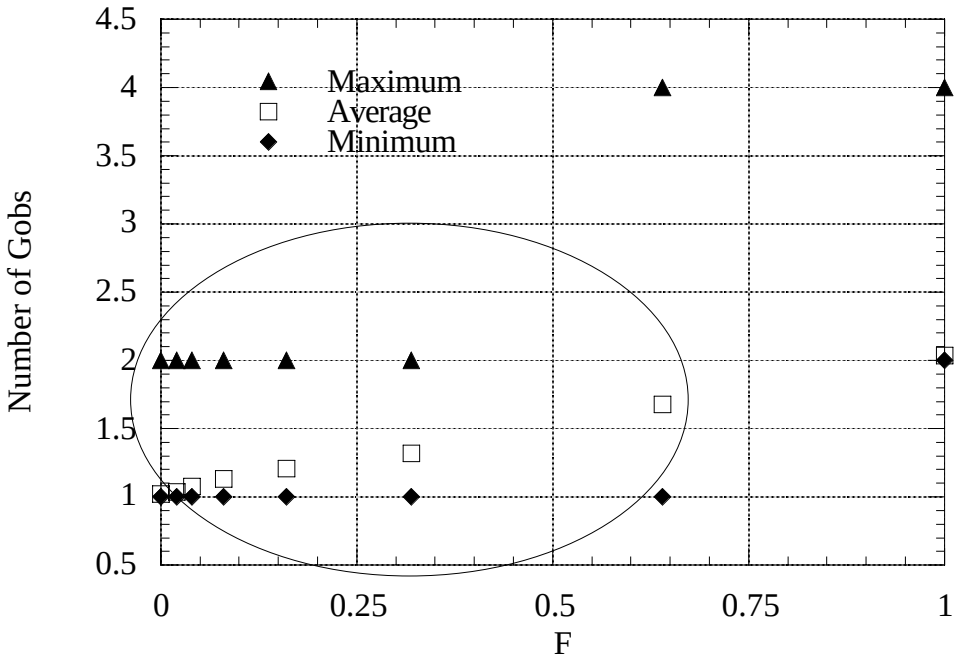

Figure 3.6. Number of Gobs as a Function of F: Model Results, AN-105

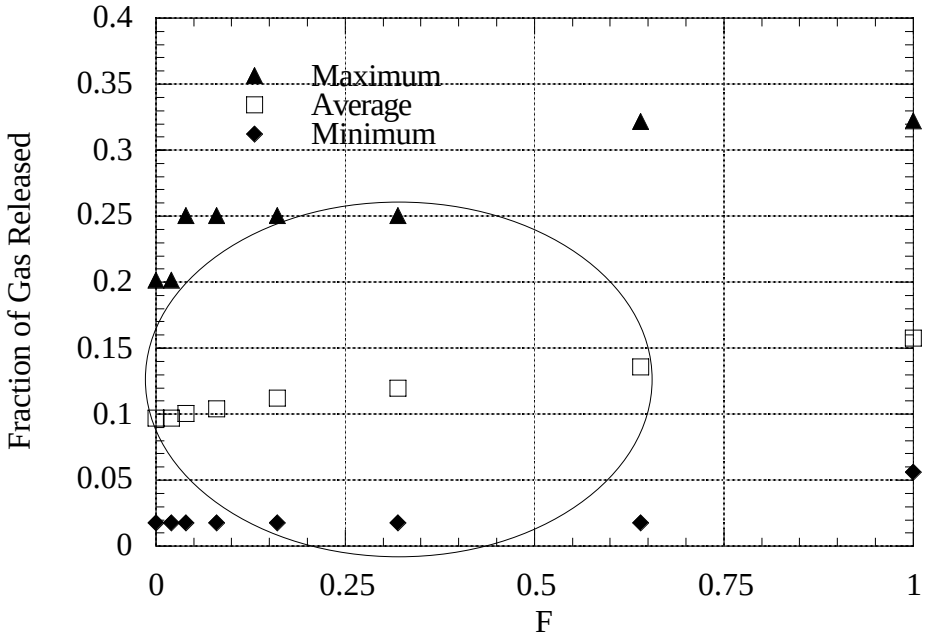

Figure 3.7. Fraction of Gas Released as a Function of F: Model Results, AN-105

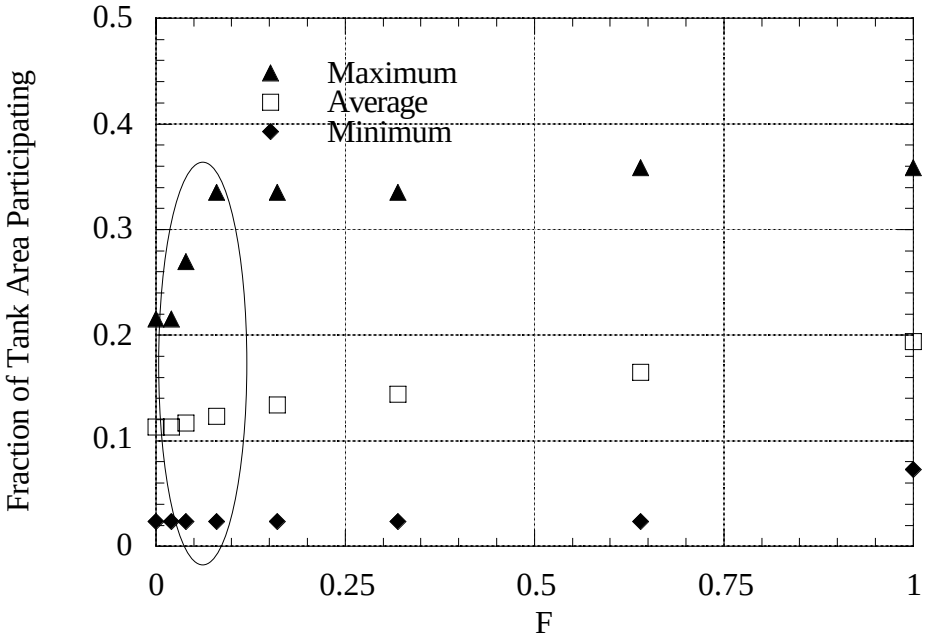

Figure 3.8. Fraction of Tank Area Participating as a Function of F: Model Results, AN-105

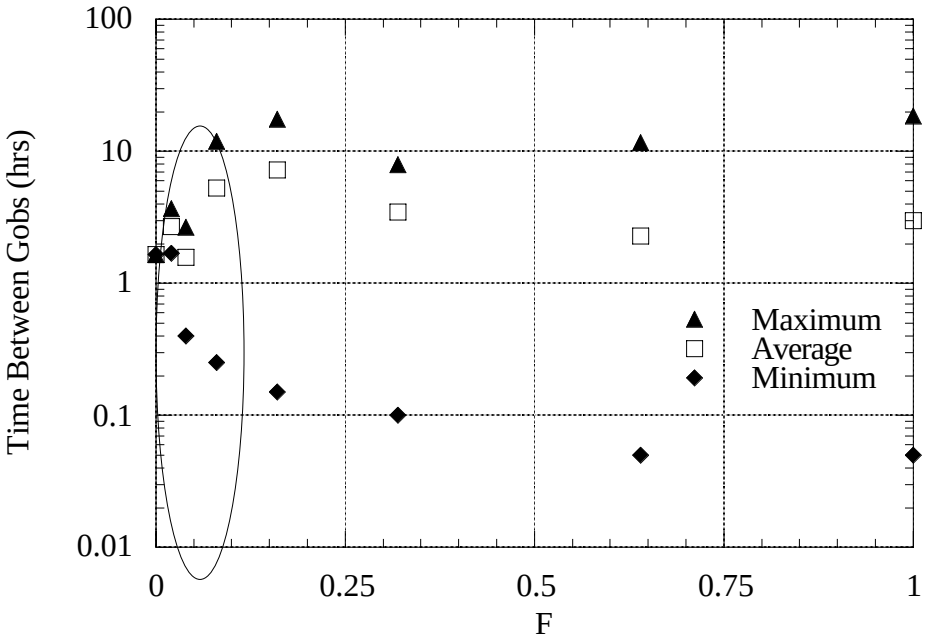

Figure 3.9. Time Between Gobs as a Function of F: Model Results, AN-105

For each parameter, the appropriate F values as determined by the model are based on the results that do not exceed the spontaneous BDGRE results. That is, at what value of F do the model results exceed the spontaneous results? The necessity of not exceeding the spontaneous results is clearly illustrated by the minimum number of gobs. Comparison of the minimum number of gobs in Table 3.6 with those in Figure 3.6 indicates that F values of 0.64 and below produce single gob GREs. Because single-gob GREs have been identified in the historical tank data, setting F above 0.64 would not represent actual tank behavior. Likewise, the comparison of the average number of gobs indicates that F values of approximately 0.5 are bounding. At this value of F, the maximum number of gobs is not exceeded. However, the occurrence of single events is much more certain than the determination of the average number. Therefore, based on the number of gobs in a GRE, F may be bounded at or below approximately 0.6. A similar process was conducted for each of the remaining parameters. On each plot, the bounding range of F is indicated by the ellipsoid.

F appears to be bounded at or below 0.64 by the fraction of gas released (Figure 3.7), at or below 0.1 by the fraction of tank area participating (Figure 3.8), and below 0.1 by the time between gobs (Figure 3.9). Based on the inherent uncertainty in the determination of the parameters for the spontaneous BDGREs and the general behaviors observed in the simulation results, no definitive F values can be identified. We have therefore selected a distribution that has the most probable F values between 0.1 and 0.6, and the probability decreases at either end of the distribution to the physical limits of zero and unity. This distribution is used for each of the tanks, and the input probability distributions are shown in Appendix C.

It is interesting to consider the relationship between the time between gobs and the time to the peak release rate. Given our assumption that multiple BDGREs occur due to the suspension of solids into the supernatant at the same rate as the gas release, it is reasonable to expect that as the time to the peak release rate is increased (slower buildup of solids in the supernatant) the time between gobs would also increase. This is reflected in the selected spontaneous BDGRE data (selected as above) for all four tanks as shown in Figure 3.10. While it is certainly not conclusive, this behavior does support our assumptions for gob interaction mechanisms.

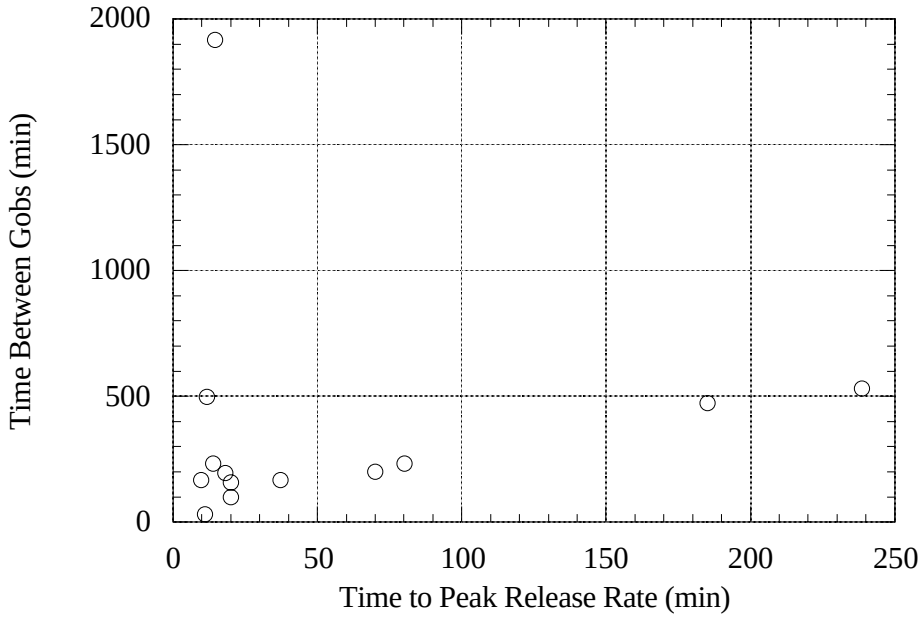

Figure 3.10. Time Between Gobs as a Function of the Time to Peak Release Rate

3.2.5 Monte Carlo Simulation Method

From the preceding discussion of the input parameters, it is apparent that the majority have significant quantified uncertainties. A deterministic calculation with all parameters set to bounding values has no physical or statistical meaning. Instead, we must account for all the parameter uncertainties and establish the overall probability distribution for the model's predictions. To accomplish this, a large number of model simulations are run with input parameter sets selected from their respective distributions. The collection of output values from all the model simulations then forms the desired overall probability distribution.

A Monte Carlo simulation approach was used. This approach can be employed to determine the uncertainty of modeling results when the input parameters have uncertainty distributions. For each retrieval operation modeled, 10,000 simulation runs were conducted. Simulating a large number of cases allows all important physical effects included in the model to influence the predicted behavior. The result is a set of 10,000 model outputs, each with its own set of predicted results, that constitutes a probability distribution over those predicted results. This allows us to predict the probability of a given result given the input probability distributions.

Each value used for the inputs is randomly sampled from an infinite population based on the specified distribution. The commercial code S+ was used to generate these inputs. In addition to the constraints specified above, the liquid and sediment layer densities were selected from the same half of their respective distributions (i.e., a liquid density above its median required a sediment density above its respective median, or vice-versa). Ten-thousand input distributions that met all of the constraints were created for each retrieval operation modeled. A Visual Basic code written around the Excel®-based model was used to generate results for each of the 10,000 simulations.

3.3 Analysis of GREs Induced by Supernate Decant in AN-105

While supernate decant simulations were performed for each of the four tanks of interest (AN-103, AN-104, AN-105, and AW-101), Tank AN-105 was selected to be presented in detail because it has experienced BDGREs with the highest headspace hydrogen concentration, it is one of the first tanks scheduled to be retrieved for vitrification, and it is reasonably representative of the other tanks.

Four cases were run to investigate the sensitivity of the results to the decant rate and the effects of two postulated control strategies:

1. **Base Case:** The decant rate was set at a constant 200 gpm. The model was run until essentially the entire supernatant layer was removed. The 200-gpm decant rate was chosen as the maximum flow rate likely to be achieved by available transfer pumps.
2. **Decant Rate Sensitivity:** The decant rate was reduced to 30 gpm. A lower decant rate was expected to reduce the peak hydrogen concentration. The 30-gpm flow rate was selected as the minimum practical decant rate.
3. **Stop-Start Control Strategy:** The base case was rerun with logic to stop the decant when the headspace hydrogen concentration exceeded 6,250 ppm and to restart decant when the hydrogen concentration fell below 500 ppm. This was postulated as a means to reduce the peak hydrogen concentration by preventing back-to-back BDGREs. A hydrogen concentration of 6,250 ppm is the action level for gas monitoring controls (CHG 2000); 500 ppm was the restart point in the SY-101 mixer pump tests (Sullivan et al. 1995).
4. **Water Backfill Control Strategy:** The base case was rerun with logic to add water at the same rate as decant, assuming that the water did not mix with the supernate. This was postulated as a method to maintain the hydrostatic pressure and prevent BDGREs.

The results of each of these cases for AN-105 are presented in the following sections. The method of presentation of the results is explained in Section 3.3.1, results of the base case are shown in Section 3.3.2, and the decant sensitivity study in section 3.3.3. The start-stop and water backfill control strategies are presented in Sections 3.3.3 and 3.3.4, respectively. The overall conclusions of these studies are summarized in Section 3.3.5. The results of the simulations for the other three tanks are given in Section 3.4.

3.3.1 Method of Presenting Analysis Results

As described in Section 3.2, the Monte Carlo simulation method propagates the probability distributions for the input parameters through the model to produce probability distributions of the results. This is done by performing a large number of simulations with different sets of parameter values chosen at random from the input probability distributions. It was found that 10,000 simulations were adequate to accurately represent the full range of inputs.

Each of these 10,000 simulations consists of a single supernate decant operation from start to finish, nominally calculating 1,000 time steps of 3 minutes each for a total of 50 hours. At each time step, data are recorded describing the state of the tank, including the condition of each gob. These data allow, for example, the headspace hydrogen concentration to be plotted as a function of time through the entire operation. This is shown schematically in Figure 3.11.

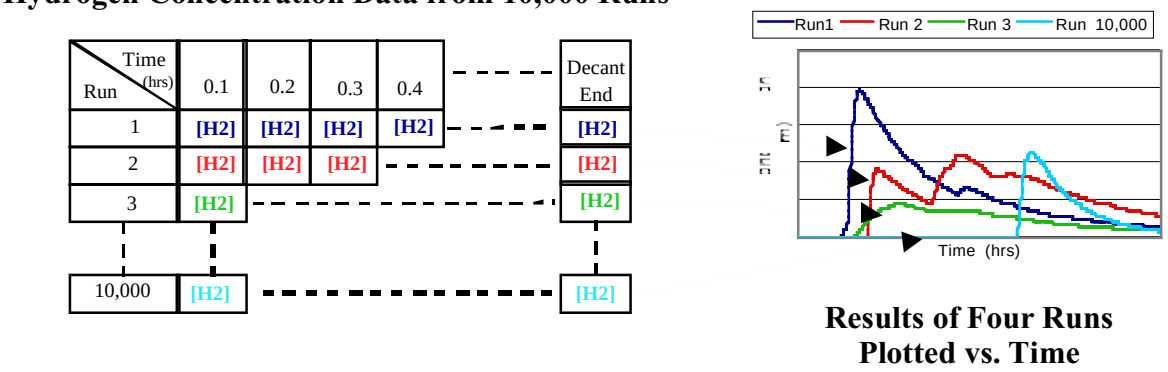

Figure 3.11. Schematic of Hydrogen Concentration Data

The peak hydrogen concentration attained during decant is the most useful result for assessing the flammable gas hazard. A set of 10,000 peak hydrogen concentrations is created from the results of the 10,000 Monte Carlo simulations performed for each case, each produced by a different set of input parameters. These data are sorted into 100 uniform bins to produce a fine-scale histogram describing the probability distribution for the peak hydrogen concentration. This process is represented by the sketch in Figure 3.12.

The frequency and cumulative frequency are plotted with the median and the 95th percentile values (95% confidence limit [CL]) identified by a dashed line. These probability distributions are plotted for both the peak hydrogen concentration and the fraction of gas in the sediment layer released during decant. The transient hydrogen concentrations for one or two representative runs are also plotted to better illustrate the dynamic gas release behavior and to show the sequence of BDGREs. The median and 95th percentile values for the base case are shown on the three succeeding cases to illustrate the effect of the changes involved.

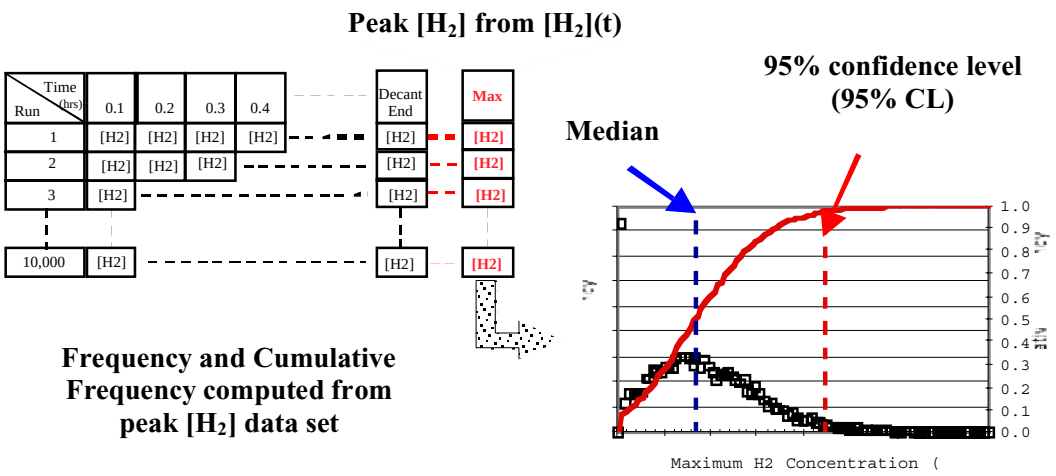

Figure 3.12. Derivation of Output Probability Distribution

3.3.2 Base Case

The distribution of peak hydrogen concentration for the base case is shown in Figure 3.13. This case used a constant 200-gpm decant rate with 100 scfm of ventilation. The median of the peak hydrogen concentration data set is 2,800 ppm, and the 95th percentile value is 8,300 ppm, lower than 25% of the LFL in AN-105 but higher than the action level of 6,250 ppm. The initial high value of the frequency indicates that 14.4%, or 1,440, of the 10,000 runs had only small gas releases (peak hydrogen concentrations less than 210 ppm). There were no BDGREs induced at all in 1,356 of the runs, so the hydrogen concentration remained below the initial steady-state value, which was approximately 23 ppm for the input hydrogen generation and ventilation rates.

The distribution of the fraction of retained gas released from the sediment layer for the AN-105 base case is shown in Figure 3.14. The full supernate decanting process releases a relative small fraction of the total retained gas volume. The median release fraction is 0.09, while the 95th percentile value is 0.22. The relatively high frequency of 0.136 at zero gas release corresponds to the 1,356 runs with no BDGREs. The largest spontaneous BDGRE in AN-105 released on the order of 20% of the retained gas in the sediment layer.

The headspace hydrogen concentration transient for a typical simulation is plotted in Figure 3.15. This run reached a peak hydrogen concentration of about 6,500 ppm. The figure shows results of five BDGREs triggered during the decant. The first large GRE, composed of one gob, began at about 10 hours, and a small single-gob release occurred at 26 hours. The second large GRE began at 30 hours and involved three more gobs. No BDGREs were induced in the last 20 hours of the decant.

These results show that decanting the supernate from AN-105 will be unlikely to challenge the LFL, though the peak headspace hydrogen concentration approaches 25% of the LFL (nearly 10,000 ppm in AN-105) at the 95% confidence level. The highest hydrogen concentrations are most likely to occur in the first 20 hours of decant, when the headspace is least and the hydrostatic pressure is highest. The decant process is expected to release less than a quarter of the gas.

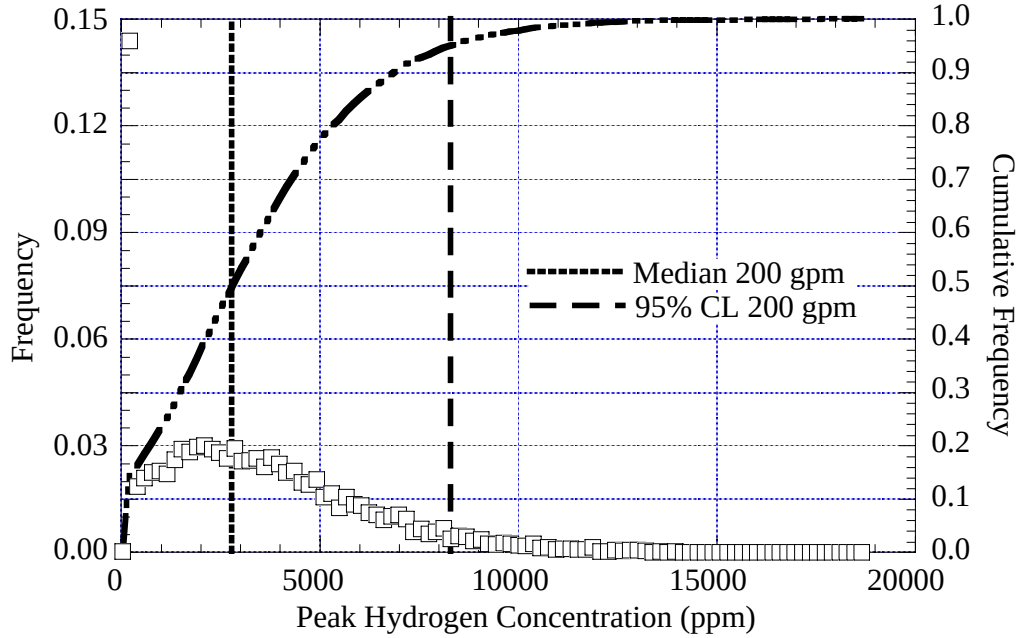

Figure 3.13. Peak Hydrogen Concentration for the AN-105 Base Case

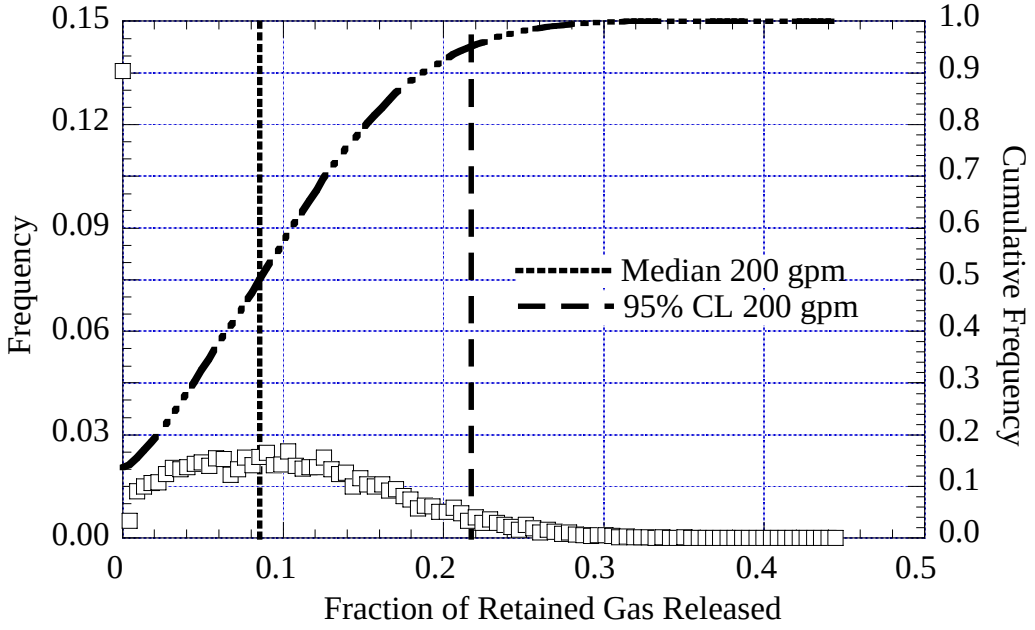

Figure 3.14. Gas Release Fraction for the AN-105 Base Case

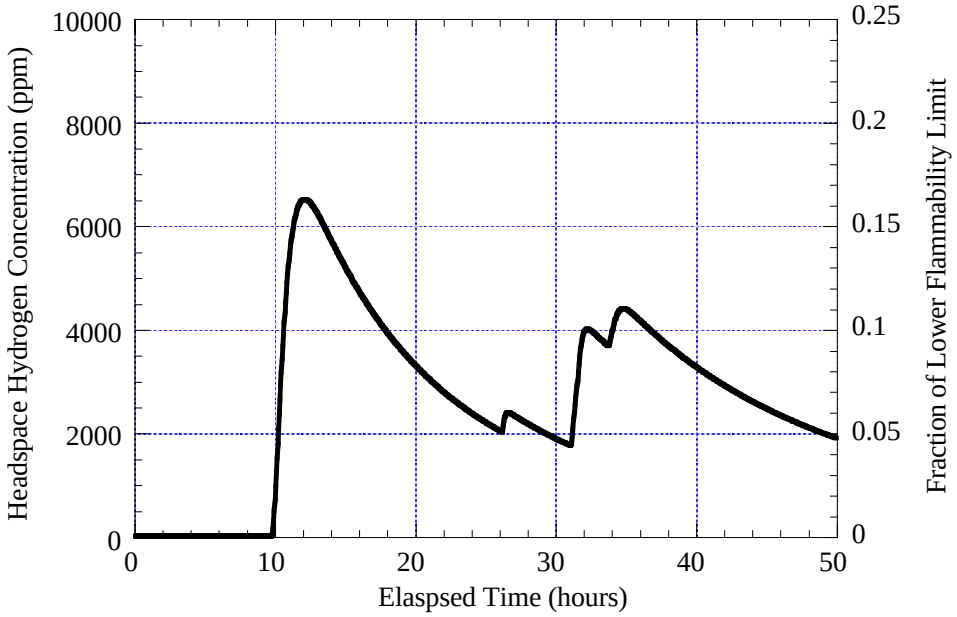

Figure 3.15. Representative Hydrogen Concentration History for the AN-105 Base Case

Because the gas releases are rapid compared with the ventilation rate (see Section 3.2), the maximum hydrogen concentration results are relatively insensitive to changes in the ventilation rate. Varying the ventilation rate by a factor of 2 alters the maximum hydrogen concentration at the 95% confidence level by approximately 10%.

3.3.3 Effect of Decant Rate

The decant flow rate is the only parameter over which the operators have direct control. It would be beneficial if a lower decant rate would reduce the peak hydrogen concentration by increasing the time between induced BDGREs. A case was run at a decant rate of 30 gpm, less than 1/6 of that used in the base case, to investigate this. The 30-gpm rate was chosen as the minimum rate practical for future operations.

Figure 3.16 shows the distribution of peak hydrogen concentrations for the 30-gpm decant rate. The median and 95th percentile value for the base case are also shown. While the lower decant rate lowered the peak hydrogen concentrations measurably, the difference was not significant. The median value decreased from 2,800 ppm in the base case to 2,600 ppm and the 95th percentile value from 8,300 ppm to 8,000 ppm. The number of runs in which no BDGREs occurred (1356) remained the same as in the base case.

The distribution of the fraction of retained gas released (Figure 3.17) is virtually identical to the base case, showing that a given reduction in hydrostatic pressure releases the same fraction of retained gas regardless of the rate at which it is reduced (assuming suspended solids do not settle out). This also will be shown for the stop-start control strategy. The main consequence of the lower decant rate is to lengthen the time required for decant from 50 hours to almost two weeks.

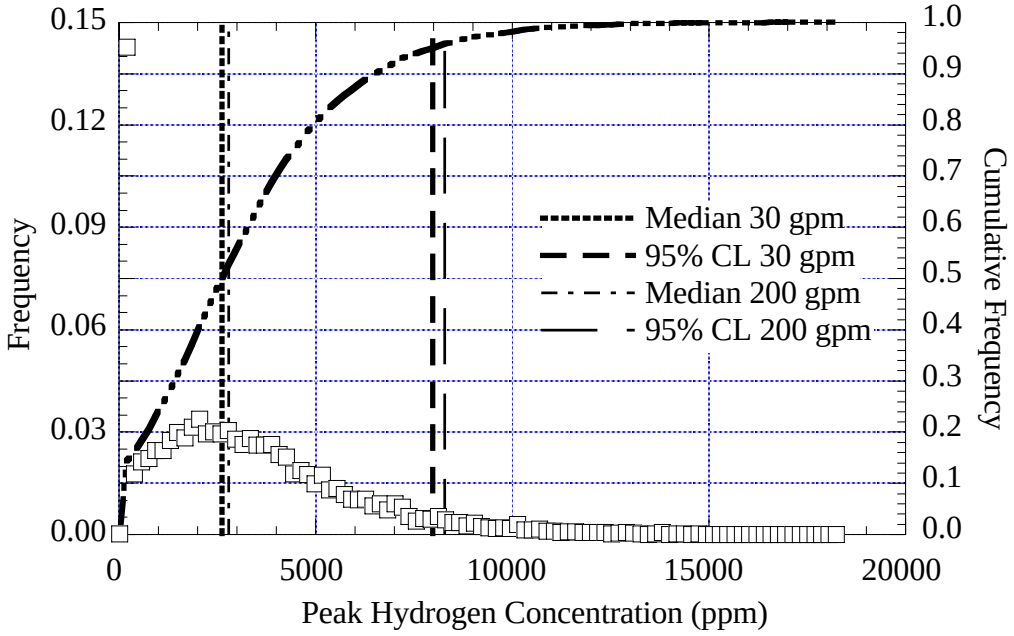

Figure 3.16. Hydrogen Concentration for 30 gpm Decant Rate in AN-105

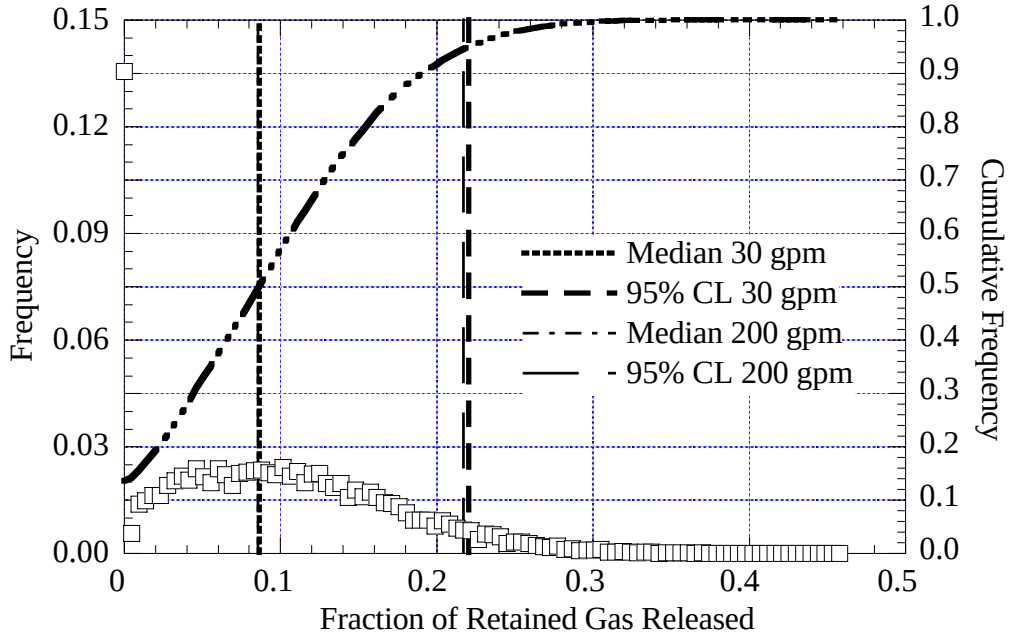

Figure 3.17. Fraction of Gas Released for 30 gpm Decant Rate in AN-105

3.3.4 Stop-Start Control Strategy

Tank farm operations are required to be halted if the gas monitoring instruments measure a hydrogen concentration exceeding 6,250 ppm in the headspace (CHG 2000). This control was set to prevent the concentration from reaching the LFL on the assumption that the operation was causing the gas release. Operations can theoretically resume when the hydrogen concentration drops back below 6,250 ppm; however, a lower restart threshold is usually used. The SY-101 mixer pump safety assessment (Sullivan 1995) specified 500 ppm for restart.

To check the effect of a stop-start control strategy, the base case was rerun with the decant rate set to 0 at hydrogen concentrations above 6,250 ppm and restarted at 500 ppm. The resulting peak hydrogen concentration distribution is shown in Figure 3.18. The indicators for the base case are also shown. The stop-start control strategy had less effect on the peak hydrogen concentration than the decant rate. The median of 2,800 ppm is identical to the base case, and the 95th percentile value is lowered only slightly to 8,200 ppm. The distribution of gas release fraction, given in Figure 3.19, and the number of runs with no BDGREs (1365) are also virtually identical to the base case.

As with the 30-gpm decant rate case, the main result of the start-stop control strategy was to prolong decant by about 100 hours. This is illustrated in Figure 3.20, where the hydrogen concentration transients in the start-stop case and base case are plotted for runs using the same set of input. The first GRE, composed of one gob, began at about 10 hours; decant was halted at about 11.5 hours, when the hydrogen concentration rose above 6,250 ppm. However, the BDGRE was already under way and drove the hydrogen concentration to the same peak value as the base case. Decant restarted at about 37.5 hours, and the second GRE, composed of four gobs, started about 14.5 hours later, at 52 hours.

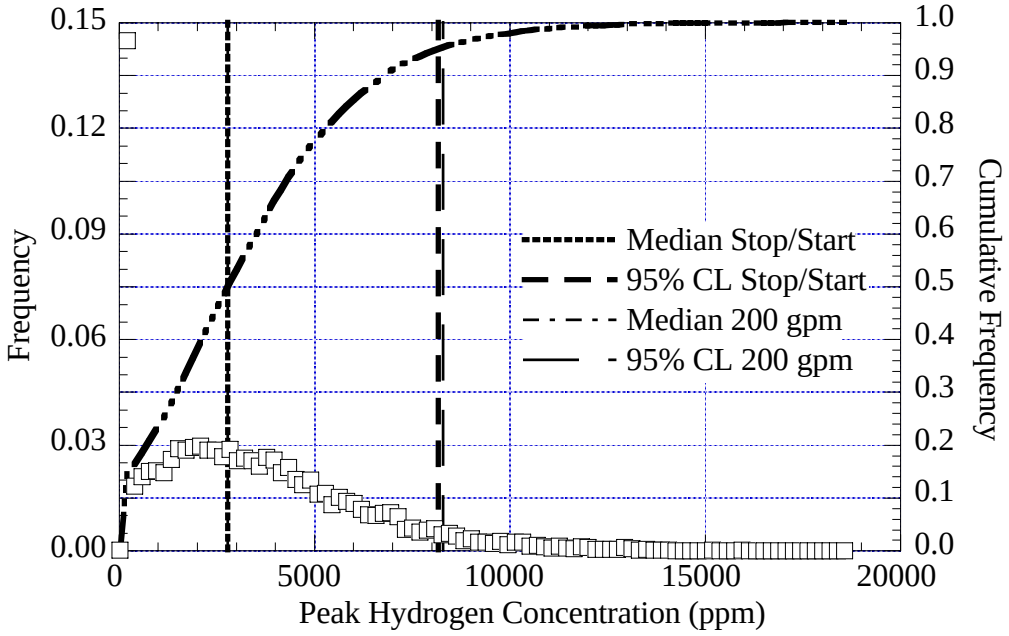

Figure 3.18. Peak Hydrogen Concentration for the Stop-Start Case in AN-105

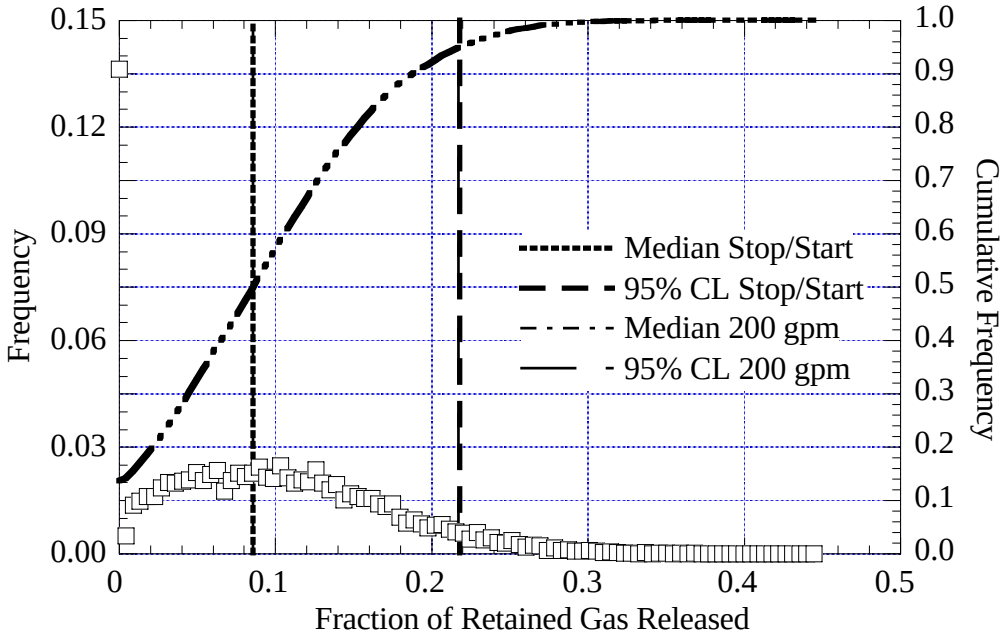

Figure 3.19. Gas Release Fraction for the Stop-Start Case in AN-105

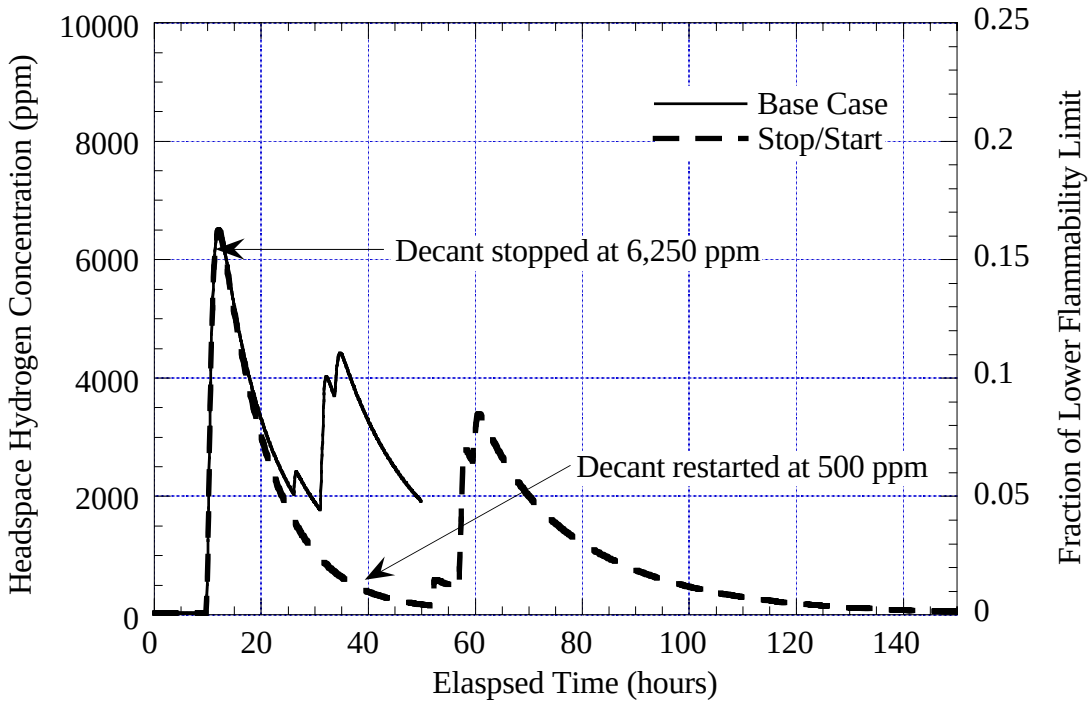

Figure 3.20. Hydrogen Concentration Transient for Stop-Start Case in AN-105

There were 1,262 runs out of the 10,000 with hydrogen concentrations reaching 6,250 ppm, requiring 1266 stop-start periods (four runs had two stop-start periods apiece). During these periods the hydrogen concentration kept rising, reaching a maximum 2.5 hours after decant stopped. The median peak concentration during a stop-start period was about 7,600 ppm, and the 95th percentile value was almost 12,000 ppm. Because a hydrogen concentration rising past 6,250 ppm is generally the result of a BDGRE in progress and the gas release from gobs already at the surface is not affected by decanting, stopping the decant does not reduce the peak hydrogen concentration.

3.3.5 Water Backfill Control Strategy

Since decant-induced BDGREs are the result of decreasing hydrostatic pressure, it was believed that maintaining the pressure by backfilling with water might prevent or reduce the frequency of BDGREs. However, because water is much less dense than the concentrated supernate, the hydrostatic pressure cannot be maintained, and some potential for induced BDGREs remains. In AN-105, the initial hydrostatic pressure on the retained gas is about 2.0 atm. A full supernate decant reduces the pressure to 1.3 atm, while the minimum pressure for a water backfill is 1.8 atm. However, a negative side effect of the backfill is that the tank headspace does not increase (except minimally due to gas release) as supernate is removed. This means that the same gas release results in a higher hydrogen concentration. This is exacerbated by the higher gas release fraction coincident with the higher hydrostatic pressure.

The results of these combined effects are illustrated in the distribution of peak hydrogen concentration shown in Figure 3.21. The most striking effect of the water backfill is that the median peak hydrogen concentration is at the steady-state background concentration of 23 ppm. This is the direct result of there being no BDGREs in 7,653 of the 10,000 runs. However, due to the smaller headspace, the peak hydrogen concentration at the 95th percentile value, 7,600 ppm, was essentially the same as that of the base case. The fraction of retained gas released is also much lower than the base case, as shown in Figure 3.22. The median is 0 and the 95th percentile value 0.13—base case is 0.22. This means that many fewer BDGREs occurred in all runs.

The behavior of induced BDGREs during water backfill is presented more clearly in the hydrogen concentration transient in Figure 3.23. Plots for the same set of input values in the base case and stop-start case are also shown. The water backfill plot shows that the first BDGRE occurs about 20 hours later than in the other cases but cause a higher hydrogen concentration because of the smaller headspace. The remaining four BDGREs (base case run has five BDGREs total) are not triggered. These results show that, while water backfill does not reduce the bounding hydrogen concentration, it does reduce the probability of BDGREs and the total volume of gas released significantly.

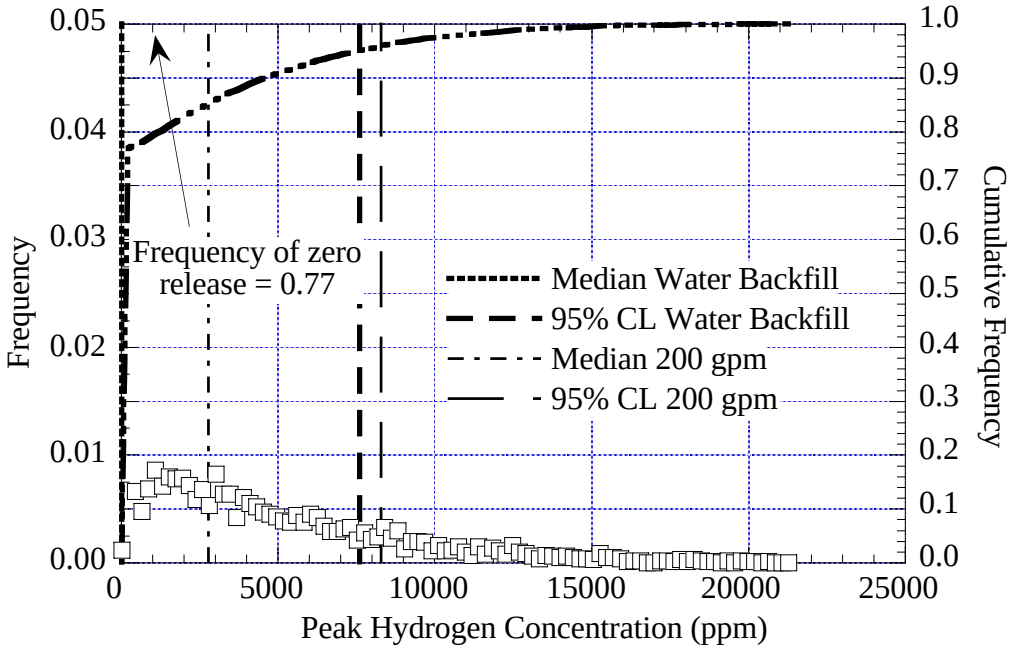

Figure 3.21. Peak Hydrogen Concentration for Water Backfill in AN-105

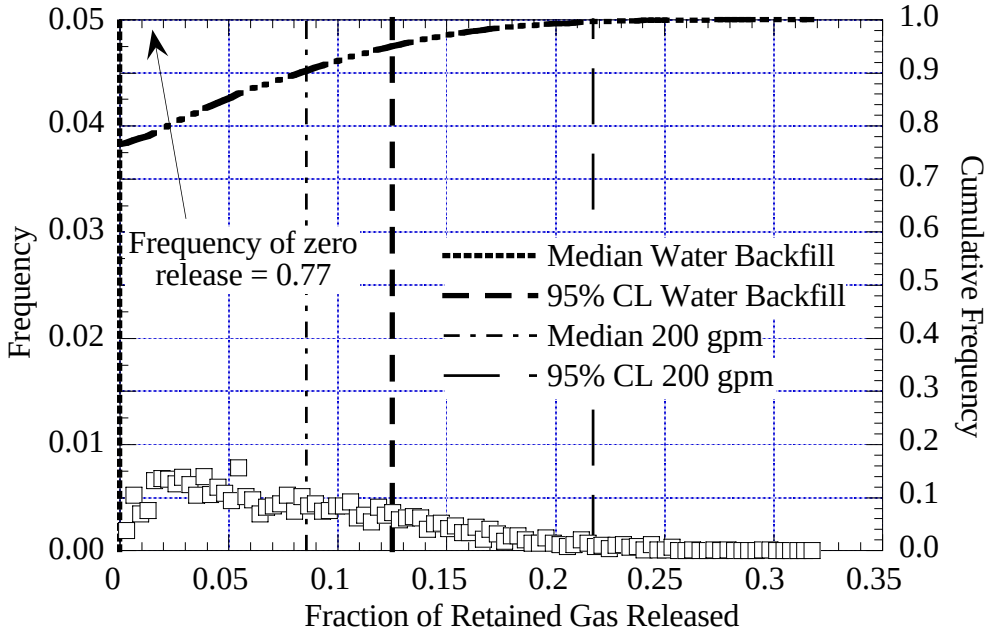

Figure 3.22. Fraction of Gas Released for Water Backfill in AN-105

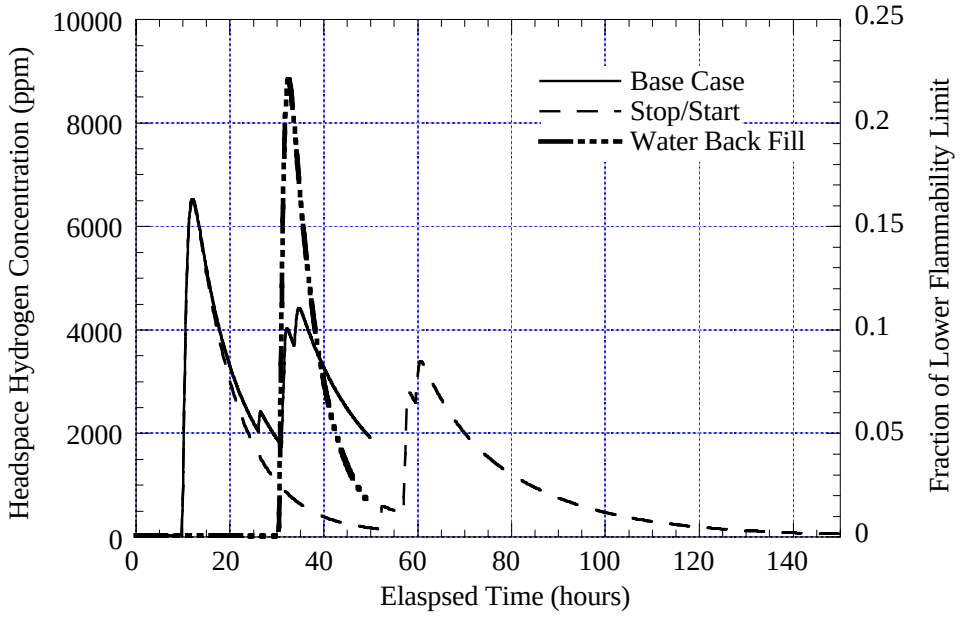

Figure 3.23. Hydrogen Concentration Transient for Water Backfill in AN-105

3.3.6 Summary of Analyses for AN-105

Gas releases induced by supernate decant in AN-105 are very unlikely to approach flammability. The median value of the peak hydrogen concentration during decant was about 3,000 ppm, and about 8,000 ppm at the 95% confidence level. It is relatively insensitive to decant rate and was not reduced by stopping the decant at the action level of 6,250 ppm. Backfilling with water significantly reduced the median peak hydrogen concentration, though it did not reduce the bounding value of peak hydrogen concentration. It also greatly reduced the probability of BDGREs. More than 75% of the water backfill runs did not have a BDGRE. The fraction of total gas released during decant was virtually identical in the base case, the reduced decant rate, and the stop-start control strategy case at 22%. Only the water backfill reduced it significantly. These results are summarized in Table 3.7.

Table 3.7. Summary of Decant Analysis Results in AN-105

Run	Quantity	Median	95% CL
Base Case	Hydrogen (ppm)	2,800	8,300
	Fraction Gas Release	0.09	0.22
30 gpm Decant	Hydrogen (ppm)	2,600	8,000
	Fraction Gas Release	0.09	0.22
Stop-Start Control	Hydrogen (ppm)	2,800	8,200
	Fraction Gas Release	0.09	0.22
Water Backfill	Hydrogen (ppm)	23	7,600
	Fraction Gas Release	0.00	0.13

3.3.7 Sensitivity Analysis

A sensitivity analysis was conducted on the AN-105 decant results to determine which variables have the most impact on the output results. Only the results of the base case are shown because analysis results for the other cases proved to be very similar.

The set of inputs and outputs is assumed to be a multivariate normal distribution. A multivariate analysis of variance (MANOVA) was performed on the data. The analysis compares the matrix of hydrogen concentration outputs (1,000 results per simulation) to the set of inputs. The error associated with the model is assumed to be distributed multivariate normal with mean zero and variance matrix Σ. It is assumed that no significant interactions exist between the independent variables in the data. The results are shown in Table 3.8. Low p-values (<0.05) indicate highly significant impact on the results. In the scheme of the decant model, gob 1 has the highest initial average gas fraction, gob 2 has the second highest average gas fraction, and so on.

No unexpected results are achieved. The model results are most sensitive to the liquid density, sediment layer density, and the gas fraction and diameter of gob 1. The layer densities dictate the gas fraction at which a gob may become buoyant (also affected by sediment yield stress), and the liquid density affects the pressure change for a volume of supernate removed and amount of gas released in a BDGRE. The gas fraction in gob˚1, the highest gas fraction in the gobs, directly affects the likelihood of a BDGRE occurring during decant, the diameter of this gob directly affects the quantity of gas released, and the hydrogen concentration in the retained gas dictates the volume of hydrogen in the headspace. The gas fraction profile in the gob dictates the rate at which the gas fraction changes with decant and thus directly impacts the

Table 3.8. Sensitivity Results from Base Case

Parameter	P-Value
Crust thickness	< 0.0001
Sediment yield stress	< 0.0001
Liquid density	0.0000
Sediment layer density	0.0000
Hydrogen concentration in retained gas	< 0.0001
Fraction of gob material suspended into supernate	< 0.0001
Time to peak release rate, gob 1	< 0.0001
Time to peak release rate, gob 2	< 0.0001
Time to peak release rate, gob 3	0.0009
Gob gas fraction, gob 1	0.0000
Gob gas fraction, gob 2	< 0.0001
Gob gas fraction, gob 3	0.0091
Gob diameter, gob 1	0.0000
Gob diameter, gob 2	< 0.0001
Gob gas fraction profile, gob 1	< 0.0001
Gob gas fraction profile, gob 2	< 0.0001
Gob gas fraction profile, gob 3	0.0468
Gob gas fraction profile, gob 4	0.0085

results. The time to peak release rate affects the hydrogen concentration and stimulates subsequent BDGREs in conjunction with the fraction of the gob material suspended in the supernate.

3.4 Supernate Decant in AN-103, AN-104, and AW-101

Decant-induced gas releases in the three other tanks were also analyzed. Four cases were run to investigate the sensitivity of the results to the decant rate and the effects of the two postulated control strategies. The initial conditions for each tank were determined from historical data and measurements the same way as AN-105 (see Section 3.2). Both 5,000 and 10,000 simulations were conducted for the base case in each tank. Because the results of these simulations were equivalent, only 5,000 simulations were conducted to investigate the effects of varying the decant rate and of the control strategies in an effort to control computational time. The favorable comparison of the base case runs indicates that the validity of the results is not compromised by the decrease in run count. The decant results for all of the tanks are summarized in Section 3.5.

3.4.1 AN-103 Decant Results

Tank AN-103 contains by far the highest retained gas volume of the four tanks considered in this study. It also has exhibited the fewest and smallest spontaneous BDGREs, so there are relatively few good observations from which to input parameter distributions. By all indications (i.e., direct void measurements, barometric pressure response, surface level rise, and lack of large GREs), the entire waste volume is very near neutral buoyancy. This required a distribution for the gob gas fraction that was skewed toward the neutral buoyant gas fraction (see Section 3.2.3) to satisfy the constraint on total gas volume.

Because a high percentage of the gobs in the tank are initially very close to neutral buoyancy, BDGREs occur relatively early in every run (only 2% of the runs had no BDGREs occur). This results in rather high hydrogen concentration results. The peak hydrogen concentration and the gas release fraction results for the base case are shown in Figures 3.24 and 3.25. The median of the peak hydrogen concentration is 10,500 ppm, and the 95th percentile value is 21,100 ppm, or about 50% of the LFL. None of the runs exceeded the LFL. The median and 95th percentile values of the gas release fraction are 0.18 and 0.33, respectively.

Results for the 30-gpm decant are similar to those for the base case (Figures 3.26 and 3.27). The stop-start control results are shown in Figures 3.28 and 3.29. In almost 80% of the runs the hydrogen concentration exceeded 6,250 ppm, requiring 4,811 stop-start periods. About 1% of the runs required three stop-start periods (6,250 ppm was exceeded three times during the decant for 1% of the simulations) and over 20% required at least two stop-start periods. The hydrogen concentration during these stopped periods kept rising, reaching a maximum approximately 3.5 hours after decant stopped. The median peak concentration during a stop-start period was about 9,400 ppm, and the 95th percentile value was almost 50% of the LFL at 19,400 ppm.

The water backfill control results are shown in Figures 3.30 and 3.31. As with AN-105, the control strategies do not significantly alter the 95th percentile results, and median results for the water backfill case are notably lower. Only 45% of the water backfill runs had no BDRGEs.

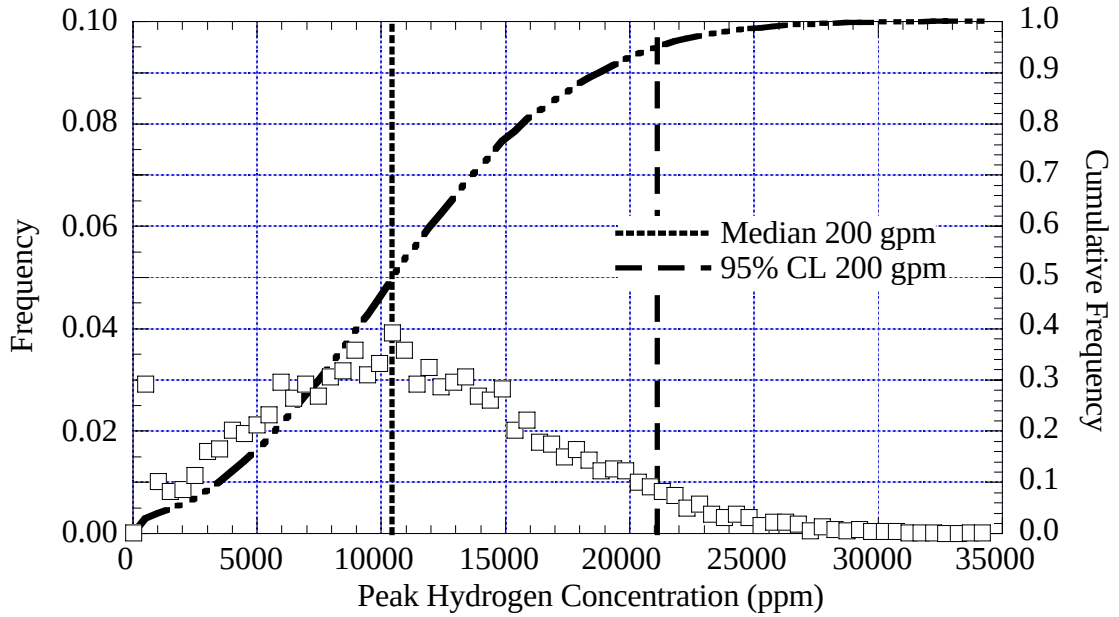

Figure 3.24. Peak Hydrogen Concentration for the AN-103 Base Case

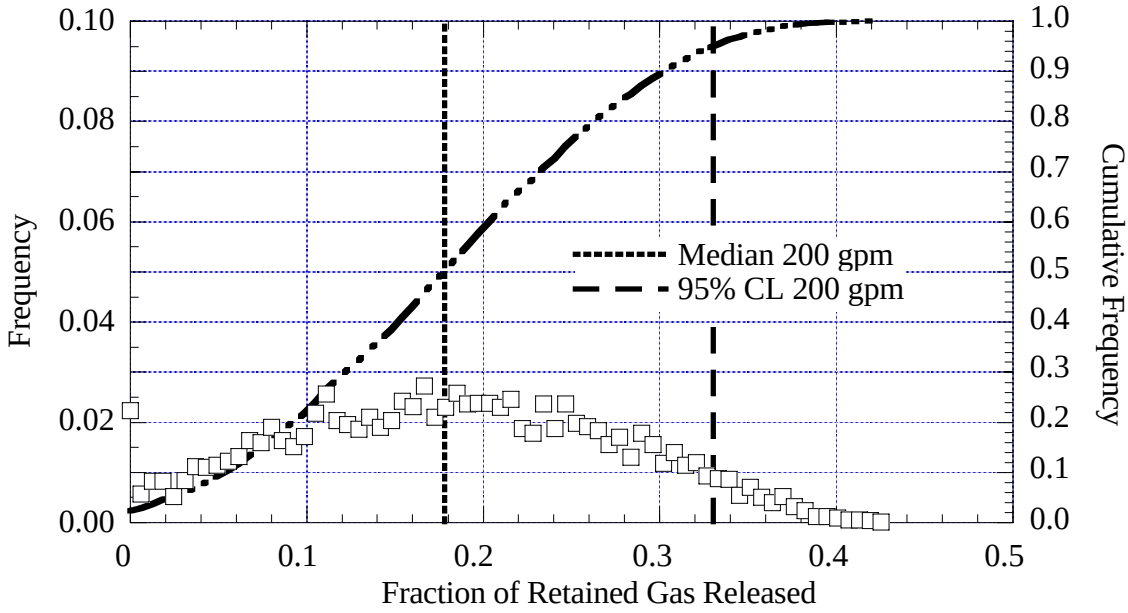

Figure 3.25. Gas Release Fraction for the AN-103 Base Case

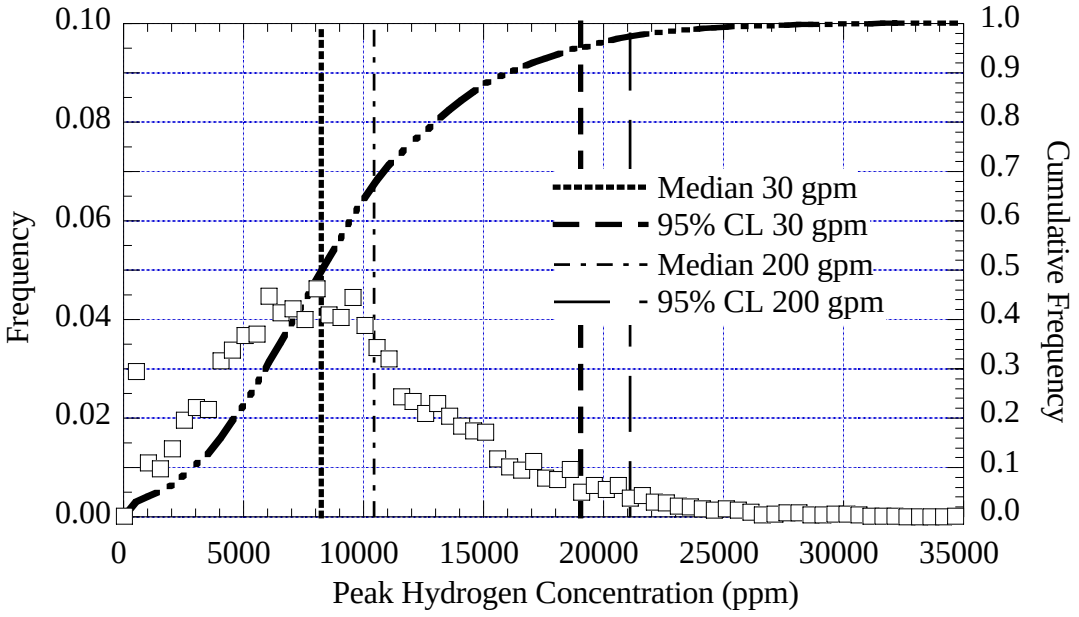

Figure 3.26. Peak Hydrogen Concentration for 30 gpm Decant Rate in AN-103

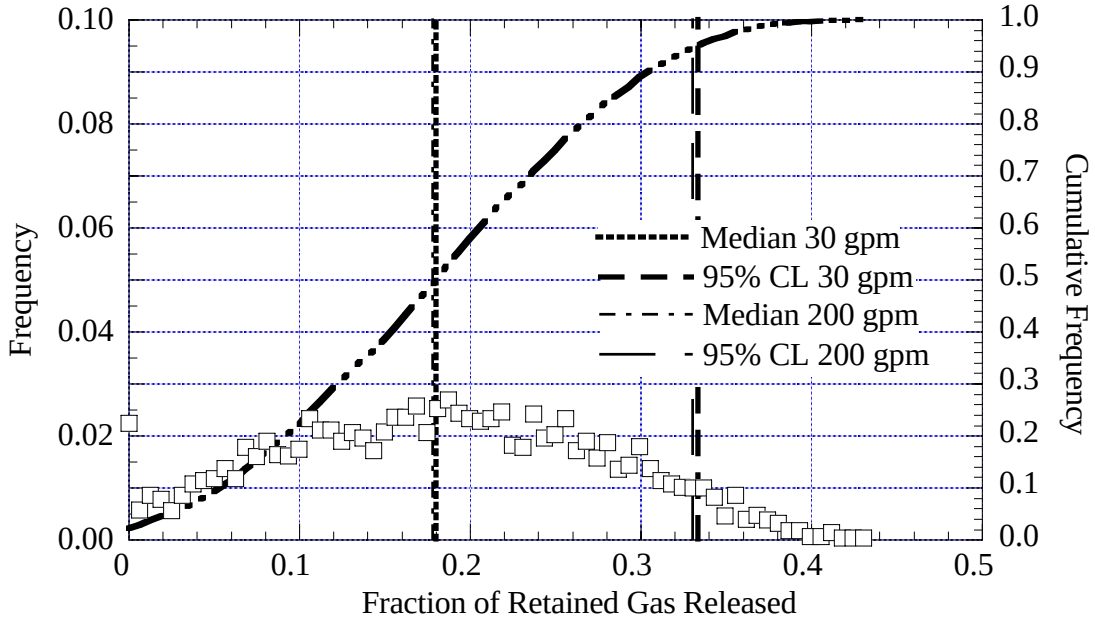

Figure 3.27. Gas Release Fraction for 30 gpm Decant Rate in AN-103

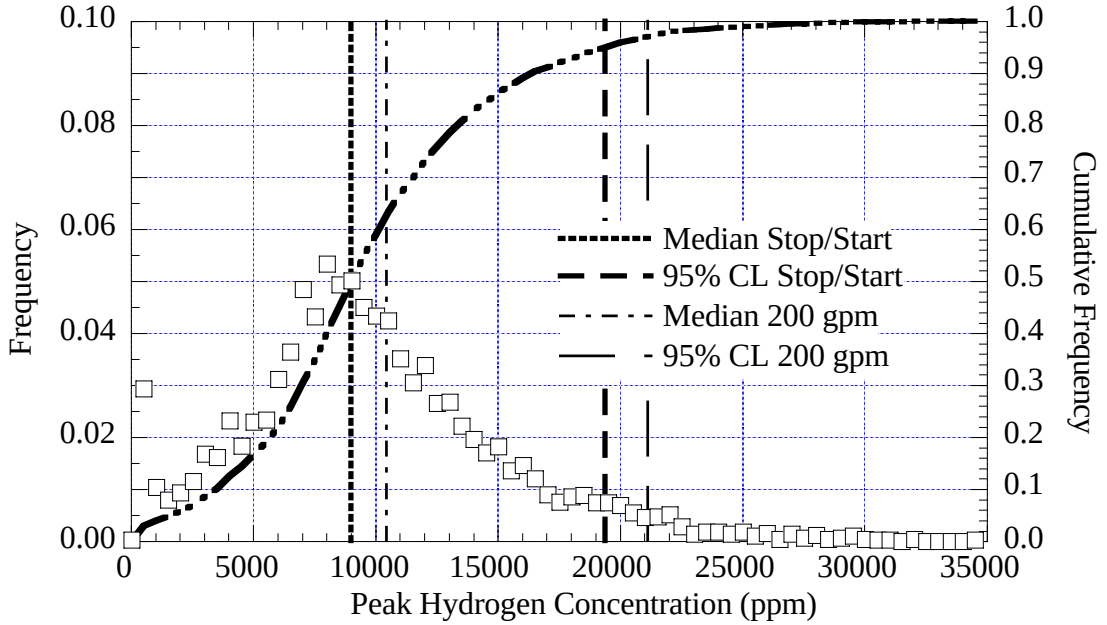

Figure 3.28. Peak Hydrogen Concentration for the Stop-Start Case in AN-103

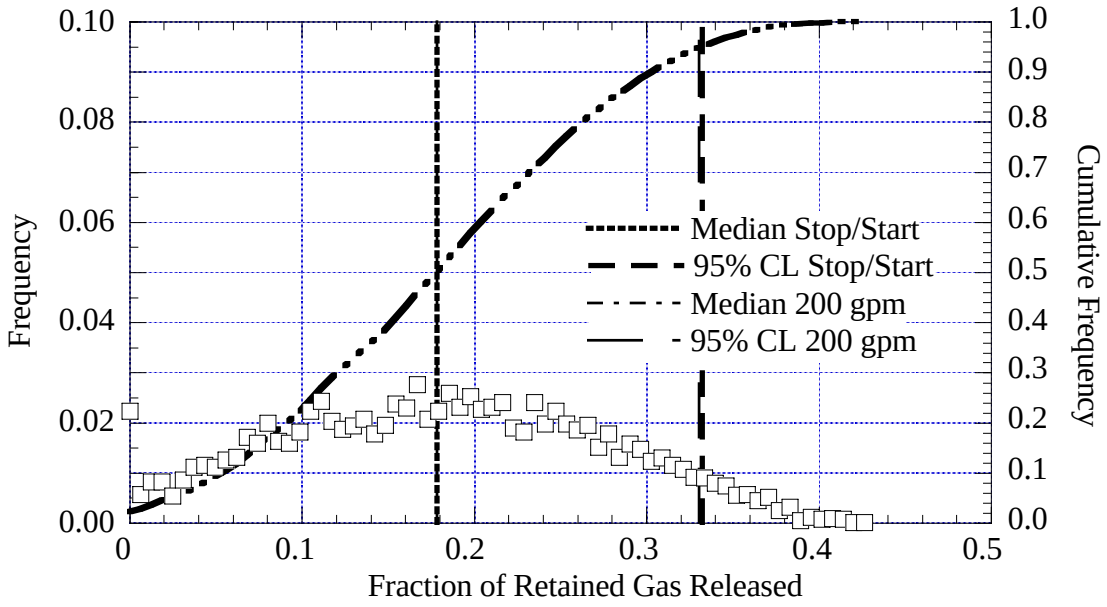

Figure 3.29. Gas Release Fraction for the Stop-Start Case in AN-103

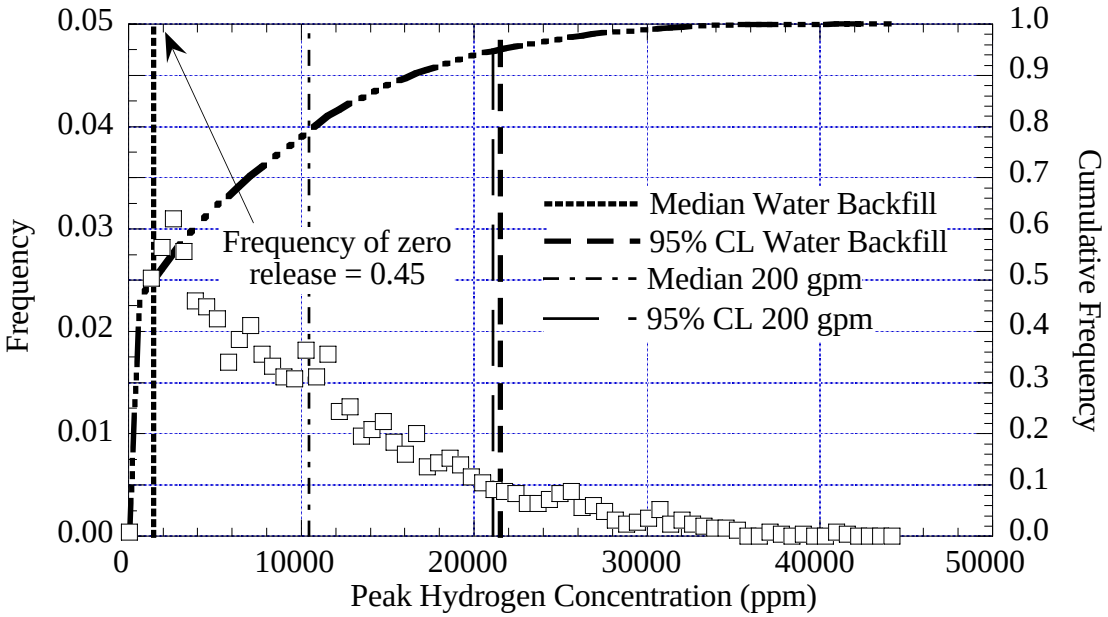

Figure 3.30. Peak Hydrogen Concentration for Water Backfill in AN-103

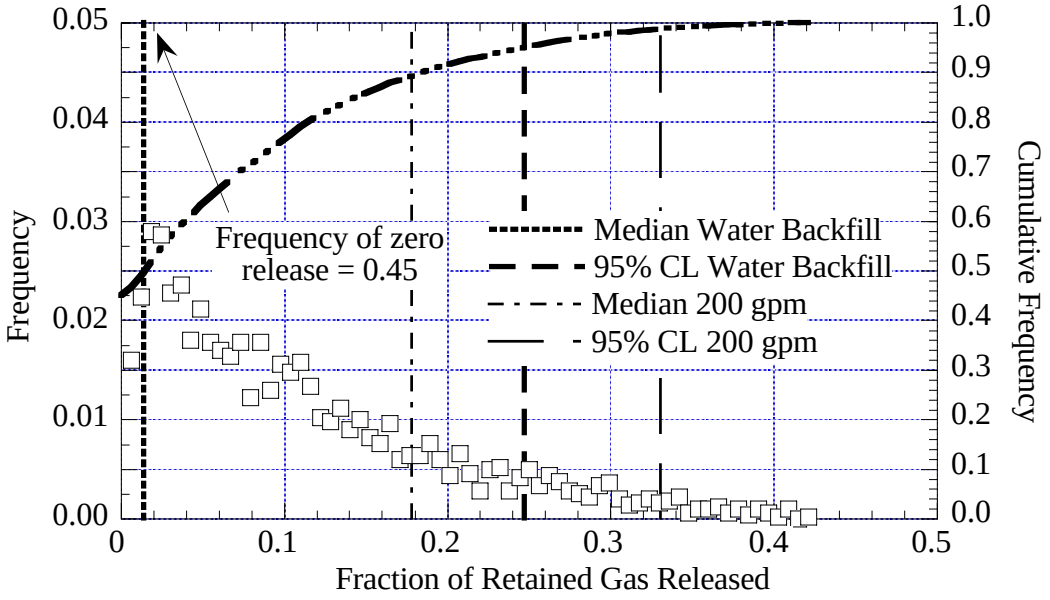

Figure 3.31. Gas Release Fraction for Water Backfill in AN-103

3.4.2 AN-104 Decant Results

The retained gas volume in AN-104 is somewhat larger than in AN-105, but its headspace is larger. The spontaneous gas release history is very similar to that of AN-105. The net result is that AN-104 and AN-105 exhibit similar behavior during decant. The distributions of the peak hydrogen concentration and gas release fraction for the base case are given in Figures 3.32 and 3.33, respectively. The median and 95th percentile values of the peak hydrogen concentration distribution are 2,800 ppm and 7,100 ppm, respectively. The gas release fraction has a median of 0.12 and a 95th percentile value of 0.27. A total of about 10% of the base case runs did not experience a BDGRE during the decant.

As with AN-105, the results for the 30 gpm decant are similar to those of the base case (Figures 3.34 and 3.35). The stop-start control results are shown in Figures 3.36 and 3.37. Approximately 8% of the runs had hydrogen concentrations that exceeded 6,250 ppm. The maximum hydrogen concentration during these stopped periods typically occurred two hours after the decant stopped. The median peak concentration during the stop-start periods was about 7,200 ppm, and the 95th percentile value was just over 25% of the LFL at 10,400 ppm.

Results for the water backfill control strategy are shown in Figures 3.38 and 3.39. The control strategies do not significantly alter the 95th percentile results, and the median results for the water backfill case return to the background concentration and zero BDGRE gas release, with about 70% of the simulations having no BDGREs.

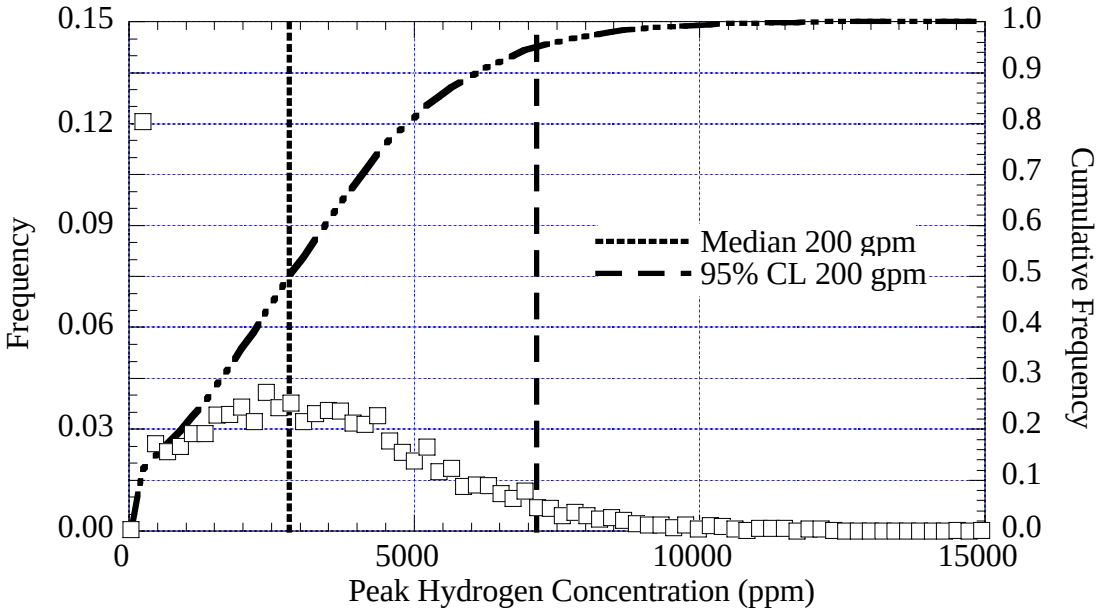

Figure 3.32. Peak Hydrogen Concentration for the AN-104 Base Case

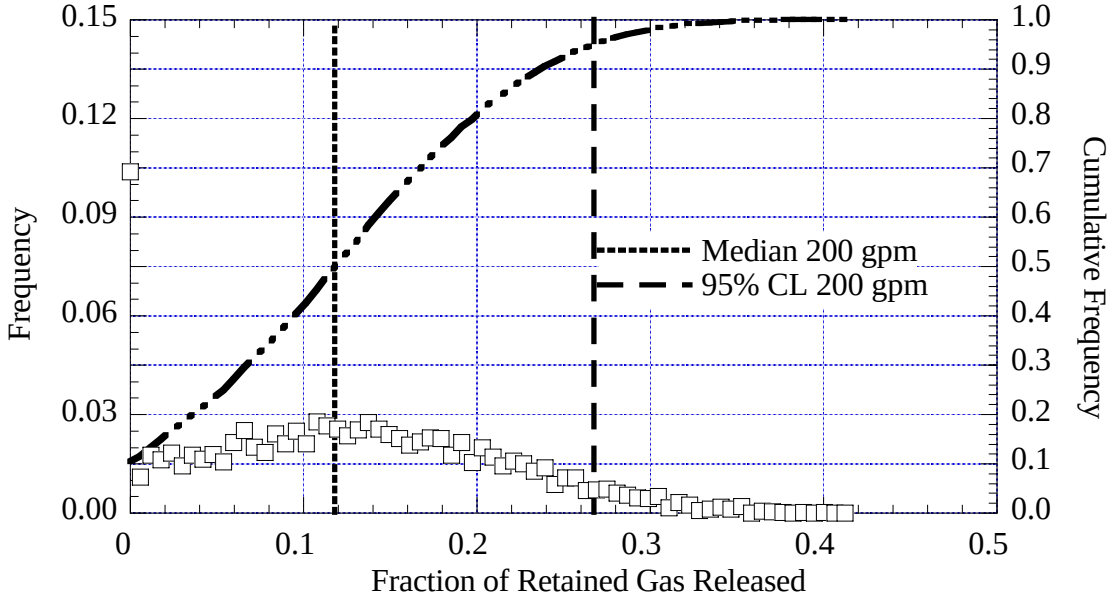

Figure 3.33. Gas Release Fraction for the AN-104 Base Case

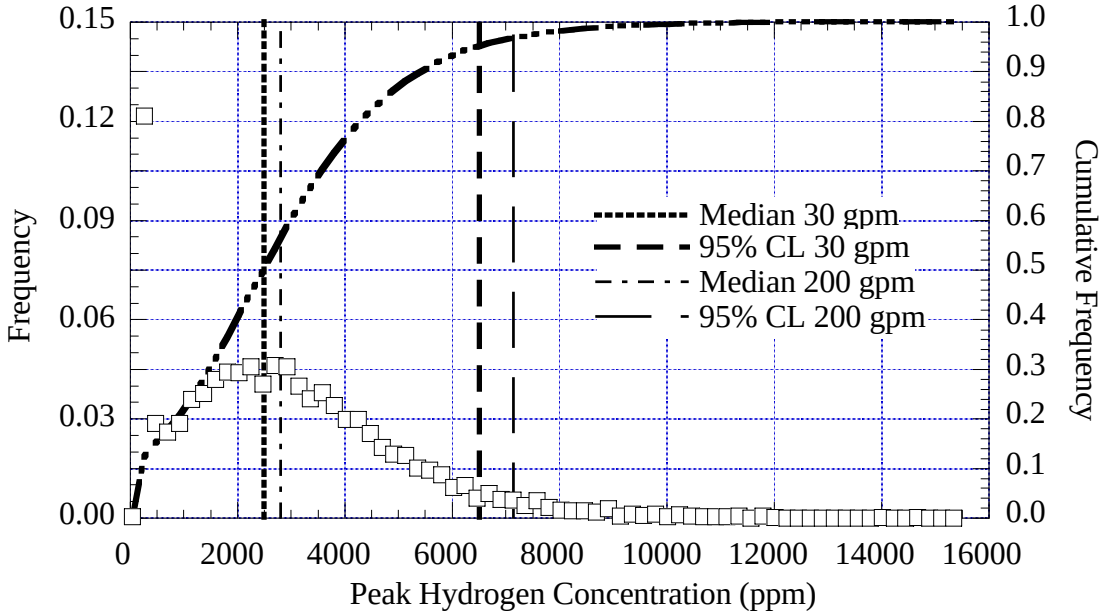

Figure 3.34. Peak Hydrogen Concentration for 30 gpm Decant Rate in AN-104

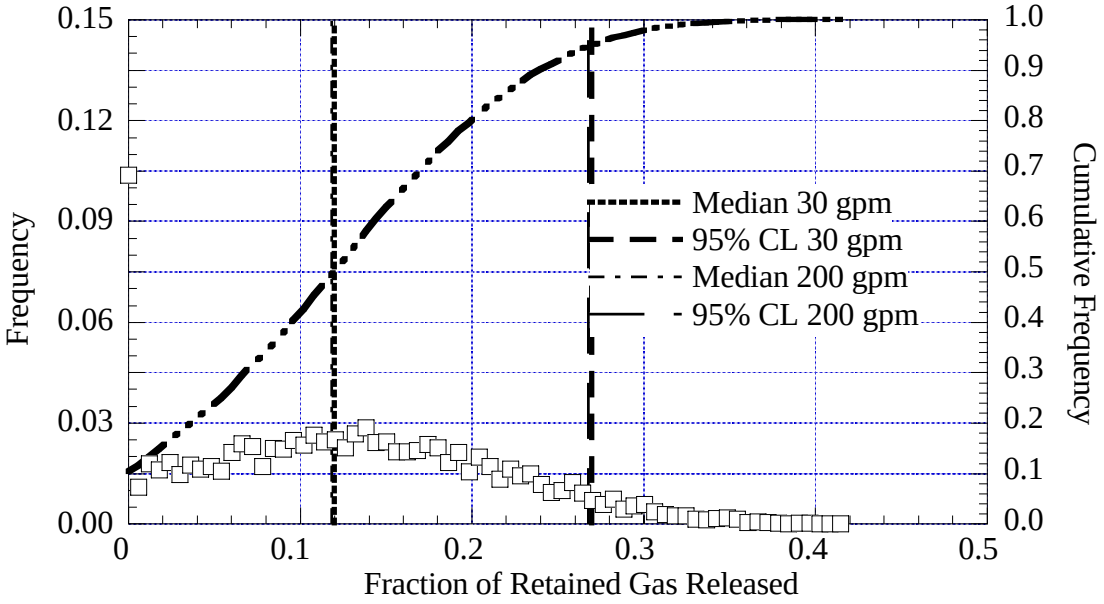

Figure 3.35. Gas Release Fraction for 30 gpm Decant Rate in AN-104

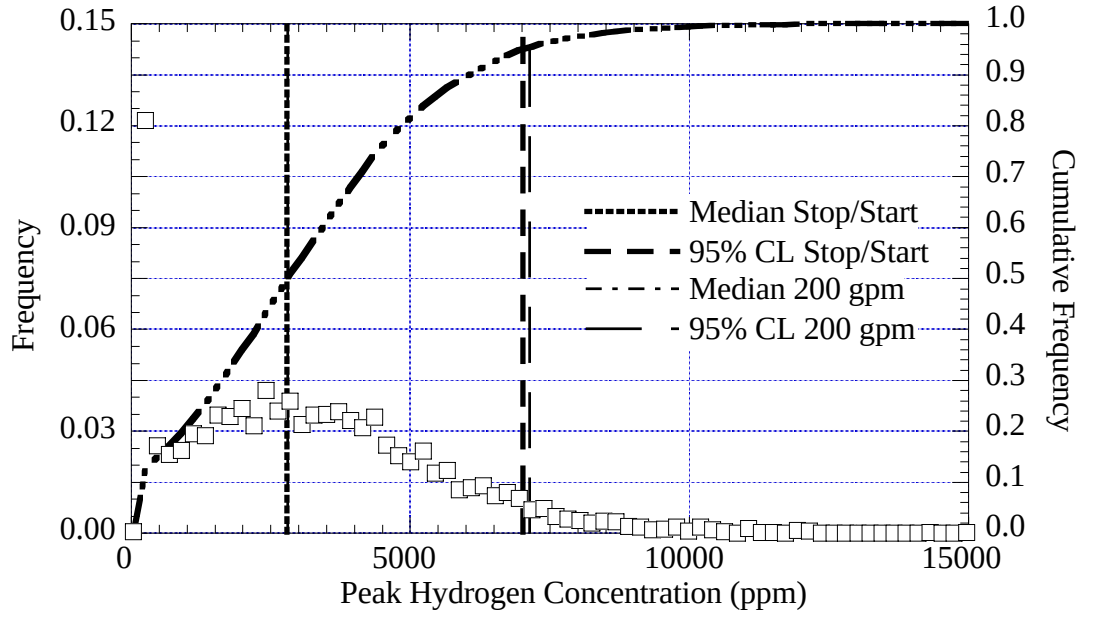

Figure 3.36. Peak Hydrogen Concentration for the Stop-Start Case in AN-104

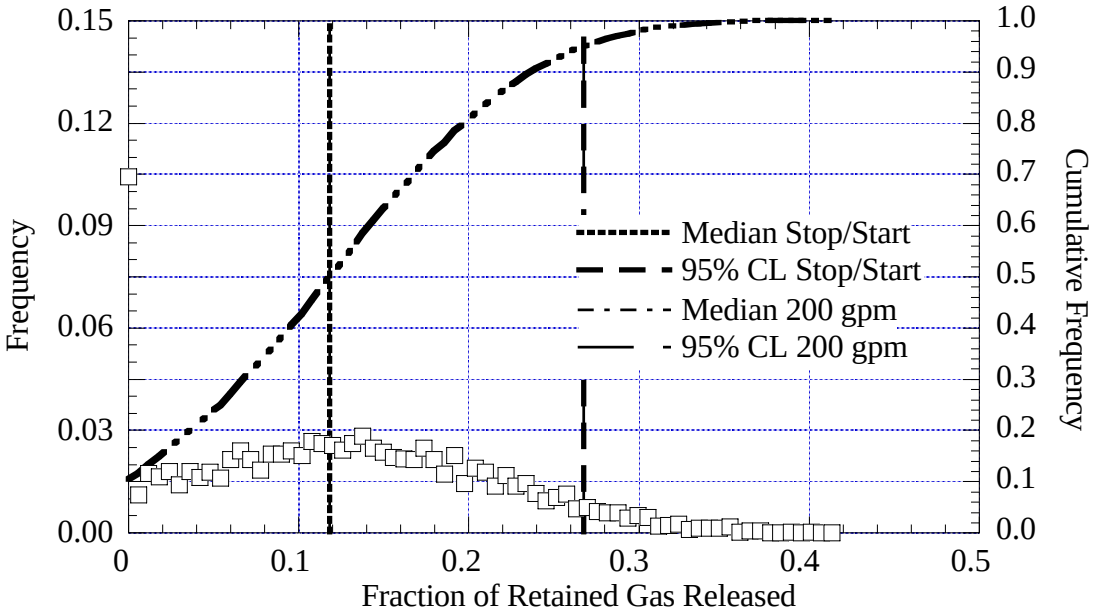

Figure 3.37. Gas Release Fraction for the Stop-Start Case in AN-104

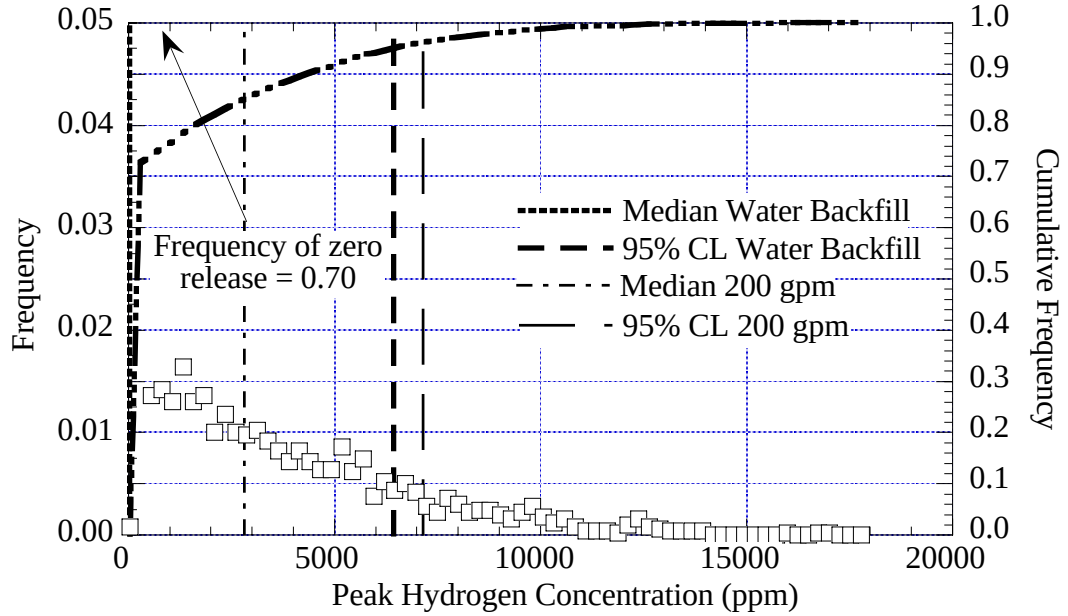

Figure 3.38. Peak Hydrogen Concentration for Water Backfill in AN-104

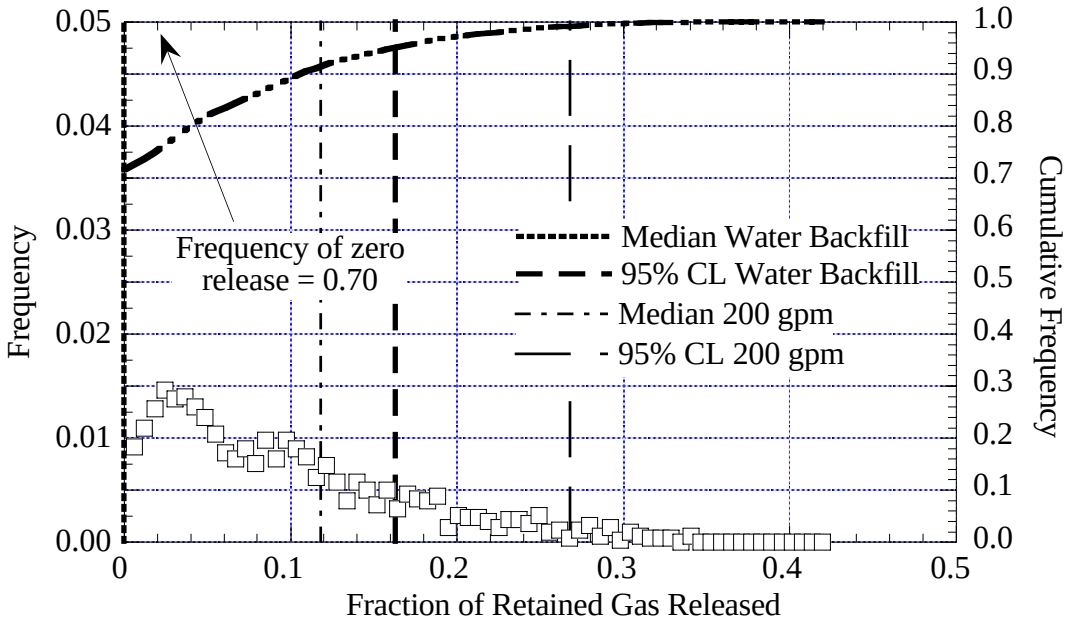

Figure 3.39. Gas Release Fraction for Water Backfill in AN-104

3.4.3 AW-101 Decant Results

Tank AW-101 is notable for having the least retained gas volume of the four tanks under consideration. In fact, the stored gas volume is barely sufficient to bring the tank headspace to the LFL if all of it were instantaneously released. Because a much lower fraction of it is released during decant, and the releases are spaced out over a relatively long time, the peak hydrogen concentration is much lower. The distributions of peak hydrogen concentration and gas release fraction for the base case are provided in Figures 3.40 and 3.41, respectively. The median and 95th percentile values of the peak hydrogen concentration are only 400 ppm and 1,500 ppm, respectively. Approximately 15% of the runs did not have a BDGRE. The median gas release fraction was 0.05 and 0.17 at the 95th percentile.

As shown in Figures 3.42 and 3.43, the results for the 30 gpm decant are similar to those of the base case. The stop-start control was not applicable to this tank, as the maximum concentration did not exceed 6,250 ppm in the base case. The water backfill control results are shown in Figures 3.44 and 3.45. Both the 95th percentile and median water backfill results are significantly lower than the base case as 86% of the runs had no BDGREs occur, and gas release was significantly reduced in those runs that did have BDGREs.

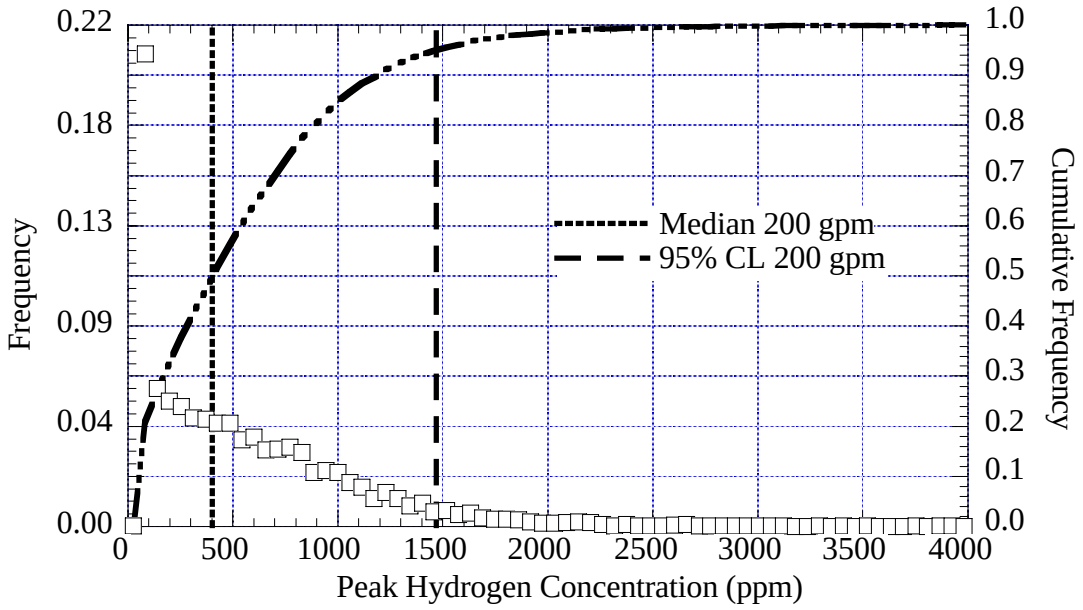

Figure 3.40. Peak Hydrogen Concentration for the AW-101 Base Case

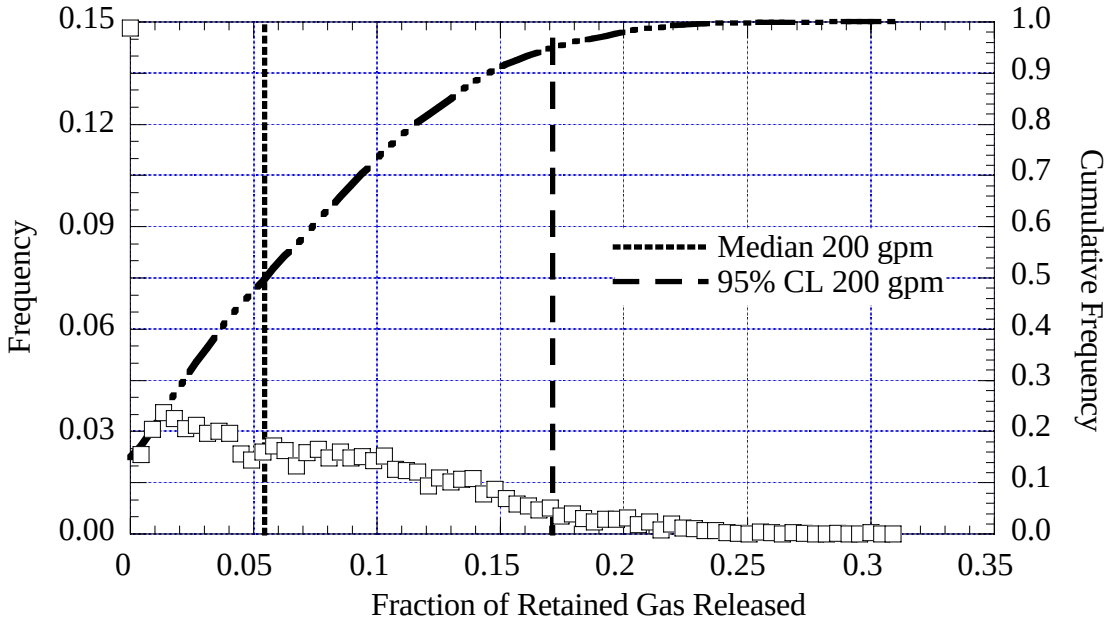

Figure 3.41. Gas Release Fraction for the AW-101 Base Case

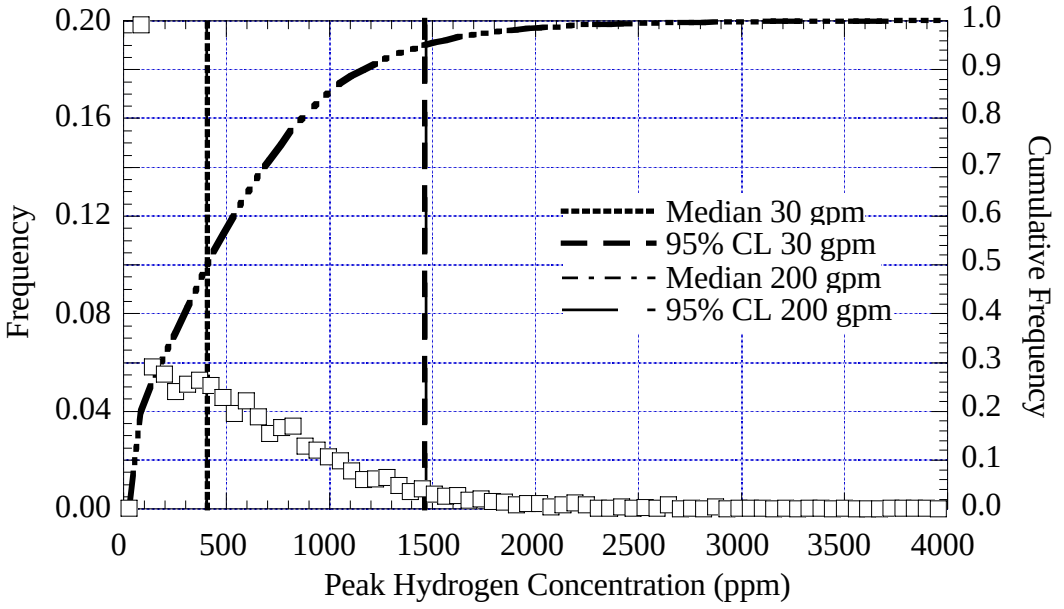

Figure 3.42. Peak Hydrogen Concentration for 30 gpm Decant Rate in AW-101

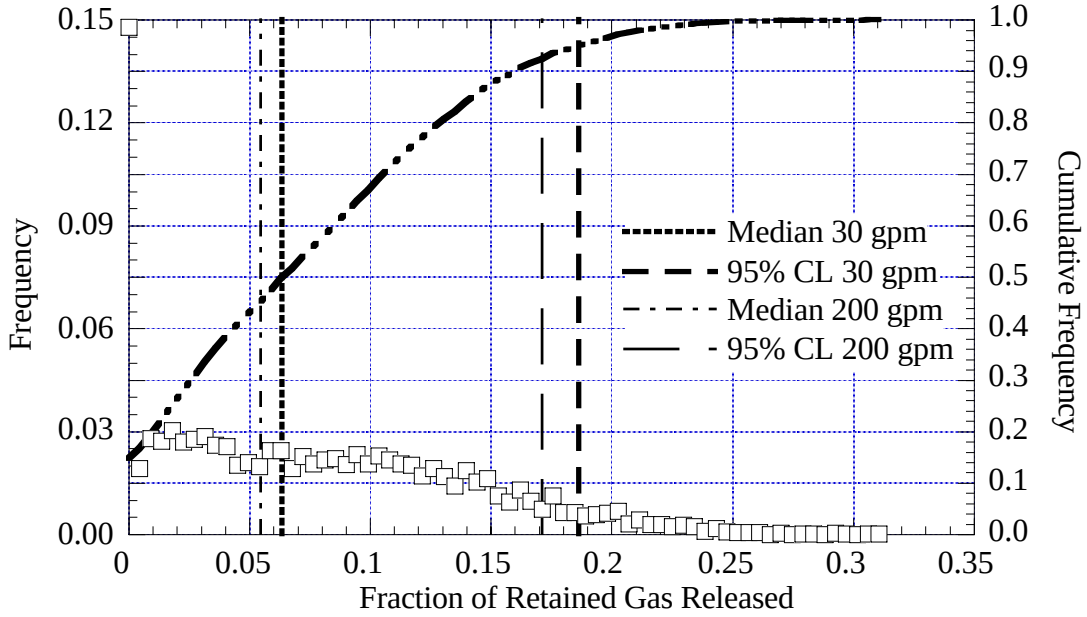

Figure 3.43. Gas Release Fraction for 30 gpm Decant Rate in AW-101

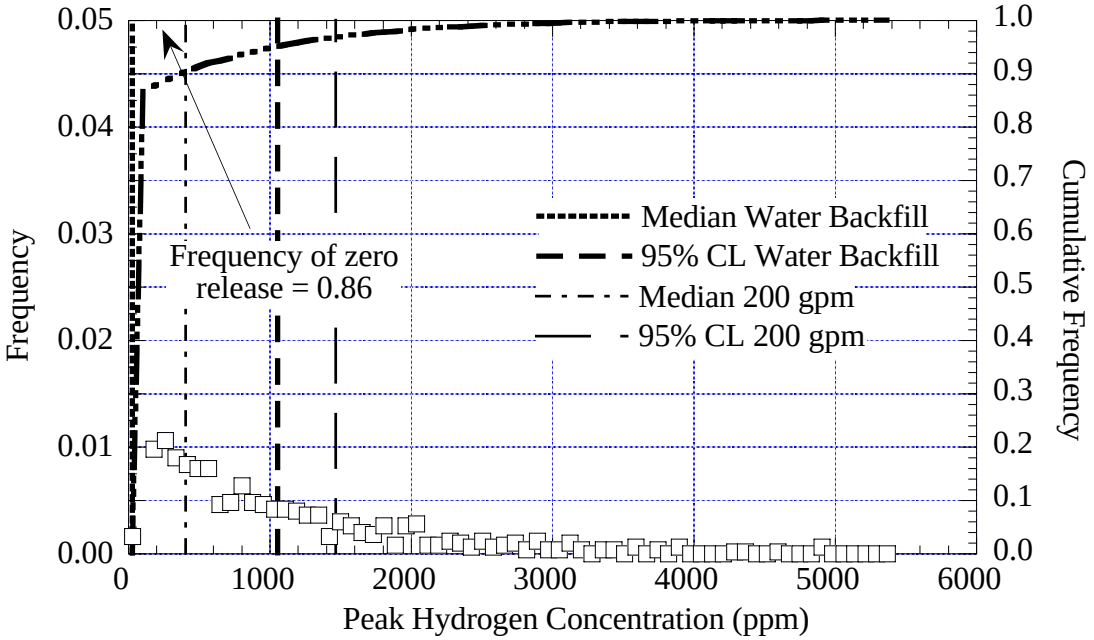

Figure 3.44. Peak Hydrogen Concentration for Water Backfill in AW-101

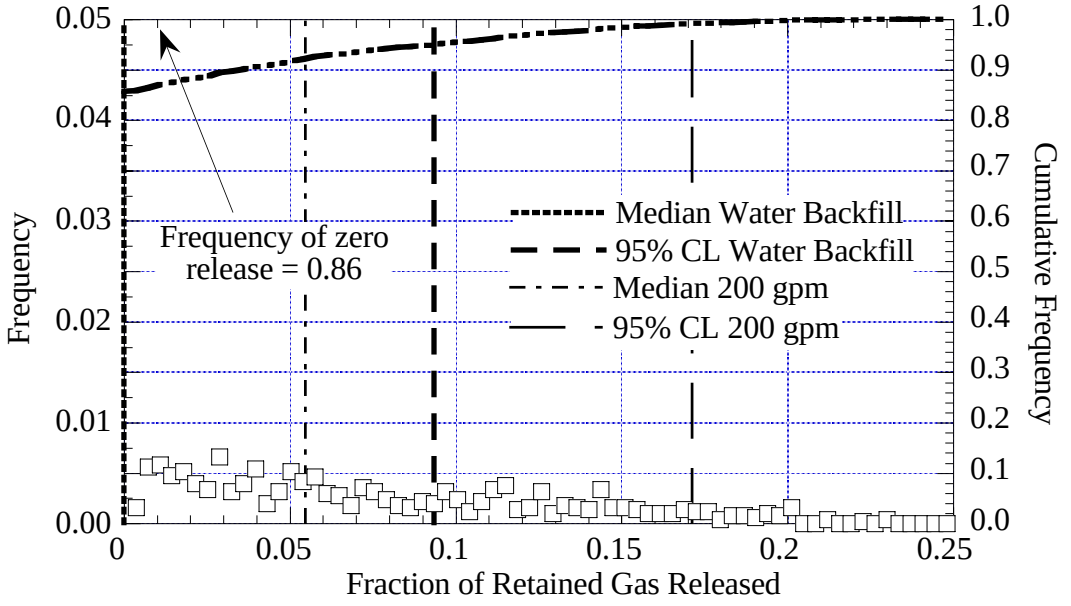

Figure 3.45. Gas Release Fraction for Water Backfill in AW-101

3.5 Conclusions from Supernate Decant Modeling Results

The numerical results are summarized in Table 3.9. Except for AN-103, the peak hydrogen concentrations resulting from gas releases predicted to be induced by supernate decant correspond roughly to those produced by the larger spontaneous GREs. AN-103 is an exception because its history of very small, infrequent gas releases does not match the expectation based on its waste configuration. Nevertheless, none of the runs for AN-103 reached the LFL, even though the majority of the runs had BDGREs occur relatively early in the decant. AW-101 lies

Table 3.9. Summary of Decant Analysis Results

Tank	Run	Quantity	Median	95% CL
AN-105	Base Case	Hydrogen (ppm)	2,800	8,300
		Fraction Gas Release	0.09	0.22
	30 gpm Decant	Hydrogen (ppm)	2,600	8,000
		Fraction Gas Release	0.09	0.22
	Stop-Start Control	Hydrogen (ppm)	2,800	8,200
		Fraction Gas Release	0.09	0.22
	Water Backfill	Hydrogen (ppm)	23	7,600
		Fraction Gas Release	0.00	0.13
AN-104	Base Case	Hydrogen (ppm)	2,800	7,100
		Fraction Gas Release	0.12	0.27
	30 gpm Decant	Hydrogen (ppm)	2,500	6,500
		Fraction Gas Release	0.12	0.27
	Stop-Start Control	Hydrogen (ppm)	2,800	7,000
		Fraction Gas Release	0.12	0.27
	Water Backfill	Hydrogen (ppm)	34	6,400
		Fraction Gas Release	0.00	0.16
AN-103	Base Case	Hydrogen (ppm)	10,500	21,100
		Fraction Gas Release	0.18	0.33
	30 gpm Decant	Hydrogen (ppm)	8,200	19,100
		Fraction Gas Release	0.18	0.33
	Stop-Start Control	Hydrogen (ppm)	9,000	19,400
		Fraction Gas Release	0.18	0.33
	Water Backfill	Hydrogen (ppm)	1,500	21,600
		Fraction Gas Release	0.01	0.25
AW-101	Base Case	Hydrogen (ppm)	400	1,500
		Fraction Gas Release	0.05	0.17
	30 gpm Decant	Hydrogen (ppm)	400	1,500
		Fraction Gas Release	0.06	0.19
	Stop-Start Control	Hydrogen (ppm)	Not Applicable	Not Applicable
		Fraction Gas Release	Not Applicable	Not Applicable
	Water Backfill	Hydrogen (ppm)	27	1,100
		Fraction Gas Release	0.00	0.09

at the other extreme in that its predicted peak hydrogen concentrations are far below even the 6,250-ppm action level. These analysis results indicate that removing the supernatant liquid from these four tanks will not induce gas releases that cause the tank headspace to reach the LFL.

These results are not sensitive to the decant rate, and the peak hydrogen concentration is not reduced by stopping the decant at the action level of 6,250 ppm hydrogen. However, backfilling with water during the decant has a significant probability of preventing BDGREs, though the peak hydrogen concentration approximates the base case if they do occur (excepting AW-101).

4.0 Analysis of Gas Releases Induced by Mixer Pump Operation

Mixing induced by submerged jets is capable of mobilizing sediment by creating hydrodynamic shear and pressure forces that exceed the strength of the material. This disruption of sediment causes the release of retained gas bubbles that eventually enter the tank headspace. Thus, gas release is expected from the region of waste that is actually disrupted. A powerful mixer pump may potentially affect a large waste volume at a relatively high rate, which, by design, suspends a large fraction of the mobilized solids in the liquid layer. As described in Section 2.1, this increases the density of the supernatant, reducing the neutral buoyancy gas fraction and potentially inducing BDGREs in gobs that were not buoyant when mixing started.

The model developed to simulate this process treats gas releases both from the direct disturbance of the waste by the mixer pump and from subsequent induced BDGREs. It consists of two independent parts: the first estimates the volume of waste actually mobilized by a mixer pump of known characteristics running at a given speed and duration; the second determines the headspace hydrogen concentration resulting from a specified schedule of pump runs, each of which mobilizes a given volume of waste. The first model is built on turbulent free jet theory and is described in Section 4.1. The second is a direct adaptation of the detailed supernatant decant model derived in Section 3.1, with relatively minor modifications as described in Section 4.2. Parameters for the gas release model are defined in Section 4.3. Results of applying the model to mixing in AN-105 are presented in Section 4.4 and those for the other three tanks in Section 4.5. Conclusions on mixer pump-induced gas releases are given in Section 4.6.

4.1 Modeling the Effect of the Mixer Pump Jet on the Waste

Ideally, when the mixer pump is initially operated, one would like to know how much gas will be released in terms of the mixer pump operational parameters such as flow rate (or motor rpm), run time, and nozzle orientation. In that way, the pump can be operated in a safe manner. From a fluid mechanics point of view, one would like to understand the role of the waste configuration and physical properties as well. These include waste strength, layer densities, and rheology.

In this section we develop a model for estimating gas release as a function of all the pertinent operational parameters, waste configuration, and waste physical properties. This is a difficult undertaking because of the complexity of the system and the limited availability of data. However, by applying fairly straightforward physical principles, a useful model can be developed for gas release during mixer pump operation. We attempt to validate the model against a very limited data set from initial mixer pump operation in Tank SY-101 and present recommendations for further model validation.

4.1.1 The Theory of Jet-Induced Gas Release

In this section we review and extend the basic theory of jet-induced gas release. The goal is to provide the theoretical basis to develop a model for estimating gas release during mixer pump operation.

4.1.1.1 Important Physical Parameters

In general, we would expect gas release during mixer pump operation to depend on a number of physical parameters. These parameters and an explanation of their importance are as follows:

Discharge velocity **(U_0)**: The velocity of fluid discharging from the mixer pump nozzles is important for several reasons. Energy and momentum imparted to the gas-retaining sediment layer depend upon the local fluid velocities. Local velocities, in turn, scale with discharge velocity. Discharge velocity also determines the volume or mass flow rate. These can be important because the physical volume of the discharge must displace some waste, potentially releasing gas in the process. For a given pump operating in a given fluid, discharge velocity will be proportional to motor rpm; hence they can be used somewhat interchangeably.

Nozzle diameter **(d_0)**: The nozzle diameter is important because the total hydraulic power depends on the nozzle area. The nozzle diameter also determines the scale for velocity decay. Additionally, mass and volume flow rate depend on nozzle diameter.

Density **(ρ_0)**: The density of the jet discharge contributes to the momentum, energy, hydraulic power, and mass flow rate. The density of the waste affects its inertia. The relative density of the discharging fluid ($\Delta\rho$) and the surrounding waste dictates buoyancy, which can have a significant effect on jet behavior.

Yield strength **(τ)**: The yield strength of the sediment layer is important for several reasons. First, if the yield strength is large, it is more difficult for a jet to mobilize and break up the sediment layer material; hence it releases less gas. Also, the propensity for the sediment layer material to cave in after being eroded by the jet increases with decreasing yield strength. Finally, the strength of the solid/liquid matrix determines how firmly gas bubbles are held in place.

Viscosity **(μ)**: The viscosity of the waste is unimportant as long as fluid velocities are high. Here the hydrodynamic forces are dominated by inertia resulting in turbulent conditions. As jet velocities decrease (far from the nozzle), viscous forces dominate. The magnitude of the viscosity (or effective viscosity for materials with complex rheology) affects mixing and velocity decay far from the nozzle.

Gas (void) fraction **(α)**: Gas release during mixer pump operation is clearly affected by the gas fraction in the sediment layer. All things being equal, we would expect waste with larger void fraction to release more gas during a mixer pump operation than waste with a smaller void fraction.

***Pressure* (p)**: The average pressure at which gas is stored in the sediment layer is important because it contributes to the total number of moles of gas at a given void fraction. During gas release, the volume of released gas expands into the tank headspace, with final volume depending on initial pressure.

***Pump run time* (t)**: Pump run time is important to gas release during mixer pump operation. The longer the pump is operated, the more mass, fluid volume, and hydraulic power are delivered to the waste. The rate of gas release likely changes during a pump run. Eventually, gas release likely diminishes for long pump run times.

In general then, we can say that the total gas release volume during mixer pump operation should depend on the above-mentioned parameters. This is expressed mathematically as

$$V_{rel} = f(U_0, d_0, \rho_0, \Delta\rho, \tau, \mu, \alpha, p, t) \tag{4.1}$$

4.1.1.2 Important Physical Processes

The function in Eq. (4.1) can be found if we model the conservation laws adequately for mass, momentum, and energy. In fluid dynamics, these laws form the Navier-Stokes equations. In the case of a multiphase medium (gas, liquid, and solid), the equations become exceedingly complex and certainly intractable. As an alternative, we consider simplified expressions for the important physical mechanisms and processes.

Mass flow: Mass is conserved during mixer pump operation. The total flow rate of liquid, solids, and gas discharging from the nozzle is equal to the total flow rate of material entering the pump inlet. If the density of the discharge and inlet streams is the same, the volume flow rate is also the same. The mass flow rate is given by

$$\dot{m}_0 = \rho_0 U_0 A_0 \tag{4.2}$$

where $A_0 = \frac{\pi}{4} d_0^2$ is the nozzle area. The total mass of fluid that is discharged in time t is

$$M(t) = \rho_0 U_0 A_0 t \tag{4.3}$$

Similarly, the volume flow rate is given by

$$Q_0 = U_0 A_0 \tag{4.4}$$

and the total volume of fluid discharged during time t is

$$V(t) = U_0 A_0 t \tag{4.5}$$

Because volume is approximately conserved, Eq. (4.5) sets an upper bound on the volume of waste that can be disturbed during mixer pump operation.

Momentum flux: Moving fluids are associated with momentum. This momentum creates forces on the sediment layer material as the fluid impinges on it. The momentum flux discharging from the nozzle is given by

$$P = \rho_0 U_0^2 \tag{4.6}$$

The momentum flux has units of pressure and in fact can be thought of as a pressure. The momentum flux is independent of nozzle area.

Kinetic energy: The kinetic energy flux of the discharging fluid from the nozzle is given by

$$ke = \frac{1}{2}\rho_0 U_0^3 \tag{4.7}$$

The power of the discharge is given by

$$\dot{P}_k = \frac{1}{2}\rho_0 U_0^3 A_0 \tag{4.8}$$

The power shown in Eq. (4.8) is approximately equal to the power produced by the pump minus any losses in the ductwork and an amount that accounts for pressure differences between the inlet and nozzle.

The total kinetic energy discharged in time *t* is

$$KE(t) = \frac{1}{2}\rho_0 U_0^3 A_0 t \tag{4.9}$$

The energy shown in Eq. (4.9) is not conserved downstream of the jet discharge. As soon as the fluid discharges from the nozzle, turbulent motions, slip between solid and liquid phases, viscous shear stresses, and other irreversible interactions cause the energy to be dissipated. Even so, Eq. (4.9) sets the upper limit on the amount of energy delivered to the sediment layer material matrix.

Potential Energy: If the density of the discharging fluid is different from that of the surrounding material in the sediment layer, the jet will possess potential energy. This potential energy can be either negative (dense jet) or positive (buoyant jet). The potential energy flux is given by

$$pe = (\rho_0 - \rho_S) g h U_0 \tag{4.10}$$

where ρ_S is the density of the sediment layer, g is the gravitational constant, and h can be thought of as the distance from the nozzle to the top of the sediment layer. The rate of buoyant energy production, or "buoyant power," is given by

$$\dot{P}_b = (\rho_0 - \rho_S) g h U_0^2 A_0 \tag{4.11}$$

and the total buoyant energy discharged from the nozzle is

$$PE(t) = (\rho_0 - \rho_S) g h U_0^2 A_0 t \tag{4.12}$$

To get an idea of the relative magnitudes of the kinetic and potential energy, we divide Eq. (4.9) by Eq. (4.12) to obtain

$$PE/KE = \frac{(\rho_0 - \rho_S)}{\rho_0} \frac{2gh}{U_0} \tag{4.13}$$

For typical conditions for retrieval systems in DSTs (U_0 ~10–20 m/s, h ~2–4 m, ρ_0 ~ 1.4–1.6 g/cc, ρ_s ~1.6–1.7 g/cc), the ratio ranges from about 0–1.7. Hence potential energy can be a significant factor, depending primarily on the relative density of the discharge and surrounding material.

Strain energy: For gas to be released from the sediment layer material, energy, or work, is required to deform the material. The minimum energy required to deform gas-retaining sediment layer material of volume V is approximately τV. The rate of work, or power for yielding the material, is given by

$$\dot{P}_y = \tau u_f S \tag{4.14}$$

where u_f is the speed of the yielding front and S is the surface area. The work done on the sediment layer material as a function of time is given by

$$YE(t) = \tau u_f S t \tag{4.15}$$

Equations (4.14) and (4.15) set a lower bound on the amount of energy or power required to release the gas stored in a given volume of sediment layer material. This energy, at a minimum, must be supplied by the mixer pump. Of course, because energy is not conserved, the actual amount of energy required will be greater than the strain energy.

Onset of Yield: For material to begin to yield, the pressure acting on the material surface must exceed the yield strength. The pressure of a jet is made up of both static and dynamic components. The static component is negligible because both the moving fluid and the static, unyielded sediment layer material will be at the same pressure. The dynamic component of pressure is $1/2\ \rho u^2$, where ρ is the local jet density and u is the local jet velocity. The dynamic pressure must exceed the yield strength for deformation to occur. This leads to the following requirement for local sediment layer yield:

$$\rho u^2 / 2\tau > 1 \tag{4.16}$$

Equation (4.16) relates to the normal stress acting on a surface of sediment layer material. Shear stresses resulting from jet flow also may erode the sediment layer and will generally be

proportional to $1/2\ \rho u^2$, with the constant of proportionality being the friction coefficient. Hence, a condition similar to Eq. (4.16) can be written if the friction coefficient is known.

Entrainment: Another potential mode of sediment layer yield leading to gas release is the phenomenon of entrainment. Entrainment is similar to erosion by shear stress but is due to a fundamentally different mechanism. Entrainment in turbulent jets results from large-scale turbulent eddies that engulf regions of quiescent fluid that are outside the core of the jet. It is not known what role entrainment plays when a turbulent jet is surrounded by a pseudo solid. One likely criterion is that the local pressure fluctuation due to eddies is greater than the yield stress. Because pressure fluctuations scale locally with $1/2\ \rho u^2$ for Newtonian turbulent flows, it is reasonable to assume a condition similar to Eq. (4.16) applies to entrainment as well.

Collapse: Another likely mechanism for sediment layer yield is collapse. As the jet bores into the sediment layer by some combination of the processes and mechanisms discussed, the material above should eventually collapse into the jet cavity. The collapsed material may release gas spontaneously during the collapse or during subsequent jet action. Collapse generally occurs when the lithostatic pressure differences exceed the yield stress locally. Because most sediment layers have relatively low yield stress (40 to 300 Pa), it is fairly easy for material to collapse.

4.1.1.3 System Configuration Issues

In addition to the physical processes and mechanisms described in the previous section, there are a number of other factors associated with the mixer pump system that affect gas release behavior. The first is the orientation of the discharge. Nozzles aimed toward the center of the tank will likely produce gas release in different amounts than those aimed at or near a wall. The wall necessarily will turn the jet flow upward and along the wall. The elevation of the nozzles above the tank bottom is also important. Jet flows parallel to a solid surface generally turn toward that surface and *attach* themselves. The characteristics of these attached jet flows are somewhat different from jet flows that are not influenced by solid surfaces.

For several reasons, perhaps the most important system configuration issue is the location of the pump inlet. First, if the inlet is far from the nozzle (either higher or lower), the density of the discharge will likely be different from that of the surrounding waste. If the inlet is near the surface or above the sediment layer, supernatant will be drawn into the pump. This is the case for the mixer pump installed in Tank SY-101. Because the supernatant may be significantly less dense than the sediment layer, buoyant effects may be very significant in or even dominate the resulting jet flow structure. Aside from buoyancy, the need to conserve volume may also force the jet up through the sediment layer to provide a return path for the discharged fluid.

If the mixer pump inlet is near the tank bottom (the location planned for waste retrieval operations), density effects will be minimized. However, another phenomenon may occur. The possibility of discharge "short circuiting" is increased for this situation. The jet may act more like a confined jet, where at some distance from the nozzle the jet stops, turns, and then returns to the inlet. Under these conditions, the gas release characteristics could vary significantly from a case where the inlet is in the supernatant like it was in SY-101.

4.1.2 Observations and Data from Initial Mixing of SY-101

Because the initial phases of mixer pump testing in SY-101 released gas from the waste, as intended, the tank data taken during that period are potentially useful in understanding and predicting gas releases from other tanks as they are degassed by mixing. Our objective in reviewing the SY-101 data was to glean any correlations between any of the pump operational parameters and the amount of gas released. These data can potentially be used to validate or calibrate a working model of mixer-pump-induced gas release.

Caley et al. (1998) were the first to use the SY-101 pump testing data as a way to estimate possible gas releases during mixer pump degassing of AN-105. They noted that the maximum daily gas release during high-speed mixer pump testing in SY-101 (Phase B) was 14.3 m^3 (408 ft^3) and that it was produced by a run that delivered 18.2 kW-hr (24.4 hp-hr) of energy to the waste. Because this same amount of energy is supplied to the AN-105 waste by one W-211 pump operating at its lowest allowable speed of 700 rpm for 24 minutes, a degassing run of the same speed and duration would not produce unacceptably large gas releases in AN-105.

4.1.2.1 Total Gas Release

For this study we revisited the SY-101 pump testing data with a more detailed approach. The SY-101 pump runs that were most pertinent to initial degassing operations are those toward the beginning of Phase B, when high-speed runs were aimed at waste regions that were as yet undisturbed or minimally disturbed by pumping. Prior disturbance by GREs cannot be ruled out. Eight such runs were identified and are listed in Table 4.1. The jet discharge velocity U_0 was determined from the pump speed by using the pump performance correlation in Figure 2.7 of Caley et al. (1998) and a nozzle diameter d_0 of 0.066 m (2.6 in.).

The exponential gas release model (Hedengren et al. 2000) discussed in Section 2.3 in the analysis of historical gas release data was used to examine the behavior of gas releases during the selected pump runs listed in Table 4.1. This model was originally developed for analysis of spontaneous gas releases in the waste tanks, where the stimulus for an event is not generally known. Examination of hydrogen concentration histories in the headspace of SY-101 for days with pump runs, however, reveals that the induced gas releases exhibit behavior similar to spontaneous releases (see Sections 2.3 and 4.1.2.2).

The general shape of a plot of the hydrogen concentration data versus time for the days of interest shows a characteristic steep rise to a relatively sharp peak at the initiation of the pump run followed by an approximately exponential decay (subsection 4.1.2.2). In many cases, there appear to be secondary releases in the hours following the pump run, similar to the multiple releases discussed in Section 2.3. These releases may be part of the response of the waste to the disturbance due to the pump run, or they may in some cases be induced BDGREs. In either case, the individual gas releases making up the GRE have essentially the same character and are analyzed using the exponential gas release model. The analysis evaluated the hydrogen concentration data for the entire day for each pump run using the multiple-release analysis approach described in Section 2.3. This analysis was performed for the eight pump runs.

Table 4.1. SY-101 Pump Runs That Disturbed Fresh Waste

Date	Direction (degrees)	Pump Speed (rpm)	Run Duration (minutes)	U_0 (m/s)	Comment
7/26/93	0/180	997	9.3	21.1	More than 20 pump runs in this direction in the preceding 22 days, but most of these were less than a minute long or were at 719 rpm or less. Considering the greater speed and duration of this run, it is expected to have disturbed fresh waste.
10/22/93	35/215	509	19.7	11.0	One run in this direction the day before, a run at 36 and 216 degrees that lasted less than a minute.
11/5/93	65/245	359 509 719 919	19.7 19.7 19.7 19.7	7.9 11.0 15.3 19.6	No earlier runs in this direction.
11/10/93	95/275	359	20	7.9	No earlier runs in this direction.
11/11/93	95/275	359 509 719 919	19.7 19.7 19.7 19.7	7.9 11.0 15.3 19.6	The run on the previous day would have disturbed a small amount of waste in this direction, but much fresh waste must have been reached by this run.
11/12/93	125/305	359 509 719 919	19.7 19.7 19.7 19.7	7.9 11.0 15.3 19.6	No earlier runs in this direction.
11/13/93	155/335	359 509 719 919	19.7 19.7 19.7 19.7	7.9 11.0 15.3 19.6	No earlier runs in this direction.
11/21/93	125/305	749	60	15.9	Although the ramp-up run of 11/12/93 had been in this direction, this run was also included as a nonramp-up run for comparison.

Table 4.2 presents the total gas release volume for the respective pump runs as well as results for a selected subset of the data consisting of only the initial gas release event at the beginning of the pump run. The initial gas release or the first peak of the data is relevant to the analyses presented in Sections 4.2 through 4.6.

From the point of view of establishing a relationship between pump run parameters and releases from undisturbed waste, the full data set from Phases A and B is somewhat ambiguous. Large releases occurred on the days listed in Table 4.1 but also on days when pump runs were not carried out, or when there were only short low-speed runs, or when the jets were directed into waste that had already been disturbed.

The arguments developed in Section 4.1.1 from theoretical consideration of jet mixing behavior suggest that the quantities $\rho_0(U_0 d_0)^2$, $tU_0 d_0^2$, and $t\,\rho_0 U_0^3 d_0^2$ (corresponding to discharge momentum, volume, and power, respectively) could be related to the volume of waste disturbed by the pump jets. Figures 4.1 to 4.3 show the daily gas release volume (in excess of background)

Table 4.2. Gas Releases Associated with SY-101 Pump Runs of Interest

Pump Run Date	Total Gas Release (m^3)	Initial Gas Release	
		Total Gas Release (m^3)	Time to Peak Gas Release Rate (min)
7/26/93	1.73	1.16	6.0
10/22/93	0.39	0.39	20.0
11/5/93	3.62	2.71	38.0
11/10/93	0.14	0.14	17.9
11/11/93	4.13	1.61	20.0
11/12/93	5.07	2.82	29.0
11/13/93	4.83	2.41	20.2
11/21/93	3.41	1.12	32.4

plotted versus these three parameters (the waste density has not been included to keep it simple). In the cases of the ramp-up runs on November 5, 11, and 13, 1993, the values used were the weighted averages of each incremental step.

In Figure 4.1 we see little correlation with discharge momentum, evidently because run time has not been taken into account. However, Figures 4.2 and 4.3 show the consistent trend of increasing gas release volume for the quantities $tU_0d_0^2$ and $tU_0^3d_0^2$, although there is scatter at the higher values. From the limited data available, parameter groups associated with volume flow and power are fairly equivalent in terms of how they tie in with gas release.

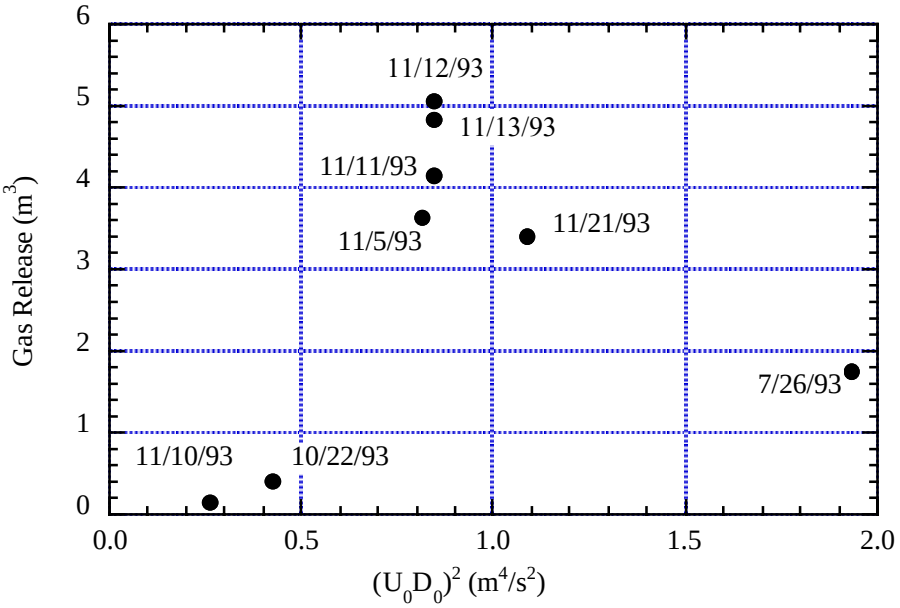

Figure 4.1. Gas Release from SY-101 Mixer Pump Operation Correlated with Jet Momentum Scaling

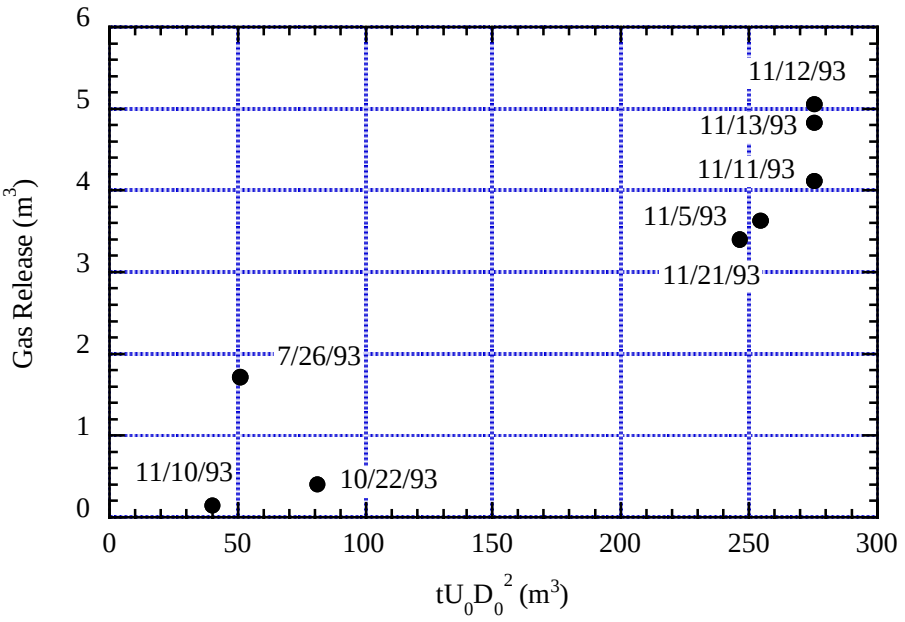

Figure 4.2. Gas Release from SY-101 Mixer Pump Operation Correlated with Jet Volume Flow Scaling

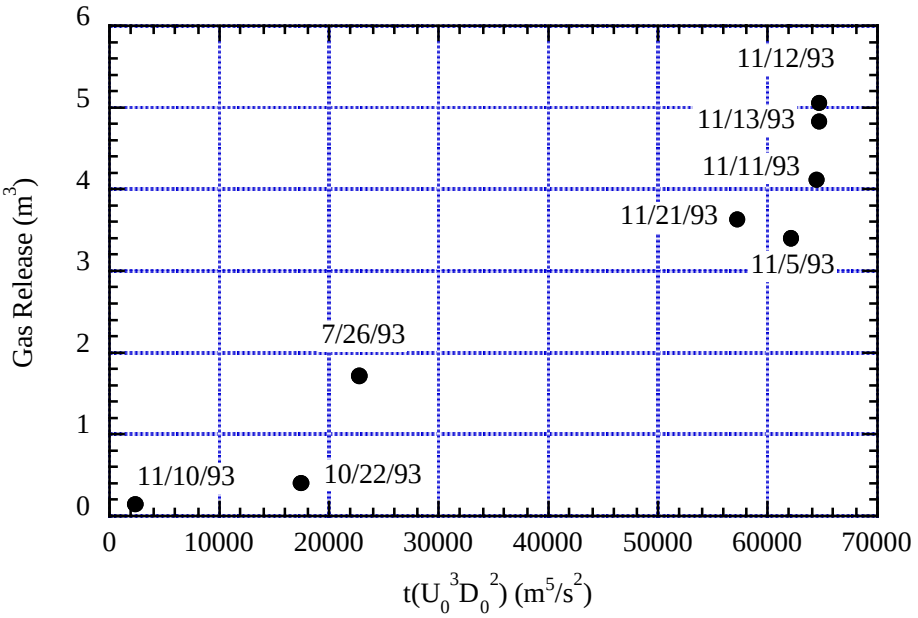

Figure 4.3. Gas Release from SY-101 Mixer Pump Operation Correlated with Jet Hydraulic Power Scaling

4.1.2.2 Gas Release Delay

Another perspective on the relationship between the pump run duration and gas release was found by examining the time profiles of the headspace hydrogen for the days of interest. These profiles are shown in Figures 4.4 through 4.11. All of the data indicate that time to peak gas release from the start of the pump run exceeds pump run time. Figure 4.12 shows that the time to peak gas release increases with the gas release volume. While the reason for these trends cannot be known precisely, the behavior is consistent with a gas holdup mechanism the crust might provide. Figures 4.13 and 4.14 show gas release delay plotted versus the volume flow, $tU_0d_0^2$, and the jet power, $tU_0^3d_0^2$. Again, a reasonable relationship can be seen for both scaling groups, with little indication of which provides a better correlation.

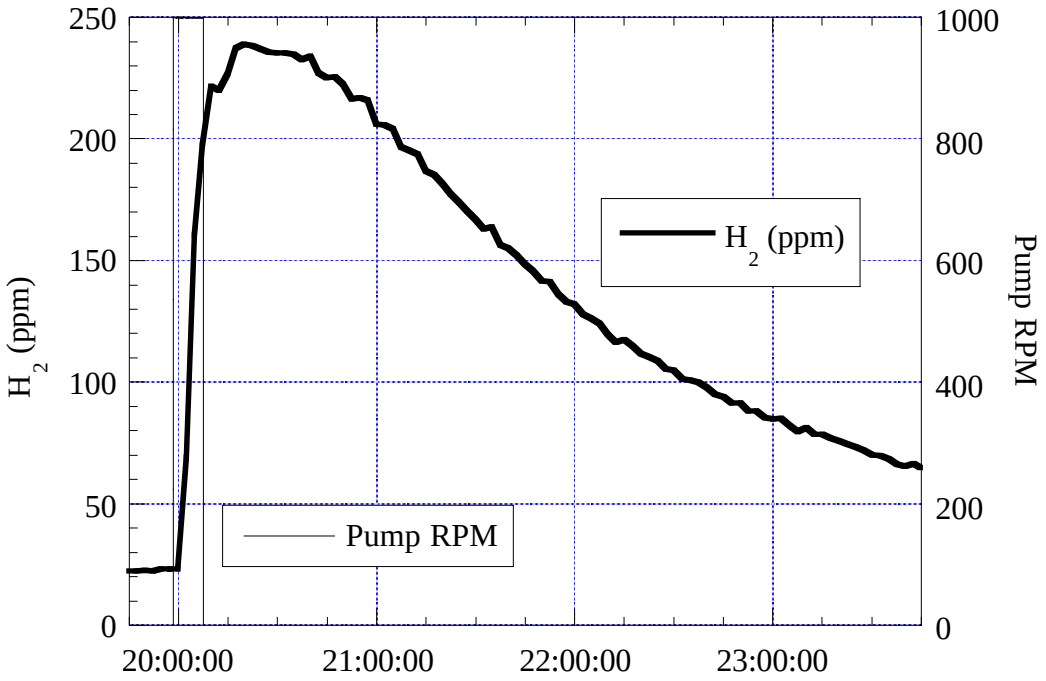

Figure 4.4. July 26, 1993 Pump Run and GC Data

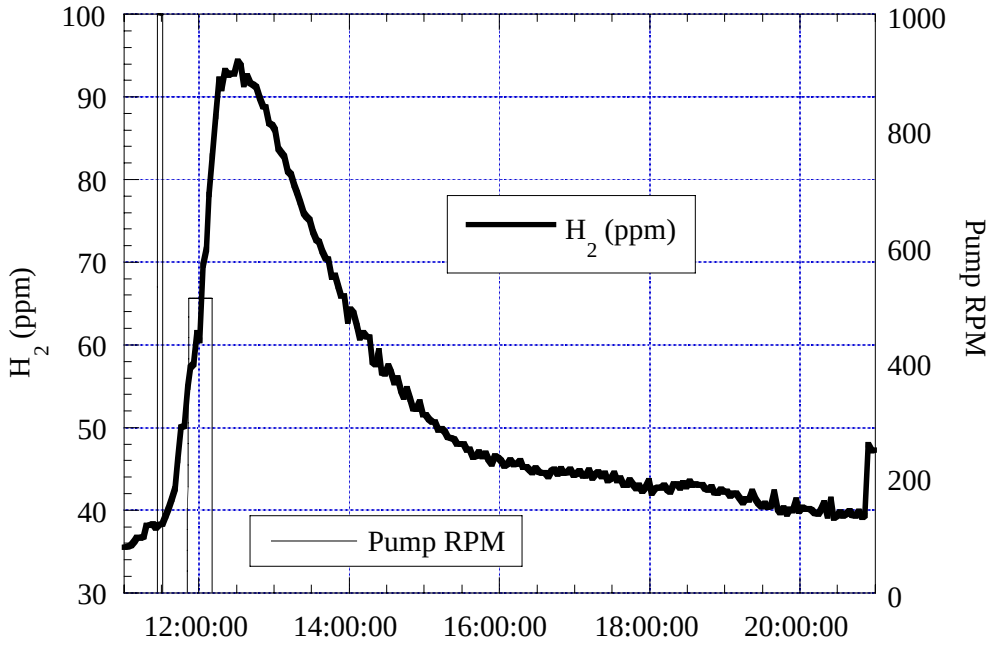

Figure 4.5. October 22, 1993 Pump Run and GC Data

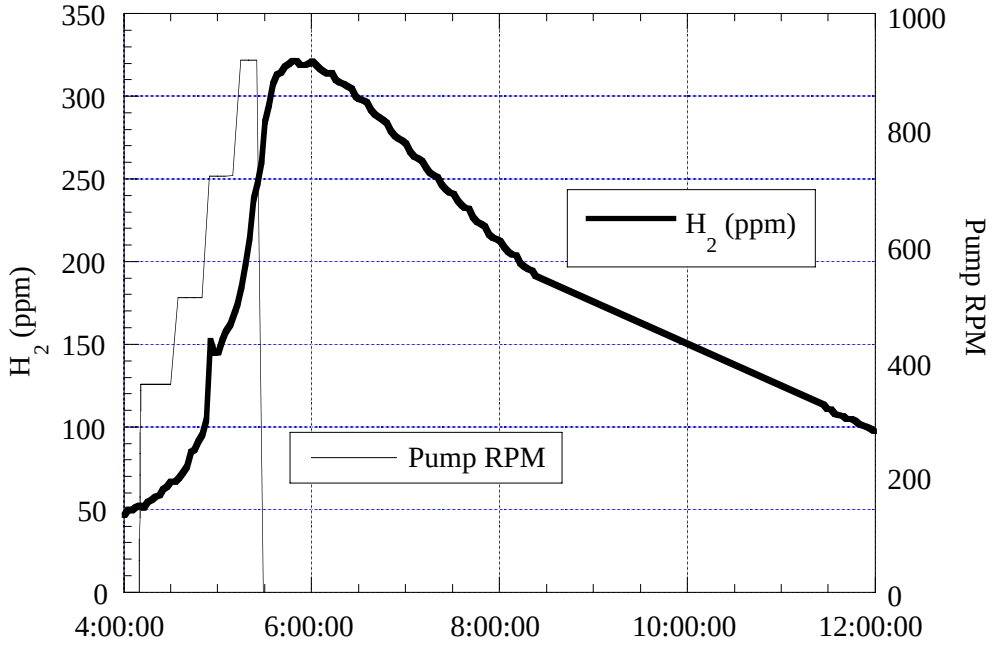

Figure 4.6. November 5, 1993 Pump Run and GC Data

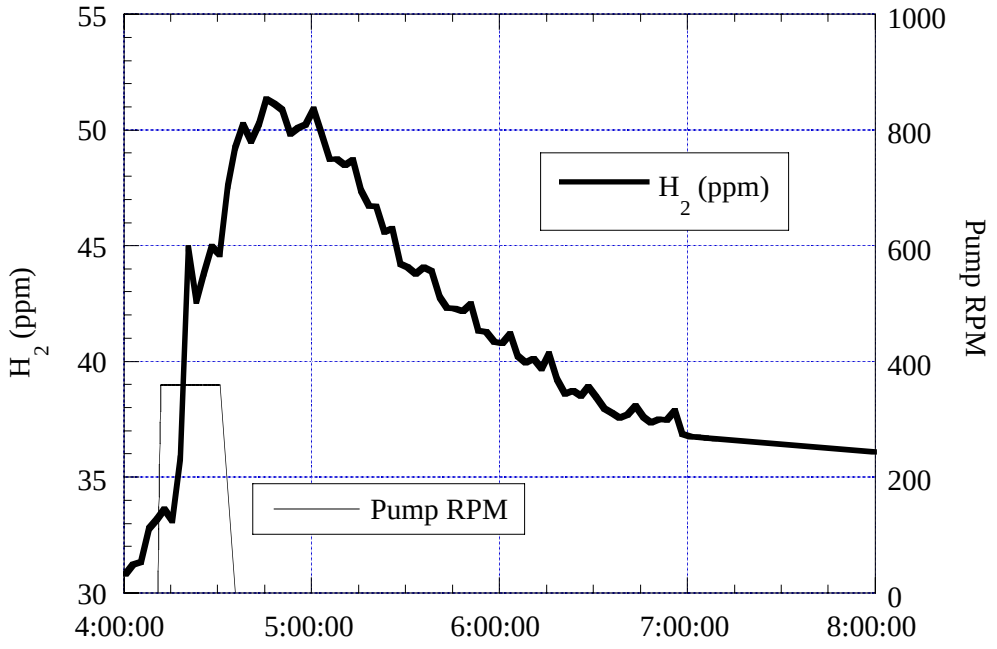

Figure 4.7. November 10, 1993 Pump Run and GC Data

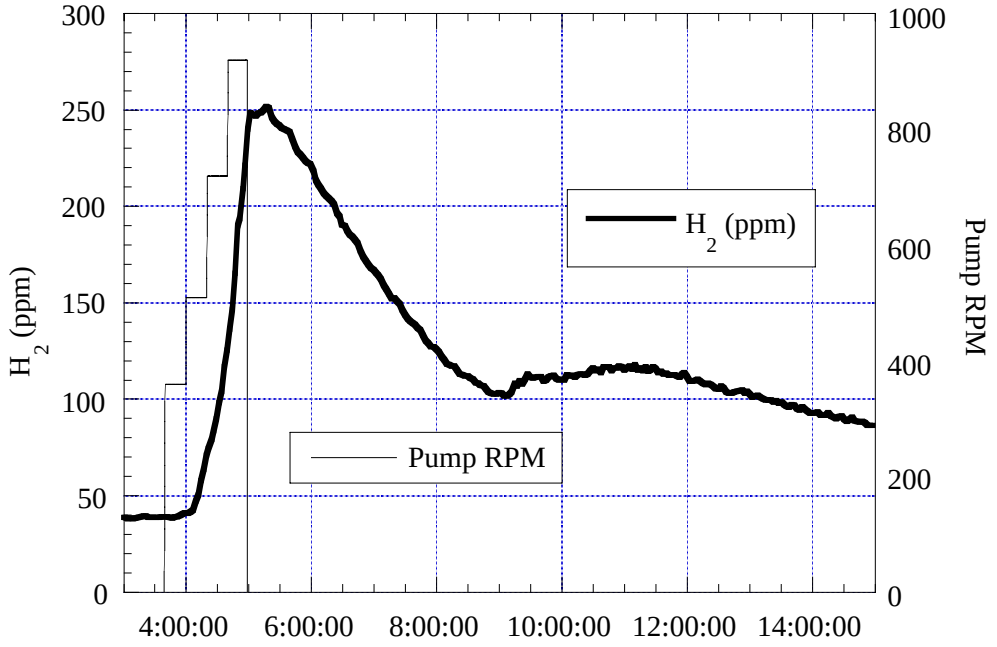

Figure 4.8. November 11, 1993 Pump Run and GC Data

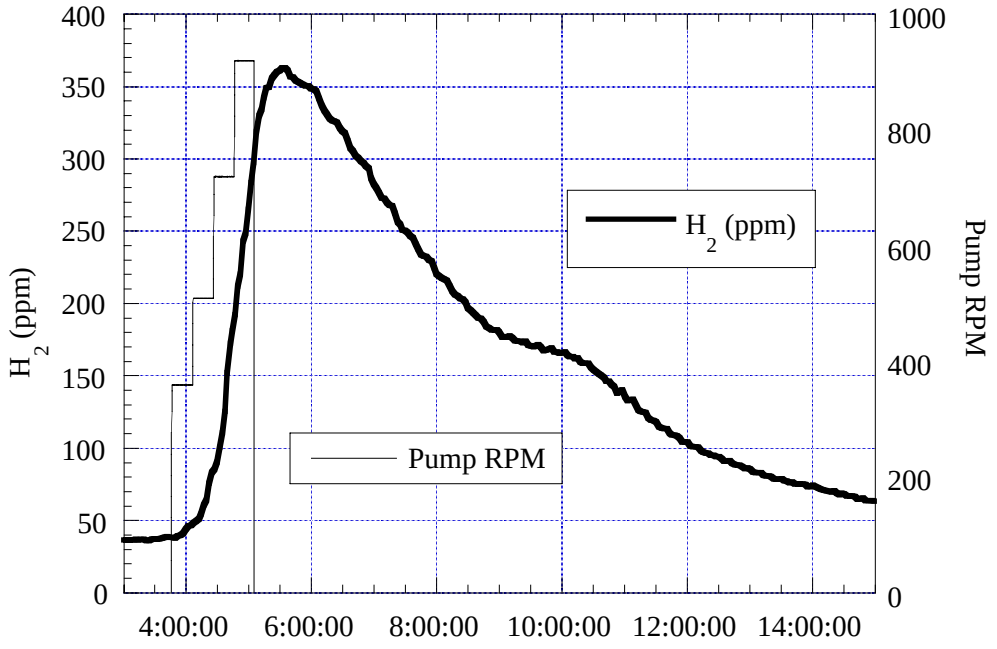

Figure 4.9. November 12, 1993 Pump Run and GC Data

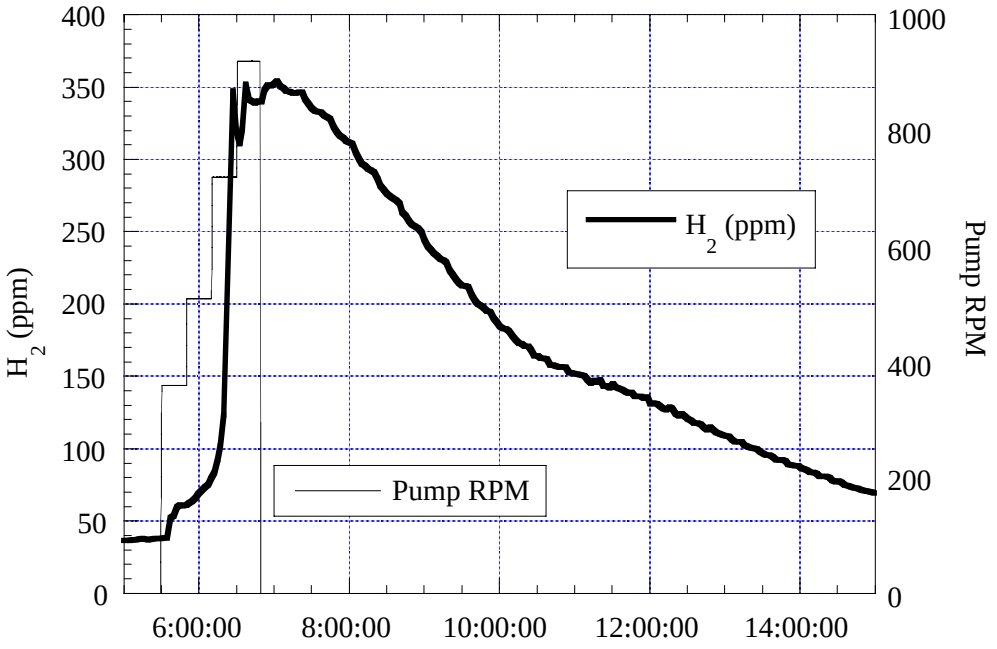

Figure 4.10. November 13, 1993 Pump Run and GC Data

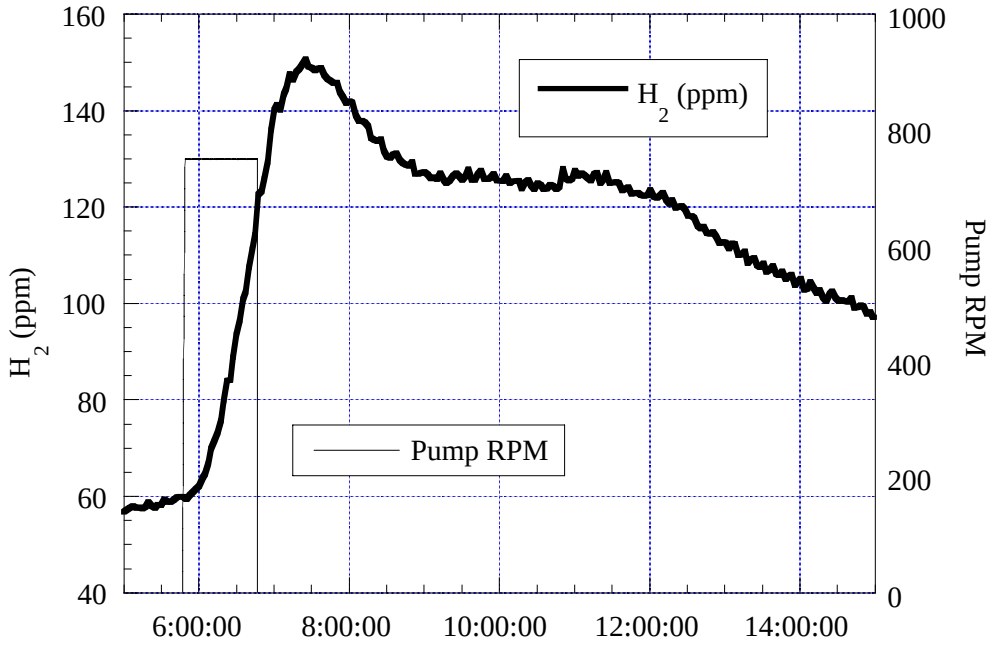

Figure 4.11. November 21, 1993 Pump Run and GC Data

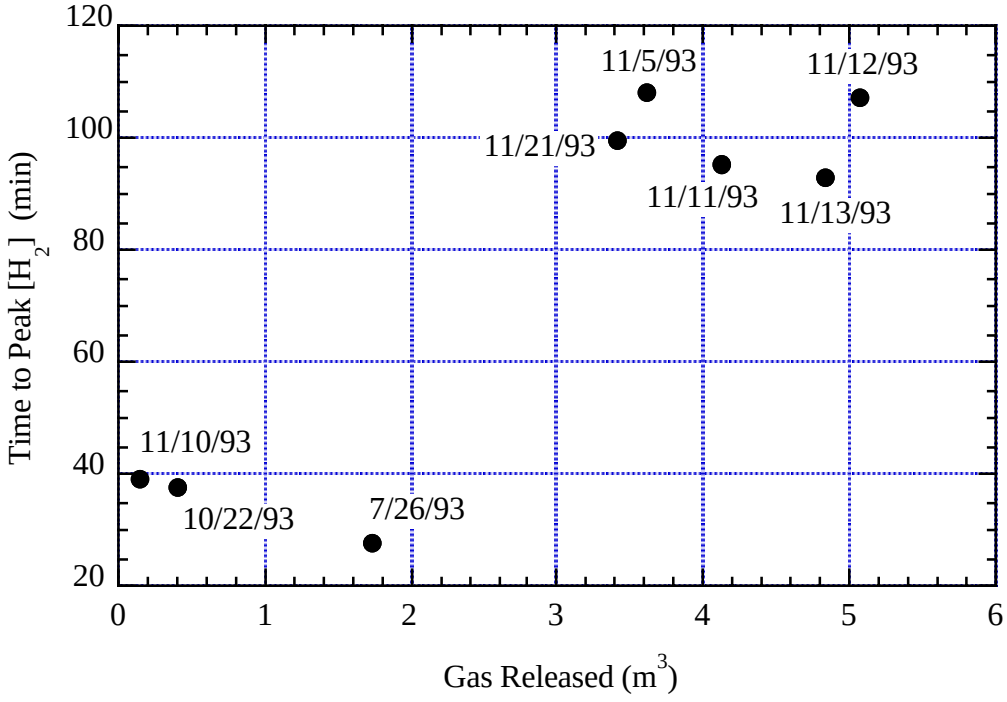

Figure 4.12. Relation Between Peak H_2 Delay and Total Gas Release

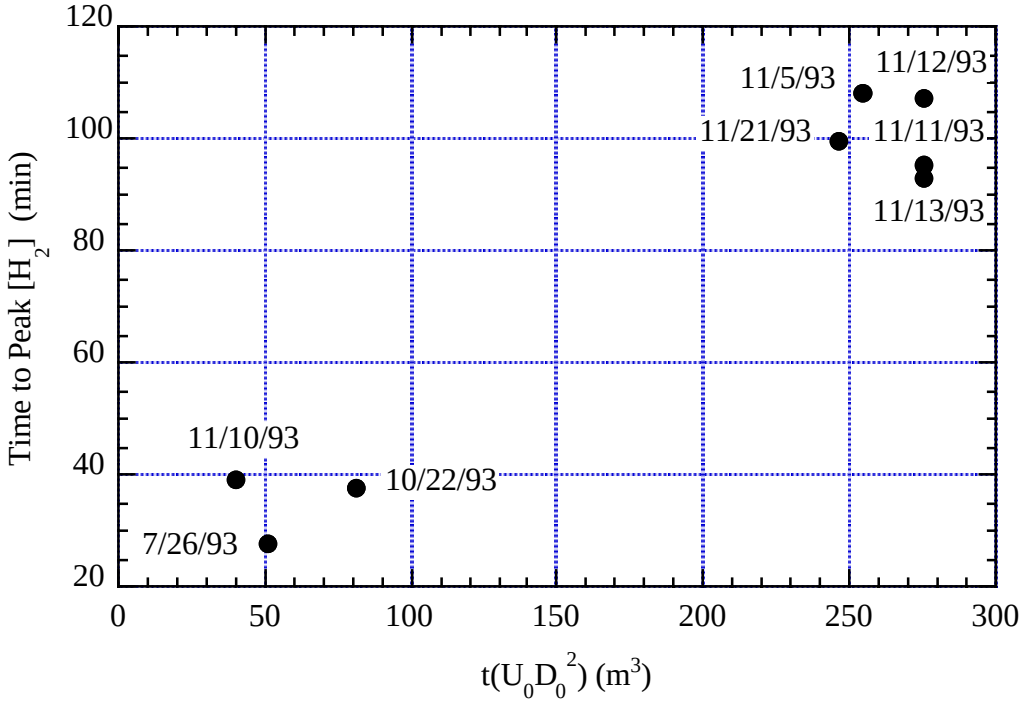

Figure 4.13. Relation Between Peak H_2 Delay and Jet Flow Rate Scaling

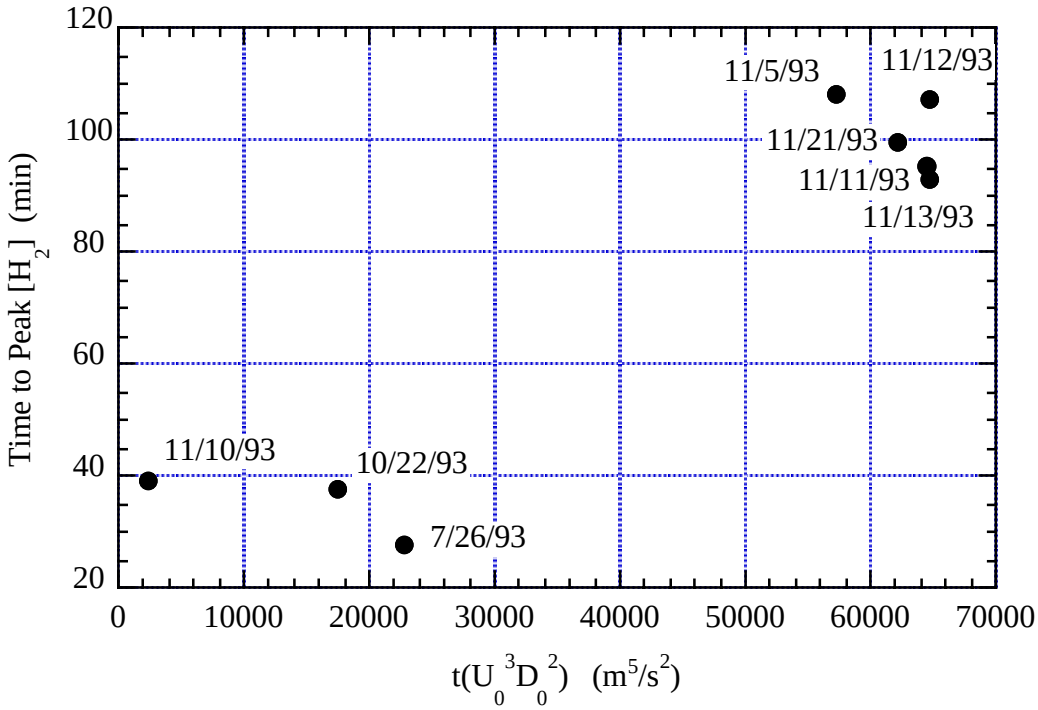

Figure 4.14. Relation Between Peak H_2 Delay and Jet Hydraulic Power Scaling

4.1.3 Energy Balance Model for Waste Disturbance

We now attempt to develop a model for determining the gas release as a function of mixer pump parameters and waste properties.

4.1.3.1 The Free Turbulent Jet

We begin by considering the behavior of free, nonbuoyant turbulent jets in Newtonian fluids. While the jet created by the mixer pump is not free (the unmobilized nonconvective layer may act as a solid surface) and may not be Newtonian, some of the basic relations and scaling may still be applicable. Figure 4.15 shows the basic features of the free jet.

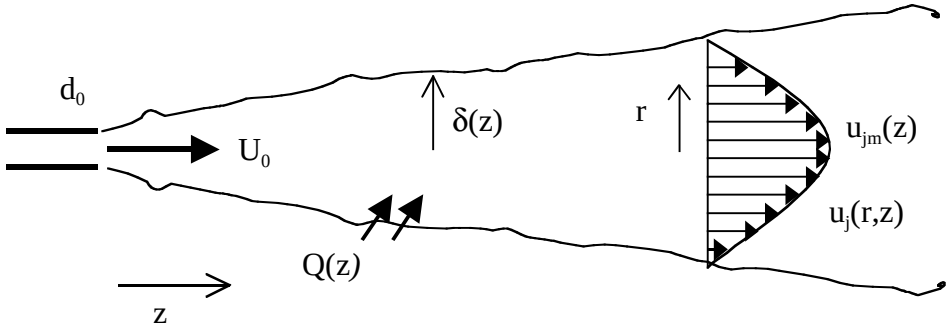

Figure 4.15. The Free Turbulent Jet

The jet has a time-averaged velocity profile that varies in the both the z and r directions. The peak velocity, u_{jm}, varies according to

$$u_{jm}(z) = \frac{6U_0 d_0}{z} \tag{4.17}$$

The radial variation can be approximated by a Gaussian:

$$u_j(r,z) = u_{jm}(z) e^{-4.6\left(\frac{r}{\delta}\right)^2} \tag{4.18}$$

where δ is the half jet spread angle. The average jet velocity at any z location is approximately given by

$$\bar{u}_j(z) = \frac{u_{jm}(z)}{\delta^2(z)} \int_0^\infty r e^{-4.6\left(\frac{r}{\delta(z)}\right)^2} dr \tag{4.19}$$

which can be evaluated to give

$$\bar{u}_j(z) \approx 0.11 u_{jm}(z) \tag{4.20}$$

The jet spreads at a constant half-angle θ so that

$$\delta(z) = \theta z \tag{4.21}$$

Turbulent jets spread at about 15 degrees total angle, corresponding to θ = 0.13 rad. The swept volume of the jet cone is given by

$$V(z) = \frac{\pi}{3}\delta^2 z = \frac{\pi}{3}\theta^2 z^3 \tag{4.22}$$

Finally, the total entrainment rate into the jet up to location z is given by (Rajaratnam 1974):

$$Q(z) \approx 0.3 Q_0 z / d_0 \tag{4.23}$$

where Q_0 is the discharge flow rate given by Eq. (4.4)

Finally, consider the efficiency of the jet from a hydraulic power point of view. The initial power of the jet at the nozzle is given by Eq. (4.8). The power at any station z is given by

$$\bar{\dot{p}}_j(z) = \frac{1}{2}\rho u^3{}_{jm}(z)\int_0^\infty r e^{-3\cdot 4.6\left(\frac{r}{\delta(z)}\right)^2} dr \tag{4.24}$$

which is evaluated to give

$$\bar{\dot{p}}_j(z) = \frac{0.036}{2}\rho u^3{}_{jm}(z)\delta^2 \tag{4.25}$$

Here we see that the average power at any location is only about 3.6% of the power computed from maximum velocity at the same location. This power is very much less than the initial power of the jet as it leaves the nozzle. Hence it is evident that a great deal of energy is dissipated in the turbulent jet, and only a small fraction of the initial energy is available for yielding the sediment layer material.

4.1.3.2 A Model for Jet Penetration in a Pseudo Solid

Now we consider the case of a turbulent jet penetrating into a weak pseudo solid such as the sediment layer. Consider a conceptual model for the penetration, as shown in Figure 4.16. Here the jet has a distinct solid front with area A_f and is moving at some average velocity u_f into the pseudo solid with strength τ. Well behind the front, we assume the jet looks similar to the free turbulent jet. The spread angle and the entrainment may be different, but we assume the functional forms in Eq. (4.17) to (4.23) still hold, possibly with modified constants. If the front velocity u_f is smaller than the equivalent free jet velocity u_j that would be present at the same location, the fluid must turn outward radially or return toward the nozzle to satisfy continuity.

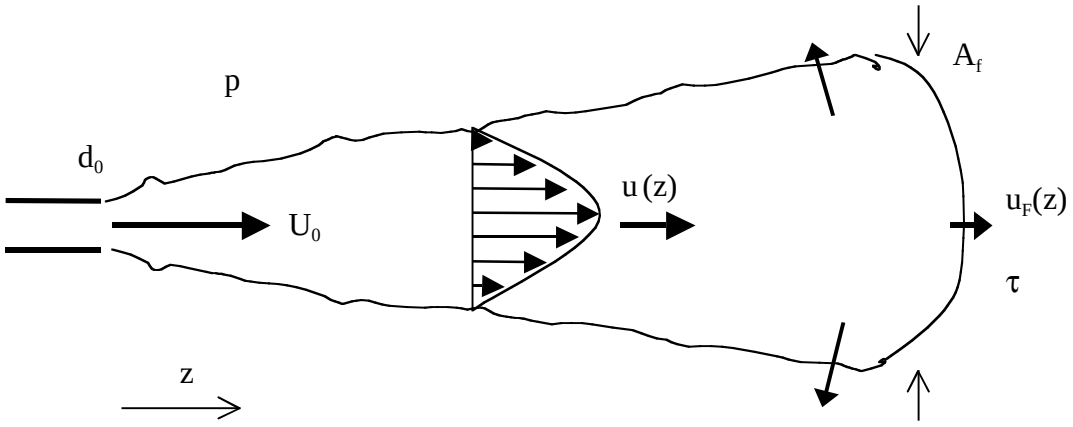

Figure 4.16. A Model for Jet Penetration into a Solid

4.1.3.3 An Energy Balance

We now attempt to develop and expression for the movement of the jet front. If this can be done, the swept volume can be determined as a function of time, and the associated gas release can be computed.

Consider an energy balance on the moving front:

$$\begin{array}{l}\text{Rate of work}\\ \text{applied to front}\end{array} = \begin{array}{l}\text{Power required}\\ \text{to yield solid}\end{array} - \begin{array}{l}\text{Losses due to}\\ \text{dissipation}\end{array} + \begin{array}{l}\text{Hydraulic power}\\ \text{of fluid at moving}\\ \text{front}\end{array}$$

This is expressed mathematically by

$$(p_f - p_0)A_f u_f = \tau A_f u_f + \Phi + \frac{1}{2}\rho u_f^2 A_f u_f \tag{4.26}$$

where p_f is the local pressure at the front and p_0 is the ambient pressure in the sediment layer at the elevation of the jet. The total dissipation Φ takes into account all viscous loss mechanisms. We assume the dissipation is proportional to the net work on the front so that

$$\Phi = c(p_f - p_0 - \tau)A_f u_f \tag{4.27}$$

So Eq. (4.2) can be written

$$\frac{1}{2}\rho u_f^2 = e(p_f - p_0 - \tau) \tag{4.28}$$

where $e = 1 - c$ is the efficiency of the process. When c = 0 (no dissipation), e = 1, and from Eq. (4.28) we see that all the net pressure work is converted into kinetic energy of the front.

The total pressure p_{tf} at the front is given by

$$p_{tf} = p_f + \frac{1}{2}\rho u_f^2 \tag{4.29}$$

The total pressure, p_{tf}, will be approximately equal to the total pressure that would be present at the same location for a free turbulent jet, p_{tj}. This is indicated from experimental data for free jets impinging on solid walls (Rajaratnam 1974). Therefore, we can write

$$p_f + \frac{1}{2}\rho u_f^2 \approx p_0 + \frac{1}{2}\rho u_{jm}^2 \tag{4.30}$$

We expect that the motion of the front is slow enough so that the dynamic component in Eq. (4.30) is negligible compared to the static component. With this approximation we get

$$p_f - p_0 \approx \frac{1}{2}\rho u_{jm}^2 \tag{4.31}$$

The pressure term in Eq. (4.28) can be evaluated with the aid of Eq. (4.31) to obtain

$$\frac{1}{2}\rho u_f^2 = e\left(\frac{1}{2}\rho u_{jm}^2 - \tau\right) \tag{4.32}$$

In the limit of no shear strength, the local efficiency would be 1 (because no yield process would occur), and Eq. (4.32) shows that the front velocity becomes the free jet velocity.

When the free jet velocity given by Eq. (4.17) is substituted into Eq. (4.32), we obtain an expression for the front velocity as a function of position z_f:

$$u_f(z_f) = U_0\sqrt{e\left(\left(\frac{6d_0}{z_f}\right)^2 - \frac{2\tau}{\rho U_0^2}\right)} \tag{4.33}$$

Noting that $u_f = dz_f / dt$, Eq. (4.33) can be integrated to obtain the front position as a function of time, we can write Eq. (4.33) as

$$\frac{dz_f'}{dt'} = \sqrt{e\left(\left(\frac{6}{z_f'}\right)^2 - \gamma\right)} \tag{4.34}$$

where

$$z_f' = z_f / d_0 \tag{4.35}$$

$$t' = tU_0 / d_0 \tag{4.36}$$

$$\gamma = \frac{2\tau}{\rho U_0^2} \tag{4.37}$$

The term γ is the ratio of material strength to jet momentum. For $\gamma << 1$, the material is weak compared with the jet's penetrating strength, and we expect significant penetration. For $\gamma \sim 1$, we expect the jet to do very little, or very slow, penetrating. For $\gamma > 1$ we expect that the jet will not penetrate into the waste sediment.

Equation (4.34) can be integrated to obtain

$$z_f'(t') = \frac{6}{\sqrt{\gamma}}\left(1 - \left(1 - \frac{\gamma\sqrt{e}t'}{6}\right)^2\right)^{1/2} \tag{4.38}$$

The time to steady state (when the front no longer progresses) is

$$t'_{max} = \frac{6}{\gamma\sqrt{e}} \tag{4.39}$$

In terms of dimensional variables, this is

$$z_f(t) = \frac{6d_0}{\sqrt{\gamma}}\left(1 - \left(1 - \frac{\gamma\sqrt{e}\ tU_0}{6d_0}\right)^2\right)^{1/2} \tag{4.40}$$

$$t_{max} = \frac{6d_0}{\gamma\sqrt{e}U_0} = \frac{3\rho}{\tau\sqrt{e}}U_0 d_0 \tag{4.41}$$

The penetrated volume as a function of time can be found by substituting Eq. (4.40) into Eq. (4.22):

$$V(t) = 72\pi\theta^2 \frac{d_0^3}{\gamma^{3/2}}\left(1 - \left(1 - \frac{\gamma\sqrt{e}tU_0}{6d_0}\right)^2\right)^{3/2} \tag{4.42}$$

The volume of gas contained in the swept volume is

$$V_{gas} = \alpha p V \tag{4.43}$$

So from Eq. (4.42) we obtain

$$V_{gas}(t) = 72\pi\theta^2\alpha p \frac{d_0^3}{\gamma^{3/2}}\left(1 - \left(1 - \frac{\gamma\sqrt{e}tU_0}{6d_0}\right)^2\right)^{3/2} \tag{4.44}$$

The maximum gas release according to the model is

$$V_{max} = 72\pi\theta^2\alpha p\frac{d_0^3}{\gamma^{3/2}} = 72\pi\theta^2\alpha p\left(\frac{\rho}{2\tau}\right)^{3/2}\left(U_0 d_0\right)^3 \tag{4.45}$$

From Eq. (4.45) we can write Eq. (4.44) as

$$\frac{V_{gas}}{V_{max}} = \left(1-\left(1-\frac{t}{t_{max}}\right)^2\right)^{3/2} \tag{4.46}$$

For short times, the nonlinear term in Eq. (4.46) can be approximated to obtain

$$\frac{V_{gas}}{V_{max}} \approx \left(\frac{2t}{t_{max}}\right)^{3/2} \qquad \frac{t}{t_{max}} << 1 \tag{4.47}$$

In terms of the physical parameters, Eq. (4.47) can be written

$$V_{gas}(t) \approx \frac{72}{\sqrt{27}}\pi\theta^2\alpha p(e)^{3/4}\left(U_0 d_0 t\right)^{3/2} \qquad t << \frac{3\rho}{\tau\sqrt{e}}U_0 d_0 \tag{4.48}$$

Eq. (4.47) and (4.48) are referred to as the linearized model, which applies only during short times, as quantified in the equations. Figure 4.17 plots Eq. (4.46) and (4.47) together.

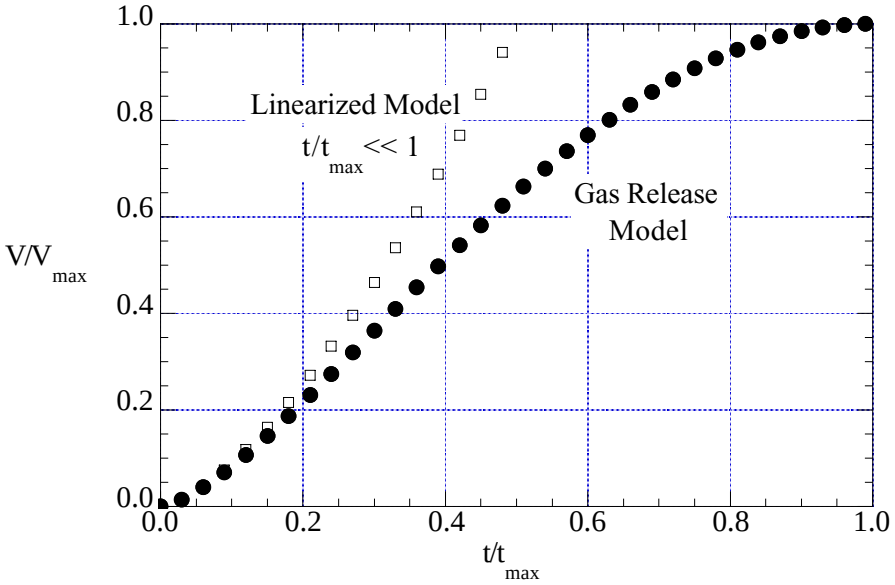

Figure 4.17. Gas Release Model Results for Eq. (4.46) and (4.47)

We can make several observations from these modeling results:

- The gas release volume depends on all the parameters initially expected,[(a)] which are shown in Eq. (4.1).
- Unlike the correlation attempts made in Section 4.2, the time dependence is not simple because it is both nonlinear and dependent on a number of parameters.
- The cubic dependence on $U_0 d_0$ in Eq. (4.45) is unlike jet volume flow, momentum, or power. This functional dependence is corroborated by an alternative analysis based on solid mechanics. This is presented in Appendix D.
- For short times, the penetrated volume (and associated gas release) does not depend on shear strength or density (Eq. 4.48).

4.1.4 Gas Release Model

We now apply the model derived in the previous section. We begin by using gas release data from SY-101 mixer pump operation to demonstrate the functional form of the model and adjust the free constants as appropriate.[(b)] The model is then applied to conditions in Tank AN-105.

4.1.4.1 Results for Tank SY-101

We now evaluate Eq. (4.44) for conditions corresponding to the various SY-101 pump runs discussed in Section 4.2. Table 4.3 shows the pertinent parameters for the tank waste and pump runs. Also shown are the parameter γ and $\sqrt{e}t_{max}$ (e is left explicit for now because it will need to be evaluated from the data). For the pump runs where the discharge was ramped up, gas

Table 4.3. Model Input Parameters for Tank SY-101 Mixer Pump Tests

Date	U_0 (m/s)	α	Duration (min)	$e^{1/2}t_{max}$ (s)
7/26/93	21.1	0.00056	9.3	33.4
10/22/93	11.0	0.00256	19.7	15.7
11/10/93	7.9	0.00424	20	12.2
11/5/93	7.9	0.00401	19.7	12.5
11/11/93	11.0	0.00207	19.7	17.4
11/12/93	15.3	0.00107	19.7	24.2
11/13/93	19.6	0.00065	19.7	31.0
11/21/93	15.9	0.00100	60	25.0
For all runs: d_0 = 0.066m, ρ = 1600kg/m^3, τ = 200pa, α = .08, p = 2.				

(a) Exceptions are density difference and viscosity. Buoyancy effects associated with the density difference have not been treated to simplify the analysis. The viscosity is treated implicitly because turbulent jet theory applies to flows with large Reynolds number and hence the viscosity is not important. In actuality, the flow near the penetrating front may be slow enough that viscous effects are important.
(b) The gas release model was derived for a single jet. Hence, when applying to mixer pump systems with two opposed jets, the results are multiplied by 2.

release was computed for each step, then the total computed as the sum of the individual step contributions. Figure 4.18 compares gas release computed with Eq. (4.44) the actual gas releases from the mixer pump runs. The jet spread angle θ was set to 4.07 degrees, and the efficiency, e, was set to 0.00005. The reduced jet spread angle is consistent with the expectation that the finite strength of the sediment layer reduces entrainment. The efficiency, however, is quite low. From Eq. (4.25) we expect an efficiency of 0.036 if the average jet power is completely converted to yielding the sediment layer. The value of 0.00005 is only 0.2% of this value, suggesting the process is very inefficient. Perhaps a better explanation is that much of the useful power of the jet is not being applied to penetration. This is consistent with the observation from SY-101 thermocouple data, which suggests the jet becomes buoyant and finds a "leak" path to the top of the sediment layer rather quickly.

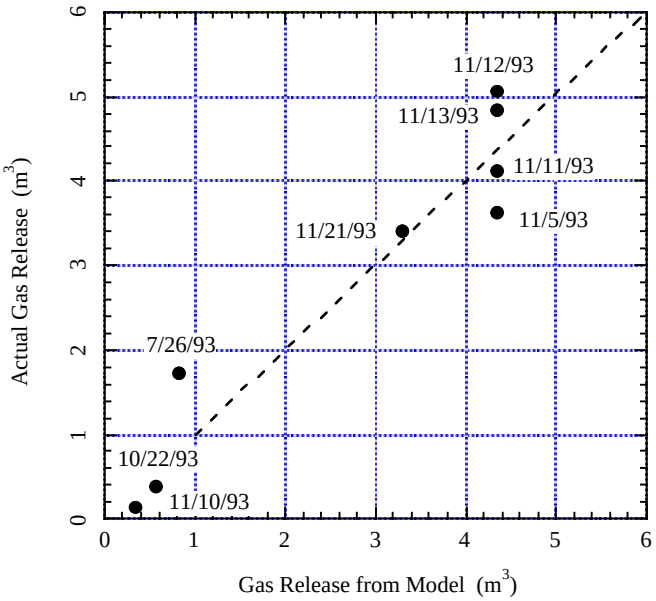

Figure 4.18. Comparison of Predicted Gas Release from Model (Eq. 4.44) and Observed Releases in SY-101 (data from Table 4.4; θ = 4.7 degrees and e = 0.00005)

4.1.4.2 Results for Tank AN-105

Using the values in Table 4.4, Eq. (4.44) and (4.48) are evaluated and become

$$V_{gas} = 16.8\left(1-\left(1-\frac{t}{125}\right)^2\right)^{3/2} \tag{4.49}$$

$$V_{gas} \approx 0.034(t)^{3/2} \qquad t << 125\,\text{min} \tag{4.50}$$

where t has been changed to have units of minutes and gas release volume remains in cubic meters. Eq. (4.49) and (4.50) are plotted in Figure 4.19.

Table 4.4. Model Parameter Values for Tank AN-105

Parameter	Value
Nozzle discharge velocity U_0 (m/s)	11.6 m/s
Nozzle diameter d_0 (m)	0.152
Nonconvective layer density ρ (kg/m^3)	1500
Yield strength τ (Pa)	150
Average void fraction α	0.06
Nonconvective layer average pressure ratio p	2
Jet spread angle θ (degrees)	4.07
Penetration Efficiency e	0.00005

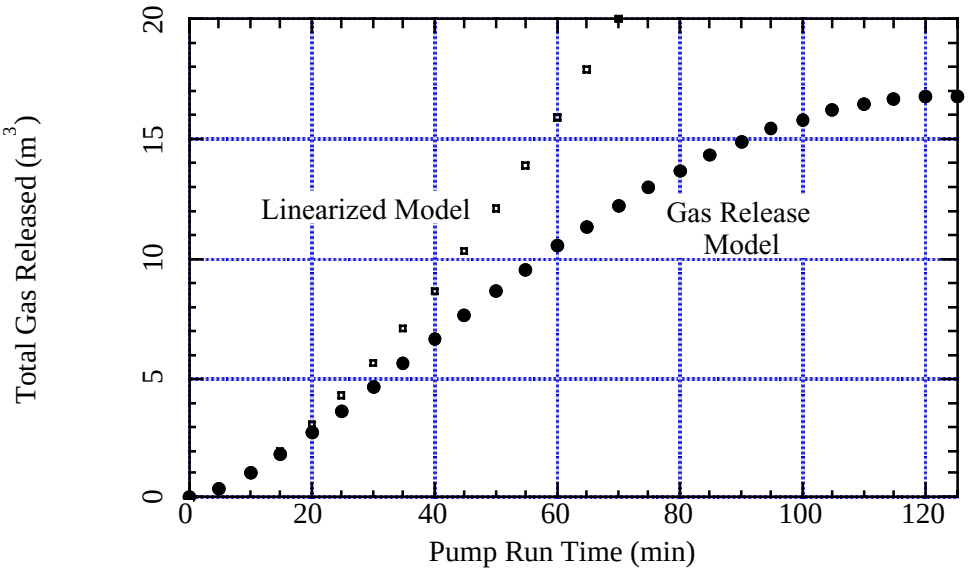

Figure 4.19. Predicted Gas Release Volume from Operation of a Single Mixer Pump in Tank AN-105

4.1.5 Recommendations for Further Modeling and Validation

This section presents a discussion of the limitations and uncertainties associated with the gas release model and presents suggestions for further modeling and validation.

4.1.5.1 Model Limitations and Uncertainties

Mixer pump-induced gas release in Hanford waste tanks is complex. The models presented should be thought of as a first-order attempt to capture some of the important features of the process. There are a number of model limitations and uncertainties that should be strengthened

in order to have confidence in actual mixer-pump induced gas release behavior. The following is a brief list and discussion of various issues:

- The model does not account for buoyant effects, yet buoyancy was clearly an important feature in the data set from Tank SY-101, which was used for model calibration.
- The small value of the efficiency parameter e is consistent with the observed behavior in SY-101—that the jet quickly penetrated the top of the sediment layer due to buoyancy. Larger values of e are likely if buoyancy effects are minimized (as will be the case for Tank AN-105). This would likely cause the gas release to occur more quickly.
- Gas release from the model "turns off" after the maximum jet penetration is attained. Clearly, there would be additional gas release from whatever recirculating currents are established in the waste.
- The model does not consider collapse of sediment layer material into penetrated regions. Basic scaling suggests that collapse is very likely. Collapse could introduce additional gas retaining material into the path of the jet and thereby increase the overall amount of gas released.
- The model assumed uniform waste properties. Regarding yield stress, it has been observed from the ball rheometer data that yield stress tends to increase with increasing depth in the sediment layer (Stewart et al. 1996b). This type of yield stress gradient will likely cause the jet to turn upward. The net effect would likely be to decrease gas release.
- The model assumes nothing regarding the return path of the discharge flow. For SY-101, this is likely acceptable because the pump inlet was in the convective layer far from the nozzle and jet. For Tank AN-105, the lower inlet will likely result in a strong recirculating flow. The features of this flow are not clear, and the applicability of the current model to this situation is unclear.

4.1.5.2 Recommendations

To improve our ability to predict gas release in Tank AN-105 (and other tanks) there are several activities that would be beneficial:

- Extend the current model to account for buoyancy effects that may dominate the flow, depending on the location of the pump inlet.
- Develop a theoretical model for the recirculating jet that would likely be present. This would be based on a cavity-type flow for which there are some experimental data.
- Address the phenomenon of sediment layer collapse into the jet penetration region.
- Develop additional data for model validation. A great deal of information would be gleaned from lab-scale experiments with jets in simulated gas-retaining sediment layers. Because we are primarily after first-order behavior, many of the technical issues associated with developing representative simulants would not be of concern.
- Perform computational fluid dynamics simulations (TEMPEST; Onishi and Trent 1998) with the goal of examining the penetration and collapse features. In this way, model development could be guided. It is also possible to develop a gas release model for the TEMPEST code. This feature would allow gas to be released as the pump is operated.

4.2 Model for Direct and Induced Gas Releases

Operation of a mixer pump in the sediment layer of a tank will serve not only to release gas from the disturbed region but also to mix and suspend solids into the supernatant layer, which can induce BDGREs. Therefore, the effect of mixer pump operation on the headspace hydrogen concentration must include the possibility of induced BDGREs as well as the direct release of gas from the mixer pump operation.

4.2.1 Modeling Mixer Pump Operations

To investigate the flammable gas issues associated with mixer pump operation, that is, what effect does the amount of sediment material mobilized by a given pump operation or run have on the tank headspace hydrogen concentration, we have simply specified that a mixer pump operation will disturb a set amount of the sediment layer. The volume of sediment disturbed determines the volume of the retained gas released and the amount of material suspended into the supernatant liquid to potentially induce BDGREs. By varying the amount of sediment layer disturbed and observing the resulting headspace hydrogen concentration transient, we can determine bounds on mixer pump operation in terms of the maximum disturbed volume and the waiting time necessary between runs. The mixing model described in Section 4.1 can then be used to determine the pump speed and duration that will produce the given disturbance.

Modeling of the headspace hydrogen concentration during mixer pump operation was based on the following assumptions:

- All of the gas in the volume of sediment layer disturbed by the mixer pump is released.
- The gas is released into the headspace at a time-varying rate similar to that of a BDGRE.
- The mixing and suspension of the sediment are instantaneous.

To model BDGREs induced by suspension of sediment in the supernate, the mixer pump model was coupled with the decant model (with the decant rate set to zero) described in Section 3.1. This coupling also allowed us to use the initial conditions of gob count, size, and gas fraction distributions that were created for the decant analysis (see Section 3.2). The Monte Carlo simulation method was likewise used to produce probability distributions of the model results (see Section 3.2.5).

The pump operations or runs are modeled by specifying the volume of sediment layer material disturbed by each run. Mixer pump runs occur at set intervals in time until the entire sediment layer has been disturbed. During the mixer pump operations, BDGREs are allowed to occur exactly the same way presented in Section 3 except that now we have only the minimal depressurization due to gas release, so the effect of solids suspension during mixing is the dominant initiation mechanism. The total hydrogen concentration in the headspace is therefore a combination of mixer pump-driven releases and BDGREs.

The methodology for determining the characteristics of the sediment layer that will be affected by subsequent mixer pump operations (i.e., what gobs are affected) is presented in Section 4.2.2, and the changes to the decant model are discussed in detail in Section 4.2.3.

4.2.2 Partitioning the Waste Disturbance Among Gobs

Actual mixer pump operations in the tank will disturb different areas of the sediment layer as the pump is manipulated (e.g., changing orientation, speed, and duration). As was discussed in Section 3, the sediment layer consists of a collection of semi-independently evolving gobs of varying sizes with different degrees of gas retention and relative buoyancy. The gas release from a pump run therefore depends on which gobs or portions of gobs are affected by that run.

The decant model did not consider the actual geometric location of individual gobs, and, though nonphysical, the collection of circular gobs was assumed to occupy the entire circular tank area. The assumed shape, size, and gas fractions of these gobs are discussed in Section 3.2. The same assumptions are retained in the mixer pump model. To account for the gob or gobs disturbed by a pump run, the set of gobs is ordered randomly and disturbed sequentially.

A given fraction of the sediment layer is assumed to be disturbed by each mixer pump run. The first gob in the input set is disturbed first. If the gob's volume is less than the volume disturbed by the pump, that gob volume is set to zero and the second gob disturbed. If the second gob volume is less than the pump-disturbed volume minus the volume of the first gob, then the third gob is affected, and so on. If the subsequent gob volume is greater than the remaining volume to be disturbed by the pump, the difference is subtracted from that gob, leaving a smaller gob with its original gas fraction to be disturbed on the next run or to experience a BDGRE.

This process illustrated in Figure 4.20. The input set of gobs is represented by the top row of circles. Their sizes represent the varying size and gas fraction of the input set. The total volume disturbed by the first mixer pump run is denoted by the vertically hashed ellipsoid. The "volume" of the mixer pump operation requires that the first gob is entirely disturbed, while just a portion of the second gob is disturbed. The second mixer pump run, which occurs a set interval after the first run, is represented by the horizontally slashed ellipsoid. It disturbs the remainder of the second gob, all of the third gob, and a portion of the fourth gob. This process continues until all of the gobs (i.e., sediment layer volume) have been disturbed.

The disturbance of a gob results in all of the disturbed portions' gas being released at a time-varying rate and a fraction of its solids being suspended in the supernatant liquid for the duration of mixer pump operations. At any time during this process, BDGREs may be induced as described in Sections 2 and 3. If, for example, the third gob in Figure 4.20 had an induced BDGRE between the first and second mixer pump operations, the gob's bulk and gas volumes would have been reduced, as specified in Section 3. The second mixer pump run would then have disturbed this altered gob, and more of the fourth gob would have been disturbed.

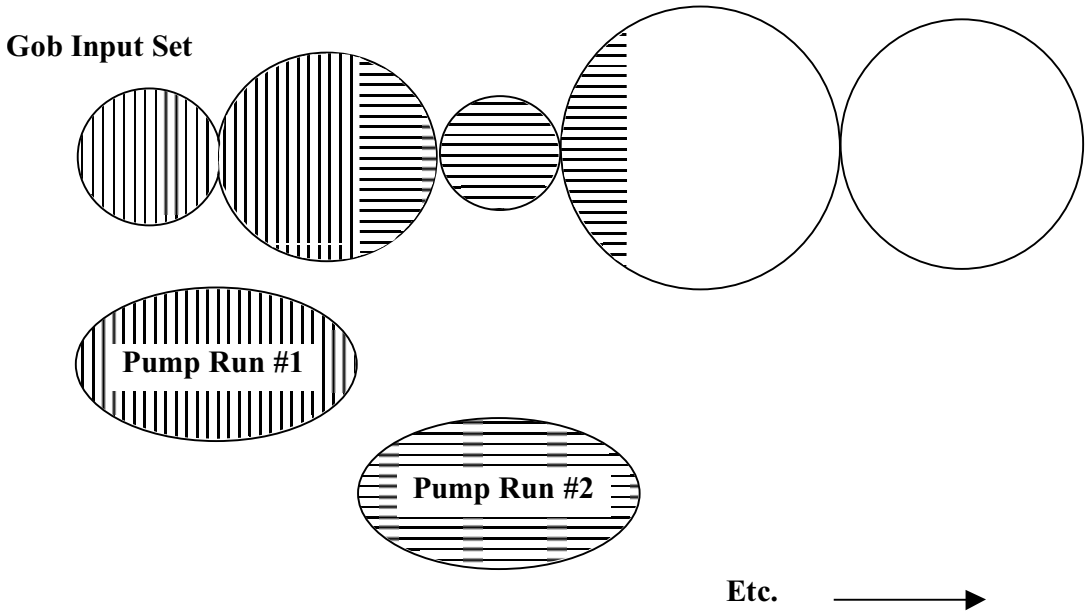

Figure 4.20. Schematic of Mixer Pump Operation and Effect on Gob Distribution

The bulk of the changes to the decant model are therefore bookkeeping steps to account for whether a portion or all of a gob has been disturbed by the mixer pump and whether those gobs or portions of gobs may experience a BDGRE. Those gobs that do experience BDGREs must then be "tracked" after their release for future mixer pump disturbance.

4.2.3 Modification of Decant Model

As discussed, the mixer pump model was coupled into the decant model presented in Section 3.1. All modeling remains the same unless otherwise noted in this section. The bulk sediment layer volume disturbed by a mixer pump run is given by

$$V_{Pm} = \Psi h_S A_T \tag{4.51}$$

where the subscript m denotes which mixer pump operation, Ψ, is the fraction of the sediment layer volume disturbed by a single pump operation; h_S is the sediment layer depth; and A_T is the tank area. This disturbed volume is composed of a gob or gobs, as discussed above. The initial bulk gob volume is computed from

$$V_{gb0,n} = \frac{\pi}{4} D_n^2 h_S \tag{4.52}$$

where the subscript n denotes the gob and D is the gob diameter (see Section 3.2.2). Mixer pump operations or a BDGRE can change the gob volume by

$$V_{gbi,n} = V_{gbi-1,n} - V_{Pm,n} - \frac{V_{re\,ln\,i-1(BDGRE)}}{P_S} - V_{gobSi-1,n(BDGRE)} \tag{4.53}$$

where the subscript i denotes the time step. The subscript (BDGRE) implies that a BDGRE occurred at the previous time step in that gob. Therefore, $\frac{V_{re\,ln\,i-1(BDGRE)}}{P_S}$ is the total in situ gas volume released from the gob when the gob was released at the preceding time step (term is zero otherwise) where P_S is the average hydrostatic pressure in the sediment layer (see Eq. 3.1 and 3.23). Likewise, $V_{gobSi-1,n(BDGRE)}$ is the total volume of nongaseous gob material suspended into the supernate when the gob was released at the preceding time step (term is zero otherwise; see Eq. 3.27–3.29).

The total gas released from a gob in the disturbed region is

$$V_{PGi,n,m} = V_{gasAi,n}\left(1 - \frac{V_{gbni}}{V_{gbni-1}}\right) \tag{4.54}$$

where $V_{gasAi,n}$ is the average volume of gas in the gob computed by

$$V_{gasAi,n} = \alpha_{Ai,n} V_{gbi,n} - V_{PGi,n} - \frac{V_{re\,ln\,i-1(BDGRE)}}{P_{Si-1}} \tag{4.55}$$

where $\alpha_{Ai,n}$ is the average gas fraction in a gob (Eq. 3.8). If the gob has already experienced a BDGRE, the average volume of gas in the gob is given by

$$V_{gasAi,n} = V_{gasAi-1,n} - V_{PGi,n} \tag{4.56}$$

The total pump gas release rate at atmospheric conditions is

$$V_{PGi} = \frac{1}{\Delta t} \sum_{n=1}^{disturbed\_gobs} V_{PGi,n} P_{Si} \tag{4.57}$$

This gas volume is released into the tank headspace at a time varying rate computed equivalently to Eq. (3.26) as

$$Q_{PGi} = \frac{V_{PGi}}{\Delta t}\left[\left(\frac{t_i - t_{0,n}}{\tau_P} + 1\right)e^{\frac{t_{0n} - t_i}{\tau_P}} - \left(\frac{t_{i+1} - t_{0,n}}{\tau_P} + 1\right)e^{\frac{t_{0,n} - t_{i+1}}{\tau_P}}\right] \tag{4.58}$$

where Δt is the time step, t_{0n} is the gas release start time, and τ_P is the time to the peak release rate for mixer pump operations (see Section 4.3).

The headspace hydrogen concentration given by Eq. (3.39) is then

$$C_{Hi} = \frac{C_{Hi-1} + \frac{\left(Q_{GASi} + Q_{PGi}\right) \cdot \chi_H}{V_{HSi}} \Delta t}{1 + \frac{\left(Q_{VIN} + Q_{GASi} + Q_{PGi}\right)}{V_{HSi}} \Delta t} \tag{4.59}$$

where χ_H is the volume fraction of hydrogen in the waste gas, Q_{GASi} is the release rate of gas from BDGREs (see Eq. 3.26), Q_{VIN} is the headspace vent rate, and V_{HS} is the headspace volume (Eq. 3.32). The supernatant liquid level in Eq. (3.32) is now given by

$$h_{Li} = h_{Li-1} - \frac{\Delta t}{A_T}\left(\frac{Q_{GASi-1}}{P_{Si-1}} + \frac{Q_{PGi}}{P_{Si}}\right) \tag{4.60}$$

Solids from disturbed gobs mix into the supernate layer, and a fraction of these solids is assumed to remain suspended, increasing the liquid density. The nongaseous sediment layer volume disturbed by pump operation and suspended in the supernatant liquid is determined from

$$V_{PSi,m} = FP\left(V_{Pi,m} - V_{PGi,m}\right) \tag{4.61}$$

where FP is the fraction of the solids that remain suspended (see Section 4.3).

The liquid density (ρ_L) at time i must now account for the suspension of solids from mixer pump operation and BDGREs, and is given by

$$\rho_{Li} = \frac{\left(h_{Li}A_T + \sum_{t=1}^{i-1} V_{gobSt} + \sum_{t=1}^{i-1} V_{PSt}\right)\rho_{Li-1} + \left(V_{gobSi} + V_{PSi}\right)\rho_S}{h_{Li}A_T + \sum_{t=1}^{i-1} V_{gobSt} + \sum_{t=1}^{i-1} V_{PSt} + V_{gobSi} + V_{PSi}} \tag{4.62}$$

4.3 Parameter Definitions and Constraints

With the exception of the time to the peak gas release rate for mixer pump operations, τ_p, and the fraction of solids mobilized by the pump that remain suspended, FP, the input distributions were exactly equivalent to those used in the decant model as presented in Section 3.2 and shown in Appendix C.

Gas releases due to mixer pump operations were evaluated on the initial operations of the SY-101 mixer pump (discussed in Section 4.1.2). The time to the peak gas release rate was determined from hydrogen concentration histories (Section 4.1.2 and Table 4.2) via the methods in Section 2.3. As with spontaneous BDGREs, no definitive value for τ_p was identifiable. Thus, for each simulation a τ_p was assigned from the distribution created from the SY-101 analysis (Figure 4.21).

As discussed, solids suspended into the liquid layer can induce BDGREs. The spontaneous releases observed in SY-101 during initial mixer pump operations may have been caused by this phenomenon. A distribution for the fraction of the solids mobilized by the pump that remain suspended was assigned based on the mixer pump performance in SY-101. Prior to disturbance by the mixer pump, the sediment layer in SY-101 was approximately 5.8 m deep. After the tank was fully mixed, the unsuspended settled solids depth was estimated to be approximately 1.25 to 2 m (50 to 80 in.). These results indicate that approximately 60 to 80% of the solids from the sediment layer were suspended. These results are corroborated by the solid particle sizes measured in SY-101 (Reynolds 1993), which indicate that about 75% of the solids would have settling velocities such that they would remain suspended for significant periods. Because a significant fraction of larger particles would settle out quickly, long-term suspension of 100% of the solids was assigned a zero probability. With no data defining a lower end, a symmetric distribution was chosen, as shown in Figure 4.22.

Values for the time to the peak gas release rate for mixer pump operations and the fraction of the solids mobilized by the pump that remain suspended were randomly selected from these distributions and formed additional inputs for the decant inputs sets. These are shown in Appendix C. As specified in Section 3.2.5, 10,000 runs were conducted in a Monte Carlo simulation for each retrieval operation, so the outputs represent all possible physical scenarios given the conditions constraining the inputs.

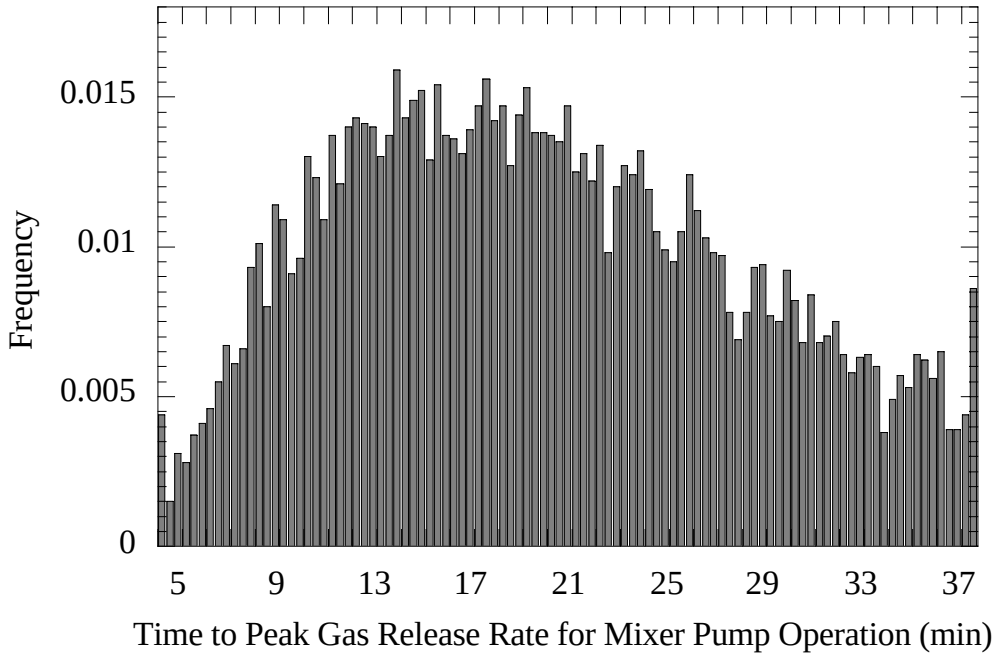

Figure 4.21. Distribution for Time to Peak Gas Release Rate for Mixer Pump Operations

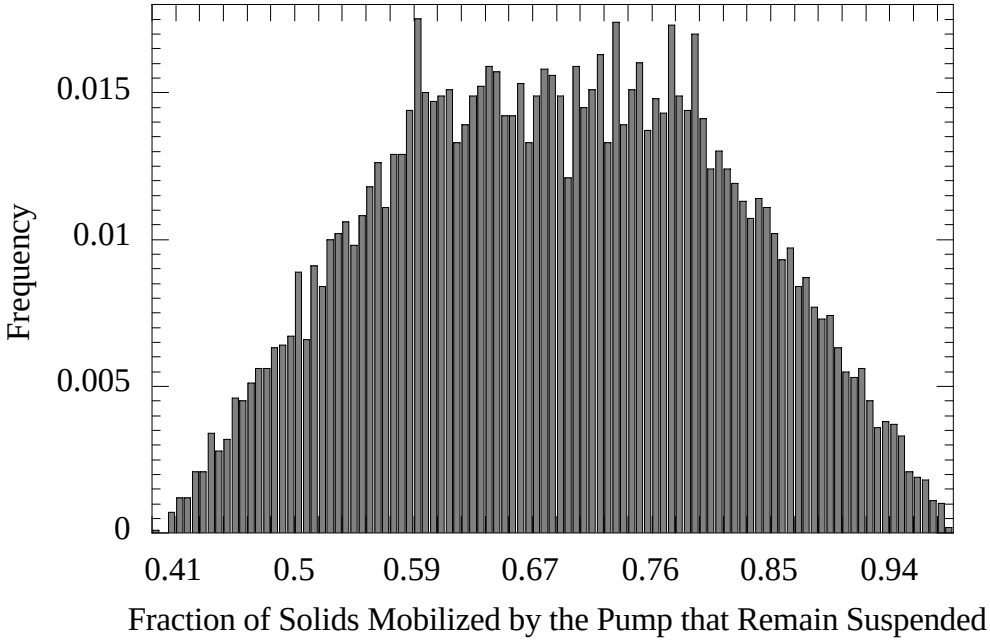

Figure 4.22. Distribution for Fraction of Solids, Mobilized by Pump, that Remain Suspended

4.4 Analysis of Mixing-Induced Gas Releases in AN-105

As with the supernate decant simulations, Tank AN-105 was selected for special consideration for mixer pump-induced gas releases because 1) it has experienced BDGREs with the highest headspace hydrogen concentration, 2) it is one of the first tanks scheduled to be retrieved for vitrification, and 3) it is representative of the other tanks. The results of mixing analyses for the other three tanks (AN-103, AN-104, and AW-101) are presented in Section 4.5.

The mixing model developed in Section 4.1 assumes that the flow from the pump nozzles behaves as a turbulent jet impinging on and slowly penetrating a wall of weak solid material. The net hydraulic power of the jet deposited on the waste at the penetration zone is set equal to the power required to yield the solid matrix. Jet theory applied to this energy balance shows that the maximum volume of waste disturbed is proportional to the quantity $(u_0 d_0)^3$, where u_0 and d_0 are the initial jet velocity and nozzle diameter, respectively, while the time required to achieve this disturbance is proportional to $u_0 d_0$. The model was used to extrapolate gas release data from initial mixing tests in SY-101, at 150 hp, to degassing AN-105 with one of the 300-hp W-211 mixer pumps. The model predicts that running a single mixer pump in AN-105 at a fixed azimuth for about 26 minutes at 1200 rpm (maximum speed) will theoretically mobilize 5% of the sediment volume. A 76-minute run at the same speed mobilizes about 20% of the sediment. Combinations of pump speed and run time to achieve disturbances of 5, 10, and 20% of the sediment are given in Table 4.5. Maximum theoretical disturbance at the given speed is also listed.

Table 4.5. Fraction of Sediment Disturbed for Given Mixer Pump Run Conditions

Pump Speed	Fraction of Sediment Disturbed per Run	Run Time (min)
1200 rpm	0.050	26
	0.100	44
	0.200	76
	0.409 (max)	199
1000 rpm	0.050	32
	0.100	54
	0.200	104
	0.255 (max)	170
900 rpm	0.050	35
	0.100	62
	0.193 (max)	155
775 rpm	0.050	41
	0.100	77
	0.137 (max)	138
700 rpm	0.050	48
	0.100	110
	0.102 (max)	125

Cases were run (mixer pump operations were conducted at the set schedule until the entire sediment layer was disturbed) to investigate the sensitivity of the peak hydrogen concentration during mixing to the pump operation as follows:

1. **Base Case:** Mixer pump runs are assumed to release gas from 5% of the sediment layer per run. One run is made every 24 hours until the entire sediment layer has been mixed (20 runs).
2. **Pump Speed Sensitivity:** The base case was rerun with the fraction of sediment disturbed increased to 20%. It was anticipated that larger disturbance would increase the peak hydrogen concentration in at least direct proportion. The 20% was selected as the maximum practical fraction of waste disturbed by one pump running at a fixed azimuth.
3. **Pump Schedule Sensitivity:** The base case was rerun with one pump run every 8 hours.

The input conditions are described in Sections 3.2 and 4.3 and listed in Appendix C. A Monte Carlo simulation approach was used as outlined in Section 3.2.5, and results of each of these cases for AN-105 are presented in separate subsections. The method of presentation of the results is the same as used in Sections 3.3 and 3.4. Results of the base case are shown in Section 4.4.1 and the pump speed sensitivity study in Section 4.4.2. The pump schedule sensitivity study results are presented in Section 4.4.3, and the overall conclusions of these studies are summarized in Section 4.4.4. The results of the base case simulations and selected other cases for the other three tanks are given in Section 4.5, and the mixing results are summarized in Section 4.6.

4.4.1 Base Case in AN-105

The distribution of the peak hydrogen concentration for the base case is presented in Figure 4.23. This case had 5% of the sediment layer disturbed every 24 hours. The median of the peak hydrogen concentration is 7,500 ppm and the 95% confidence limit is 15,100 ppm. The 95% confidence limit exceeds 25% LFL (15,100 ppm corresponds to about 38% LFL).

The majority of the simulations had induced BDGREs. The distribution for the fraction of the retained gas released by BDGREs during the simulations is shown in Figure 4.24. Quantities of retained gas released by mixer pump-induced BDGREs were similar to that released during decant operations (Section 3.3). The median release fraction is 0.09, and the 95% confidence level is 0.23. The high frequency of 0.13 at zero gas release indicates that for 1,300 of the 10,000 simulations, no BDGREs were triggered.

The headspace hydrogen concentration for a simulation representing the 95% confidence level peak hydrogen concentration is plotted in Figure 4.25. The repeated pump runs can be seen in spikes every 24 hours. The varied concentration results over the pump runs from 80 to 380 hours are caused by the gas volume distribution in the gobs affected by the subsequent pump runs (see Section 4.2). The maximum concentration is caused by two induced BDGREs immediately following the fourth pump operation. A final BDGRE induced at 384.5 hours can be seen in the increased hydrogen concentration in the second-to-last pump run.

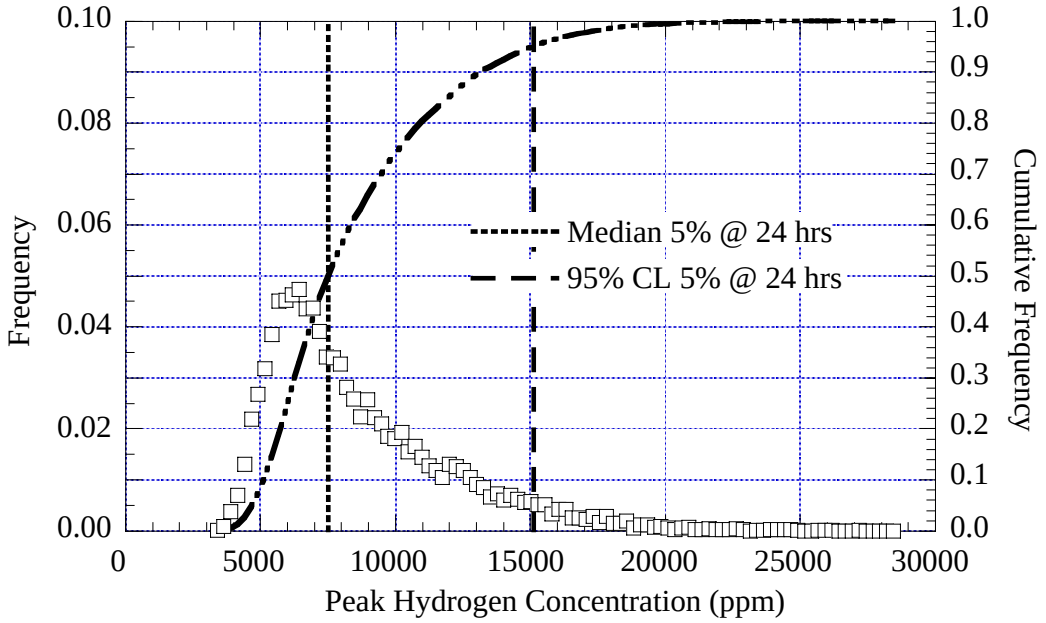

Figure 4.23. Peak Hydrogen Concentration: 5% Disturbance Every 24 Hours in AN-105

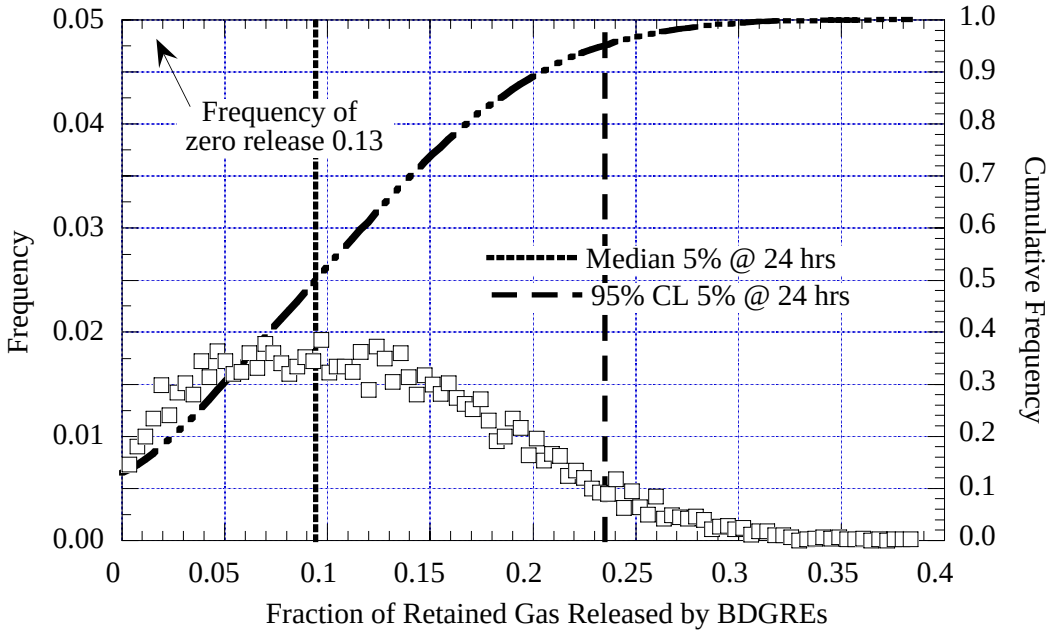

Figure 4.24. Gas Released by BDGREs: 5% Disturbance Every 24 Hours in AN-105

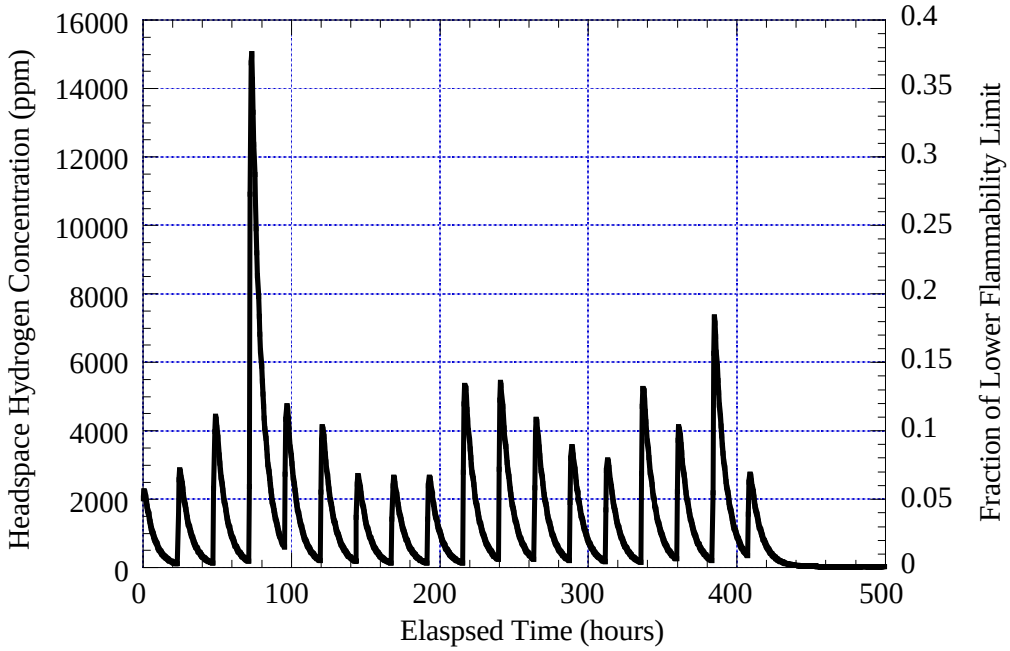

Figure 4.25. Example Simulation Hydrogen Concentration: 5% Disturbance Every 24 Hours in AN-105

The results show that, for 5% of the sediment layer disturbed by mixer pump operations every 24 hours, it is highly likely in the 95% confidence level that the hydrogen concentration will exceed 25% of the LFL. However, it is highly unlikely to reach the LFL. The highest hydrogen concentrations during the mixer pump operation are caused by induced BDGREs adding to the gas release caused directly by the mixer pump. As with decant operations, the gas releases are more rapid than the ventilation rate (see Sections 3.2 and 4.3). Varying the ventilation rate for the mixer pump operations by a factor of two alters the predicted maximum hydrogen concentration at the 95% confidence level by approximately 15%.

4.4.2 Pump Speed Sensitivity

The amount of sediment disturbed by the mixer pump operation is a function of the pump speed. The base case was rerun with the fraction of sediment disturbed increased to 20%. It was anticipated that a larger disturbance would increase the peak hydrogen concentration.

Figure 4.26 shows the distribution of peak hydrogen concentrations for 20% of the sediment layer disturbed every 24 hours. The median and 95% confidence level from the base case (5% at 24 hours) are also shown. The median value increased from 7,500 ppm in the base case to 20,300 ppm and the 95% confidence level from 15,100 to 28,400 ppm. In five of the 10,000 simulations, the peak hydrogen concentration exceeded the LFL. Clearly, increasing the amount of sediment layer material disturbed by a mixer pump run increases hydrogen concentration.

The fraction of the retained gas released by BDGREs during the simulations was slightly less than the base case (Figure 4.27). This results directly from the loss of gobs with the potential for BDGREs to the more vigorous effect of the mixer pump. A total of 1,785 simulations had no BDGREs, up from 1,300 in the base case.

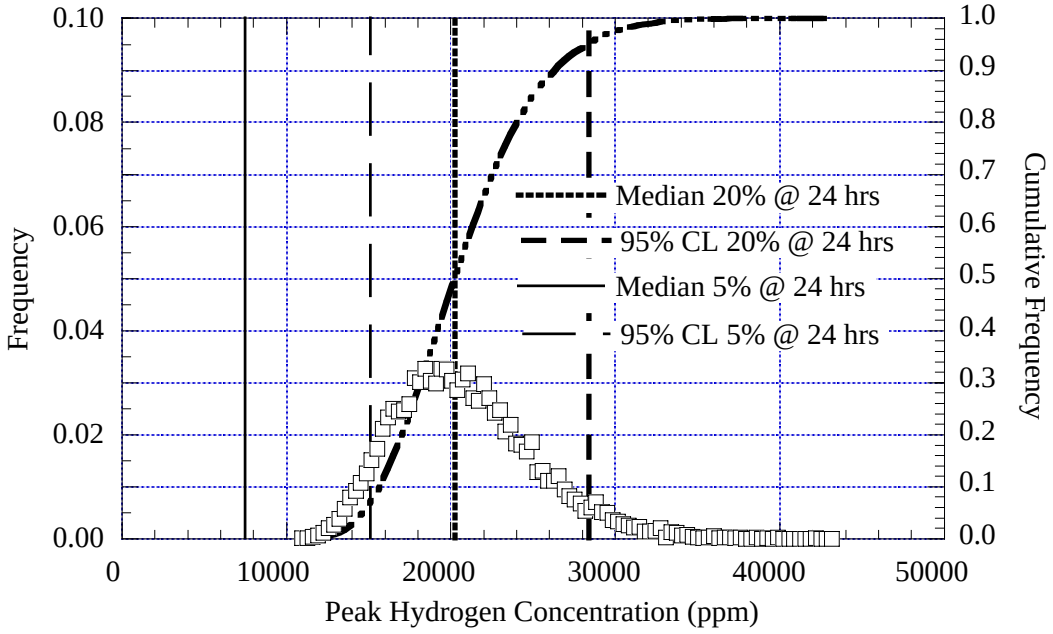

Figure 4.26. Peak Hydrogen Concentration: 20% Disturbance Every 24 Hours in AN-105

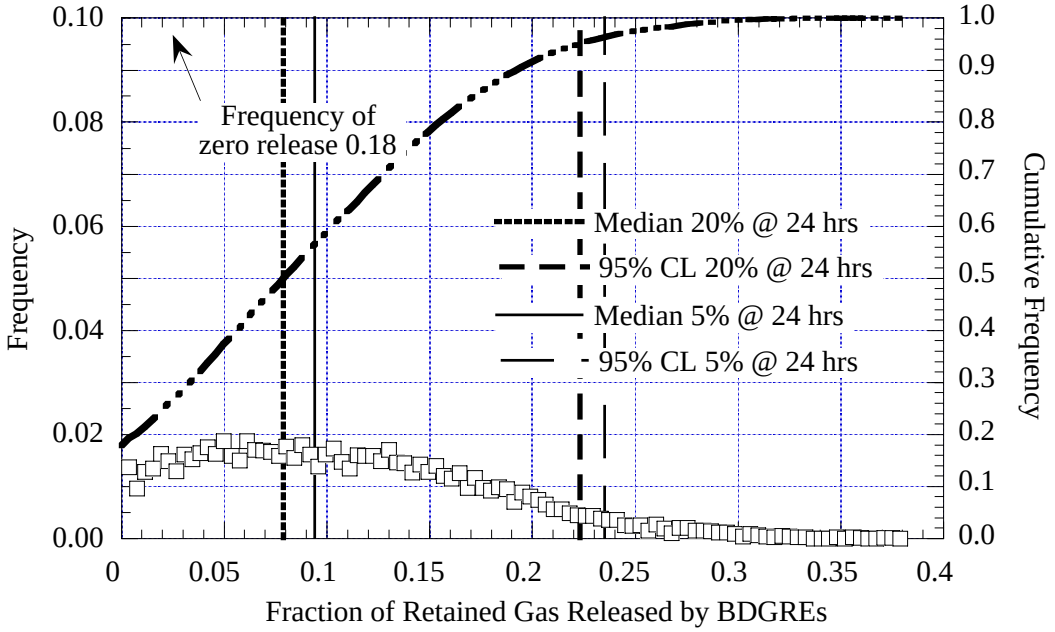

Figure 4.27. Gas Released by BDGREs: 20% Disturbance Every 24 Hours in AN-105

The headspace hydrogen concentration for a simulation representing the 95% confidence level of the peak hydrogen concentration (same simulation as base case, Figure 4.25) is plotted in Figure 4.28. The spikes due to the pump runs are now significantly larger, as expected. The

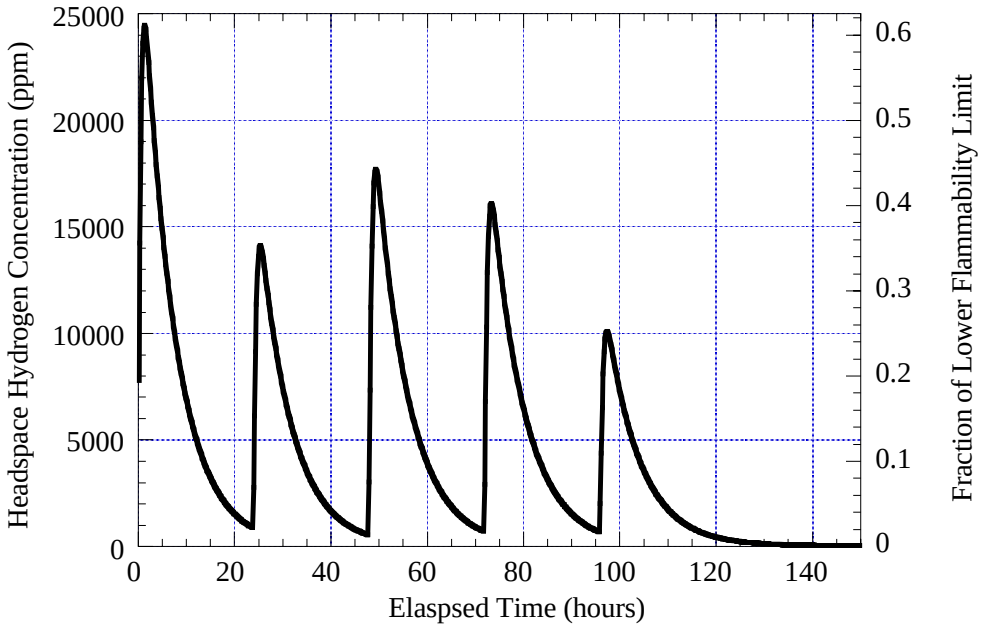

Figure 4.28. Example Simulation Hydrogen Concentration: 20% Disturbance Every 24 Hours in AN-105

same two gobs that are triggered after the fourth pump operation in the base case happen immediately after the first pump operation. The final BDGRE from the base case is not triggered because it is affected by the mixer prior to achieving buoyancy. Notice also that the total mixing time has been reduced from approximately 410 hours to 100 hours.

4.4.3 Pump Schedule Sensitivity

The elevation of the hydrogen concentration by subsequent pump runs is postulated to be affected by altering the separation of the pump operations in time, allowing a longer or shorter time for the headspace to clear between runs. To investigate this, the base case was rerun with one pump run every 8 hours instead of every 24 hours.

The change in the distribution of the peak hydrogen concentration when the wait time between pump runs is decreased to 8 hours is presented in Figure 4.29. The median of the peak hydrogen concentration is 9,800 ppm, compared with 7,500 ppm in the base case, and the 95% confidence limit is 17,100 ppm, exceeding 25% LFL by 70% (15,100 ppm in the base case).

As in the base case, 1,300 of the 10,000 simulations had no BDRGEs. This may be seen in the distribution for the fraction of the retained gas released by BDGREs during the simulations (Figure 4.30). The median release fraction is 0.09, and the 95% confidence level is 0.23, equivalent to the base case results.

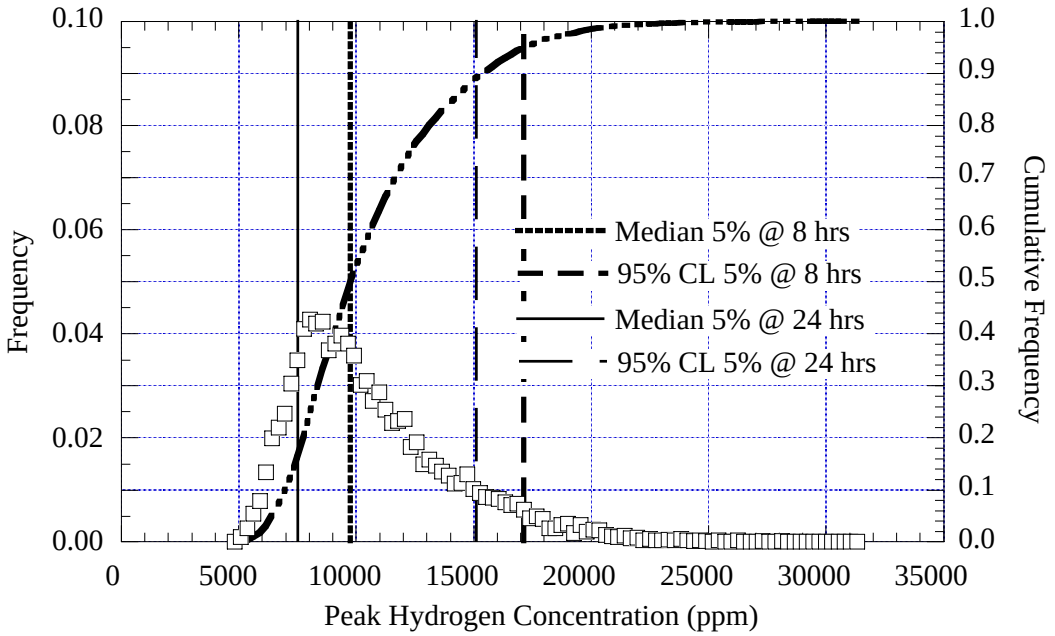

Figure 4.29. Peak Hydrogen Concentration: 5% Disturbance Every 8 Hours in AN-105

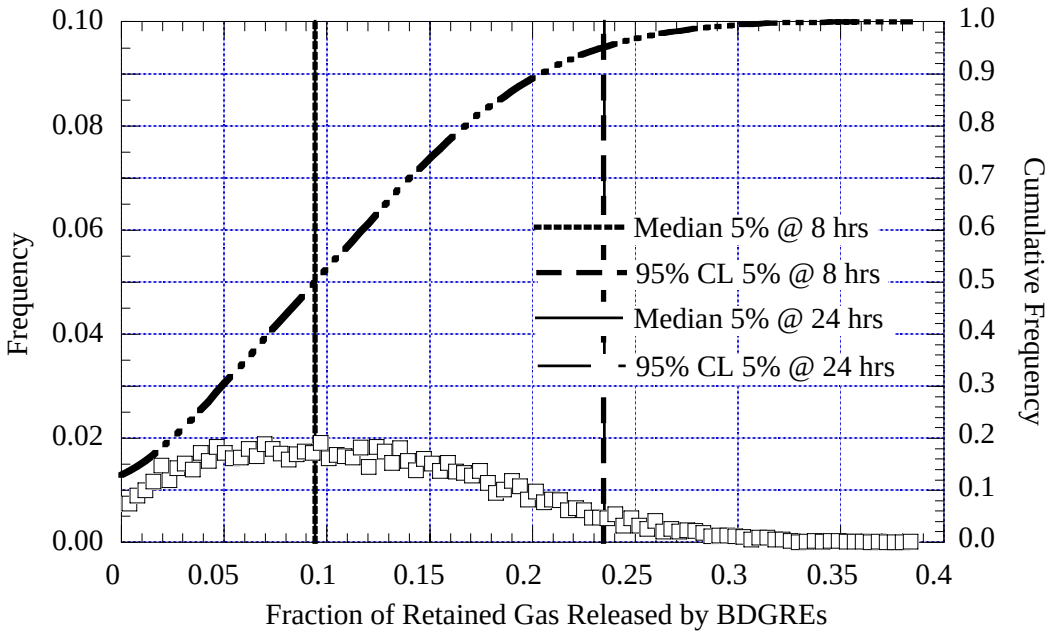

Figure 4.30. Gas Released by BDGREs: 5% Disturbance Every 8 Hours in AN-105

The headspace hydrogen concentration for a simulation representing the 95% confidence level peak hydrogen concentration is plotted in Figure 4.31 (same simulation as base case). Again, the repeated pump runs can be seen in spikes every eight hours, and the highest headspace hydrogen concentrations are due to spontaneous BDGREs. Two BDGREs are triggered immediately after the fourth pump run at 24 hours, and the final BDGRE is triggered on the next to the last pump run at 128 hours. The gas volume distribution in the gobs affected by the subsequent pump runs is again directly evident in the varied concentration results over the pump runs (see Section 4.2). The total mixing time is approximately 140 hours.

The average hydrogen concentration in Figure 4.31 is greater than that in Figure 4.25, suggesting the potential for increased risk with a higher initial concentration. As illustrated in Figure 4.29, however, this effect does not have significant impact on the 95% confidence level of the peak hydrogen concentration.

The results show that for 5% of the sediment layer disturbed by mixer pump operations every eight hours, it is highly likely in the 95% confidence level that the hydrogen concentration will exceed 25% of the LFL. However, it is highly unlikely it will reach the LFL. Lengthening the time between pump runs to 24 hours, as in the base case, clearly allows more time for hydrogen in the headspace to dissipate, but this does not appear to reduce the peak concentrations significantly.

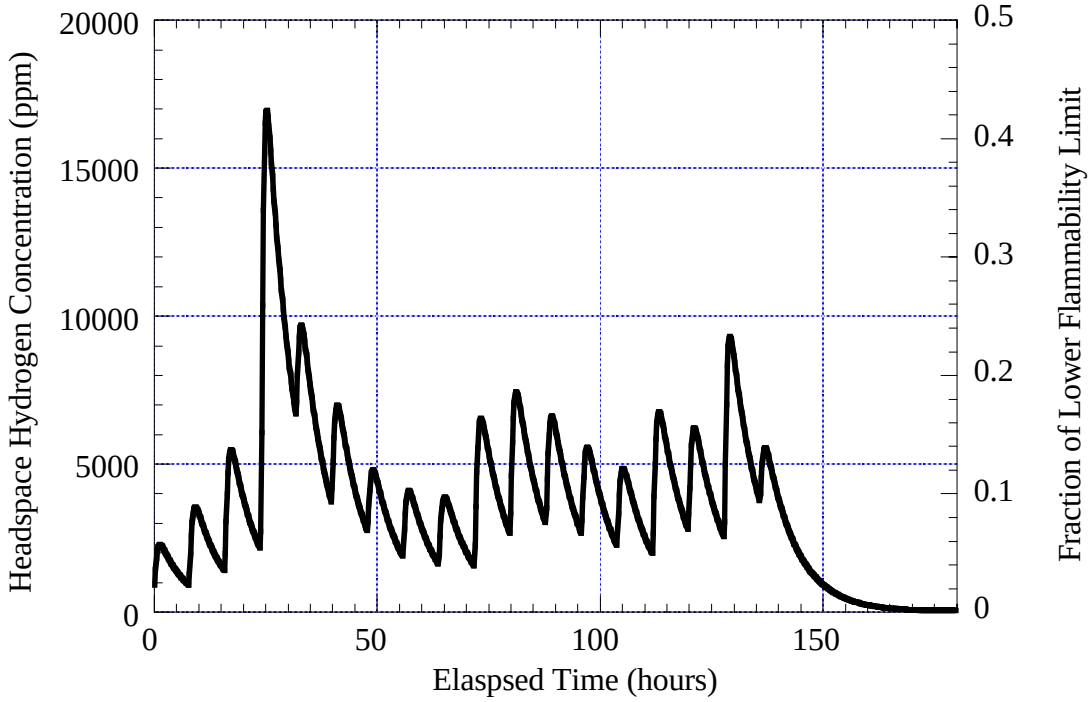

Figure 4.31. Example Simulation Hydrogen Concentration: 5% Disturbance Every 8 Hours in AN-105

4.4.4 Summary of Mixer Pump Analyses for AN-105

The mixing results for AN-105 are summarized in Table 4.6. The gas releases due to mixer pump operation and induced BDGREs are not likely to approach flammability as long as pump operations are carefully controlled. The results indicate that pump runs that disturb on the order of 5% of the sediment layer repeated every 24 hours provide an acceptable margin between the peak headspace hydrogen concentration and the flammability limit. Increasing the pump speed and/or duration to disturb 20% of the waste produces hydrogen concentrations approaching within almost 75% of the LFL. Decreasing the waiting time between runs to eight hours increases the peak hydrogen concentration by 13%.

Table 4.6. Summary of Mixer Pump Analysis Results in AN-105

Tank	Run	Quantity	Median	95% CL
AN-105	5% at 24 hours	Hydrogen (ppm)	7,500	15,100
		Fraction Gas Release by BDGREs	0.09	0.23
	20% at 24 hours	Hydrogen (ppm)	20,300	28,400
		Fraction Gas Release by BDGREs	0.08	0.22
	5% at 8 hours	Hydrogen (ppm)	9,800	17,100
		Fraction Gas Release by BDGREs	0.09	0.23

4.5 Analysis of Mixing-Induced Gas Releases in Other Tanks

Mixing-induced gas releases in the three other tanks were analyzed. The initial conditions for each tank were determined from historical data and measurements the same way as AN-105, as described in Sections 3.2 and 4.3. Based on the results of the decant analysis (Sections 3.3 to 3.5) and the mixing results in AN-105 (Section 4.4), only select cases were run in each tank, as discussed below. The mixing results for all of the tanks are summarized in Section 4.6.

4.5.1 AN-103 Mixing Results

As discussed and as reflected in the decant results (Sections 3.3 to 3.5), AN-103 contains by far the highest retained gas volume of the four tanks considered in this study. Therefore, the base case (5% disturbance every 24 hours) was the only case run in AN-103 because this produced the lowest headspace hydrogen concentration in AN-105 (Section 4.4).

The distribution of the peak hydrogen concentration for the base case is presented in Figure 4.32. The median of the peak hydrogen concentration is 15,300 ppm, and the 95% confidence limit is 25,800 ppm. Only 58 of the 10,000 simulations had no induced BDGREs. The distribution for the fraction of the retained gas released by BDGREs during the simulations is shown in Figure 4.33. The median release fraction is 0.20 and the 95% confidence level 0.33.

The results show that for 5% of the sediment layer disturbed by mixer pump operations every 24 hours, it is highly likely in the 95% confidence level that the hydrogen concentration will exceed 50% of the LF. Ten of the 10,000 simulations exceeded the LFL.

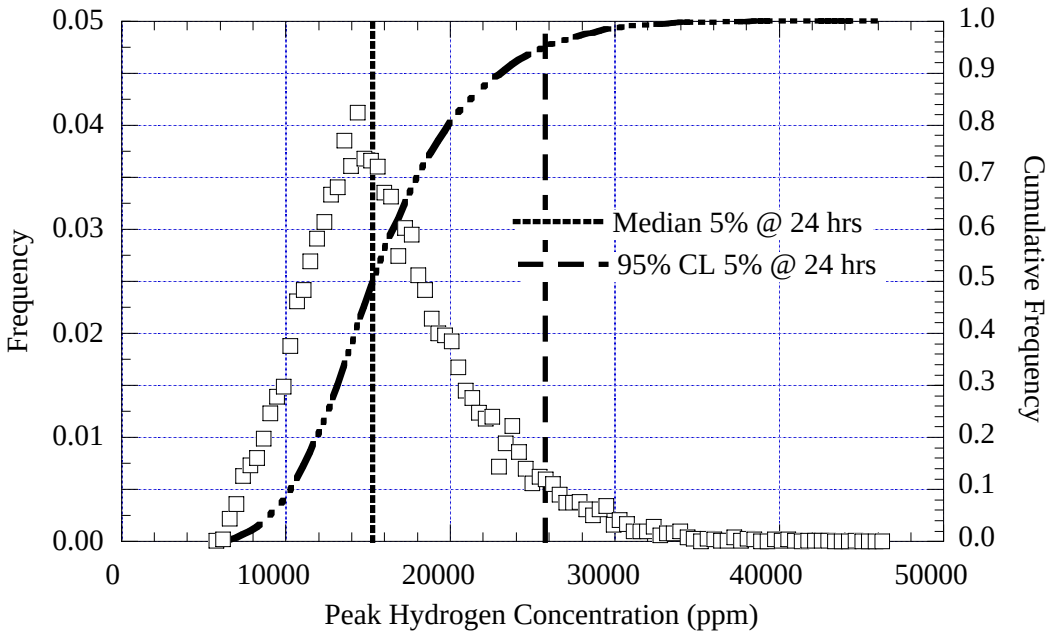

Figure 4.32. Peak Hydrogen Concentration: 5% Disturbance Every 24 Hours in AN-103

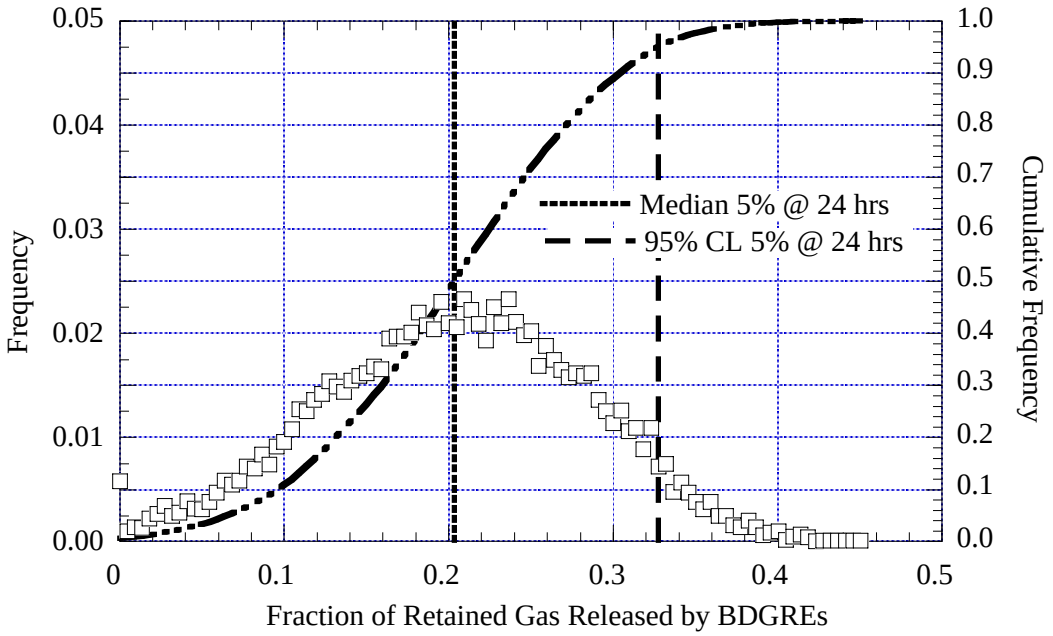

Figure 4.33. Gas Released by BDGREs: 5% Disturbance Every 24 Hours in AN-103

4.5.2 AN-104 Mixing Results

Tank AN-104 has a larger retained gas volume and a larger headspace than AN-105 and exhibited behavior similar to AN-105 in the decant analysis (Sections 3.3 through 3.5). Thus it is expected that effects of the accelerated pump schedule (pump run every eight hours) will be similar, so only the base case (5% disturbance every 24 hours) and the 20% disturbance every 24 hours were analyzed in AN-104.

The distributions of the peak hydrogen concentration and BDGRE gas release fraction for the base case are given in Figures 4.34 and 4.35, respectively. The median of the peak hydrogen concentration is 5,500 ppm and the 95% confidence limit 10,600 ppm, slightly exceeding 25% LFL. The median BDGRE release fraction is 0.12, the 95% confidence level is 0.26, and 846 of the 10,000 simulations had no induced BDGREs.

As with AN-105, the 20% disturbance every 24 hours peak hydrogen concentration results are higher than the base case results (Figure 4.36). The median is 12,900 ppm (~32% LFL), and the 95% confidence level is 18,500 ppm (~46% LFL). The distribution for the fraction of the retained gas released by BDGREs during the simulations is shown in Figure 4.37. The median fraction of the retained gas released by BDGREs is 0.10 and the 95% confidence level is 0.25, with 1,233 of the simulations having no induced BDRGEs.

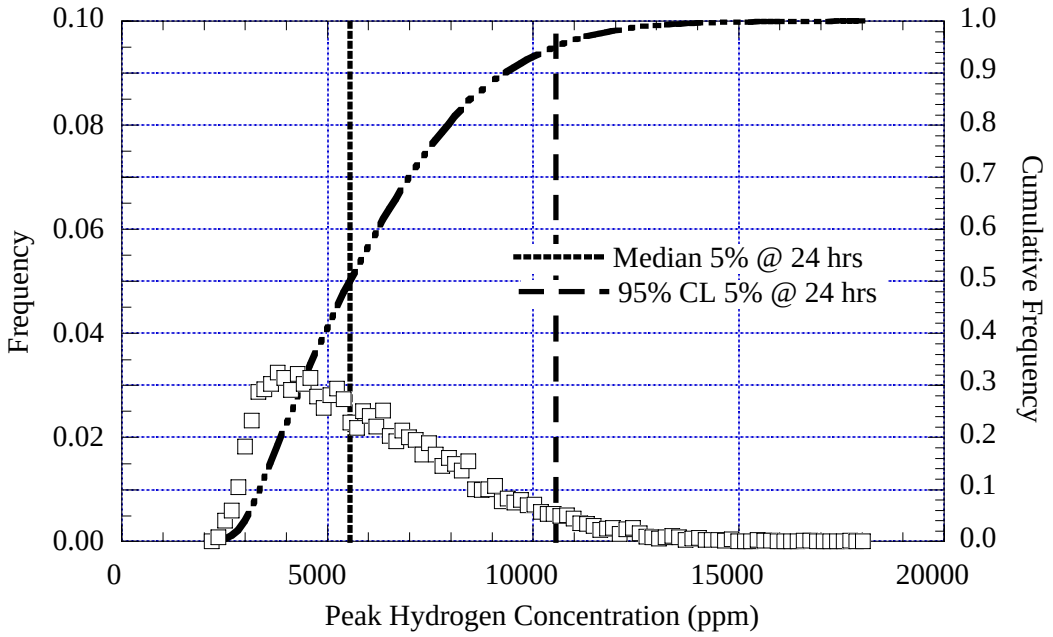

Figure 4.34. Peak Hydrogen Concentration: 5% Disturbance Every 24 Hours in AN-104

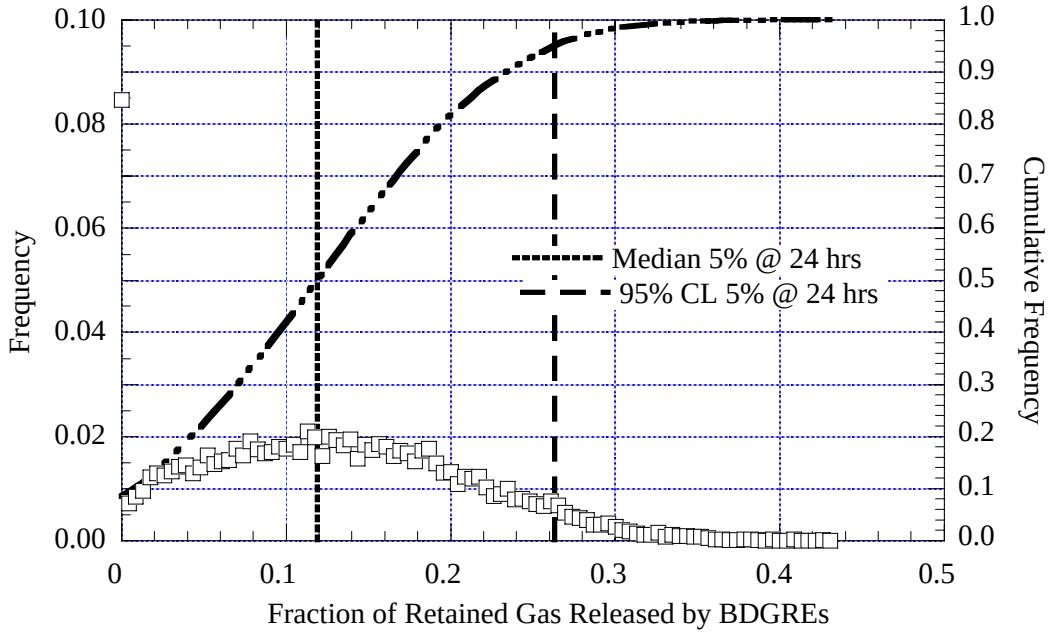

Figure 4.35. Gas Released by BDGREs: 5% Disturbance Every 24 Hours in AN-104

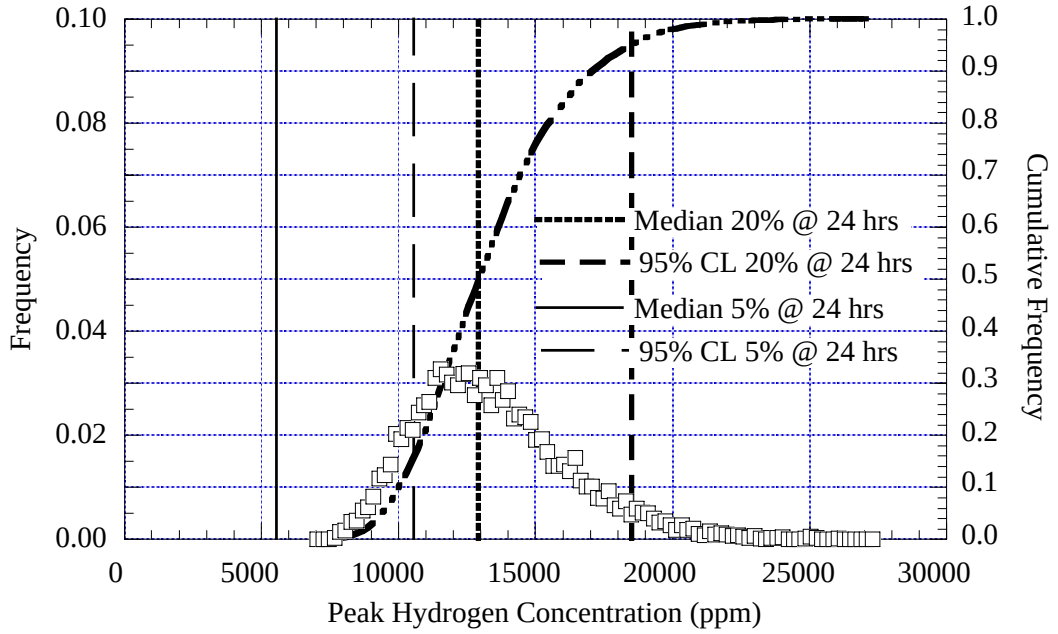

Figure 4.36. Peak Hydrogen Concentration: 20% Disturbance Every 24 Hours in AN-104

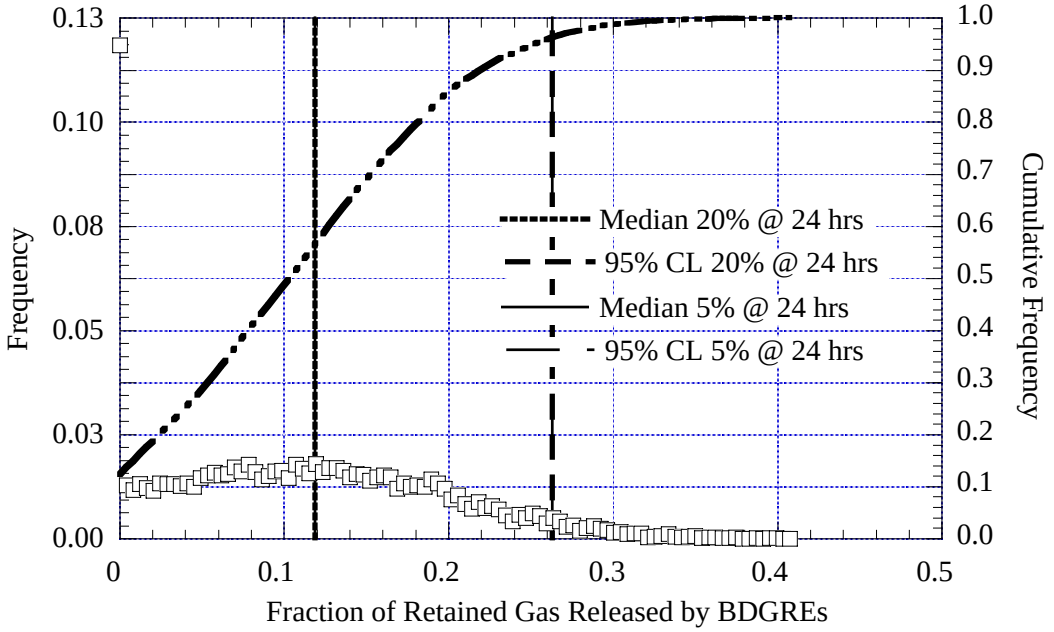

Figure 4.37. Gas Released by BDGREs: 20% Disturbance Every 24 Hours in AN-104

4.5.3 AW-101 Mixing Results

Tank AW-101 is notable for having the least retained gas volume of the four tanks under consideration. This was reflected in the decant results in Sections 3.4 and 3.5. Therefore, in addition to the base case, a 20% disturbance every eight hours case was also evaluated.

The distributions of peak hydrogen concentration and gas release fraction for the base case are provided in Figures 4.38 and 4.39, respectively. The median and 95th percentile values of the peak hydrogen concentration are only 1,800 ppm (~5% LFL) and 2,700 ppm (~7% LFL), respectively. The fraction of the retained gas released by BDGREs is 0.00 at the median and 0.14 at the 95th percentile, with over 64% of the simulations having no BDGREs.

The 20% disturbance every eight hours in peak hydrogen concentration and the fraction of the retained gas released by BDGREs results are shown in Figures 4.40 and 4.41, respectively. The median peak hydrogen concentration is 6,900 ppm, and the 95% confidence level is still below 25% LFL at 8,800 ppm. The median fraction of the retained gas released by BDGREs is 0.00, and the 95% confidence level is 0.13. Almost 70% of the simulations had no induced BDGREs. These results indicate that in AW-101, even for the maximum feasible mixing schedule and operations, the LFL will not be threatened.

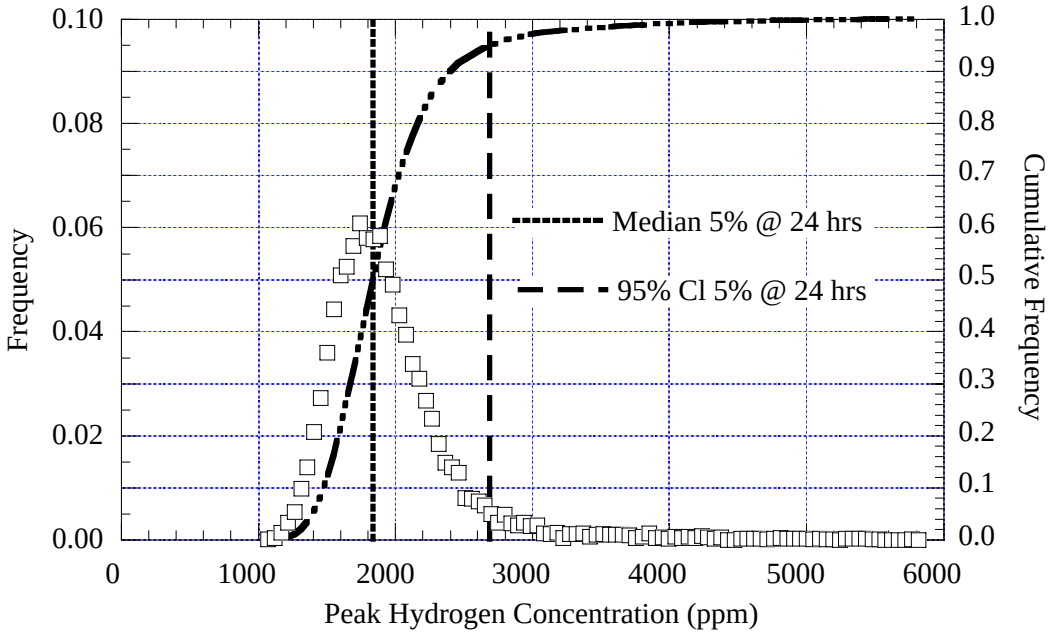

Figure 4.38. Peak Hydrogen Concentration: 5% Disturbance Every 24 Hours in AW-101

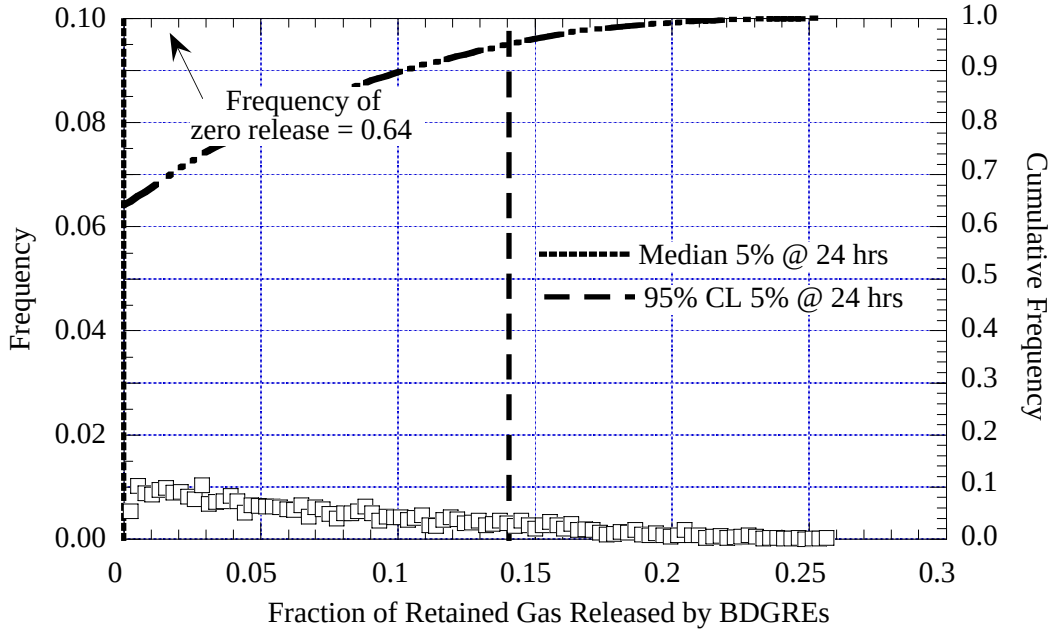

Figure 4.39. Gas Released by BDGREs: 5% Disturbance Every 24 Hours in AW-101

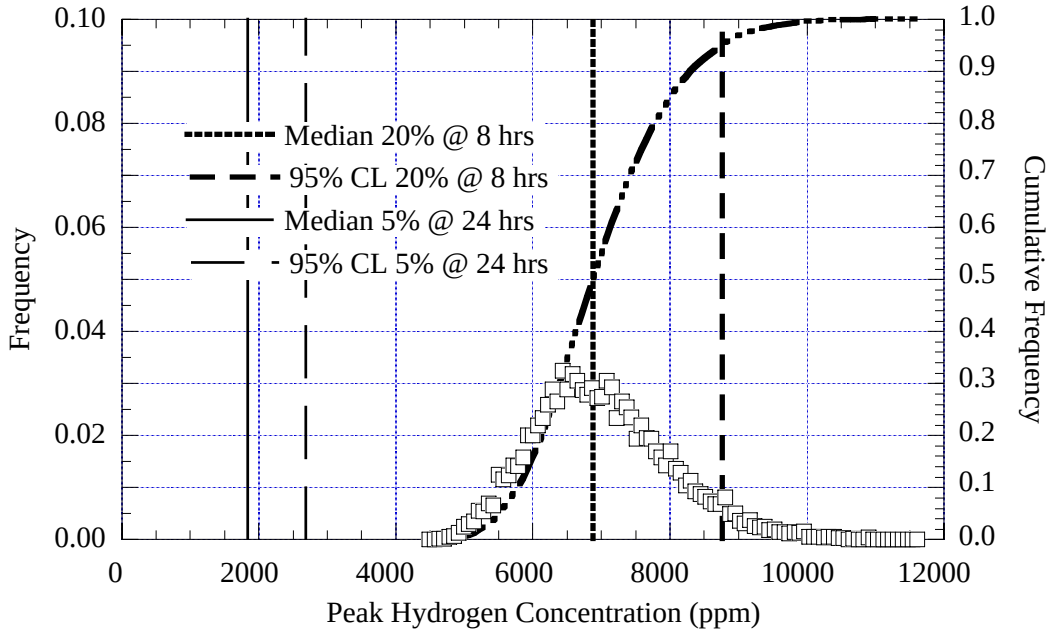

Figure 4.40. Peak Hydrogen Concentration: 20% Disturbance Every 8 Hours in AW-101

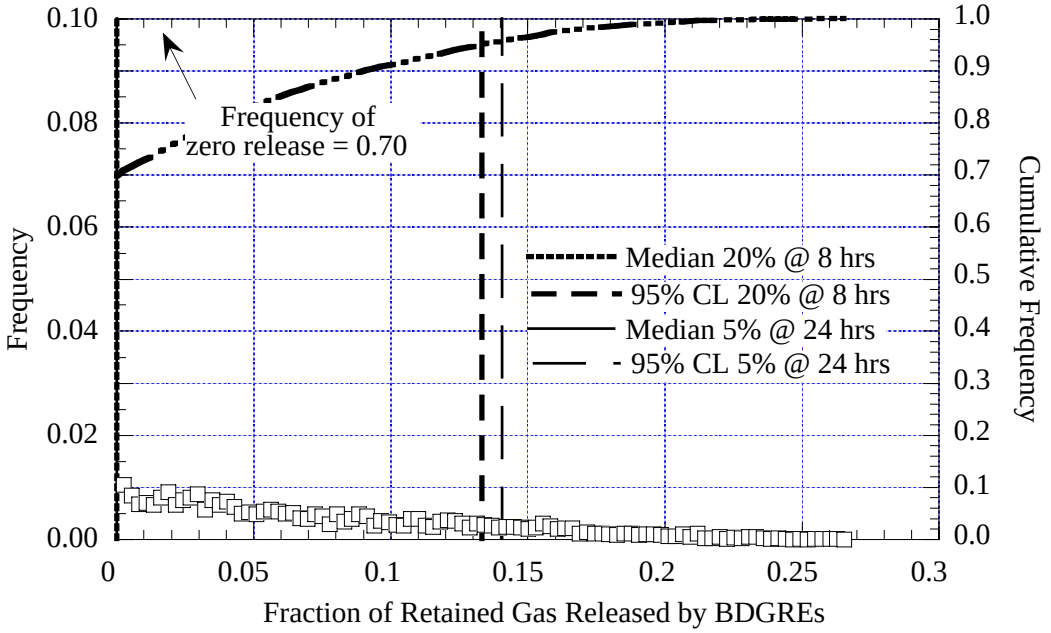

Figure 4.41. Gas Released by BDGREs: 20% Disturbance Every 8 Hours in AW-101

4.6 Conclusions from Mixing-Induced Gas Release Modeling Results

The mixing results are summarized in Table 4.7. Except for AW-101, the base case (5% disturbance every 24 hours) had results at the 95% confidence level that exceeded 25% LFL. However, none of the tanks exceeded LFL at the 95% confidence level. Increasing the volume of waste disturbed produces elevated hydrogen concentrations. To a lesser extent, decreasing the waiting time between pump runs also elevates the peak hydrogen concentrations. The peak hydrogen concentrations during mixing operations are caused by induced BDGREs.

Table 4.7. Summary of Mixing Analysis Results

Tank	Run	Quantity	Median	95% CL[(a)]
AN-105	5% at 24 hours	Hydrogen (ppm)	7,500	15,100
		Fraction Gas Release by BDGREs	0.09	0.23
	20% at 24 hours	Hydrogen (ppm)	20,300	28,400
		Fraction Gas Release by BDGREs	0.08	0.22
	5% at 8 hours	Hydrogen (ppm)	9,800	17,100
		Fraction Gas Release by BDGREs	0.09	0.23
AN-104	5% at 24 hours	Hydrogen (ppm)	5,500	10,600
		Fraction Gas Release by BDGREs	0.12	0.26
	20% at 24 hours	Hydrogen (ppm)	12,900	18,500
		Fraction Gas Release by BDGREs	0.10	0.25
AN-103	5% at 24 hours	Hydrogen (ppm)	15,300	26,000
		Fraction Gas Release by BDGREs	0.20	0.33
AW-101	5% at 24 hours	Hydrogen (ppm)	1,800	2,700
		Fraction Gas Release by BDGREs	0.00	0.14
	20% at 8 hours	Hydrogen (ppm)	6,900	8,800
		Fraction Gas Release by BDGREs	0.00	0.13

CL = confidence level.

5.0 Conclusions and Recommendations

A thorough review was conducted of buoyant displacement gas release mechanisms and how they can be induced and exacerbated by supernate decanting and mixer pump operation. A detailed analysis of historic gas release data has provided a much better understanding of tank behavior, and new methods have been developed for quantifying the jet mixing process. The result of these efforts is a new, robust model to predict the headspace hydrogen concentration during various retrieval operations. The derivation of this model and its application to supernate decanting and mixer pump degassing in Tanks AN-103, AN-104, AN-105 and AW-101 are the subject of this report. Overall conclusions from the analyses are given in Section 5.1 and recommendations in Section 5.2.

5.1 Conclusions

Except for AN-103, the peak hydrogen concentrations resulting from gas releases predicted to be induced by supernate decant roughly correspond to those produced by the larger spontaneous GREs and remain well below the LFL. AN-103 is an exception because its history of very small, infrequent gas releases does not match the expectation based on its waste configuration. Nevertheless, none of the runs for AN-103 reached the LFL, even though the majority of the runs had BDGREs occur relatively early in the decant. AW-101 lies at the other extreme in that its predicted peak hydrogen concentrations are far below even the 6,250-ppm action level. These analysis results indicate that removing the supernatant liquid from these four tanks will not induce gas releases that cause the tank headspace to reach the LFL.

These results are not sensitive to the decant rate, and the predicted peak hydrogen concentration is not reduced by stopping the decant at the action level of 6,250 ppm hydrogen. However, backfilling with water during the decant has a significant probability of preventing BDGREs, though the peak hydrogen concentration approximates the base case if they do occur (excepting AW-101).

The gas releases that occur during mixer pump degassing are not likely to approach flammability as long as the pump operations are carefully controlled. The modeling results indicate that pump runs that disturb on the order of 5% of the sediment layer repeated every 24 hours provide an acceptable margin between the peak headspace hydrogen concentration and the LFL. Increasing the pump speed or duration to disturb 20% of the waste produces significantly elevated hydrogen concentrations. Decreasing the waiting time between runs to 8 hours elevates the peak hydrogen concentration to a lesser extent. Based on the jet mixing model developed in this study, operating one W-211 mixer pump at fixed azimuth for 26 minutes at 1,200 rpm (full power) or 48 minutes at 700 rpm (idle) would disturb approximately 5% of the waste. A 20% waste disturbance would require 76 minutes at 1,200 rpm.

5.2 Recommendations

Development of the jet mixing model was hindered by the lack of good data on the transient mobilization of sediment and corresponding gas release. The only available data on gas release were from SY-101 and were complicated by the high uncertainty in the retained gas volume and the complexity of the mixer pump operations. While the model correlates these data very well, the extrapolation to the larger W-211 pumps with their different design and location in the tank is quite uncertain. The following two activities could greatly reduce the technical risk of waste feed delivery:

- Additional data for model validation should be developed from lab-scale experiments with jets in simulated gas-retaining sediment layers. Because we are looking primarily for first-order behavior, many of the technical issues associated with smaller scale and with developing representative waste simulants would not be of concern.

- Computational fluid dynamics simulations (TEMPEST; Onishi and Trent 1998) should be performed with the goal of looking at the penetration and collapse mechanisms and the effects of gradients in material strength. Information from these simulations would provide unique and valuable insights into the actual processes involved.

We believe that the modeling results show that decanting and mixing retrieval operations have a conservative margin with regard to flammable conditions and, with reasonable care, can be safely conducted in the tanks we analyzed. However, the most conservative approach to remove the uncertainty inherent in these analytical model results would be to perform decant or mixing operations in a tank that does not have sufficient gas to render the headspace flammable even if it were all released instantaneously. Tanks AW-101 and SY-103 meet this criterion.

6.0 References

Alleman RT, ZI Antoniak, WD Chavala, LE Efferding, JG Fadeff, JR Friley, WB Gregory, JD Hudson, JJ Irwin, NW Kirch, TE Michener, FE Panisko, CW Stewart, and BM Wise. 1994. *Mitigation of Tank 241-SY-101 by Pump Mixing: Results of Testing Phases A and B.* PNL-9423, Pacific Northwest Laboratory, Richland, WA.

Brewster ME, NB Gallagher, JD Hudson, and CW Stewart. 1995. *The Behavior, Quantity, and Location of Undissolved Gas in Tank 241-SY-101*. PNL-10681, Pacific Northwest Laboratory, Richland, WA.

Caley SM, CW Stewart, ZI Antoniak, JM Cuta, LA Mahoney, and FE Panisko. 1998. *Investigation of Flammable Gas and Thermal Safety Issues for Retrieval of Waste from Tank 241-AN-105.* PNNL-11996, Pacific Northwest National Laboratory, Richland, WA.

CHG. 2000. *Tank Waste Remediation System Technical Safety Requirements*, Rev. 2 as amended. HNF-SD-WM-TSR-006, CH2MHILL Hanford Group, Inc., Richland, WA.

Hedengren DC, KM Hodgson, WB Barton, CW Stewart, JM Cuta, and BE Wells. 2000. *Data Observations on Double-Shell Flammable Gas Watch List Tank Behavior*. RPP-6655 Rev. 0, CH2MHILL Hanford Group, Inc., Richland, WA.

Hu TA. 2000. *Empirical Rate Equation Model and Rate Calculations for Hydrogen Generation for Hanford Tank Waste*. HNF-3851 Rev. 0A, CH2MHILL Hanford Group, Inc., Richland, WA.

Huckaby JL, JC Hayes, L Jensen, LL Buckley, RD Cromar, LD Pennington, and SR Wilmarth. 1997. *Homogeneity of Passively Ventilated Waste Tanks.* PNNL-11640, Pacific Northwest National Laboratory, Richland, WA.

Mahoney LA, JL Huckaby, SA Bryan, and GD Johnson. 2000. *Overview of the Flammability of Gases Generated in Hanford Waste Tanks*. PNNL-13269, Pacific Northwest National Laboratory, Richland, WA.

Mahoney LA, ZI Antoniak, JM Bates, and ME Dahl. 1999. *Retained Gas Sampling Results for the Flammable Gas Program*. PNNL-13000, Pacific Northwest National Laboratory, Richland, WA.

McCain DJ. 2001. *Results of Vapor Space Monitoring of Flammable Gas Watch List Tanks*. HNF-SD-WM-TI-797 Rev. 6, CH2MHILL Hanford Group, Inc., Richland, WA.

Meyer PA and CW Stewart. 2001. *Preventing Buoyant Displacement Gas Release Events in Hanford Double-Shell Waste Tanks*. PNNL-13337, Pacific Northwest National Laboratory, Richland, WA.

Meyer PA, ME Brewster, SA Bryan, G Chen, LR Pederson, CW Stewart, and G Terrones. 1997. *Gas Retention and Release Behavior in Double–Shell Waste Tanks*. PNNL-11536 Rev. 1, Pacific Northwest National Laboratory, Richland, WA.

Moore DJ, SA Barker, WB Barton, and MA Kufahl. 2000. *The Gas Release Event Safety Analysis Tool Relational Data Base for Hanford Tanks*. HNF-SD-WM-TI-806 Rev. 3, CH2MHILL Hanford Group, Inc., Richland, WA.

Onishi Y and DS Trent. 1998. *TEMPEST Code Modifications and Testing for Erosion-Resisting Sludge Simulations*. PNNL-11787, Pacific Northwest National Laboratory, Richland, WA.

Reynolds DA. 1993. *Tank 101-SY Window E Core Sample: Interpretation of Results*. WHC-EP-0628, Westinghouse Hanford Company, Richland, WA.

Rajaratnam N. 1976. *Turbulent Jets*. American Elsevier Publishing Company, Inc., New York.

Stewart CW, ME Brewster, PA Gauglitz, LA Mahoney, PA Meyer, KP Recknagle, and HC Reid. 1996a. *Gas Retention and Release Behavior in Hanford Single-Shell Waste Tanks*. PNNL-11391, Pacific Northwest National Laboratory, Richland, WA.

Stewart CW, JM Alzheimer, ME Brewster, G Chen, RE Mendoza, HC Reid, CL Shepard, and G Terrones. 1996b. In Situ Rheology and Gas Volume in Hanford Double-Shell Waste Tanks. PNNL-11296, Pacific Northwest National Laboratory, Richland, WA.

Sullivan HL. 1995. *A Safety Assessment for Proposed Pump Mixing Operations to Mitigate Episodic Gas Releases in Tank 241-SY-101: Hanford Site, Richland, Washington*. LA-UR-92-3196 Rev. 14, Los Alamos National Laboratory, Los Alamos, NM.

Appendix A
Current Tank Conditions

Appendix A
Current Tank Conditions

Tanks AN-103, AN-104, AN-105, and AW-101 were studied extensively using the void fraction instrument (VFI), ball rheometer, and retained gas sampler (RGS) during 1995–1996. The retained gas volume and its composition, waste density and rheology, and the waste layer dimensions are well quantified (Meyer et al. 1997; Hedengren et al. 2000). A continuous record of waste level and temperature is also available from which earlier gas volume calculations can be updated. This appendix summarizes this monitoring information to describe the current state of the waste in tanks.

Each of the four tanks has the "typical" double-shell tank (DST) waste configuration that consists of a nonconvective layer of settled solids under a deep layer of convective liquid. A relatively thin gas-liquid-solid layer or "crust" floats on the liquid. This waste configuration is subject to buoyant displacement gas release events (BDGRE) in which gas accumulates in the nonconvective layer until a portion, or "gob," becomes buoyant with respect to the overlying liquid. At that point the gob detaches from the rest of the nonconvective layer and rises rapidly to the surface. As it rises, the gob releases its buoyant potential energy by expansion of the gas, which liquefies the material and allows a large fraction of the gas to escape into the tank headspace. The BDGRE process depends on the thickness and density of both the convective and nonconvective layers.

A.1 Temperature Profiles and Temperature History

The temperature profiles measured by the validation probe that is operated in multifunction instrument trees (MIT) describe the waste configuration. They provide a measurement of the height of the nonconvective layer and the thickness of the floating crust layer. Because the temperature gradient in a nonconvective heat-generating region is parabolic and that in a convective region is uniform, the layer boundary is located where the uniform and parabolic temperature profiles intersect. This is usually accomplished by visually interpreting a graph. The uncertainty is estimated as half the distance between temperature measurements, though it may be higher if the transition is indistinct or lower if it is particularly clear. Changes in waste configuration can be detected by comparing temperature profiles at different times. Validation probe temperature profiles from 1996 and 2000 for each of the four tanks are plotted in Figures A.1 through A.4.

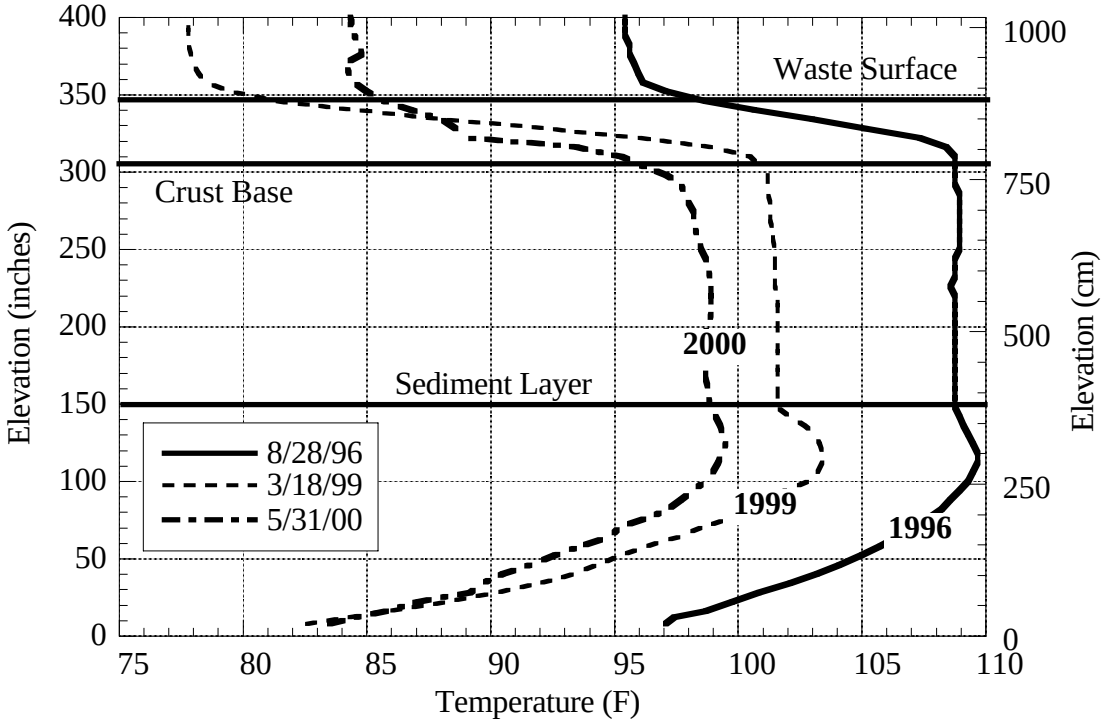

Figure A.1. Validation Probe Temperature Profiles for AN-103

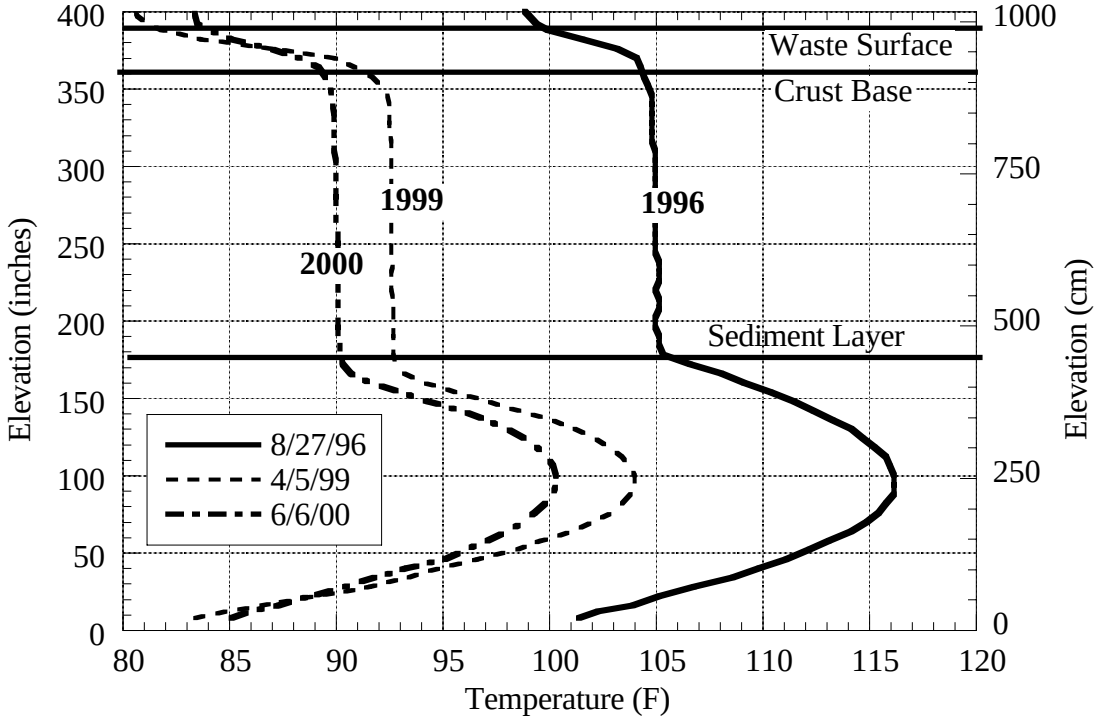

Figure A.2. Validation Probe Temperature Profiles for AN-104

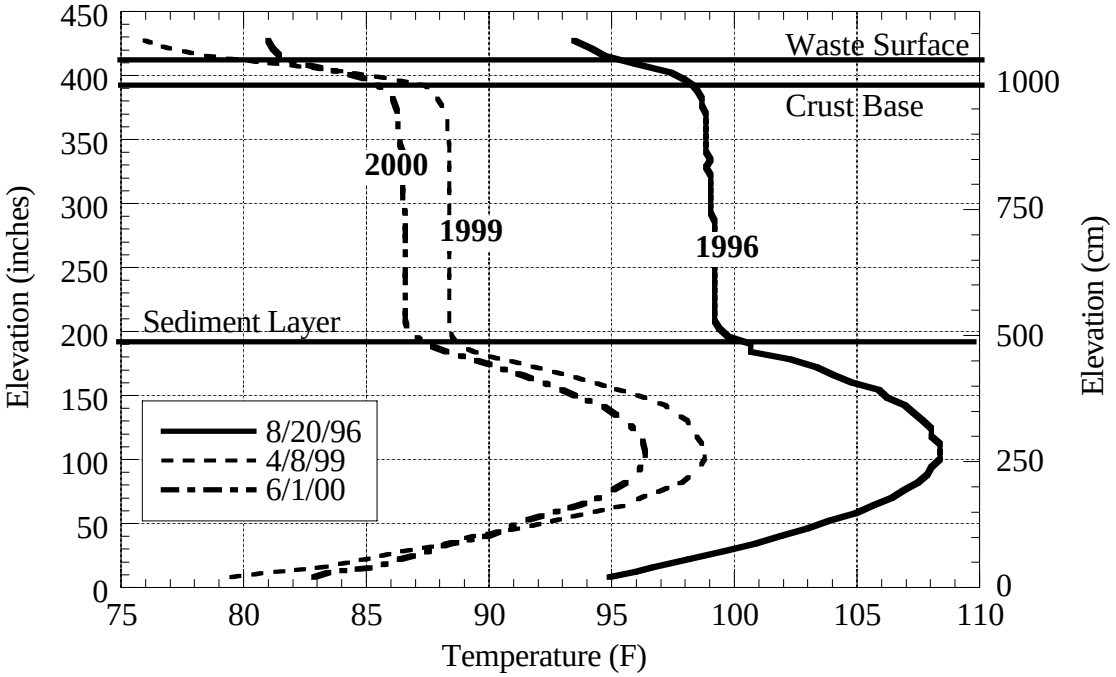

Figure A.3. Validation Probe Temperature Profiles for AN-105

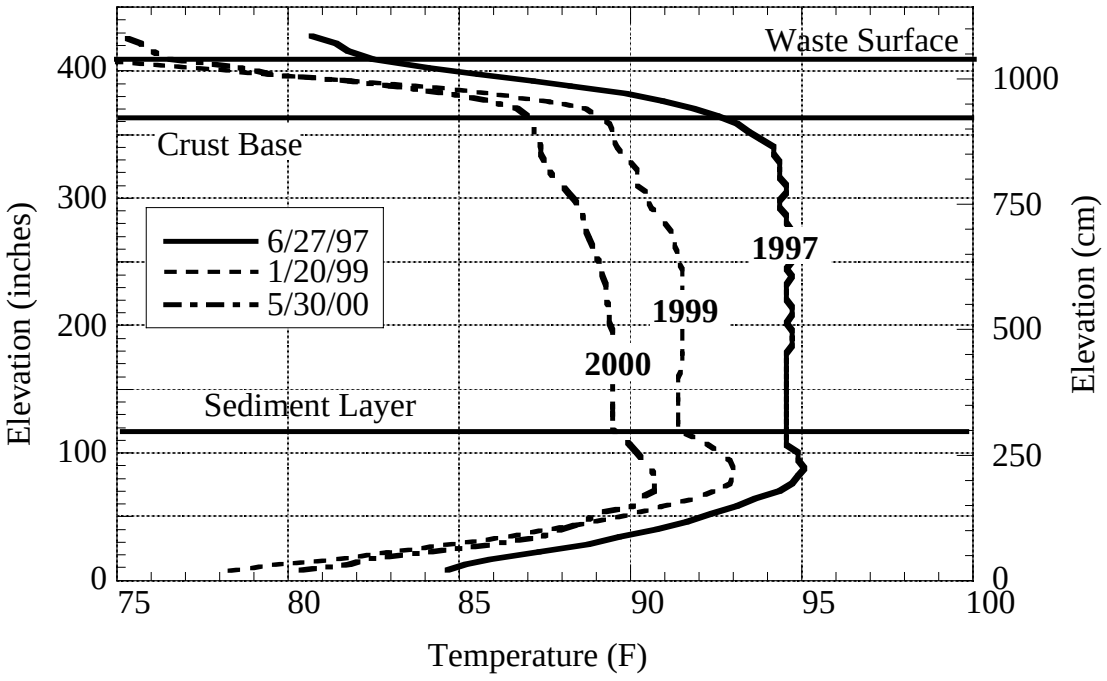

Figure A.4. Validation Probe Temperature Profiles for AW-101

All four tanks have cooled significantly since 1996 as a result of increased ventilation flow. The AN tank farm annulus flow rates were increased to approximately 200 cfm in mid-1995. Constant rate flow controllers were installed in the headspace ventilation system of AW-101 in mid-1996 and in AN-103, AN-104, and AN-105 in early 1997. These controllers increased the primary ventilation flow rate from 20–30 cfm to around 100 cfm (Hedengren et al. 2000).

Aside from the temperature decrease, the waste configuration has not changed significantly except in AW-101, where both the crust and the nonconvective layers appear to have become thicker. However, the lower portion of the crust evidently allows some convection, and the base of the "true" conductive crust is actually higher than in the earlier profile.

The temperature histories of the four tanks from 1990 to the present are shown in Figures A.5 through A.8. The temperature histories attempt to characterize the thermal behavior of the whole tank. Curves are plotted for thermocouples 1, 5, and 11 on the original thermocouple trees that are used in lieu of the MIT data, which were not available for most tanks until late 1996. The first thermocouple is at an elevation of 4 inches, corresponding to the very bottom of the nonconvective layer. The elevation of thermocouple 5 is 100 inches, corresponding to the central portion of the nonconvective layer, and thermocouple 11 is located in the convective liquid layer. Each of the tanks show a decreasing temperature trend of 5 to 7°C starting in mid-1995 that matches the change shown in the temperature profiles in Figures A.1 through A.4.

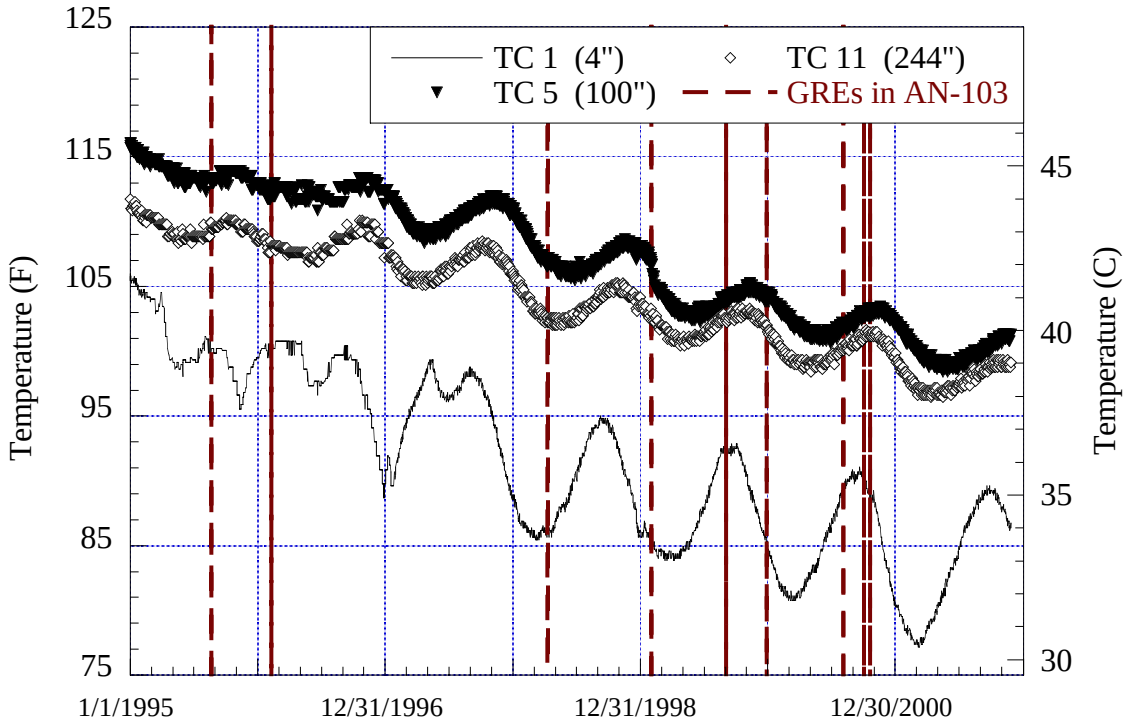

Figure A.5. AN-103 Temperature History

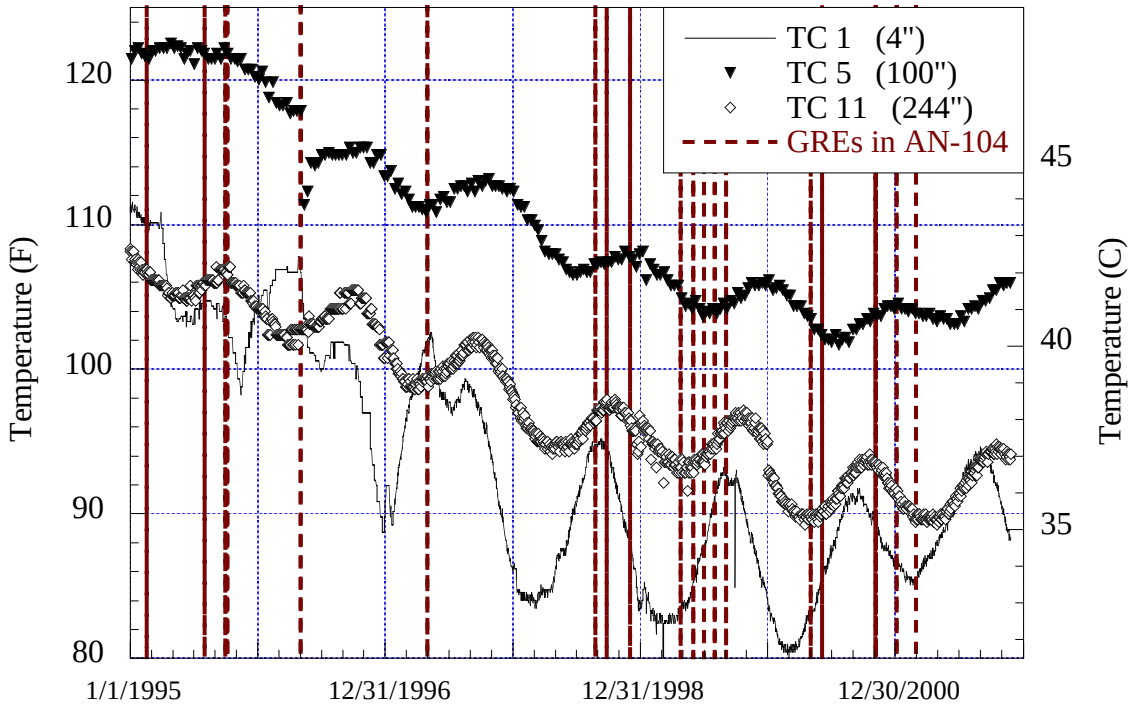

Figure A.6. AN-104 Temperature History

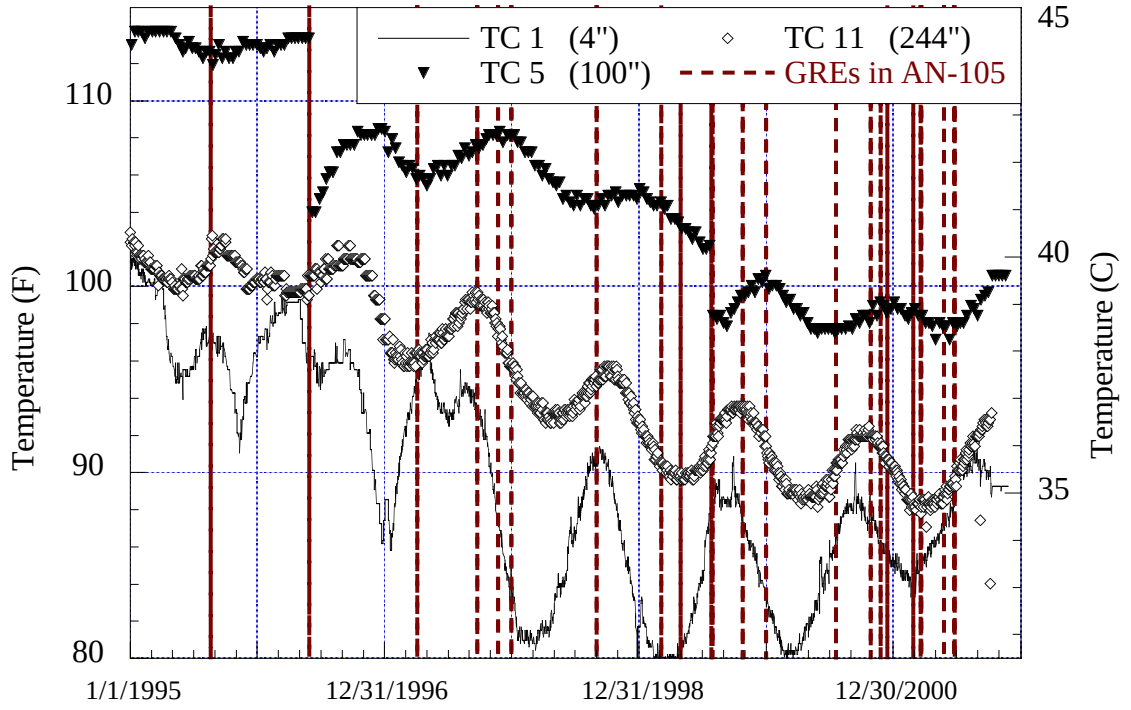

Figure A.7. AN-105 Temperature History

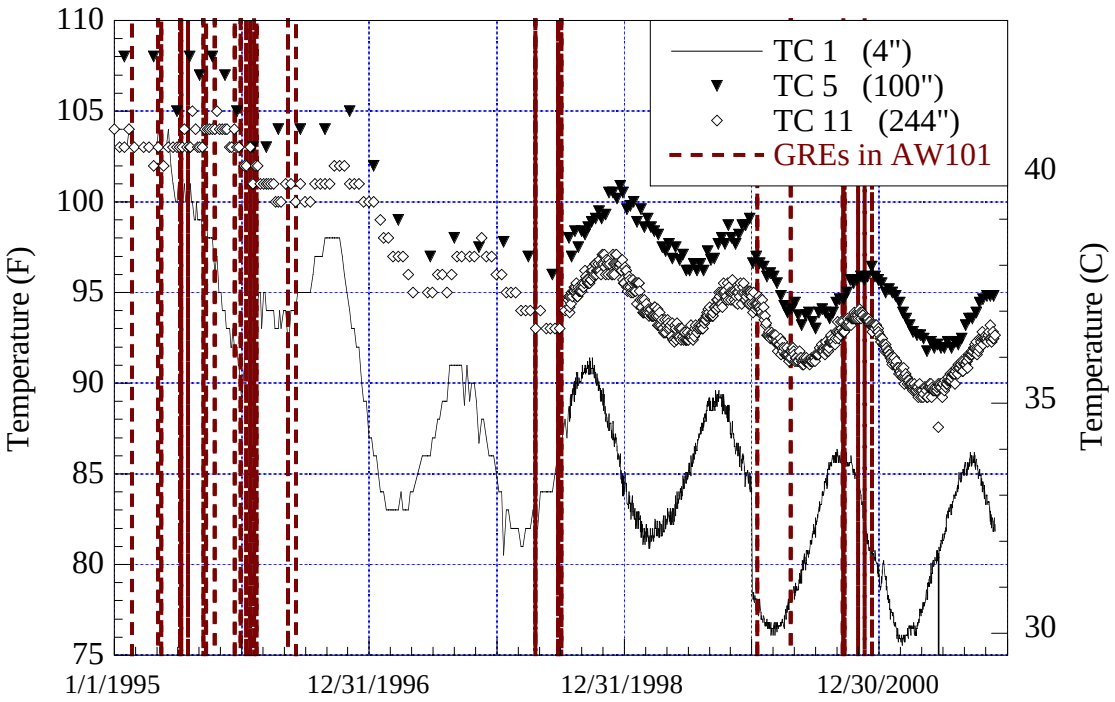

Figure A.8. AW-101 Temperature History

A.2 Waste Level History

The waste level histories in AN-103, AN-104, AN-105, and AW-101 from 1990 to December 31, 2001 are plotted in Figures A.9 through A.12, respectively. Occurrence of BDGREs as indicated by the SHMS data are also shown on the level plots.

In AN-103 a seasonal trend in level becomes more obvious with the increased ventilation flow and installation of the more precise Enraf® gauge (see Figure A.9). It also appears that the long-term level rise trend may have slowed or even reversed in about 1998. AN-104 shows a three-inch level drop since January 1996 and a discernable seasonal trend beginning in 1997 (see Figure A.10). The average level in AN-105 has dropped only about one inch with a similar seasonal trend showing up in 1997 (Figure A.11). There is no explanation for the "plateaus" occurring in February through April 1996, February and August through November 1997, and September through November 1998. The AW-101 level has also dropped about one inch and shows a seasonal variation beginning in the last half of 1996 (Figure A.12). Finally, note the change in data quality in 1994 and 1995, when the Enraf buoyancy gauge replaced the Food Instrument Corporation (FIC) contact probes.

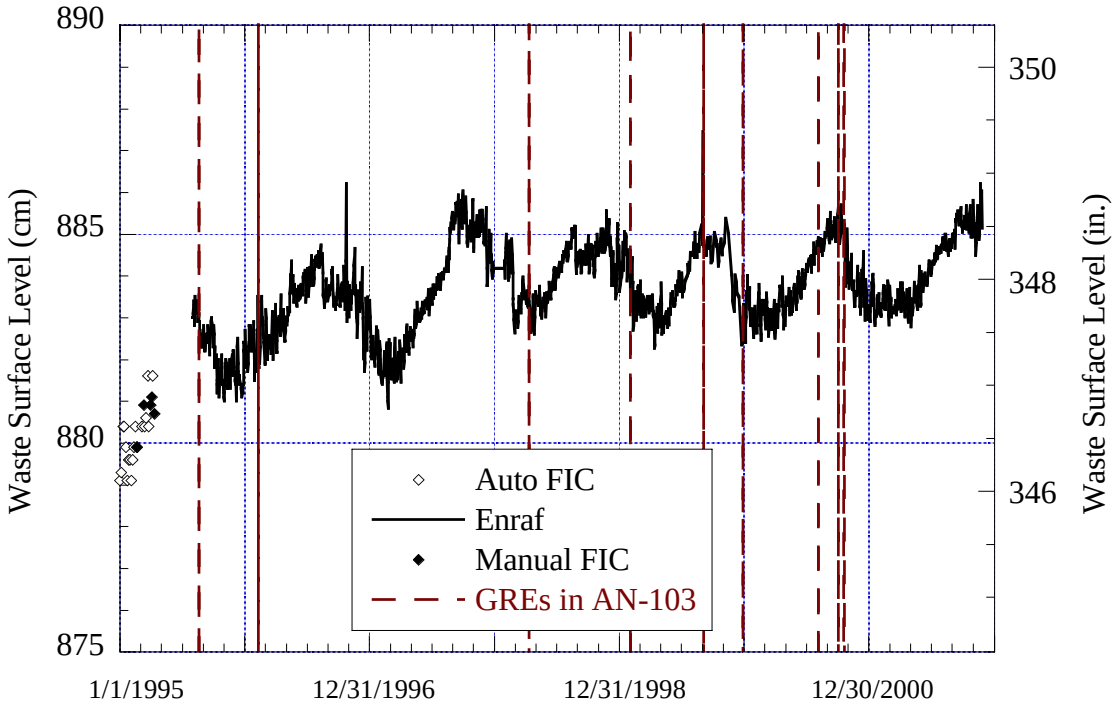

Figure A.9. AN-103 Level and GRE History

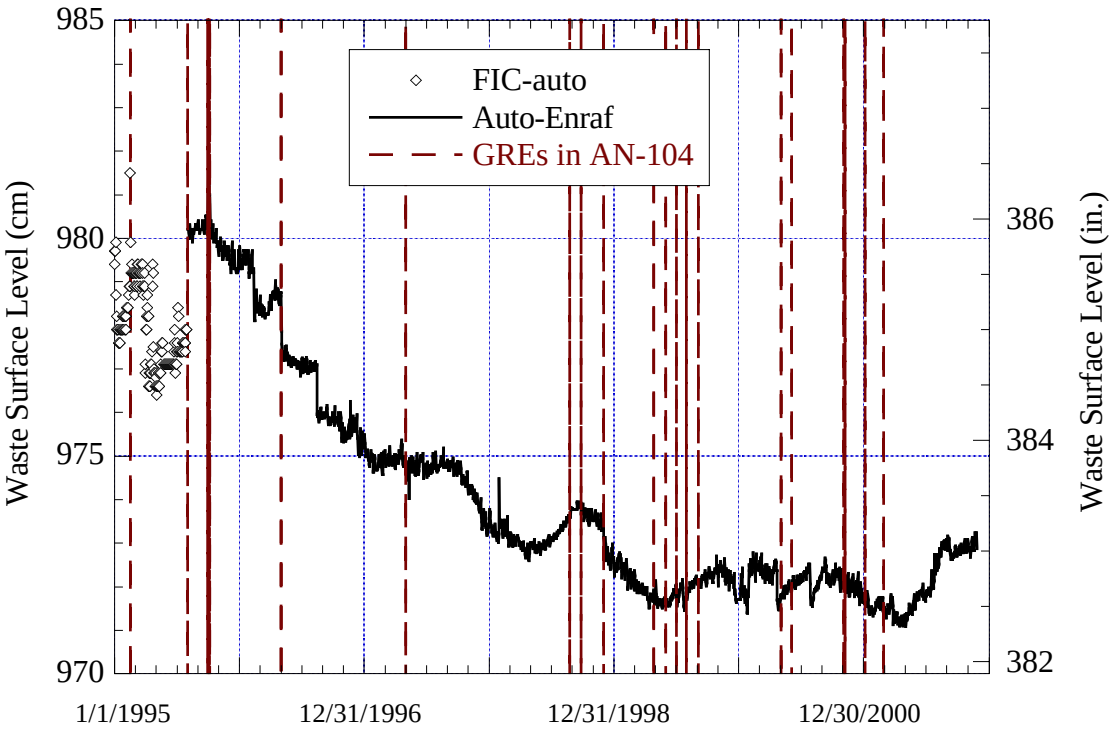

Figure A.10. AN-104 Level and GRE History

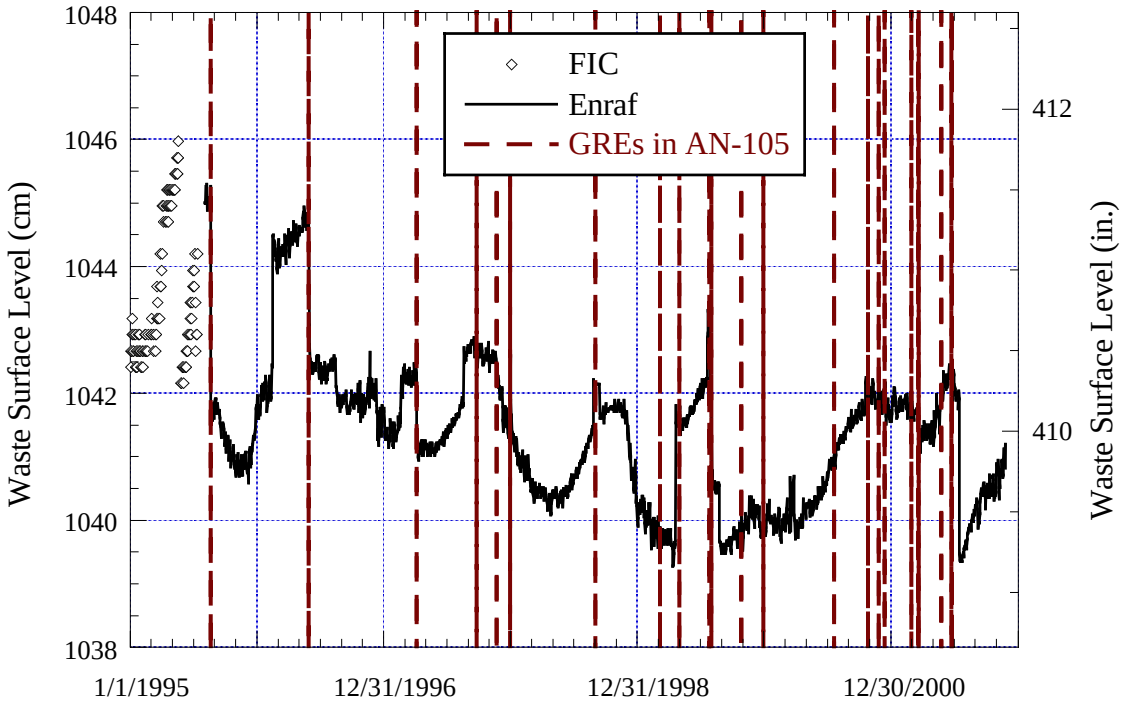

Figure A.11. AN-105 Level and GRE History

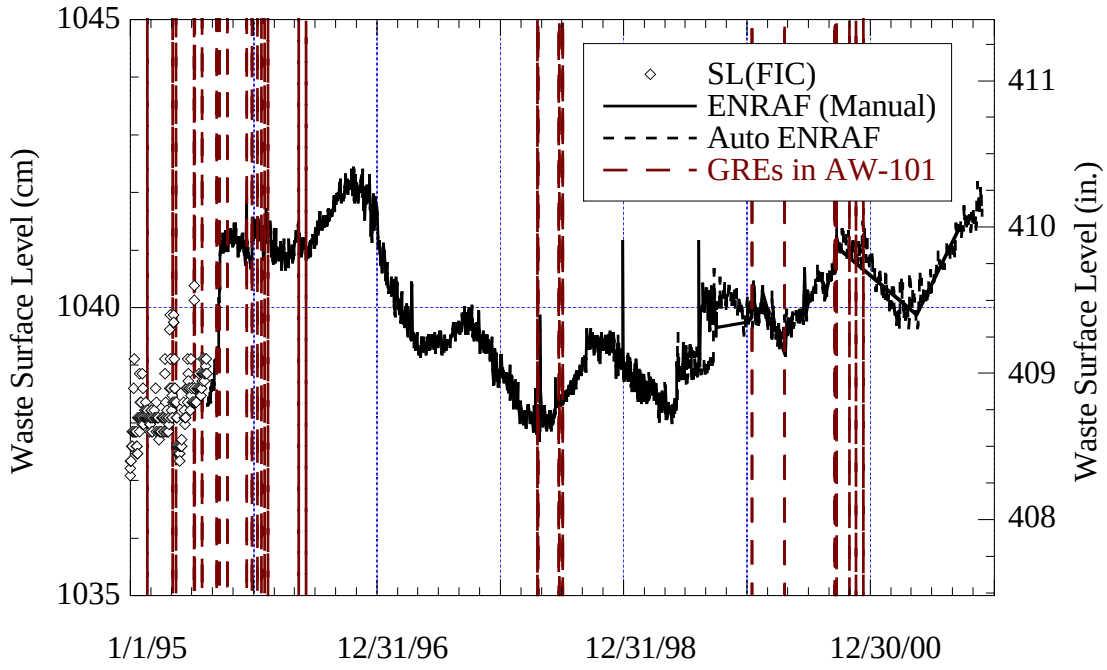

Figure A.12. AW-101 Level and GRE History

Appendix B
Determination of the Rise Distance of a Buoyant Gob

Appendix B
Determination of the Rise Distance of a Buoyant Gob

The distance a buoyant gob rises, h (Eq. 3.16 in the main report), is the distance the centroid of the participating gob may travel between its initial state in the sediment layer and its end state at neutral buoyancy at the surface. It is assumed that the gob is a right circular cylinder in shape and has an initial thickness of h_{G0} with the upper surface at the top of the sediment layer, as depicted in Figure B.1. Further, it is assumed that the gob does not release any gas prior to reaching its neutral buoyant position.

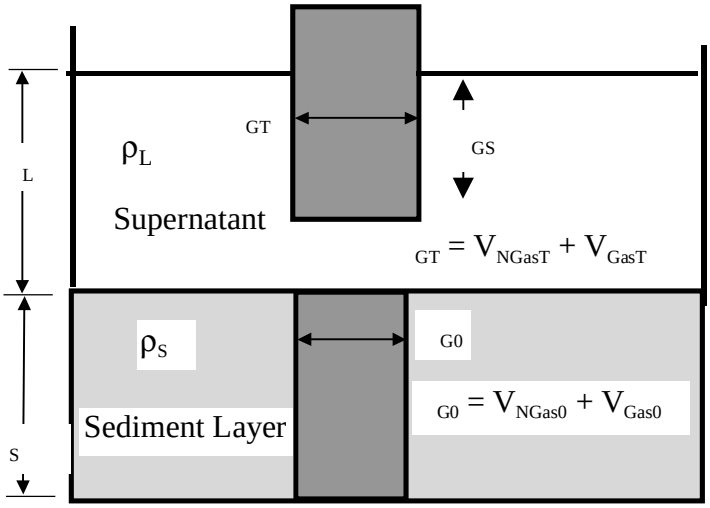

Figure B.1. Rise of Buoyant Gob

From Archimedes principle, the weight of liquid displaced by the submerged portion of the gob must equal its weight, or

$$\rho_L V_{GS} = \rho_{GT} V_{GT} \tag{B.1}$$

where V_{GS} is the submerged volume of the gob, ρ_L is the supernatant liquid density, and ρ_{GT} and V_{GT} are the density and volume of the gob at its end state, respectively. The height of the gob that is submerged is given by solving Eq. (B.1) for V_{GT} and dividing by the gob cross-sectional area:

$$h_{GS} = \frac{\rho_{GT}}{\rho_L}\frac{V_{GT}}{A_{GT}} = \frac{\rho_{GT}}{\rho_L} h_{GT} \tag{B.2}$$

where h_{GT} is the height of the gob at the waste surface. The volume of the gob at its end state at the waste surface is assumed to differ from its initial volume only by gas expansion due to reduction in hydrostatic pressure. This is expressed by

$$V_{GT} = V_{GasT} + V_{NGasT} = \frac{p_S}{p_{amb}} V_{G0}\alpha_0 + (1-\alpha_0)V_{G0} \tag{B.3}$$

where V_{GasT} and V_{NGasT} are the gas and non-gas volumes of the gob at the waste surface, V_{G0} is the initial total gob volume, α_0 is the initial volumetric gas fraction in the gob, p_S is the average pressure of the gas in the sediment layer, and p_{amb} is the ambient headspace pressure (essentially one atmosphere). The density of the gob at the waste surface may be expressed as follows, using conservation of mass between the two states:

$$\rho_{GT} = \left(1 - \frac{\left(\frac{p_S}{P_{amb}}\right) V_{G0}\alpha_0}{\left(\frac{p_S}{p_{amb}}\right) V_{G0}\alpha_0 + (1-\alpha_0)V_{G0}} \right) \rho_S \tag{B.4}$$

where ρ_S is the sediment layer density.

The expansion of the gob as it rises from its initial position to its neutrally buoyant position is assumed to occur both in the horizontal and vertical directions such that the aspect ratio of the gob remains constant. The ratio of the diameter of the gob to its height at the waste surface is then given by

$$\frac{D_{GT}}{h_{GT}} = \frac{D_{G0}}{h_{G0}} \tag{B.5}$$

where D_{GT} and D_{G0} denote the gob diameter at the waste surface initially. From Eq. (B.3) and (B.5), the height of the gob at the surface can be computed by

$$h_{GT} = h_{G0}\left[\frac{p_S}{P_{amb}}\alpha_0 + (1-\alpha_0) \right]^{\frac{1}{3}} \tag{B.6}$$

The gob submergence at the surface can then be determined from Eq. (B.2), (B.4), and (B.6):

$$h_{GS} = \frac{\rho_S}{\rho_L} h_{G0}\left(\frac{p_S}{p_{amb}}\alpha_0 + (1-\alpha_0) \right)^{-\frac{2}{3}} (1-\alpha_0) \tag{B.7}$$

The elevation of the gob centroid at its end state is computed by

$$h = \frac{h_{G0}}{2} + h_{LGT} + \frac{h_{GT}}{2} - h_{GS} \tag{B.8}$$

The height of the supernate (h_{LGT}) after the gob has risen to the waste surface is necessarily the initial height plus the increase due to gob expansion minus the decrease due to the gob no longer being completely submerged. However, for the tanks under consideration, this effect contributes approximately 0.01% to the total distance the gob may travel. It is therefore neglected, and h_L (supernate depth) is used without modification. Substituting Eq. (B.6) and (B.7) into Eq. (B.8), the distance a buoyant gob rises is given as

$$h = h_L + h_{G0}\left\{\frac{1}{2} + \frac{1}{2}\left[\frac{p_S}{p_{amb}}\alpha_0 + (1-\alpha_0)\right]^{\frac{1}{3}} - \frac{\rho_{NCL}}{\rho_L}(1-\alpha_0)\left[\frac{p_S}{p_{amb}}\alpha_0 + (1-\alpha_0)\right]^{-\frac{2}{3}}\right\} \qquad \text{(B.9)}$$

Appendix C
Model Parameter Probability Distributions

Appendix C
Model Parameter Probability Distributions

C.1 Introduction to Model Parameter Probability Distributions

The shape and summary statistics for the input parameter distributions presented in Section 3.2 of the report are shown in the following sections for each tank evaluated. The shape is depicted by a histogram with an accompanying outlier box plot, while the summary statistics are listed in the text portion of each description. The summary statistics comprise several quantiles across each distribution: the mean, standard deviation, standard error of the mean, upper and lower 95% confidence intervals around the mean, and the total number of observations used for that particular input distribution. Tank AN-103 is presented in Section C.2, AN-104 in Section C.3, AN-105 in Section C.4, and AW-101 in Section C.5.

The histogram serves as a visual explanation for the shape of data. Each bar shows the frequency of occurrence of the value or range of values represented on the abscissa, which is separated into intervals. Through observation of a histogram plot, one may quickly ascertain the general shape as normal (Gaussian), skewed, uniform, bimodal, etc. For example, the histogram for the total waste thickness in AN-103 shows a normal distribution (Figure C.2.4), while the histogram for the crust thickness in AN-103 shows a uniform distribution (Figure C.2.3). The apparent deviations from the distributions listed in Table 3.4 of the main document are caused by the imposed constraints presented in Section 3.2. The sediment and liquid layer density distributions clearly illustrate this effect. Measured values for these parameters indicate that they may be approximated by a normal distribution, as specified in Table 3.4. However, by constraining the waste configuration with the inferred gas volume (Section 3.2.2), bimodal distributions of these parameters are generated.

Accompanying the histogram is an outlier box plot. The outlier box plot is a schematic that lets one see the sample distribution and identify points with extreme values, or outliers, that cannot be so easily seen on the histogram due to small numbers of points at the tails. The ends of the box are the 25th and 75th quantiles, also called the quartiles. The difference between these two quartiles is called the interquartile range. The line across the middle identifies the median. The ends of the whiskers are the outermost data points from their respective quartiles that fall within the distance computed as 1.5 times the interquartile range. These outer points are very evident on the outlier box plot for the AN-103 total waste thickness example. These outer points, however, are not easily seen in the histogram. Thus, both plots together (the histogram and the outlier box plot) provide a more complete picture of the distribution. The bracket along the edge of the box identifies the shortest half of the distribution, which is the densest 50% of the observations.

The quantiles shown below each histogram are values that divide a distribution into two groups where the Pth quantile is larger than P% of the values. For example, 97.5% of the data fall at or below 8.9031 in the AN-103 total waste thickness distribution. The 50^{th} quantile is also

the median, where half of the data fall at or below that number. In the AN-103 total waste thickness distribution, the median is 8.84.

The mean is the average of the data. If a distribution is symmetric, then the mean will be equivalent to the median. In the AN-103 total waste thickness example, the mean and median are equal. However, if a distribution is skewed, the mean will be pulled in the direction of the extreme values. This occurs in the AN-103 time to the peak gas release rate distribution (Figure C.2.11). This is an obviously skewed distribution where the median is 11.18 while the mean is 25.51. Clearly, the mean is being pulled by the extreme values in the right tail of the distribution, skewing the mean of the distribution to the right. Therefore, the time to the peak gas release rate is a "skewed right" distribution. For this reason, it is best to use the median as a measure of central tendency as opposed to the mean, as the mean will be biased to the right.

The standard deviation shows the spread of the data around the mean and is calculated by

$$\sigma = \sqrt{\frac{\sum_{i=1}^{n}(y_i - y_A)^2}{(N-1)}} \tag{C.1}$$

where y is each observation, y_A is the mean of the observations, and N is the total number of observations.

The standard error of the mean estimates the standard deviation of a distribution of means, each calculated from a sample size of N. In other words, it represents how much the mean will vary if this sample was run repeatedly. This is the standard deviation of all the means that would result if the same simulation were run many times, and is calculated by

$$SEM = \frac{\sigma}{\sqrt{N-1}} \tag{C.2}$$

The standard error of the mean is used to calculate the upper and lower 95% confidence intervals around the mean. If we repeatedly sample from this population and constructed confidence intervals, 95% of the intervals would contain the true population mean. The formula to determine the upper and lower 95% confidence interval for the mean is

$$CI_m = y_A \pm t \cdot SEM \tag{C.3}$$

where t is the student's t-value.

C.2 AN-103 Input Distributions

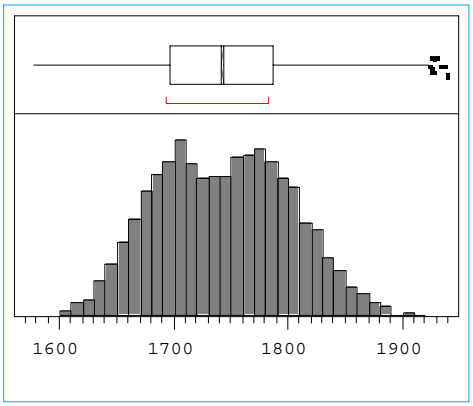

Figure C.2.1. Sediment Density, ρ_S (kg/m^3)

Quantiles		
maximum	100.0%	1939.5
	99.5%	1903.3
	97.5%	1864.0
	90.0%	1823.2
quartile	75.0%	1788.0
median	50.0%	1743.5
quartile	25.0%	1697.5
	10.0%	1666.0
	2.5%	1635.1
	0.5%	1609.0
minimum	0.0%	1577.9

Moments	
Mean	1744.04
Std Dev	60.98
Std Error Mean	0.61
Upper 95% Mean	1745.24
Lower 95% Mean	1742.85
N	10000.00
Sum Weights	10000.00

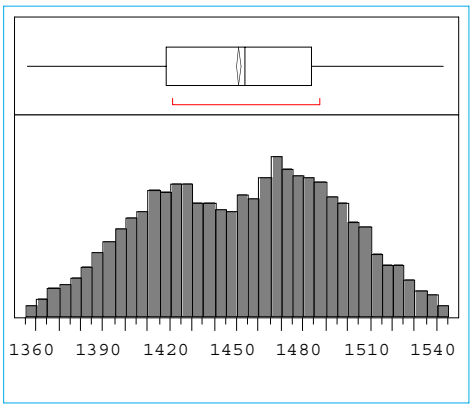

Figure C.2.2. Supernatant Liquid Density, ρ_L (kg/m^3)

Quantiles		
maximum	100.0%	1543.9
	99.5%	1539.9
	97.5%	1528.3
	90.0%	1506.9
quartile	75.0%	1484.5
median	50.0%	1454.1
quartile	25.0%	1418.4
	10.0%	1394.8
	2.5%	1372.4
	0.5%	1360.4
minimum	0.0%	1356.2

Moments	
Mean	1451.77
Std Dev	42.30
Std Error Mean	0.42
Upper 95% Mean	1452.60
Lower 95% Mean	1450.94
N	10000.00
Sum Weights	10000.00

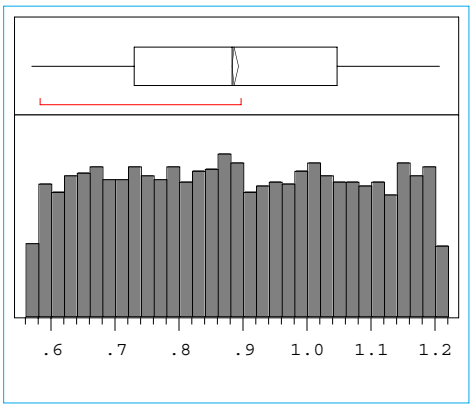

Figure C.2.3. Crust Thickness, h_C (m)

Quantiles		
maximum	100.0%	1.2100
	99.5%	1.2075
	97.5%	1.1945
	90.0%	1.1490
quartile	75.0%	1.0479
median	50.0%	0.8857
quartile	25.0%	0.7306
	10.0%	0.6360
	2.5%	0.5861
	0.5%	0.5724
minimum	0.0%	0.5701

Moments	
Mean	0.89
Std Dev	0.18
Std Error Mean	0.00
Upper 95% Mean	0.89
Lower 95% Mean	0.89
N	10000.00
Sum Weights	10000.00

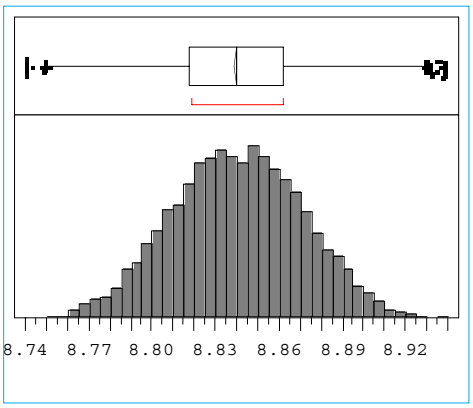

Figure C.2.4. Total Waste Thickness, h_T (m)

Quantiles		
maximum	100.0%	8.9390
	99.5%	8.9224
	97.5%	8.9031
	90.0%	8.8818
quartile	75.0%	8.8623
median	50.0%	8.8401
quartile	25.0%	8.8180
	10.0%	8.7985
	2.5%	8.7761
	0.5%	8.7582
minimum	0.0%	8.7410

Moments	
Mean	8.84
Std Dev	0.03
Std Error Mean	0.00
Upper 95% Mean	8.84
Lower 95% Mean	8.84
N	10000.00
Sum Weights	10000.00

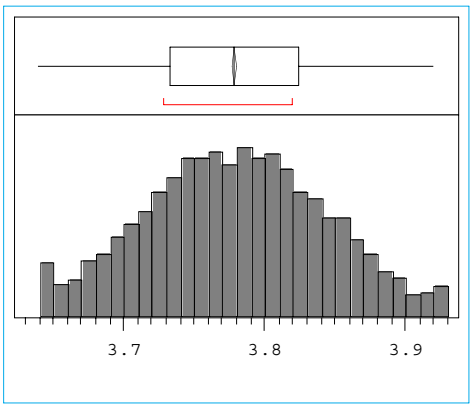

Figure C.2.5. Sediment Thickness, h_S (m)

Quantiles		
maximum	100.0%	3.9200
	99.5%	3.9200
	97.5%	3.9061
	90.0%	3.8653
quartile	75.0%	3.8245
median	50.0%	3.7792
quartile	25.0%	3.7333
	10.0%	3.6931
	2.5%	3.6552
	0.5%	3.6400
minimum	0.0%	3.6400

Moments	
Mean	3.78
Std Dev	0.06
Std Error Mean	0.00
Upper 95% Mean	3.78
Lower 95% Mean	3.78
N	10000.00
Sum Weights	10000.00

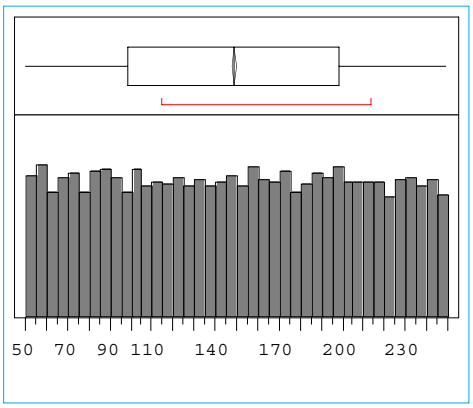

Figure C.2.6. Sediment Yield Stress, τ_y (Pa)

Quantiles		
maximum	100.0%	249.92
	99.5%	248.80
	97.5%	244.36
	90.0%	229.54
quartile	75.0%	199.09
median	50.0%	149.60
quartile	25.0%	99.34
	10.0%	69.39
	2.5%	54.86
	0.5%	51.00
minimum	0.0%	50.03

Moments	
Mean	149.35
Std Dev	57.68
Std Error Mean	0.58
Upper 95% Mean	150.48
Lower 95% Mean	148.22
N	10000.00
Sum Weights	10000.00

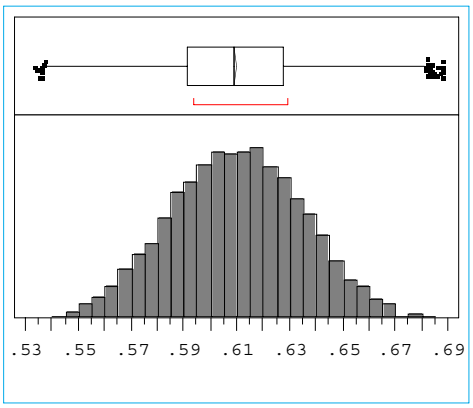

Figure C.2.7. Hydrogen Concentration in Gas Stored in Sediment Layer, χ_H

Quantiles		
maximum	100.0%	0.68800
	99.5%	0.67648
	97.5%	0.66048
	90.0%	0.64280
quartile	75.0%	0.62781
median	50.0%	0.60992
quartile	25.0%	0.59193
	10.0%	0.57621
	2.5%	0.55977
	0.5%	0.54774
minimum	0.0%	0.53334

Moments	
Mean	0.61
Std Dev	0.03
Std Error Mean	0.00
Upper 95% Mean	0.61
Lower 95% Mean	0.61
N	10000.00
Sum Weights	10000.00

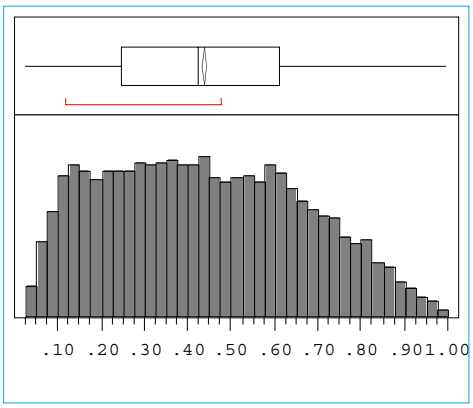

Figure C.2.8. Fraction of Released Sediment Material that Remains Suspended in the Supernate

Quantiles		
maximum	100.0%	0.99941
	99.5%	0.96160
	97.5%	0.88491
	90.0%	0.76348
quartile	75.0%	0.61500
median	50.0%	0.42727
quartile	25.0%	0.24882
	10.0%	0.13653
	2.5%	0.07337
	0.5%	0.04084
minimum	0.0%	0.02508

Moments	
Mean	0.44
Std Dev	0.23
Std Error Mean	0.00
Upper 95% Mean	0.44
Lower 95% Mean	0.44
N	10000.00
Sum Weights	10000.00

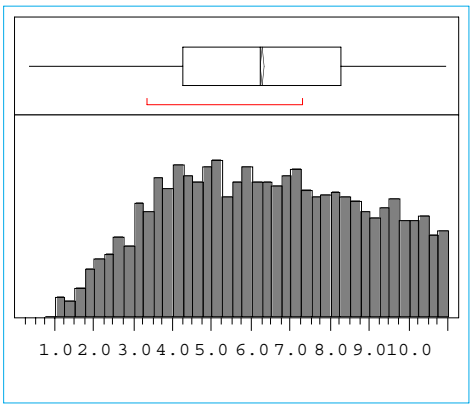

Figure C.2.9. Gob Diameter

Quantiles		
maximum	100.0%	11.000
	99.5%	10.938
	97.5%	10.687
	90.0%	9.842
quartile	75.0%	8.339
median	50.0%	6.261
quartile	25.0%	4.317
	10.0%	3.048
	2.5%	1.880
	0.5%	1.147
minimum	0.0%	0.363

Moments	
Mean	6.33
Std Dev	2.50
Std Error Mean	0.02
Upper 95% Mean	6.37
Lower 95% Mean	6.28
N	10000.00
Sum Weights	10000.00

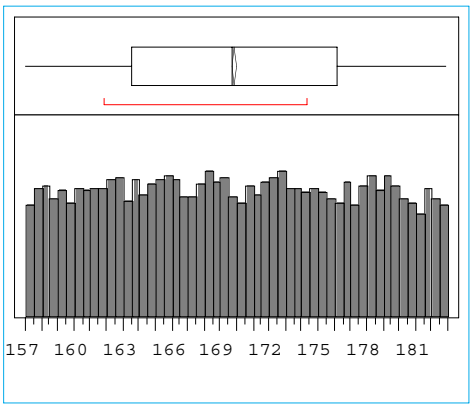

Figure C.2.10. Initial Gas Volume in Sediment Layer, V_{G0} (m^3)

Quantiles		
maximum	100.0%	183.00
	99.5%	182.84
	97.5%	182.28
	90.0%	180.18
quartile	75.0%	176.27
median	50.0%	169.81
quartile	25.0%	163.57
	10.0%	159.75
	2.5%	157.70
	0.5%	157.17
minimum	0.0%	157.00

Moments	
Mean	169.91
Std Dev	7.40
Std Error Mean	0.07
Upper 95% Mean	170.06
Lower 95% Mean	169.77
N	10000.00
Sum Weights	10000.00

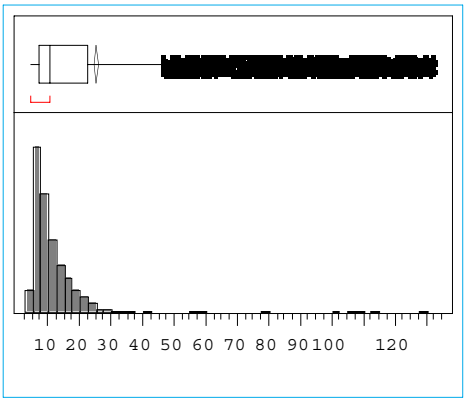

Figure C.2.11. Time to Peak Gas Release Rate, τ (min)

Quantiles		
maximum	100.0%	132.61
	99.5%	129.66
	97.5%	120.04
	90.0%	82.69
quartile	75.0%	22.88
median	50.0%	11.18
quartile	25.0%	7.23
	10.0%	5.60
	2.5%	4.91
	0.5%	4.74
minimum	0.0%	4.70

Moments	
Mean	25.51
Std Dev	31.87
Std Error Mean	0.32
Upper 95% Mean	26.13
Lower 95% Mean	24.88
N	10000.00
Sum Weights	10000.00

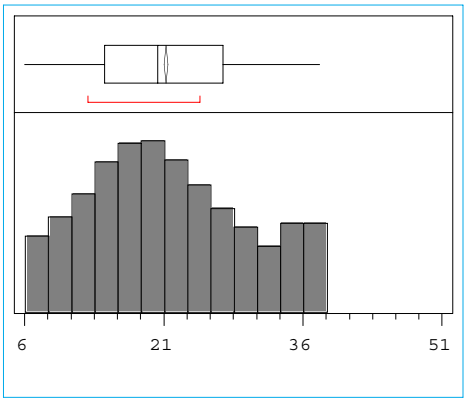

Figure C.2.12. Time to the Peak Gas Release Rate for Mixer pump Operations, τ_p (min)

Quantiles		
maximum	100.0%	37.994
	99.5%	37.824
	97.5%	37.124
	90.0%	34.549
quartile	75.0%	27.494
median	50.0%	20.529
quartile	25.0%	14.852
	10.0%	10.208
	2.5%	7.282
	0.5%	6.287
minimum	0.0%	6.019

Moments	
Mean	21.34
Std Dev	8.44
Std Error Mean	0.08
Upper 95% Mean	21.50
Lower 95% Mean	21.17
N	10000.00
Sum Weights	10000.00

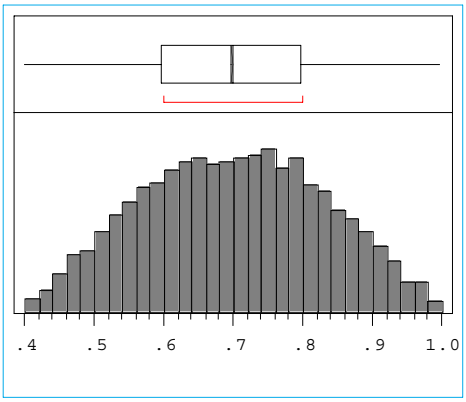

Figure C.2.13. Fraction of Solids Mobilized by the Pump that Remain Suspended, FP

Quantiles		
maximum	100.0%	0.99970
	99.5%	0.98083
	97.5%	0.94395
	90.0%	0.87796
quartile	75.0%	0.79850
median	50.0%	0.70075
quartile	25.0%	0.59908
	10.0%	0.52281
	2.5%	0.45634
	0.5%	0.41750
minimum	0.0%	0.40019

Moments	
Mean	0.70
Std Dev	0.13
Std Error Mean	0.00
Upper 95% Mean	0.70
Lower 95% Mean	0.70
N	10000.00
Sum Weights	10000.00

C.3 AN-104 Input Distributions

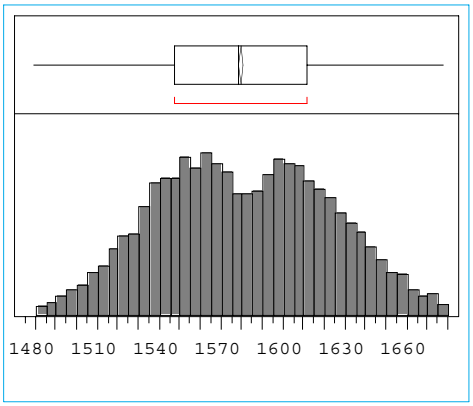

Figure C.3.1. Sediment Density, ρ_S (kg/m^3)

Quantiles		
maximum	100.0%	1678.8
	99.5%	1674.6
	97.5%	1660.8
	90.0%	1636.9
quartile	75.0%	1612.0
median	50.0%	1579.4
quartile	25.0%	1548.3
	10.0%	1525.0
	2.5%	1500.9
	0.5%	1486.0
minimum	0.0%	1479.7

Moments	
Mean	1580.34
Std Dev	42.41
Std Error Mean	0.42
Upper 95% Mean	1581.17
Lower 95% Mean	1579.50
N	10000.00
Sum Weights	10000.00

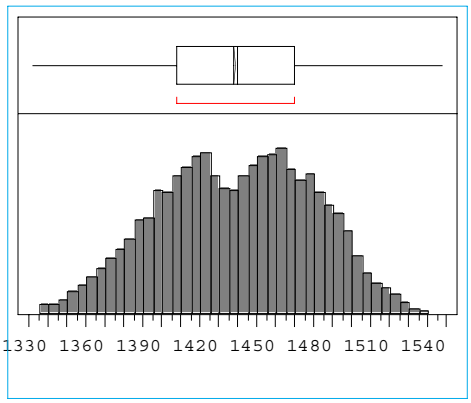

Figure C.3.2. Supernatant Liquid Density, ρ_L (kg/m^3)

Quantiles		
maximum	100.0%	1547.9
	99.5%	1531.8
	97.5%	1514.9
	90.0%	1492.1
quartile	75.0%	1470.3
median	50.0%	1440.3
quartile	25.0%	1408.1
	10.0%	1383.2
	2.5%	1358.0
	0.5%	1340.2
minimum	0.0%	1332.3

Moments	
Mean	1438.66
Std Dev	41.63
Std Error Mean	0.42
Upper 95% Mean	1439.48
Lower 95% Mean	1437.84
N	10000.00
Sum Weights	10000.00

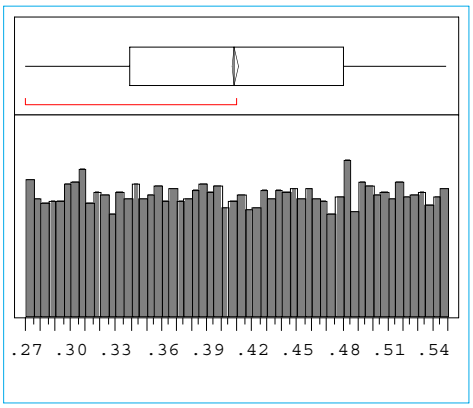

Figure C.3.3. Crust Thickness, h_C (m)

Quantiles		
maximum	100.0%	0.54994
	99.5%	0.54854
	97.5%	0.54340
	90.0%	0.52172
quartile	75.0%	0.48120
median	50.0%	0.40968
quartile	25.0%	0.33975
	10.0%	0.29796
	2.5%	0.27639
	0.5%	0.27134
minimum	0.0%	0.27001

Moments	
Mean	0.41
Std Dev	0.08
Std Error Mean	0.00
Upper 95% Mean	0.41
Lower 95% Mean	0.41
N	10000.00
Sum Weights	10000.00

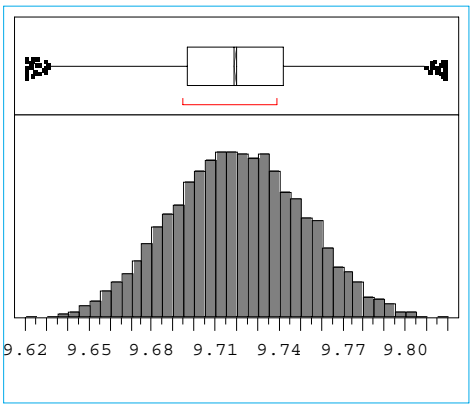

Figure C.3.4. Total Waste Thickness, h_T (m)

Quantiles		
maximum	100.0%	9.8190
	99.5%	9.8044
	97.5%	9.7849
	90.0%	9.7618
quartile	75.0%	9.7424
median	50.0%	9.7199
quartile	25.0%	9.6978
	10.0%	9.6777
	2.5%	9.6566
	0.5%	9.6372
minimum	0.0%	9.6210

Moments	
Mean	9.72
Std Dev	0.03
Std Error Mean	0.00
Upper 95% Mean	9.72
Lower 95% Mean	9.72
N	10000.00
Sum Weights	10000.00

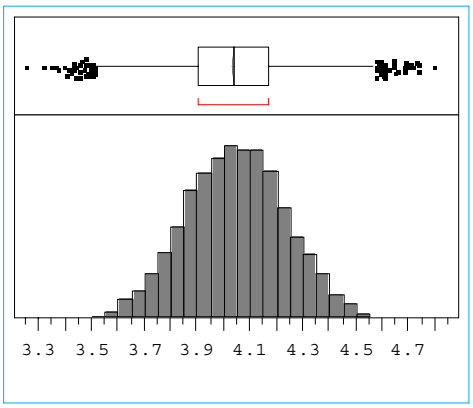

Figure C.3.5. Sediment Thickness, h_S (m)

Quantiles		
maximum	100.0%	4.8008
	99.5%	4.5501
	97.5%	4.4320
	90.0%	4.2992
quartile	75.0%	4.1760
median	50.0%	4.0458
quartile	25.0%	3.9105
	10.0%	3.7929
	2.5%	3.6572
	0.5%	3.5383
minimum	0.0%	3.2573

Moments	
Mean	4.04
Std Dev	0.20
Std Error Mean	0.00
Upper 95% Mean	4.05
Lower 95% Mean	4.04
N	10000.00
Sum Weights	10000.00

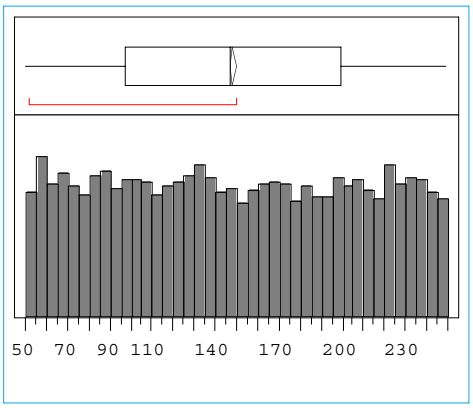

Figure C.3.6. Sediment Yield Stress, τ_y (Pa)

Quantiles		
maximum	100.0%	249.98
	99.5%	248.89
	97.5%	244.39
	90.0%	229.68
quartile	75.0%	199.83
median	50.0%	147.78
quartile	25.0%	98.42
	10.0%	68.96
	2.5%	55.31
	0.5%	51.07
minimum	0.0%	50.01

Moments	
Mean	148.94
Std Dev	57.98
Std Error Mean	0.58
Upper 95% Mean	150.07
Lower 95% Mean	147.80
N	10000.00
Sum Weights	10000.00

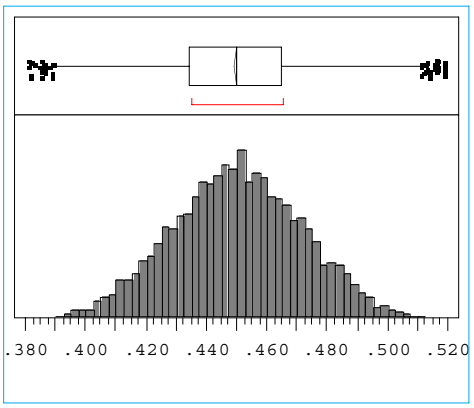

Figure C.3.7. Hydrogen Concentration in Gas Stored in Sediment Layer, χ_H

Quantiles		
maximum	100.0%	0.51900
	99.5%	0.50849
	97.5%	0.49427
	90.0%	0.47931
quartile	75.0%	0.46540
median	50.0%	0.45009
quartile	25.0%	0.43501
	10.0%	0.42108
	2.5%	0.40627
	0.5%	0.39312
minimum	0.0%	0.38100

Moments	
Mean	0.45
Std Dev	0.02
Std Error Mean	0.00
Upper 95% Mean	0.45
Lower 95% Mean	0.45
N	10000.00
Sum Weights	10000.00

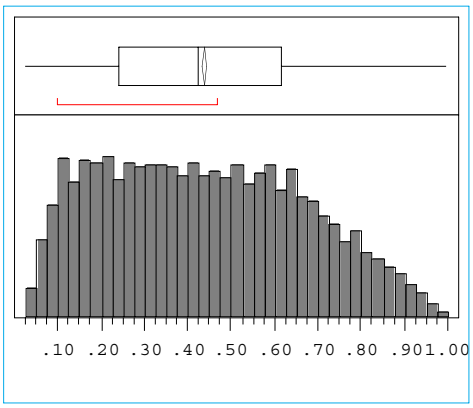

Figure C.3.8. Fraction of Released Sediment Material that Remains Suspended in the Supernate

Quantiles		
maximum	100.0%	0.99878
	99.5%	0.95641
	97.5%	0.88801
	90.0%	0.76554
quartile	75.0%	0.61811
median	50.0%	0.42733
quartile	25.0%	0.24440
	10.0%	0.13574
	2.5%	0.07304
	0.5%	0.04158
minimum	0.0%	0.02580

Moments	
Mean	0.44
Std Dev	0.23
Std Error Mean	0.00
Upper 95% Mean	0.44
Lower 95% Mean	0.43
N	10000.00
Sum Weights	10000.00

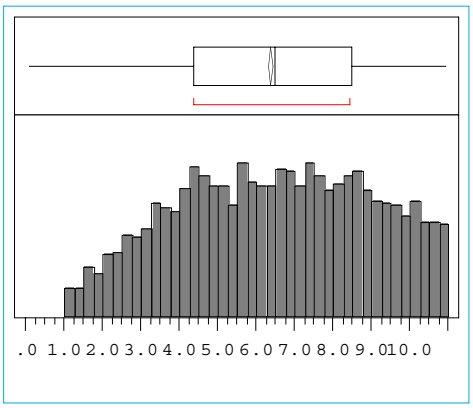

Figure C.3.9. Gob Diameter

Quantiles		
maximum	100.0%	10.997
	99.5%	10.938
	97.5%	10.706
	90.0%	9.893
quartile	75.0%	8.505
median	50.0%	6.511
quartile	25.0%	4.430
	10.0%	2.931
	2.5%	1.698
	0.5%	1.099
minimum	0.0%	0.135

Moments	
Mean	6.43
Std Dev	2.54
Std Error Mean	0.03
Upper 95% Mean	6.48
Lower 95% Mean	6.38
N	10000.00
Sum Weights	10000.00

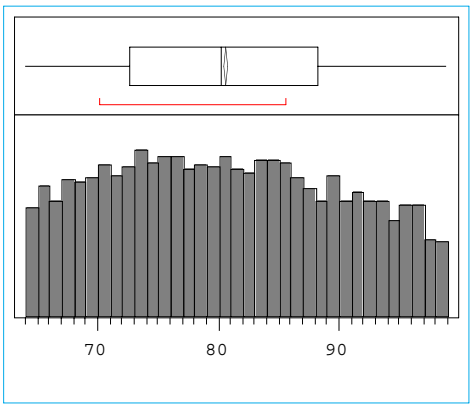

Figure C.3.10. Initial Gas Volume in Sediment Layer, V_{G0} (m^3)

Quantiles		
maximum	100.0%	98.994
	99.5%	98.689
	97.5%	97.504
	90.0%	94.109
quartile	75.0%	88.393
median	50.0%	80.322
quartile	25.0%	72.740
	10.0%	67.806
	2.5%	65.076
	0.5%	64.240
minimum	0.0%	64.001

Moments	
Mean	80.63
Std Dev	9.49
Std Error Mean	0.09
Upper 95% Mean	80.82
Lower 95% Mean	80.44
N	10000.00
Sum Weights	10000.00

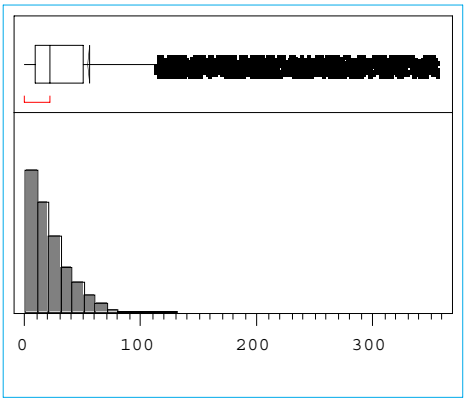

Figure C.3.11. Time to Peak Gas Release Rate, τ (min)

Quantiles		
maximum	100.0%	355.90
	99.5%	347.48
	97.5%	318.22
	90.0%	194.14
quartile	75.0%	51.58
median	50.0%	22.72
quartile	25.0%	9.77
	10.0%	4.04
	2.5%	1.75
	0.5%	1.21
minimum	0.0%	1.02

Moments	
Mean	56.52
Std Dev	82.66
Std Error Mean	0.83
Upper 95% Mean	58.14
Lower 95% Mean	54.90
N	10000.00
Sum Weights	10000.00

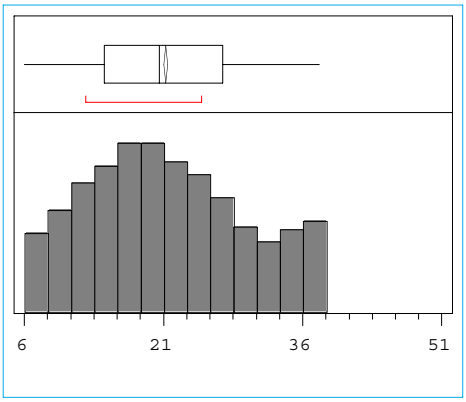

Figure C.3.12. Time to the Peak Gas Release Rate for Mixer Pump Operations, τ_p (min)

Quantiles		
maximum	100.0%	37.999
	99.5%	37.799
	97.5%	37.174
	90.0%	34.496
quartile	75.0%	27.393
median	50.0%	20.593
quartile	25.0%	14.817
	10.0%	10.115
	2.5%	7.254
	0.5%	6.283
minimum	0.0%	6.002

Moments	
Mean	21.33
Std Dev	8.44
Std Error Mean	0.08
Upper 95% Mean	21.49
Lower 95% Mean	21.16
N	10000.00
Sum Weights	10000.00

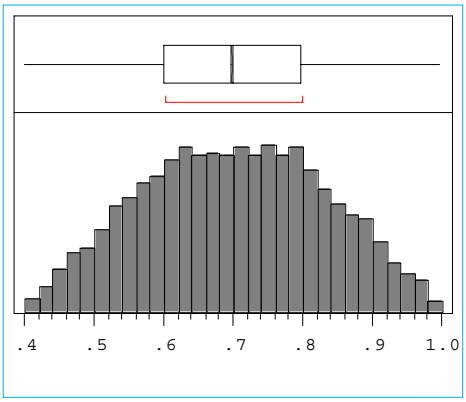

Figure C.3.13. Fraction of Solids Mobilized by the Pump that Remain Suspended, FP

Quantiles		
maximum	100.0%	0.99958
	99.5%	0.97974
	97.5%	0.94427
	90.0%	0.87912
quartile	75.0%	0.79924
median	50.0%	0.70075
quartile	25.0%	0.60011
	10.0%	0.52243
	2.5%	0.45551
	0.5%	0.41824
minimum	0.0%	0.40019

Moments	
Mean	0.70
Std Dev	0.13
Std Error Mean	0.00
Upper 95% Mean	0.70
Lower 95% Mean	0.70
N	10000.00
Sum Weights	10000.00

C.4 AN-105 Input Distributions

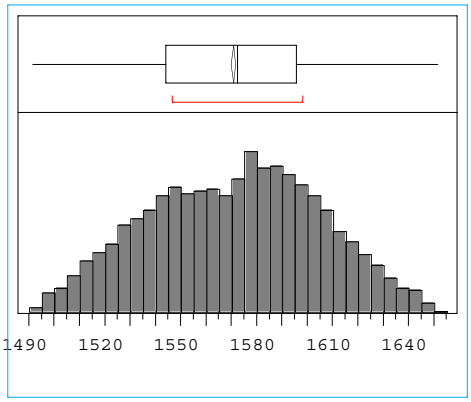

Figure C.4.1. Sediment Density, ρ_S (kg/m^3)

Quantiles		
maximum	100.0%	1651.9
	99.5%	1646.7
	97.5%	1635.6
	90.0%	1616.2
quartile	75.0%	1596.5
median	50.0%	1573.1
quartile	25.0%	1544.8
	10.0%	1524.4
	2.5%	1506.3
	0.5%	1496.0
minimum	0.0%	1492.1

Moments	
Mean	1571.04
Std Dev	34.47
Std Error Mean	0.34
Upper 95% Mean	1571.72
Lower 95% Mean	1570.36
N	10000.00
Sum Weights	10000.00

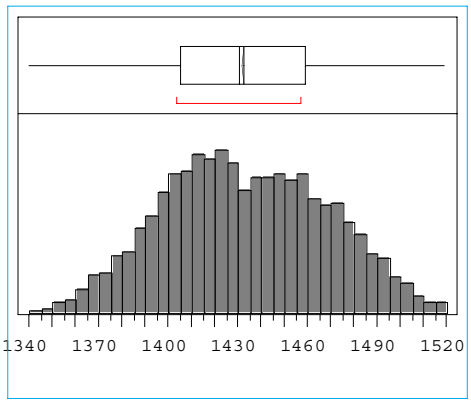

Figure C.4.2. Supernatant Liquid Density, ρ_L (kg/m^3)

Quantiles		
maximum	100.0%	1519.9
	99.5%	1514.8
	97.5%	1500.7
	90.0%	1481.4
quartile	75.0%	1459.6
median	50.0%	1431.5
quartile	25.0%	1406.2
	10.0%	1386.2
	2.5%	1364.9
	0.5%	1349.8
minimum	0.0%	1340.7

Moments	
Mean	1432.75
Std Dev	36.02
Std Error Mean	0.36
Upper 95% Mean	1433.45
Lower 95% Mean	1432.04
N	10000.00
Sum Weights	10000.00

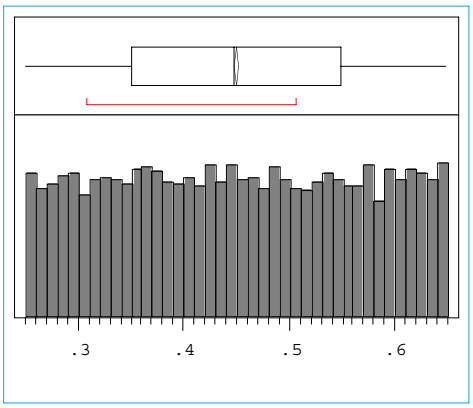

Figure C.4.3. Crust Thickness, h_C (m)

Quantiles		
maximum	100.0%	0.64993
	99.5%	0.64814
	97.5%	0.64095
	90.0%	0.61170
quartile	75.0%	0.55090
median	50.0%	0.44911
quartile	25.0%	0.35182
	10.0%	0.29076
	2.5%	0.25956
	0.5%	0.25159
minimum	0.0%	0.25003

Moments	
Mean	0.45
Std Dev	0.12
Std Error Mean	0.00
Upper 95% Mean	0.45
Lower 95% Mean	0.45
N	10000.00
Sum Weights	10000.00

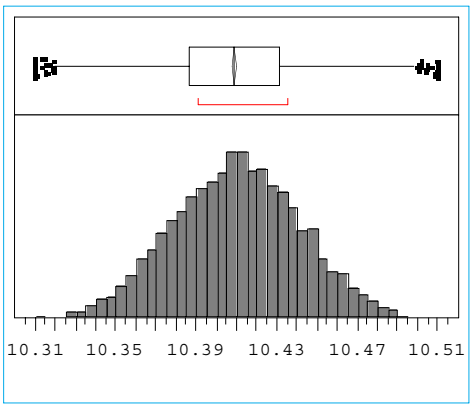

Figure C.4.4. Total Waste Thickness, h_T (m)

Quantiles		
maximum	100.0%	10.510
	99.5%	10.493
	97.5%	10.474
	90.0%	10.451
quartile	75.0%	10.432
median	50.0%	10.410
quartile	25.0%	10.387
	10.0%	10.367
	2.5%	10.344
	0.5%	10.326
minimum	0.0%	10.310

Moments	
Mean	10.41
Std Dev	0.03
Std Error Mean	0.00
Upper 95% Mean	10.41
Lower 95% Mean	10.41
N	10000.00
Sum Weights	10000.00

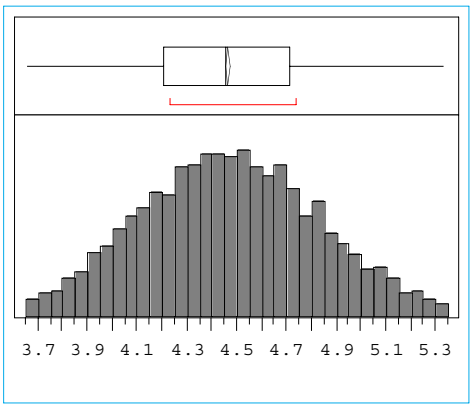

Figure C.4.5. Sediment Thickness, h_S (m)

Quantiles		
maximum	100.0%	5.3400
	99.5%	5.3105
	97.5%	5.1888
	90.0%	4.9485
quartile	75.0%	4.7183
median	50.0%	4.4640
quartile	25.0%	4.2126
	10.0%	3.9978
	2.5%	3.7964
	0.5%	3.6890
minimum	0.0%	3.6600

Moments	
Mean	4.47
Std Dev	0.36
Std Error Mean	0.00
Upper 95% Mean	4.48
Lower 95% Mean	4.46
N	10000.00
Sum Weights	10000.00

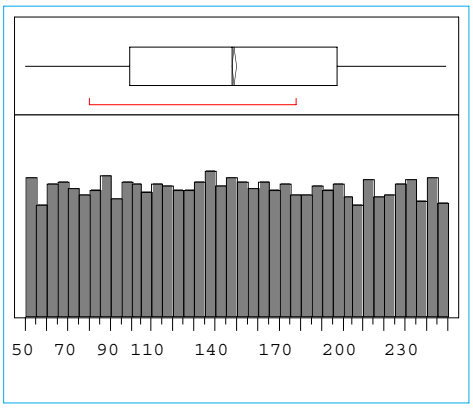

Figure C.4.6. Sediment Yield Stress, τ_y (Pa)

Quantiles		
maximum	100.0%	249.98
	99.5%	248.79
	97.5%	244.39
	90.0%	229.74
quartile	75.0%	198.43
median	50.0%	148.55
quartile	25.0%	99.92
	10.0%	69.90
	2.5%	54.49
	0.5%	50.80
minimum	0.0%	50.02

Moments	
Mean	149.32
Std Dev	57.43
Std Error Mean	0.57
Upper 95% Mean	150.44
Lower 95% Mean	148.19
N	10000.00
Sum Weights	10000.00

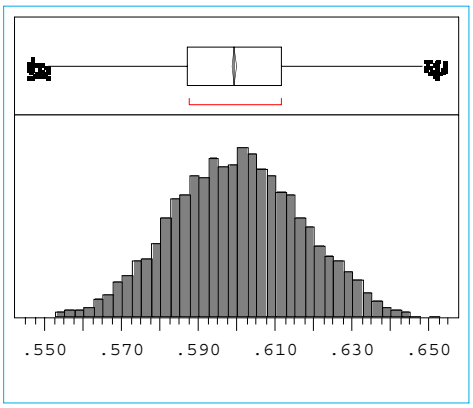

Figure C.4.7. Hydrogen Concentration in Gas Stored in Sediment Layer, χ_H

Quantiles		
maximum	100.0%	0.65400
	99.5%	0.64551
	97.5%	0.63495
	90.0%	0.62331
quartile	75.0%	0.61192
median	50.0%	0.59987
quartile	25.0%	0.58761
	10.0%	0.57688
	2.5%	0.56449
	0.5%	0.55371
minimum	0.0%	0.54600

Moments	
Mean	0.60
Std Dev	0.02
Std Error Mean	0.00
Upper 95% Mean	0.60
Lower 95% Mean	0.60
N	10000.00
Sum Weights	10000.00

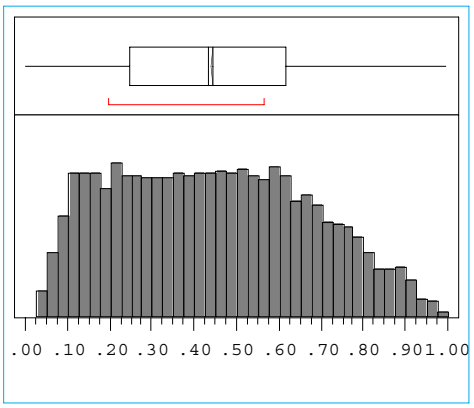

Figure C.4.8. Fraction of Released Sediment Material that Remains Suspended in the Supernate

Quantiles		
maximum	100.0%	0.99888
	99.5%	0.96279
	97.5%	0.89333
	90.0%	0.76654
quartile	75.0%	0.62016
median	50.0%	0.43653
quartile	25.0%	0.25009
	10.0%	0.13923
	2.5%	0.07677
	0.5%	0.04332
minimum	0.0%	0.00044

Moments	
Mean	0.44
Std Dev	0.23
Std Error Mean	0.00
Upper 95% Mean	0.45
Lower 95% Mean	0.44
N	10000.00
Sum Weights	10000.00

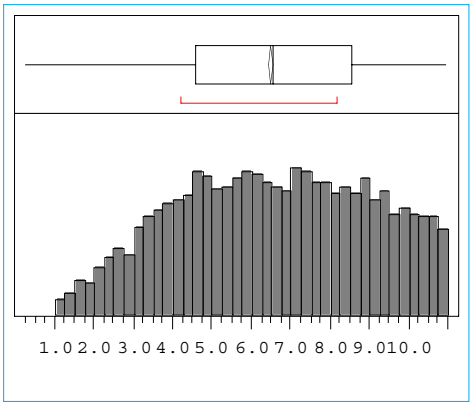

Figure C.4.9. Gob Diameter

Quantiles		
maximum	100.0%	10.997
	99.5%	10.928
	97.5%	10.695
	90.0%	9.895
quartile	75.0%	8.562
median	50.0%	6.560
quartile	25.0%	4.596
	10.0%	3.157
	2.5%	1.900
	0.5%	1.191
minimum	0.0%	0.290

Moments	
Mean	6.53
Std Dev	2.48
Std Error Mean	0.02
Upper 95% Mean	6.58
Lower 95% Mean	6.48
N	10000.00
Sum Weights	10000.00

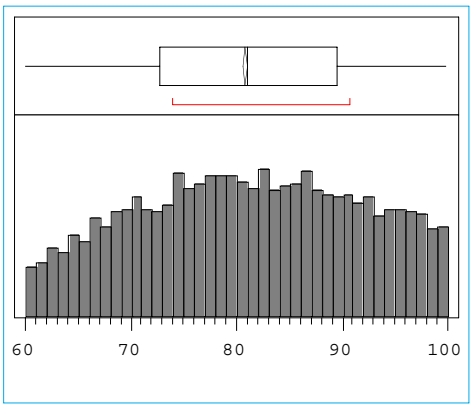

Figure C.4.10. Initial Gas Volume in Sediment Layer, V_{G0} (m^3)

Quantiles		
maximum	100.0%	99.999
	99.5%	99.777
	97.5%	98.769
	90.0%	95.461
quartile	75.0%	89.526
median	50.0%	81.093
quartile	25.0%	72.762
	10.0%	66.397
	2.5%	62.021
	0.5%	60.469
minimum	0.0%	60.012

Moments	
Mean	80.99
Std Dev	10.49
Std Error Mean	0.10
Upper 95% Mean	81.19
Lower 95% Mean	80.78
N	10000.00
Sum Weights	10000.00

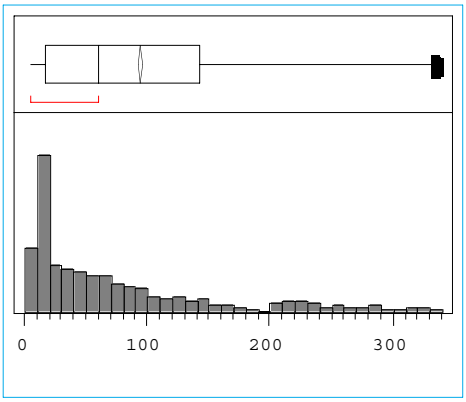

Figure C.4.11. Time to Peak Gas Release Rate, τ (min)

Quantiles		
maximum	100.0%	339.00
	99.5%	335.23
	97.5%	316.99
	90.0%	250.24
quartile	75.0%	144.23
median	50.0%	60.58
quartile	25.0%	18.84
	10.0%	10.95
	2.5%	6.72
	0.5%	5.55
minimum	0.0%	5.19

Moments	
Mean	95.11
Std Dev	92.19
Std Error Mean	0.92
Upper 95% Mean	96.92
Lower 95% Mean	93.30
N	10000.00
Sum Weights	10000.00

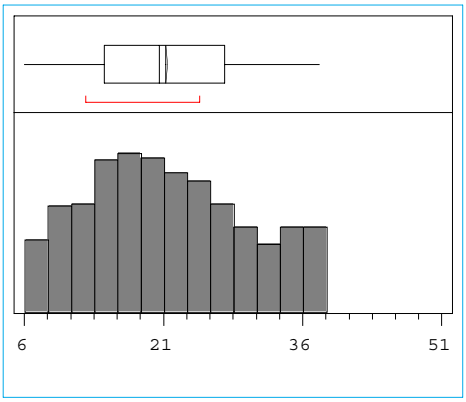

Figure C.4.12. Time to the Peak Gas Release Rate for Mixer Pump Operations, τ_p (min)

Quantiles		
maximum	100.0%	37.999
	99.5%	37.820
	97.5%	37.126
	90.0%	34.620
quartile	75.0%	27.639
median	50.0%	20.614
quartile	25.0%	14.779
	10.0%	9.981
	2.5%	7.403
	0.5%	6.339
minimum	0.0%	6.015

Moments	
Mean	21.40
Std Dev	8.47
Std Error Mean	0.08
Upper 95% Mean	21.56
Lower 95% Mean	21.23
N	10000.00
Sum Weights	10000.00

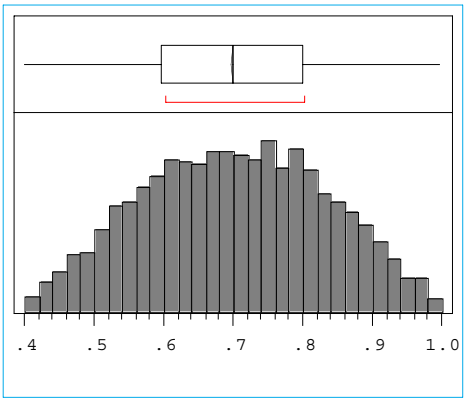

Figure C.4.13. Fraction of Solids Mobilized by the Pump that Remain Suspended, FP

Quantiles		
maximum	100.0%	0.99970
	99.5%	0.98364
	97.5%	0.94468
	90.0%	0.87897
quartile	75.0%	0.80031
median	50.0%	0.70167
quartile	25.0%	0.59985
	10.0%	0.52193
	2.5%	0.45367
	0.5%	0.41694
minimum	0.0%	0.40041

Moments	
Mean	0.70
Std Dev	0.13
Std Error Mean	0.00
Upper 95% Mean	0.70
Lower 95% Mean	0.70
N	10000.00
Sum Weights	10000.00

C.5 AW101 Input Distributions

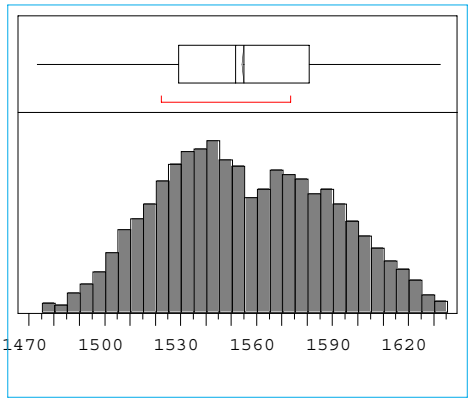

Figure C.5.1. Sediment Density, ρ_S (kg/m^3)

Quantiles		
maximum	100.0%	1632.9
	99.5%	1630.1
	97.5%	1619.9
	90.0%	1601.3
quartile	75.0%	1580.9
median	50.0%	1552.4
quartile	25.0%	1529.4
	10.0%	1511.5
	2.5%	1494.0
	0.5%	1479.7
minimum	0.0%	1473.4

Moments	
Mean	1555.09
Std Dev	33.83
Std Error Mean	0.34
Upper 95% Mean	1555.75
Lower 95% Mean	1554.42
N	10000.00
Sum Weights	10000.00

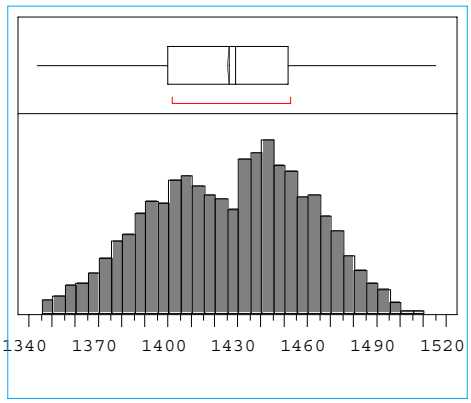

Figure C.5.2. Supernatant Liquid Density, ρ_L (kg/m^3)

Quantiles		
maximum	100.0%	1515.5
	99.5%	1502.8
	97.5%	1488.7
	90.0%	1470.2
quartile	75.0%	1451.8
median	50.0%	1429.2
quartile	25.0%	1400.7
	10.0%	1380.0
	2.5%	1359.9
	0.5%	1348.3
minimum	0.0%	1344.1

Moments	
Mean	1426.40
Std Dev	34.21
Std Error Mean	0.34
Upper 95% Mean	1427.07
Lower 95% Mean	1425.73
N	10000.00
Sum Weights	10000.00

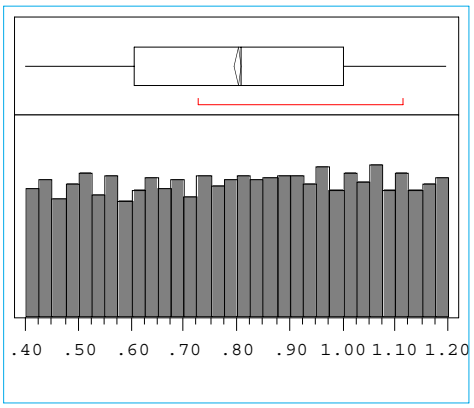

Figure C.5.3 Crust Thickness, h_C (m)

Quantiles		
maximum	100.0%	1.1999
	99.5%	1.1965
	97.5%	1.1811
	90.0%	1.1192
quartile	75.0%	1.0027
median	50.0%	0.8091
quartile	25.0%	0.6072
	10.0%	0.4839
	2.5%	0.4202
	0.5%	0.4049
minimum	0.0%	0.4001

Moments	
Mean	0.80
Std Dev	0.23
Std Error Mean	0.00
Upper 95% Mean	0.81
Lower 95% Mean	0.80
N	10000.00
Sum Weights	10000.00

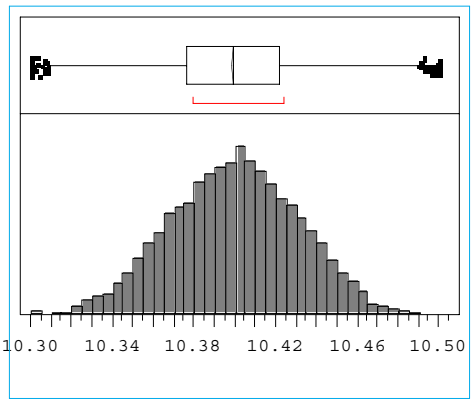

Figure C.5.4. Total Waste Thickness, h_T (m)

Quantiles		
maximum	100.0%	10.500
	99.5%	10.485
	97.5%	10.462
	90.0%	10.442
quartile	75.0%	10.422
median	50.0%	10.400
quartile	25.0%	10.377
	10.0%	10.357
	2.5%	10.333
	0.5%	10.313
minimum	0.0%	10.300

Moments	
Mean	10.40
Std Dev	0.03
Std Error Mean	0.00
Upper 95% Mean	10.40
Lower 95% Mean	10.40
N	10000.00
Sum Weights	10000.00

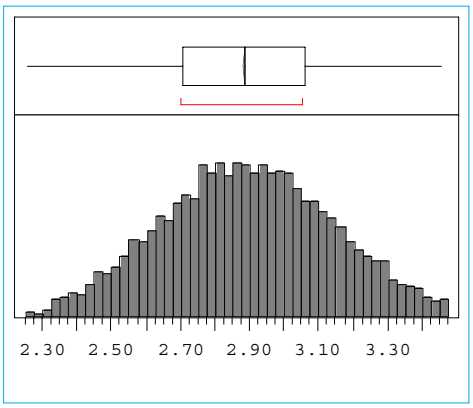

Figure C.5.5. Sediment Thickness, h_S (m)

Quantiles		
maximum	100.0%	3.4600
	99.5%	3.4518
	97.5%	3.3736
	90.0%	3.2190
quartile	75.0%	3.0630
median	50.0%	2.8875
quartile	25.0%	2.7129
	10.0%	2.5574
	2.5%	2.3982
	0.5%	2.3051
minimum	0.0%	2.2600

Moments	
Mean	2.89
Std Dev	0.25
Std Error Mean	0.00
Upper 95% Mean	2.89
Lower 95% Mean	2.88
N	10000.00
Sum Weights	10000.00

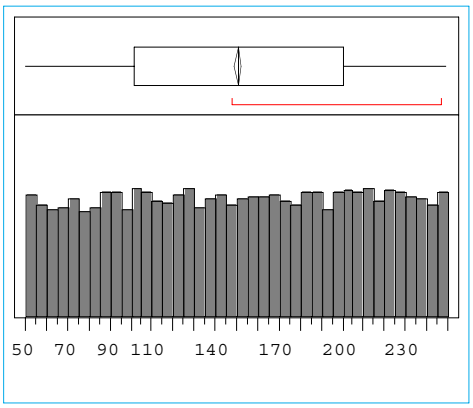

Figure C.5.6. Sediment Yield Stress, τ_y (Pa)

Quantiles		
maximum	100.0%	249.96
	99.5%	249.14
	97.5%	245.41
	90.0%	230.03
quartile	75.0%	201.50
median	50.0%	151.50
quartile	25.0%	101.62
	10.0%	71.08
	2.5%	54.67
	0.5%	50.90
minimum	0.0%	50.01

Moments	
Mean	151.05
Std Dev	57.57
Std Error Mean	0.58
Upper 95% Mean	152.18
Lower 95% Mean	149.92
N	10000.00
Sum Weights	10000.00

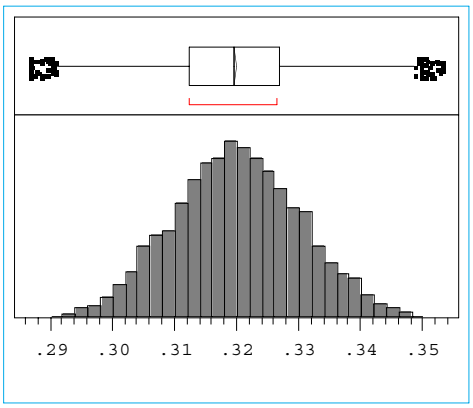

Figure C.5.7. Hydrogen Concentration in gas stored in Sediment Layer, χ_H

Quantiles		
maximum	100.0%	0.35300
	99.5%	0.34756
	97.5%	0.34129
	90.0%	0.33386
quartile	75.0%	0.32711
median	50.0%	0.31984
quartile	25.0%	0.31271
	10.0%	0.30582
	2.5%	0.29868
	0.5%	0.29131
minimum	0.0%	0.28700

Moments	
Mean	0.32
Std Dev	0.01
Std Error Mean	0.00
Upper 95% Mean	0.32
Lower 95% Mean	0.32
N	10000.00
Sum Weights	10000.00

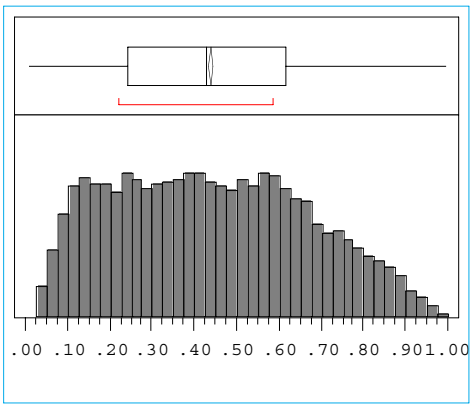

Figure C.5.8. Fraction of Released Sediment Material that Remains Suspended in the Supernate

Quantiles		
maximum	100.0%	0.99643
	99.5%	0.95349
	97.5%	0.88518
	90.0%	0.76494
quartile	75.0%	0.61616
median	50.0%	0.43022
quartile	25.0%	0.24695
	10.0%	0.13494
	2.5%	0.07312
	0.5%	0.03813
minimum	0.0%	0.01469

Moments	
Mean	0.44
Std Dev	0.23
Std Error Mean	0.00
Upper 95% Mean	0.45
Lower 95% Mean	0.44
N	10000.00
Sum Weights	10000.00

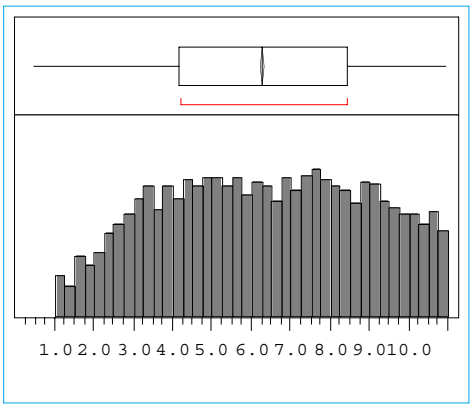

Figure C.5.9. Gob Diameter

Quantiles		
maximum	100.0%	10.999
	99.5%	10.943
	97.5%	10.692
	90.0%	9.853
quartile	75.0%	8.453
median	50.0%	6.327
quartile	25.0%	4.208
	10.0%	2.788
	2.5%	1.593
	0.5%	1.108
minimum	0.0%	0.472

Moments	
Mean	6.30
Std Dev	2.60
Std Error Mean	0.03
Upper 95% Mean	6.35
Lower 95% Mean	6.25
N	10000.00
Sum Weights	10000.00

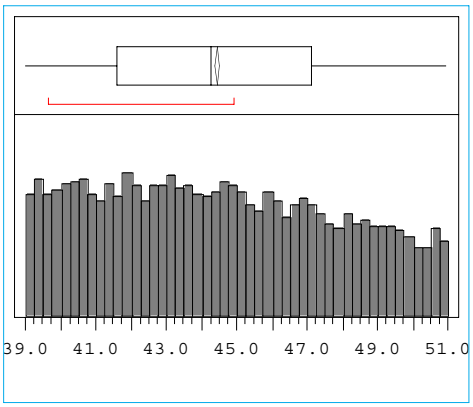

Figure C.5.10. Initial Gas Volume in Sediment Layer, V_{G0} (m^3)

Quantiles		
maximum	100.0%	50.999
	99.5%	50.907
	97.5%	50.580
	90.0%	49.305
quartile	75.0%	47.174
median	50.0%	44.312
quartile	25.0%	41.659
	10.0%	40.064
	2.5%	39.270
	0.5%	39.050
minimum	0.0%	39.000

Moments	
Mean	44.50
Std Dev	3.34
Std Error Mean	0.03
Upper 95% Mean	44.56
Lower 95% Mean	44.43
N	10000.00
Sum Weights	10000.00

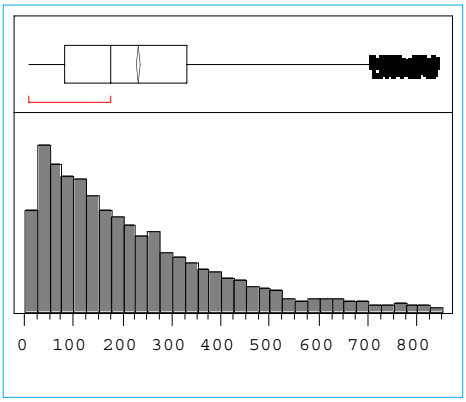

Figure C.5.11. Time to Peak Gas Release Rate, τ (min)

Quantiles		
maximum	100.0%	840.35
	99.5%	823.46
	97.5%	747.34
	90.0%	521.63
quartile	75.0%	332.72
median	50.0%	180.07
quartile	25.0%	83.38
	10.0%	37.49
	2.5%	16.57
	0.5%	11.36
minimum	0.0%	9.72

Moments	
Mean	234.81
Std Dev	193.50
Std Error Mean	1.93
Upper 95% Mean	238.61
Lower 95% Mean	231.02
N	10000.00
Sum Weights	10000.00

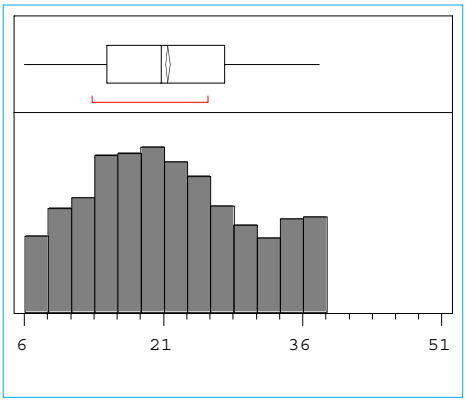

Figure C.5.12. Time to the Peak Gas Release Rate for Mixer Pump Operations, τ_p (min)

Quantiles		
maximum	100.0%	37.992
	99.5%	37.847
	97.5%	37.195
	90.0%	34.877
quartile	75.0%	27.724
median	50.0%	20.794
quartile	25.0%	14.880
	10.0%	10.122
	2.5%	7.368
	0.5%	6.417
minimum	0.0%	6.001

Moments	
Mean	21.53
Std Dev	8.54
Std Error Mean	0.09
Upper 95% Mean	21.69
Lower 95% Mean	21.36
N	10000.00
Sum Weights	10000.00

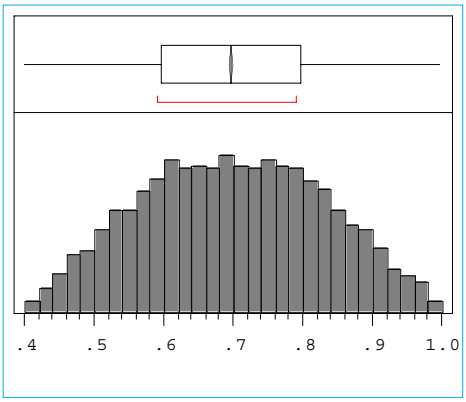

Figure C.5.13. Fraction of Solids Mobilized by the Pump that Remain Suspended, FP

Quantiles		
maximum	100.0%	0.99970
	99.5%	0.98018
	97.5%	0.94495
	90.0%	0.87738
quartile	75.0%	0.79932
median	50.0%	0.69818
quartile	25.0%	0.59803
	10.0%	0.52029
	2.5%	0.45577
	0.5%	0.41819
minimum	0.0%	0.40019

Moments	
Mean	0.70
Std Dev	0.13
Std Error Mean	0.00
Upper 95% Mean	0.70
Lower 95% Mean	0.70
N	10000.00
Sum Weights	10000.00

Appendix D

Maximum Volume of Sludge Scoured by an Impinging Jet—A Solid Mechanics Approach

Appendix D

Maximum Volume of Sludge Scoured by an Impinging Jet—A Solid Mechanics Approach

In this appendix, an alternative approach is described for determining the maximum volume of sludge scoured by a submerged turbulent jet. This approach is based on the assumption that the sludge behaves as an elastoplastic solid of known mechanical properties. Because we are not interested in determining the displacement vectors but rather the volume removed, knowledge of the Young's modulus of elasticity is not necessary. However, the yield stress of the sludge in shear τ must be known. As shown in Figure D.1, the Poisson's ratio of the sludge ν, which is a measure of its compressibility, does not have a considerable effect on the volume of sludge removed by scouring.

A turbulent jet impinging on a solid body will exert a force at the fluid-solid boundary, which in turn will give rise to a stress distribution within the solid body. Sludge material will be removed provided the state of stress within the sludge exceeds the yield stress of the material. Therefore, the first step in this approach is to determine the state of stress caused by an impinging turbulent jet within the sludge. An analytic solution for the stress distribution within a half solid mass of infinite extent caused by a force of arbitrary orientation was derived by Mindlin (1936). For simplicity, it will be assumed that the jet impingement is perpendicular to the mass of sludge, as illustrated in Figure D.1.

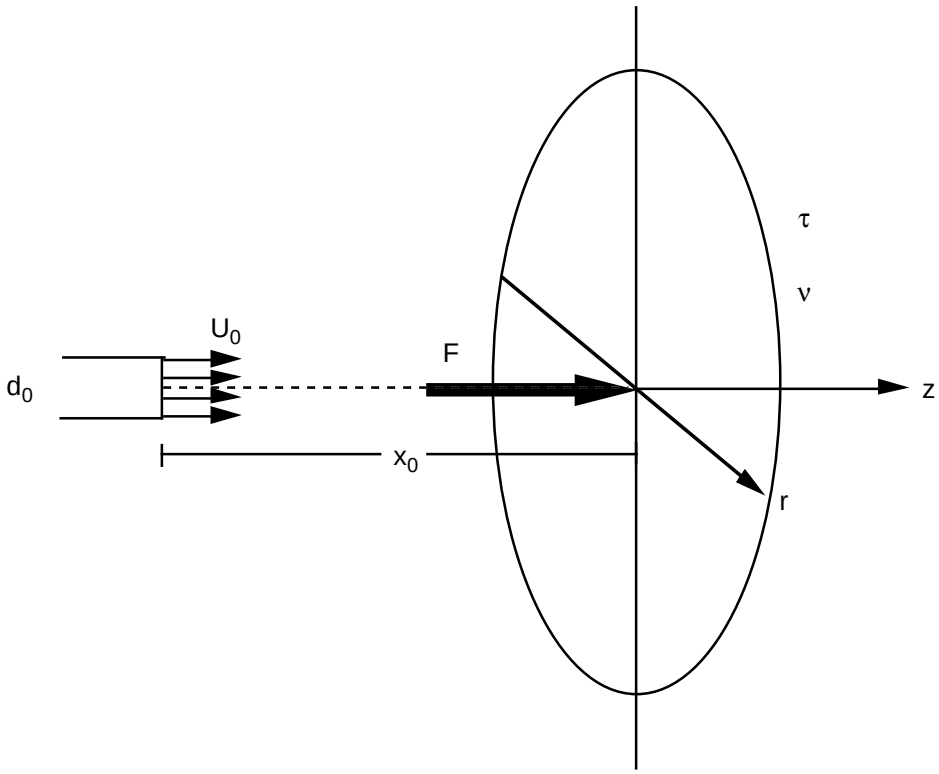

Figure D.1. Schematic of Jet Impinging Normally on an Elastoplastic Solid

Even for this simple configuration, the state of stress is three-dimensional and, in cylindrical coordinates, is given by the following stress tensor:

$$\sigma_{ij} = \frac{F}{2\pi R^3}\begin{bmatrix} (1-2\nu)\left[z - \frac{R^2}{z+R} + \frac{r^2(z+2R)}{(z+R)^2}\right] - \frac{3r^2 z}{R^2} & 0 & -\frac{3rz^2}{R^2} \\ 0 & (1-2\nu)\left(z - \frac{R^2}{z+R}\right) & 0 \\ -\frac{3rz^2}{R^2} & 0 & -\frac{3z^3}{R^2} \end{bmatrix} \quad \text{(D.1)}$$

where F is the magnitude of the force exerted on the solid mass, r is the radial coordinate, z is the axial coordinate, ν is the Poisson ratio, and $R = \sqrt{r^2 + z^2}$.

According to Rajaratnam's experimental measurements, the radial pressure distribution on a flat solid surface from the point of impingement is given by

$$p(r) = 25\rho\left(\frac{U_0 d_0}{x_0}\right)^2 \exp\left[-114\left(\frac{r}{x_0}\right)^2\right] \quad \text{(D.2)}$$

where x_0 is the normal distance between the jet nozzle and the solid boundary. Thus, the total impingement force exerted by the jet on the semi-infinite solid is

$$F = 2\pi\int_0^\infty p(r)\, r\, dr = \frac{25\pi}{114}\rho\left(U_0 d_0\right)^2 \quad \text{(D.3)}$$

To bound the volume estimate of sludge removed, we assumed that the total force exerted on the sludge is concentrated on the point of impingement. Therefore, the state of stress within the sludge mass is obtained by substituting Eq. (D.3) into Eq. (D.1). To determine whether the sludge is subjected to yielding under a three-dimensional state of stress, a suitable yielding criterion must be applied. The von Mises yielding criterion (Lubliner 1990) adequately describes the onset of yielding for a large class of solids and will be used in this analysis. For our purposes, using a different yielding criterion would have little effect on the final volume of sludge that will be dislodged. For a three-dimensional state of stress, applying a yielding criterion involves calculating an "equivalent stress" above which the material will yield. With the von Mises criterion, this is accomplished by calculating the second invariant of the deviatoric stress tensor. The deviatoric stress tensor S_{ij} is defined as the stress tensor minus the hydrostatic pressure:

$$s_{ij} = \begin{bmatrix} \sigma_{xx} & \sigma_{xy} & \sigma_{xz} \\ \sigma_{yx} & \sigma_{yy} & \sigma_{yz} \\ \sigma_{zx} & \sigma_{zy} & \sigma_{zz} \end{bmatrix} - \frac{\sigma_{xx} + \sigma_{yy} + \sigma_{zz}}{3}\begin{bmatrix} 1 & 0 & 0 \\ 0 & 1 & 0 \\ 0 & 0 & 1 \end{bmatrix} \quad \text{(D.4)}$$

The second invariant of S_{ij} is denoted by J_2 and is obtained from its characteristic polynomial, which in terms of the variable t can be written as

$$J_2 = \frac{d}{dt}\left(\left|s_{ij} - t\delta_{ij}\right|\right)\Big|_{t=0} \tag{D.5}$$

where δ_{ij} is the Kronecker delta (i.e., the components of the unit tensor). In terms of the sludge yield stress in pure shear, τ, the von Mises yielding criterion is

$$J_2 = \tau^2 \tag{D.6}$$

At any point within the sludge where the von Mises criterion is satisfied, the material will yield and thus be removed by the action of the impinging jet. There will be axial and lateral length scales within the sludge for which the force of the jet will not be sufficiently high to yield the material. To determine these length scales, it is necessary to calculate the surface that separates the region where the sludge has undergone plastic deformation from that in which only elastic deformations occur. For a given τ, the equation that defines the elastic-plastic boundary, G(r,z), is obtained by substituting Eq. (D.1), (D.3), (D.4), and (D.5) into (D.6)

$$G(r,z) = \tau - \frac{25\rho(U_0 d_0)^2}{228\sqrt{3}\,R^3}\times$$
$$\sqrt{\frac{(7-2\nu)^2 z^4 (z+R) - 3r^4(1-2\nu)\left[3z-(1-2\nu)R\right] + (rz)^2\left[18(1+\nu)z + (4\nu^2+26\nu-5)R\right]}{(z+R)^3}} \tag{D.7}$$

The maximum penetration depth of the jet into the sludge will occur along the jet axis; thus, the axial length scale L_Z is obtained from $F(0,L_Z)$:

$$L_z = \frac{5}{2}\sqrt{\frac{(7-2\nu)\rho}{38\sqrt{27}\,\tau}}\,U_0 d_0 \tag{D.8}$$

An expression for the lateral length scale L_r can be obtained in closed form under the assumption of sludge incompressibility (i.e., v = 1/2) by finding the ordinate of the maximum of the radial coordinate as a function of the axial coordinate. Equivalently, L_r is found by solving the following system of equations:

$$\begin{cases} G\left(L_r, z\right) = 0 \\ \dfrac{\partial G\left(L_r, z\right)}{\partial z} = 0 \end{cases} \tag{D.9}$$

from which it follows that

$$L_r = \frac{5}{3}\sqrt{\frac{\rho}{38\tau}}U_0 d_0 \tag{D.10}$$

Even though the precise volume enclosed by the elastic-plastic surface boundary can be calculated numerically from Eq. (D.7), a measure of the volume of sludge yielded by the action of the jet can be readily obtained by assuming that L_r is the radius of a cylinder of depth L_Z:

$$V_1 = \pi L_r^2 L_z = \frac{125\pi}{684}\sqrt{\frac{7-2\nu}{38\sqrt{27}}}\left(\frac{\rho}{\tau}\right)^{3/2}\left(U_0 d_0\right)^3 \tag{D.11}$$

Notice that the volume in Eq. (D.11) depends weakly on v. Besides the impact force imparted to the sludge by the jet, erosion plays an important role in determining the volume of sludge removed. Erosion is not easily quantifiable for a general solid material for two reasons. First, it depends on the particular microstructure of the sludge. Second, the erosion process depends on the secondary flow pattern within the cavity formed as a result of the removal of yielded material by the initial impact of the jet. Erosion will contribute to additional scouring of material beyond that given by Eq. (D.11). Therefore, a more conservative estimate of removed volume could be given by using the axial length scale alone

$$V_2 = \frac{2\pi}{3}L_z^3 = \frac{125\pi}{4104\sqrt{38\sqrt{3}}}\left[\frac{(7-2\nu)\rho}{\tau}\right]^{3/2}\left(U_0 d_0\right)^3 \tag{D.12}$$

From Eq. (D.12) it can be shown that an average value of the volume, V_2, for a range of v is

$$V_2 \approx 0.2\left(\frac{\rho}{\tau}\right)^{3/2}\left(U_0 d_0\right)^3 \tag{D.13}$$

Therefore, the maximum amount of gas released due to sludge scouring by the impinging jet is

$$V_{\max} \approx 0.2\alpha p\left(\frac{\rho}{\tau}\right)^{3/2}\left(U_0 d_0\right)^3 \tag{D.14}$$

Notice that the functional form of Eq. (D.14) is identical to Eq. (4.45) in the main report. For the parameters used to generate Figure 4.18, the value of V_{max} predicted by Eq. (4.45) is 2.6 times larger that that predicted by Eq. (D.14).

References

Lubliner J. 1990. *Plasticity Theory*. Macmillan Publishing Company, New York.

Mindlin RD. 1936. "Force at a Point in the Interior of Semi-Infinite Solid." *Physics*, Vol. 7, pp. 195–202.

Rajaratnam N. 1976. *Turbulent Jets*. Elsevier Scientific Publishing Co., Amsterdam.